Constraining Substellar Magnetic Dynamos using Brown Dwarf Radio Aurorae

Thesis by
Melodie M. Kao

In Partial Fulfillment of the Requirements for the
degree of
Doctor of Philosophy

CALIFORNIA INSTITUTE OF TECHNOLOGY
Pasadena, California

2017
Defended 30 May 2017

Melodie M. Kao
ORCID: 0000-0001-5125-1414

To the Order of the Lepton

Proceeding eighty miles into the northwest wind, you reach the city of Euphemia, where the merchants of seven nations gather at every solstice and equinox. The boat that lands there with a cargo of ginger and cotton will set sail again, its hold filled with pistachio nuts and poppy seeds, and the caravan that has just unloaded sacks of nutmegs and raisins is already cramming its saddlebags with bolts of golden muslin for the return journey. But what drives men to travel up rivers and cross deserts to come here is not only the exchange of wares, which you could find, everywhere the same, in all the bazaars inside and outside the Great Khan's empire, scattered at your feet on the same yellow mats, in the shade of the same awnings protecting them from the flies, offered with the same lying reduction in prices. You do not come to Euphemia only to buy and sell, but also because at night, by the fires all around the market, seated on sacks or barrels or stretched out on piles of carpets, at each word that one man says—such as "wolf," "sister," "hidden treasure," "battle," "scabies," "lovers"—the others tell, each one, his tale of wolves, sisters, treasures, scabies, lovers, battles. And you know that in the long journey ahead of you, when to keep awake against the camel's swaying or the junk's rocking, you start summoning up your memories one by one, your wolf will have become another wolf, your sister a different sister, your battle other battles, on your return from Euphemia, the city where memory is traded at every solstice and at every equinox.

Italo Calvino
Excerpt from *Invisible Cities*

ACKNOWLEDGEMENTS

The many challenges that I have encountered during my time in graduate school have taught me that the act of raising a graduate student is truly a community endeavor. To that end, many people and organizations deserve heartfelt gratitude for their contributions to my doctoral thesis:

First and foremost, I thank my graduate adviser Gregg Hallinan for wholeheartedly supporting me these last several years with his generosity, patience, unparalleled creativity, and fierce belief in my scientific and intellectual ability. The research group that you built and supported truly was a home for me, and our playfulness and good spirits are a reflection of the good-hearted culture that you created. Your willingness to adjust and provide guidance or space as I needed has allowed me find my own way and emerge stronger and more confident from a challenging time in my life. You have taught me how to focus on the essence of what is most important, both in my work and in life and to hold steadfastly to what I value and pursue doggedly my dreams with the utmost standard.

I also thank the members of my thesis committee, Lynne Hillenbrand, Shri Kulkarni, Sterl Phinney, and Dave Stevenson, for the insight that you have been happy to share with me, your exacting standards and enthusiasm for my science, and your concern for myself and all students.

To the National Radio Astronomy Observatory, my time in Socorro as a Grote Reber Fellow has truly been among my most happy and productive in graduate school. I thank the many radio astronomers and staff there who have helped speed me toward the completion of my thesis while providing a truly welcoming intellectual home for me, and I am grateful to the Observatory for supporting such an invaluable student program. In particular, I thank Dale Frail, Steve Myers, Preshanth Jagannathan, Amy Kimball, Lorant Sjouwerman, Drew Medlin, and Emmanuel Momjian for their kind and attentive mentorship, their happy willingness to teach me how to write stronger proposals and analyze my data more quickly and more confidently, and their efforts to embed me more deeply in the radio astronomy community and feed me in the final weeks of my PhD.

To my dear undergraduate adviser, Paul Schechter, this dissertation is a culmination of the many years of reassurance and wisdom that you have bestowed upon me since the moment I first changed course from Architecture to Physics. As an

undergraduate, I relied on your unwavering belief in my ability and judgement in times of great doubt. As a graduate student, I often recalled much of the advice that you have shared with me and I will forevermore continue to hold your wisdom as a guiding star in my life.

To Sebastian Pineda, the arc of our friendship has traveled far, and through all of it you have been truly the best friend I never knew I would ever have. You believed in me always, even when I had lost my ability to see. Your incomparable decency and selfless devotion will remain with me always as the way that I also wish to live my life. Without your compassion, love and patience, I would not be here today. I have no doubt that you will be a much loved and celebrated professor one day soon, and all of your future students will go forth in their lives bearing your light (and perhaps penchant for mischief), as I do.

To Jackie Villadsen, your singular ability to see each person's worth taught me that our love is always expanding. During my most challenging moments, the conviction of your love flowed into me and through me and buoyed me, insistent in its strength and tenacity. I treasure our many discussions, in which you challenged me to see the world beyond my blindness and shared with me the beauty of your principles, philosophies, and faith. Through your steadfast dedication to pedagogy, I learned a way to think that illuminated a particular poetry in physics that shapes all of my thinking today, and you serve as my clearest role model for how I wish to teach, mentor, and lead others. My work in graduate school — both personal and professional — is a reflection of how you bring with you a lightness and love that gently, persistently, and fiercely calls to those around you to join you in living as our best versions of ourselves wherever we may journey in life.

To the rest of my wonderfully playful research group — Michael Eastwood, Marin Anderson, Ryan Monroe, and Kunal Mooley — you have truly been my family through my metamorphosis into a radio astronomer, and your practical jokes, thoughtful discussions, and sunny demeanors have taught me how kindness and optimism build conduits of connection.

To Cameron Voloshin, together we have explored many worlds and I thank you for the thoughtful wisdom and multitude of helmets that you have given me throughout these years. Our mutual support and deep regard for one another has taught me the power of surrounding myself with those who believe in me fiercely, give generously, and whose strengths and weaknesses complement my own. You have helped me advocate for my dreams, pushed me to always grow and explore beyond my comfort

zone, and taught me how to build paths back over bridges. I am not a fearless woman, but from you I have learned how to fear fully and gracefully.

To Shane Crosby and Amy Zhou, since the beginning of a very different journey, you have both been there to listen intently to my thoughts and to share your insight. I am so glad that each morning I can look forward to starting our workday together, and I cherish our check-ins where we have cheered for each other and kept one another on task even when I lived very far from you.

To Lauren Montemayor, you have stood with me since our freshman year in college. Where you walk, you build your family, and you have taught me that true friendship is a refusal to abandon those you value.

To Matt Gethers, thank you for your steady friendship and our many coffee chats. These small moments I shared with you were among the times that I cherished most at Caltech.

To Althea, Gita, Patrick, Anu: you are among the unsung heroes in our department, who make possible the journey of a graduate student with your tireless efforts to keep our department and computers working!

Finally, to my family and especially my mom and dad: thank you for supporting me these many years and shaping the person I am today.

ABSTRACT

Brown dwarfs share characteristics with both low-mass stars and gas giant planets, making them useful laboratories for studying physics occurring in objects throughout this low mass and temperature range. Of particular interest in this dissertation is the nature of the engine driving their magnetic fields. Fully convective magnetic dynamos can operate in low mass stars, brown dwarfs, gas giant planets, and even fluid metal cores in small rocky planets. Objects in this wide mass range are capable of hosting strong magnetic fields, which shape much of the evolution of planets and stars: strong fields can protect planetary atmospheres from evaporating, generate optical and infrared emission that masquerade as clouds in the atmospheres of other worlds, and affect planet formation mechanisms. Thus, implications from understanding convective dynamo mechanisms also extend to exoplanet habitability.

How the convective dynamos driving these fields operate remains an important open problem. While we have extensive data to inform models of magnetic dynamo mechanisms in higher mass stars like our Sun, the coolest and lowest-mass objects that probe the substellar-planetary boundary do not possess the internal structures necessary to drive solar-type dynamos. A number of models examining fully convective dynamo mechanisms have been proposed but they remain unconstrained by magnetic field measurements in the lowest end of the substellar mass and temperature space. Detections of highly circularly polarized pulsed radio emission provide our only window into magnetic field measurements for objects in the ultracool brown dwarf regime, but these detections are very rare; until this dissertation, only one attempt out of ~60 had been successful.

The work presented in this dissertation seeks to address this problem and examines radio emission from late L, T, and Y spectral type brown dwarfs spanning ~1–6 times the surface temperature of Earth and explores implications for fully convective magnetic dynamo models.

PUBLISHED CONTENT AND CONTRIBUTIONS

Kao, M. M., G. Hallinan, J. S. Pineda, I. Escala, A. Burgasser, S. Bourke, and D. Stevenson. 2016. "Auroral Radio Emission from Late L and T Dwarfs: A New Constraint on Dynamo Theory in the Substellar Regime." *ApJ* 818, 24 (February): 24.

MMK was the lead author and conducted all radio observations, reduced and analyzed all radio data, and wrote the article, except for section concerning brown dwarf physical parameters. doi:10.3847/0004-637X/818/1/24. arXiv: 1511.03661 [astro-ph.SR].

TABLE OF CONTENTS

Acknowledgements v
Abstract viii
Published Content and Contributions ix
Table of Contents x
List of Illustrations xiii
List of Tables xvii
Chapter I: Introduction 1
1.1 A Case for Studying Brown Dwarf Magnetism 1
1.2 Overview of Dynamo Models 4
1.2.1 Scaling Laws 6
1.2.2 Numerical Simulations 7
1.2.3 Parameter Studies 10
1.3 Auroral Emission: A New Paradigm for Brown Dwarf Magnetism . . 12
1.3.1 Stellar Activity Paradigm 12
1.3.2 Observations of Stellar Magnetic Activity: Hints for a New Model of Magnetic Activity 13
1.3.3 Observations of Auroral Activity in Solar System Planets . . 18
1.4 Radio Activity in Brown Dwarfs 19
1.5 Overview of Dissertation Work 22
Chapter II: Methods: Developing Auroral Radio Emission into a Tool for Testing Dynamo Models 24
2.1 Testing Dynamo Models: Current Methods of Measuring Magnetic Fields 24
2.2 A Simple Formalism for Comparing Magnetic Field Measurements . 32
2.2.1 Magnetic Field Topology 32
2.2.2 Relating Magnetic Fields Measured from Auroral Radio Emission to Zeeman Techniques 35
Chapter III: Auroral radio emission from late L and T dwarfs: A new constraint on dynamo theory in the substellar regime 37
3.1 Abstract 37
3.2 Introduction 38
3.3 Target Selection Strategy 41
3.4 Targets 43
3.5 Observations 46
3.5.1 Calibrations 46
3.5.2 Source Motion 48
3.6 Results 48
3.6.1 Image Detections 48
3.6.2 Timeseries Pulse Detections & Magnetic Field Strengths . . 49

3.7 Estimating Physical Parameters of Brown Dwarfs 54
3.8 Discussion 57
3.8.1 Comparison to a Power-Based Dynamo Scaling Relation . . 57
3.8.2 Implications of Auroral Radio Emission Correlated with Brown Dwarf Weather and Hα Emission 61
3.9 Conclusions 63
3.10 Acknowledgements 64
Chapter IV: Constraints on Auroral Radio Emission from Y dwarfs 65
4.1 Abstract 65
4.2 Introduction 65
4.3 Targets 69
4.4 Observations 71
4.5 Calibrations 72
4.6 Results 73
4.7 Discussion 75
4.8 Conclusions 78
4.9 Acknowledgements 78
Chapter V: The Strongest Magnetic Fields on the Coolest Brown Dwarfs . . . 80
5.1 Abstract 80
5.2 Introduction 80
5.3 Targets 85
5.4 Observations 89
5.4.1 Calibrations 89
5.4.2 Source Motion 90
5.5 Results 90
5.5.1 Image Detections 90
5.5.2 Timeseries Pulse Detections & Magnetic Field Strengths . . 91
5.5.3 Rotation Period Measurements 100
5.6 Discussion 108
5.6.1 The Curious Case of Highly Circularly Polarized and/or Disappearing Quiescent Emission 108
5.6.2 Intermittent Pulses: Implications for ECM Emission Frequency Cutoff 111
5.6.3 Comparison to Luminosity-Driven Model 112
5.6.4 Consideration of Age-Related Models 116
5.6.5 Consideration of Models Examining the Role of Rotation . . 118
5.6.6 First Radio Detection of Planetary-Mass Object? 119
5.7 Conclusions 120
5.8 Acknowledgements 121
Chapter VI: Looking Ahead: Investigating the Relationship Between Auroral Radio Emission and Brown Dwarf Weather 122
6.1 Abstract 122
6.2 Introduction 122
6.2.1 Quiescent Radio Emission: A New Proxy for Auroral Radio Emission in Brown Dwarfs 125

6.3 Targets 126
6.4 Observations 127
6.4.1 Calibrations 127
6.5 Preliminary Results 128
6.6 Science Impact 130
Chapter VII: Conclusions 132
Bibliography 134

LIST OF ILLUSTRATIONS

Number *Page*

1.1 Illustration of $\alpha\Omega$-effect. Beginning from top left: In the Ω-effect, differential rotation shears a poloidal magnetic field into a toroidal field. In the α-effect, rising and twisting convection cells distort and twist the embedded magnetic field lines into loops, generating a current that leads to a poloidal field. Reprinted from Figure 2 in Love (1999). 5

1.2 Dipole fraction (y-axis) versus local Rossby number (x-axis) for a wide range of dynamo control parameters: Elsasser number Λ (point size), density contrast across dynamo shell $N_\rho = \ln(\rho_{\text{bottom}}/\rho_{\text{top}})$ (symbol type), and thickness of dynamo shells (red = thick, grey = thin). Dashed vertical lines denote tentative critical local Rossby number separating the multipolar/dipolar bistable regime versus the multipolar regime for the different shell thicknesses. Reproduced from Gastine et al. (2013), with permission from Astronomy & Astrophysics, © ESO. 9

1.3 **(a)** Dynamo models in the rapidly rotating (local Rossby number <0.12) and dipole-dominated regime (dipole fraction $f_{\rm dip} \geq 0.35$, where $f_{\rm dip}$ is the magnetic energy in the dipole component divided by the total energy in the 1–12 spherical harmonics). Models span several orders of magnitude in Ekman number (denoted by shapes) and Prandtl number (denoted by color: white is $\mathrm{Pr}_m = 1$, deeper shades of red are greater than 1, deeper shades of blue are less than 1) and appear to follow a scaling law between non-dimensional energy density (E_m^*, y-axis) and non-dimensional flux q^*. Black line is fitted relationship, dashed lines are 3σ uncertainties. F is an efficiency factor. **(b)** Magnetic energy density in the dynamo (left y-axis) versus a function of density and bolometric flux (x-axis). Solid and dashed black lines are the scaling relationship from (a) and 3σ uncertainties, respectively. The scale on the right y-axis is rms field strength at the dynamo surface. T Tauri stars are blue crosses, and old M dwarfs are red crosses and pink crosses (Zeeman Doppler imaging and Zeeman broadening data, respectively). Brown and grey ellipses indicate predicted locations of a $T_{\rm eff} \sim 1500$ K brown dwarf and a $7 M_{\rm J}$ extrasolar planet, respectively. Stars with rotation periods >4 days are yellow and green crosses. Both figures are reprinted from Christensen, Holzwarth, and Reiners (2009) by permission from Macmillan Publishers Ltd: *Nature*, copyright 2009. 11

1.4 **(a)** In observations of a solar active region, a power law relation with index 0.6 ± 0.1 can describe the Ca II K flux in excess of the minimum flux observed from solar-type stars. Circles are data from Skumanich, Smythe, and Frazier (1975). Reproduced from Schrijver et al. (1989) by permission of the American Astronomical Society. **(b)** The ratio of chromospheric Ca II H & K flux to bolometric flux correlates with Rossby number. Reproduced from Noyes et al. (1984) by permission of the American Astronomical Society. 12

1.5 **(a)** The Güdel-Benz relation breaks down for objects with spectral type ~M7 or later. Adapted from Williams, Cook, and Berger (2014) and reproduced by permission of the American Astronomical Society. **(b)** Some magnetic activity markers appear to drop off at low Rossby numbers but radio emission does not. Adapted from McLean, Berger, and Reiners (2012) and reproduced by permission of the American Astronomical Society. 15
1.6 Hα emission persists through mid-L dwarfs despite their cool temperatures. Reproduced from Schmidt et al. (2015) by permission of the American Astronomical Society. 16
1.7 Jupiter aurorae can be generated via co-rotation breakdown of a plasma disk in its magnetosphere. Heuristically, its large-scale magnetic field is coupled to a surrounding hot ionized plasma disk generated by volcanic activity from its moon. This disk co-rotates with Jupiter but shears when the magnetic energy density no longer dominates the plasma energy density, thus driving field-parallel currents that are necessary for producing auroral emission. Reprinted from Bagenal et al. (2014) with permission of Springer, © Springer Science+Business Media Dordrecht 2014. Original figure caption: "The Iogenic magnetospheric plasma is coupled to the rotating planet via electrical currents (brown dashed lines) that flow along magnetic field lines (blue solid lines) to the auroral regions of Jupiter's atmosphere (adapted from Cowley and Bunce 2001)." 17
1.8 Average positions of Jovian radio emission at 387 kHz, 540 kHz, and 740 kHz (observed to be right-circularly polarized) measured by the Unified Radio and Plasma Wave Experiment on the Ulysses spacecraft. A model dipole magnetic field is offset from the rotation axis by 9.6°. Reprinted from Zarka (1998) with permission from Wiley, copyright 1998 by the American Geophysical Union. Originally adapted from Ladreiter, Zarka, and Lacacheux (1994) and reprinted with permission from Elsevier. 21
2.1 Example of Zeeman broadening 25
2.2 Average spectra of Solar System auroral emission, reprinted from Zarka (1998) with permission from Wiley, copyright 1998 by the American Geophysical Union. Originally adapted from Zarka (1992) with permission from Elsevier. 31

3.1 4–8 GHz Stokes I and Stokes V imaging for full observing block. . . 48
3.2 4–8 GHz timeseries of right and left circularly polarized emission. . . 50
3.3 4–8 GHz Stokes I and Stokes V imaging for pulsed and quiescent emission. 51
3.4 Comparison of 4–8 GHz data to a luminosity-driven dynamo. 58
4.1 Y dwarfs 4–8 GHz Stokes I and Stokes V imaging for full observing block. 74
4.2 Y dwarfs 4–8 GHz timeseries of right and left circularly polarized emission. 75
4.3 Y dwarfs quiescent emission upper limits. 76
5.1 12–18 GHz timeseries: 2M1047 92
5.2 8–12 GHz timeseries: SIMP0136 & 2M1043 93
5.3 8–12 GHz timeseries: 2M1237 & SDSS0423 94
5.4 12–18 GHz Stokes I and Stokes V images of quiescent emission for 2M1047 and 8–12 GHz Stokes I and Stokes V images of quiescent emission for SIMP0136 and 2M1043. 101
5.5 8–12 GHz Stokes I and Stokes V images of quiescent emission for 2M1237 and SDSS0423. No quiescent emission is detectable from SDSS0423. 102
5.6 Periodograms 103
5.7 Phase-folded timeseries 104
5.8 Comparison of 8–18 GHz data to a luminosity-driven dynamo. 113
5.9 Comparison of magnetic field strength to age. 116
6.1 Correlation between quiescent radio and Hα luminosities for confirmed auroral emitters. 125
6.2 4–8 GHz Stokes I and Stokes V images for 2M2139+02 and WISE 1738+27 128
6.3 4–8 GHz timeseries for 2M2139+02 and WISE 1738+27. 129

LIST OF TABLES

Number		*Page*
1.1	Summary of physical properties and magnetic field characteristics for Solar System bodies.	2
3.1	4–8 GHz Survey Targets	44
3.2	4–8 GHz Summary of Observations	47
3.3	4–8 GHz Imaging and Timeseries Results	52
3.4	Brown Dwarf Physical Parameters	55
4.1	Y Dwarf Targets	70
4.2	Y Dwarf Summary of Observations	70
4.3	Archival measurements sets for J1419+5423	72
4.4	Y dwarfs: Summary of Observations	73
5.1	8–18 GHz Survey Targets	86
5.2	8–18 GHz Summary of Observations	88
5.3	8–18 GHz comparison of phase calibrator flux densities	88
5.4	8–18 GHz Initial Imaging Detections	90
5.5	12–18 GHz Pulsed and Quiescent Emission from 2M1047	91
5.6	8–12 GHz Pulsed and Quiescent Emission from SIMP0136 & 2M1043	95
5.7	8–12 GHz Pulsed and Quiescent Emission from 2M1237	96
5.8	8–12 GHz Pulsed and Quiescent Emission from SDSS0423	97
5.9	Periodogram Results	100
5.10	8–18 GHz Adopted Magnetic Fields	112

Chapter 1

INTRODUCTION

1.1 A Case for Studying Brown Dwarf Magnetism

Magnetic fields at the substellar-planetary boundary remain enigmatic creatures, having successfully eluded characterization until the last five years yet playing a pervasive role in the entire evolution of stellar and planetary environments. In particular, understanding the magnetic behavior of planets through low-mass stars is becoming increasingly important for the emerging story of habitability.

Early in the search for a habitable world outside of our Solar System, astronomers identified the need for planets to exist in a 'habitable zone' (Huang 1959, 1960), defined as an area around a host star receiving an approximately constant source of energy neither too large nor too small to preclude the requirements of a given life form and for a long enough period to allow life to develop. While this initial definition focused on the energy output of the host star, it is also important to consider habitability from the perspective of a planet. Thus, studying properties intrinsic to planets themselves also helps build a comprehensive understanding of habitability and much effort has been dedicated to investigating planetary atmospheres, including detailed studies of weather, atmospheric composition and climate, and atmospheric stability (e.g. Shields, Ballard, and Johnson 2016, and references therein). The discovery that M dwarfs, which make up the majority of stars, are reliable hosts of small, rocky planets (Dressing and Charbonneau 2013), crystallized yet another focus in the search for habitable planets at the intersection between these two previous perspectives: understanding the magnetic environment in planetary systems (e.g. France et al. 2013, 2016; Kay, Opher, and Kornbleuth 2016).

As compared to their hot Jupiter counterparts around solar-type stars, planets around active M dwarfs are predicted to experience ten times the rate of magnetized stellar plasma eruptions, known as coronal mass ejections (CMEs) (Kay, Opher, and Kornbleuth 2016). For close-in planets with weak magnetic fields, this high rate of CMEs could shrink the distance to its magnetopause, where magnetic pressure of the planetary field balances the solar wind pressure, to a mere ~1000 km above the planetary surface (Lammer et al. 2007). Additionally, the intense XUV radiation produced by active M dwarfs can inflate and ionize the atmospheres of nearby

Table 1.1: Summary of physical properties and magnetic field characteristics for Solar System bodies.

Planet	Mass[1] (10^{24} kg)	Radius[1] (km)	$\overline{\text{Density}}$[1] (kg/m^3)	MOI[2–4]	Surface $\overline{\lvert B_r \rvert}$ (μT)	Dipolarity	Dipole tilt (°)
Mercury	0.33	2440	5.4	0.33	0.30	0.71	3
Venus	4.87	6052	5.2	0.33	-	-	-
Earth	5.97	6371	5.5	0.33	38	0.61	10
Moon	0.07	1738	3.3	0.39	$\lesssim$100	-	-
Mars	0.64	3390	3.9	0.37	$\lesssim$0.1	-	-
Jupiter	1900	69911	1.3	0.25	550	0.61	9
Io	0.09	1821	3.5	0.38	-	-	-
Europa	0.05	1565	3.0	0.35	-	-	-
Ganymede	0.15	2634	1.9	0.31	0.91	0.95	4
Callisto	0.11	2403	1.9	0.35	-	-	-
Saturn	570	58232	0.7	0.21	28	0.85	<0.5
Titan	0.13	2575	1.9	0.34	-	-	-
Uranus	87	25362	1.3	0.23	32	0.42	59
Neptune	100	24624	1.6	0.23	27	0.31	45

Overbars indicate mean values. Physical property data taken from [1]Lodders and Fegley (1998), [2]de Pater and Lissauer (2001), [3]Schubert et al. (2007) for the moment of inertia (MOI) of the Galilean satellites, and [4]Iess et al. (2010) for the MOI of Titan. Magnetic field characteristics are calculated using Eqs. (2)–(4) in Schubert and Soderlund (2011) and data in Uno et al. (2009) for Mercury, IAGA Division V-MOD geomagnetic field modeling website for Earth, Yu, Leinweber, and Russell (2010) for Jupiter, Kivelson, Khurana, and Volwerk (2002) for Ganymede, Burton, Dougherty, and Russell (2009) for Saturn, and Holme and Bloxham (1996) for the ice giants. MOI is normalized with respect to the product of the mass and the square of the radius of the body. Table and caption reprinted from Schubert and Soderlund (2011), with permission from Elsevier.

planets, and for terrestrial planets without sufficient gravity or magnetism, can cause them to lose much if not all of their atmospheres (Khodachenko et al. 2007). Finally, strong fields on M dwarfs may significantly compress planetary magnetospheres, thus exposing planetary atmospheres to stellar wind stripping (Vidotto et al. 2013). To compensate and protect against atmospheric erosion, planets themselves would need to host magnetic fields as strong as hundreds to thousands of Gauss. In comparison, the surface-averaged field strengths of Solar System planets are between 0.003–5.5 Gauss (see Table 1.1), and little is known about the nature of exoplanetary magnetic fields or how such fields evolve as a planet or M dwarf ages.

In one recent and dramatic illustration of the integral role played by strong, stable, large-scale planetary fields in maintaining planetary atmospheres, measurements by the Mars Atmosphere and Volatile EvolutioN (MAVEN) mission showed that in the absence of a protective dipole planetary field, the modern-day solar wind erodes the Martian atmosphere at an astonishing ~100 g/s (Brain et al. 2015; Leblanc et al. 2015). The authors predicted that dramatically increased rates of erosion from a

more active young Sun likely caused the planet to lose its early water-supporting thick atmosphere. Earth appears to have so far escaped this fate because it possesses a large dynamo-generated dipole field. In contrast, Mars only has a comparatively weak and patchy crustal field remaining in its southern hemisphere from an earlier and now extinct dynamo, with local field strengths two orders of magnitude weaker than the mean global field of Earth (e.g. Acuna et al. 1999; Connerney et al. 1999; Lillis et al. 2008; Schubert and Soderlund 2011, and references therein). Indeed, comparisons of O^+ ion outflows from Earth and Mars show that Mars experiences a ten-fold increase in ion outflow flux as compared to Earth for the same increase in solar wind pressure (Wei et al. 2012).

As Mars clearly demonstrates, understanding the physical principles driving field generation in fully convective objects is essential to characterizing magnetic fields and their evolution in objects spanning terrestrial planets through low-mass stars. However, doing so remains challenging both observationally (§2.1) and computationally (§1.2). Convective dynamos occur in a wide breadth of cases, including rocky planet inner cores, gas giant planets, brown dwarfs, and low-mass stars, and the onset of a dynamo mechanism different in nature from solar-type dynamos has long been predicted (Durney, De Young, and Roxburgh 1993). Earlier work linking chromospheric and coronal emission to mean measured field strengths (e.g. Schrijver et al. 1989) and such emission to rotation rates (Noyes et al. 1984) pointed to a rotation-dominated dynamo operating in higher-mass stars, which helioseismology studies have shown to experience significant shear in the transition region known as a tachocline between their differentially rotating convective zones and solid-body rotating radiative cores (Thompson et al. 1996). Indeed, early theory and models suggested that the large-scale solar magnetic field depended on strong differential rotation (e.g. Parker 1955; Babcock 1961; Steenbeck and Krause 1966; Leighton 1969; Durney, De Young, and Passot 1990). However, fully convective dynamos lack a tachocline and Parker (1975) predicted that magnetic buoyancy in the solar convection zone caused the field to rise more quickly through a convective dynamo region than the timescales required to amplify them to the several thousand kilogauss that have been observed in M dwarfs (Saar and Linsky 1985; Saar 1994; Johns-Krull and Valenti 1996). Together with the discovery of a spindown time at least an order of magnitude longer for M dwarfs than for earlier-type stars (Stauffer, Hartmann, and Latham 1987), this suggested that late-type dwarfs did not possess large-scale fields. Instead, Durney, De Young, and Roxburgh (1993) showed that convection was sufficient to generate significant magnetic fields with spatial scales

on the order of convective cells even in the absence of rotation. This behavior could explain the long spindown time previously observed in M dwarfs, which become fully convective at masses less than ~0.35 $M_\odot$ or spectral type ~M4.

However, more recent Zeeman Doppler imaging studies have shown that some M dwarfs can indeed host magnetic field topologies dominated by strong large-scale fields (e.g. Donati et al. 2006; Reiners and Basri 2007; Morin et al. 2010), and our Solar System provides several examples of dipole-dominated fields in planets (Table 1.1). Newer dynamo models suggest that rapid rotators such as planets and cool brown dwarfs can in fact generate fields with large dipole fractions yet simultaneously predict other behaviors dependent on rotation (§1.2, §5.6.5). The roles of global parameters such as rotation, age, mass, and luminosity in generating these fields remain unknown in part because a lack of data has prevented direct testing of dynamo models probing physical parameters at the substellar-planetary boundary prior to this work (§2.1). Observational clues have suggested that below a certain Rossby[1] number, magnetic activity appears to cease scaling with rotation (§1.3.2). Whether this rotation-saturation effect holds through the coolest L, T, and Y dwarfs into the planetary regime, its underlying physical cause, and even if established magnetic activity tracers such as Hα emission continue to trace the same kinds of magnetic activity as in higher mass stars remain unknown, and this dissertation seeks to address these questions.

1.2 Overview of Dynamo Models

In light of the change in magnetic behavior of the lowest-mass dwarfs discussed in §1.3.2, an important outstanding problem in dynamo theory is understanding how magnetic fields are generated and sustained in such fully convective objects. Prevailing dynamo models for dwarf stars with an inner radiative zone and an outer convective envelope, like the Sun, are accepted to rely on the shearing at the interface between these two layers, where differential rotation is strongest (Parker 1975). The mechanism attributed to the generation of the Sun's field is known as an $\alpha\Omega$ dynamo, where $\alpha\Omega$ is a term in the Taylor expansion of the turbulence-generated electromotive force (EMF) in the Maxwell-Faraday equation. α describes the amplification of the large-scale field via the twisting and looping (helicity) of convection flux tubes from the star's rotation. Ω describes the generation of a toroidal field via the global stretching and winding of the field due to differential

[1]Dimensionless ratio of inertial to Coriolis forces, or a measure of how important the effects of rotation are on convective motions. Denoted by Ro.

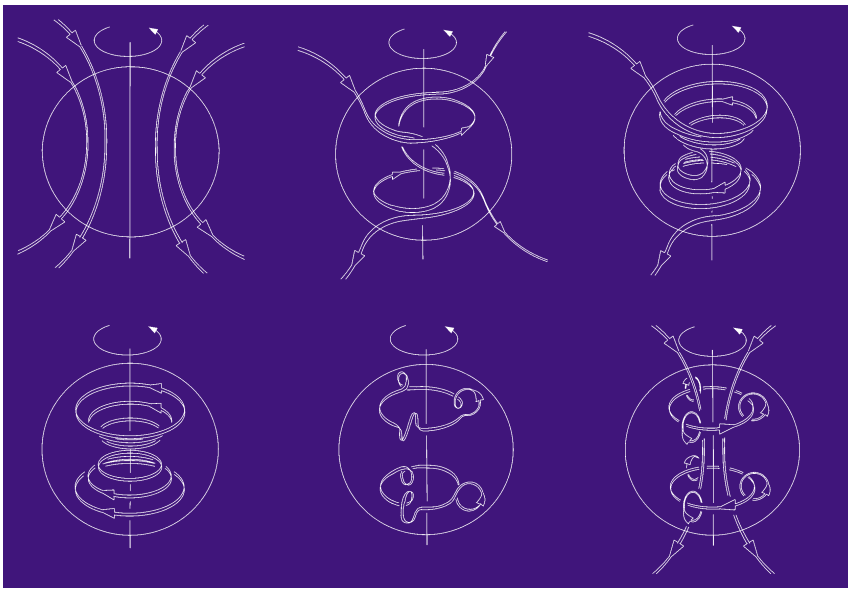

Figure 1.1: Illustration of $\alpha\Omega$-effect. Beginning from top left: In the Ω-effect, differential rotation shears a poloidal magnetic field into a toroidal field. In the α-effect, rising and twisting convection cells distort and twist the embedded magnetic field lines into loops, generating a current that leads to a poloidal field. Reprinted from Figure 2 in Love (1999).

rotation. Figure 1.1 gives a heuristic illustration of these two effects. Because both the α- and Ω-effect rely on the rotation of the object, an $\alpha\Omega$ dynamo predicts a positive correlation of magnetic activity with decreasing Ro.

However, at ~0.35 $M_\odot$ or spectral type ~M4, stars become fully convective and no longer possess the internal structures necessary to sustain such dynamos (Chabrier and Baraffe 1997). Turbulence dissipates any fossil fields present in such fully convective stars over the timescale $\tau_d \approx R_*^2/\eta \sim$ 10–100 years, where η is the turbulent magnetic diffusivity (Chabrier and Küker 2006). It is clear from observations of strong magnetic fields and persisting emission of magnetic activity tracers from ultracool dwarfs that a dynamo must operate in the fully convective regime. Accordingly, many efforts have been made to understand which physical parameters of fully convective objects dominate the behavior of their dynamos.

Because dynamos essentially transform kinetic energy into magnetic energy via induction occurring in magnetohydrodynamical fluid systems, the motions and properties of conductive fluids in dynamo regions as influenced by convection, rotation, shear, electrical conductivity, boundary conditions, heat flux, and density stratification are expected to affect dynamo action (Moffatt 1978; Christensen 2010).

However, the properties of fields resulting from these fluid motions — such as the distribution of magnetic energy into various magnetic moments, cyclical behaviors, mean strengths, and relationships with global parameters like luminosity, mass, or rotation — remain unclear. In nature, fully convective dynamos can span a wide range of fluid densities, with the density stratification ranging from ~20% in incompressible fluids such as in the geodynamo to at least $\sim 10^6$–10^{10} in stars and likely also cool brown dwarfs (Saumon, Chabrier, and van Horn 1995). In highly stratified regimes, fluids in the most diffuse regions become less efficient at transporting heat and small-scale motions become increasingly important. Computational limitations prevent the resolution of very small length scales, requiring the implementation of different control parameters and in particular fluid viscosity to avoid such small scales. Natural dynamos have almost negligible viscosity and therefore negligible viscous forces, with Ekman[2] number $E \sim 10^{-15}$ and magnetic Prandtl[3] number $\mathrm{Pr}_m \sim 10^{-6}$ for Earth. However, to avoid solving very small length scales, most models assume much larger viscosity terms, with typical Ekman numbers $E \sim 10^{-4} - 10^{-6}$ and magnetic Prandtl numbers $\mathrm{Pr}_m \sim 1$, possibly leading to the resultant differing dynamo behaviours. Despite this, exploring how dynamos correlate with observable properties of planets, brown dwarfs, and stars can give insight into the relevant physics occurring in dynamo regions of various objects and provide a means of predicting magnetic behaviors in other systems.

1.2.1 Scaling Laws

Any dynamo system will always be in an energy balance as well as in a force balance, and depending on the conditions, the energy/force of one category may be larger/smaller than the others. In Earth, where the total magnetic energy is substantially larger than the total kinetic energy by a factor ~1000, we expect that the Coriolis and Lorentz forces are the major players, and ohmic dissipation of energy should dominate viscous dissipation. This may also be true for brown dwarfs. In contrast, the magnetic energy of the Sun is expected to be comparable to the kinetic energy in its dynamo, so viscous dissipation is expected to be significant and the fluid inertial force may be a dominant player as compared to Coriolis or Lorentz forces. With this framework in mind, the evolution of planetary dynamo modeling can be described as implementations of different force and energy balance recipes in earlier approaches leading to various predicted scaling relations. In the geostrophic

[2]Ratio of viscous to Coriolis forces: $E = \nu/\Omega D^2$, where ν is viscosity, Ω is rotation rate, D is length scale of largest convective structures.

[3]Ratio of viscous to magnetic diffusion rates: $\mathrm{Pr}_m = \nu/\eta$, where η is magnetic diffusivity.

force balance approximation, pressure gradients balance Coriolis forces in the limit of rapid rotation compared to convection, small magnetic field, low viscosity, and steady flow, leading to a predicted scaling relationship $B^2 \propto \rho\Omega^2 r_c^2$, where ρ is the fluid density, Ω is the rotation rate of the dynamo region, and r_c is the radius of the dynamo region. Likewise, magnetostrophic force balances assume that Coriolis forces ($\rho\Omega u$, where u is the fluid velocity) can balance Lorentz forces ($\sigma u B^2$, where σ is electrical conductivity), leading to a different predicted scaling relationship $B^2 \propto \rho\Omega/\sigma$. This particular interpretation of a magnetostrophic balance defines a parameter in numerical models, the Elsasser[4] number. In yet another prescription known as the MAC balance (Magnetic, Archimedian, and Coriolis), Coriolis forces can balance Lorentz and buoyancy forces with the resulting scaling relationship $B^2 \propto \rho(\Omega q_c)^{1/2} r_c^{3/2}$, where r_c is the radius of the dynamo region and q_c is the convected energy flux in that region.

One scaling law of recent interest in the stellar community takes as inspiration a Zeeman Doppler imaging study by Morin et al. (2010) that found either strong and stable dipoles of order ~kG or weak dipoles of order ~0.1 kG with a time-varying multipolar component, in light of which Morin, Dormy, et al. (2011) proposed a bistable dynamo. Through order of magnitude calculations, they estimate that in such a dynamo, the surface magnetic field strength would scale as $B_{\rm surface} \propto \Omega^{1/2}$ and the ratio between the surface field strengths of the weak field and strong field would also be related to rotation as $B_{\rm wf}/B_{\rm sf} \approx {\rm Ro}^{1/2}$.

Scaling laws dependent on observable properties are attractive in that they provide testable predictions, a means of extrapolating the evolution of fields in other objects, and insight into which physical processes are dominant. However, the scaling laws are given above to serve as examples of the diversity of possible relationships and to highlight the need to discriminate between which (if any) scaling relationships can be applied to what types of dynamos. Additional scaling laws have been proposed for various other possible physical situations and we refer the reader to the review by Christensen (2010) for a more detailed discussion.

1.2.2 Numerical Simulations

In contrast to scaling laws, numerical simulations allow a more detailed study of how various physical conditions may influence observable magnetic field properties

[4]Ratio of Lorentz to Coriolis forces $\Lambda = B_{\rm rms}^2/\rho\mu\lambda\Omega$, where μ and λ are the magnetic permeability and diffusivity and $\lambda = 1/\mu\sigma$.

In a linearized three-dimensional mean-field magnetohydrodynamics (MHD) model, Chabrier and Küker (2006) argue that anisotropy in the convection zones of rapid rotators and the expectation of weak or absent differential rotation in fully convective objects causes a fourth order perturbation about the mean magnetic field to dominate the turbulence-generated EMF term that gave rise to the α-effect described earlier. Rather than an α dynamo (which dominates for slow rotators) or an $\alpha\Omega$ dynamo (whose contribution is expected to be minimal for a minimally differential rotator), the resulting dynamo is dominated by the α^2-effect. In an α^2 dynamo, fluctuations in the helicity [5] of the convective flux tubes give rise to a negative contribution in the turbulent diffusion of the mean magnetic field. This negative diffusion then causes the field lines to concentrate instead of diffuse, thus amplifying the mean field until, as it is generally believed (and implemented by Chabrier and Küker (2006)), the fields reach equipartition energy with the turbulent fluid motions. The equipartition field strengths are of order several kilogauss and depend on rotation rate. It is important to note that α requires strong density stratification and rotation in order to be non-zero, which fully convective objects such as brown dwarfs satisfy. For a $0.06 M_\odot$ object, the authors find that the resulting field is large-scale and non-axisymmetric, co-rotating with the object, and symmetric about the equatorial plane, whereas a very cool and massive brown dwarf with a conductive core exhibits a toroidal and axisymmetric field. The α^2 dynamo shares key characteristics with the $\alpha\Omega$ dynamo, namely, the magnetic flux increases with rotation and it saturates at high rotation rates. However, unlike in the Sun, cyclical variation in field strengths should not occur. Finally, Chabrier and Küker (2006) find that the large-scale field geometry from the α^2 dynamo always steady-states to a higher-order multipole, regardless of rotation rate.

The mean-field MHD model just discussed is limited in that it focuses on the generation of the large-scale field itself and gives no information about the small scale field. In a slightly different approach, Browning (2008) use non-linear three-dimensional MHD to simulate a $0.3 M_\odot$ star. They find that the characteristic convection length scales vary as a function of depth, with the smallest scales near the surface of the star and larger, more slowly overturning flows deep in the interior. Correspondingly small-scale magnetic fields are thus generated near the surface, whereas large-scale fields are anchored in the larger, deeper flows. The small-scale fields dominate the total magnetic energy of the dynamo, though the large-scale fields are quite strong ($\sim$10 kG). They find that Ro is the dominant factor in determining

[5] $\mathbf{u} \cdot (\nabla \times \mathbf{u})$

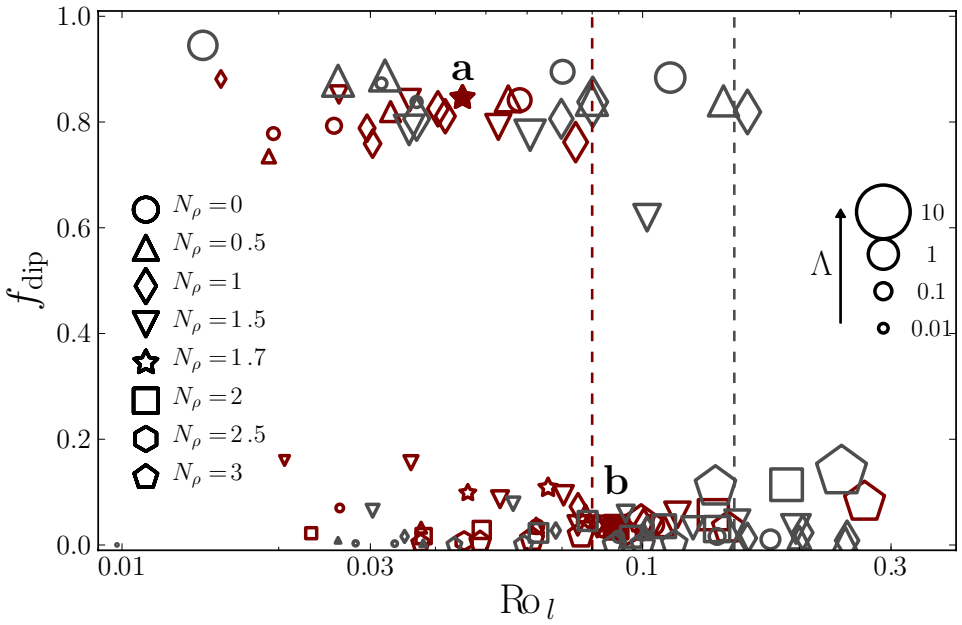

Figure 1.2: Dipole fraction (y-axis) versus local Rossby number (x-axis) for a wide range of dynamo control parameters: Elsasser number Λ (point size), density contrast across dynamo shell $N_\rho = \ln(\rho_{\rm bottom}/\rho_{\rm top})$ (symbol type), and thickness of dynamo shells (red = thick, grey = thin). Dashed vertical lines denote tentative critical local Rossby number separating the multipolar/dipolar bistable regime versus the multipolar regime for the different shell thicknesses. Reproduced from Gastine et al. (2013), with permission from Astronomy & Astrophysics, © ESO.

the field strength and geometry. Specifically, as Ro decreases, the convecting flows are increasingly influenced by Coriolis forces and the magnetic energy increases. As the magnetic energy increases with respect to the kinetic energy, they find that persistent differential rotation begins to undergo cyclical tradeoffs between differential rotation and stronger magnetic fields, and finally solid body rotation sets in as magnetic energy dominates kinetic energy. Therefore, Browning (2008) expect rapid rotators to generally exhibit strong and temporally stable large-scale fields along with small-scale fields and to rotate as solid bodies.

In contrast, a different subset of models suggest that field topologies dominated by differing geometries can be generated. For instance, in a Boussinesq model (constant density approximation) of rotating spherical shells, Simitev and Busse (2009) found that the same input parameters can result in both a stable mean dipole or a fluctuating dipole.

1.2.3 Parameter Studies

The above models can describe a plethora of possible dynamo behaviors but rely on different simplifications to ease the computational burden and additionally can only provide broad predictions for magnetic behavior. Increasing computational resources makes possible a middle ground between heuristic scaling laws and numerical simulations in the form of systematic parameter studies. These studies explore how control parameters defining the relative relationships between physical characteristics such as rotation rate, conductivity, and fluid viscosity influence the interplay occurring in force and energy balances. Varying these control parameters over several orders of magnitude provides a database of dynamo solutions, which can then be analyzed to elucidate critical control parameter numbers that define the onset of different dynamo behaviors or 'empirical' scaling relationships as a means of testing various heuristic scaling laws.

As an example of the former, Gastine et al. (2013) present yet another bistable dynamo (Figure 1.2), this time using anelastic MHD simulations that do not use a Boussinesq approximation. They find that in the dipole-dominated branch, the fraction of the magnetic energy in the dipole $f_{\rm dip} > 0.6$. In the multipolar branch, $f_{\rm dip} < 0.2$. The local Rossby number, defined as $\mathrm{Ro}_l = u_{\rm rms}/\Omega l$, where $u_{\rm rms}$ is the rms flow velocity, Ω is the rotation rate, and l is the typical flow length scale, determines whether fields are dipole-dominated or multipole-dominated. For high rotation ($\mathrm{Ro}_l < 0.1$), the dipole dominates and they attribute this behavior to α^2 dynamos. Above ($\mathrm{Ro}_l \sim 0.1$), all fields are multipolar, whereas below ($\mathrm{Ro}_l \sim 0.1$), weaker multipolar fields can still coexist with the dipole branch. They attribute multipolar fields to $\alpha\Omega$ or $\alpha^2\Omega$ dynamos.

While the scaling laws discussed earlier are useful for investigating extremes of force balance prescriptions, in reality, force balances may be more complex. Instead, an alternate approach to defining force balances is to focus on how the energy budget balances ohmic dissipation. Recent parameter studies appear to support a scaling relation in which the dominating factor in such an energy balance is convected energy flux in rapidly rotating and fully convective dipole-dominated[6] objects, such that $B^2 \propto \rho^{1/3} q_0^{2/3}$ (Christensen and Aubert 2006). Excitingly, this scaling relationship also appeared to be empiricially consistent with magnetic fields measured for planets and low mass stars, as shown in Figure 1.3 (Christensen, Holzwarth, and Reiners 2009). However, it also demonstrated that quantifying magnetic fields in objects

[6] dipole fraction $\gtrsim 0.35$

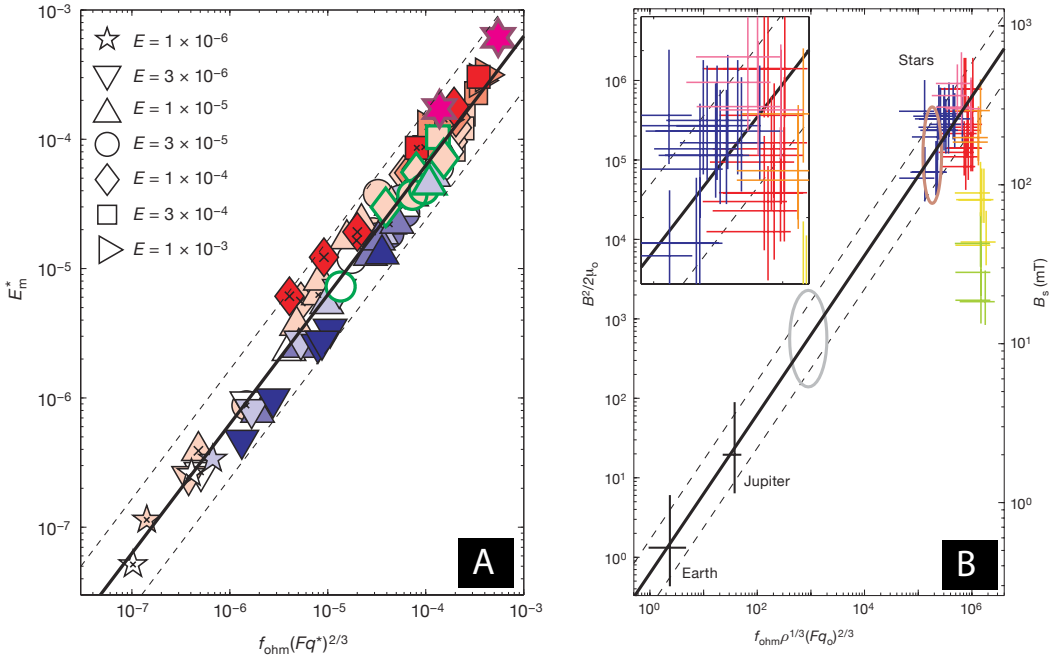

Figure 1.3: **(a)** Dynamo models in the rapidly rotating (local Rossby number <0.12) and dipole-dominated regime (dipole fraction $f_{\rm dip} \geq 0.35$, where $f_{\rm dip}$ is the magnetic energy in the dipole component divided by the total energy in the 1–12 spherical harmonics). Models span several orders of magnitude in Ekman number (denoted by shapes) and Prandtl number (denoted by color: white is $\mathrm{Pr}_m = 1$, deeper shades of red are greater than 1, deeper shades of blue are less than 1) and appear to follow a scaling law between non-dimensional energy density (E^*_m, y-axis) and non-dimensional flux q^*. Black line is fitted relationship, dashed lines are 3σ uncertainties. F is an efficiency factor. **(b)** Magnetic energy density in the dynamo (left y-axis) versus a function of density and bolometric flux (x-axis). Solid and dashed black lines are the scaling relationship from (a) and 3σ uncertainties, respectively. The scale on the right y-axis is rms field strength at the dynamo surface. T Tauri stars are blue crosses, and old M dwarfs are red crosses and pink crosses (Zeeman Doppler imaging and Zeeman broadening data, respectively). Brown and grey ellipses indicate predicted locations of a $T_{\rm eff} \sim 1500$ K brown dwarf and a $7 M_{\rm J}$ extrasolar planet, respectively. Stars with rotation periods >4 days are yellow and green crosses. Both figures are reprinted from Christensen, Holzwarth, and Reiners (2009) by permission from Macmillan Publishers Ltd: *Nature*, copyright 2009.

spanning the parameter space between planets and stars, as is the case for brown dwarfs in spectral classes late L, T, and Y, is imperative for testing generalized scaling laws such as this.

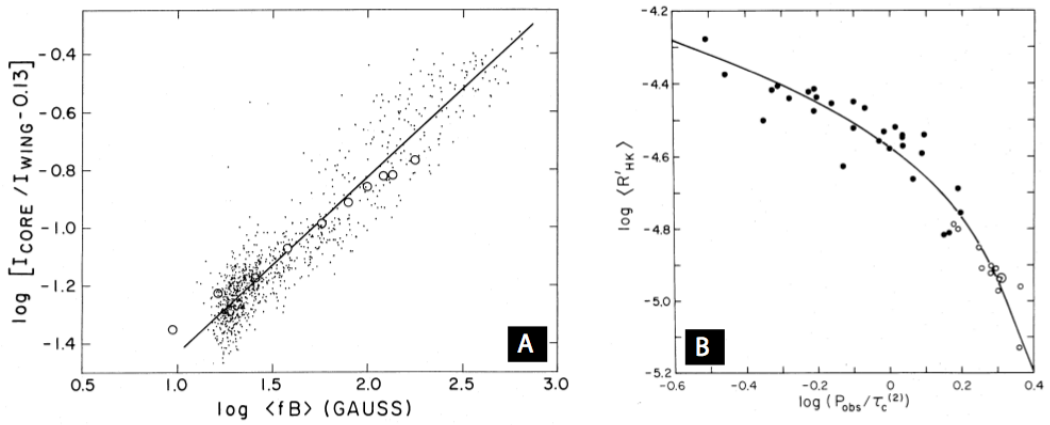

Figure 1.4: **(a)** In observations of a solar active region, a power law relation with index 0.6 ± 0.1 can describe the Ca II K flux in excess of the minimum flux observed from solar-type stars. Circles are data from Skumanich, Smythe, and Frazier (1975). Reproduced from Schrijver et al. (1989) by permission of the American Astronomical Society. **(b)** The ratio of chromospheric Ca II H & K flux to bolometric flux correlates with Rossby number. Reproduced from Noyes et al. (1984) by permission of the American Astronomical Society.

1.3 Auroral Emission: A New Paradigm for Brown Dwarf Magnetism

1.3.1 Stellar Activity Paradigm

Early observations of the Sun's chromosphere and corona revealed emission that indicated nonthermal heating (Vernazza, Avrett, and Loeser 1981). While the dissipation of acoustic (hydrodynamic) energy can account for some of this heating, emission from lines produced in these regions such as Ca II K and Hα were shown to scale with disk-averaged magnetic flux densities (e.g. Schrijver et al. 1989, see Figure 1.4a) and X-ray emission from the super-heated corona correlated with chromospheric emission (Schrijver, Dobson, and Radick 1992). Thus, Hα, Ca II H & K, and X-ray are generally attributed to stellar magnetic activity. The exact mechanisms responsible for chromospheric and coronal magnetic heating as well as other sources of emission tracing stellar magnetic activity are still debated but are all characterized by intrinsic or local processes such as the reconnection of twisting and rising magnetic field lines, the expulsion of stellar plasma, and the energy dissipation of various magnetohydrodynamical waves (Ulmschneider 2003). Given the localized nature of these heating mechanisms, one might expect that as the available magnetic energy in a star increased, the associated emission would similarly increase as these processes worked to dissipate the excess magnetic energy.

1.3.2 Observations of Stellar Magnetic Activity: Hints for a New Model of Magnetic Activity

Studies of such activity indicators have in fact yielded an activity-rotation relation, correlating Hα, Ca II H & K and X-ray emission with the increasing influence of rotation on hydrodynamical systems. In particular, the emissions appear to scale as a power law of decreasing Rossby[7] number for main sequence F through mid-M stars. At around $v \sin i \lesssim 15$ km s^{-1} or Ro ~ 0.1, the activity-rotation scaling saturates at a constant $\log L_{\mathrm{X,H}\alpha}/L_{\mathrm{bol}}$ even with increasing rotation (e.g. Pallavicini et al. 1981; Noyes et al. 1984; Soderblom et al. 1993; Stauffer et al. 1994; Delfosse et al. 1998; Pizzolato et al. 2003; Reiners, Basri, and Browning 2009; McLean, Berger, and Reiners 2012, see Figure 1.4b). The scaling relation suggests that rotation may play a dominant role in the generation and dissipation of magnetic energy in these objects in the unsaturated regime, and in fact Saar (2001) found that magnetic fluxes of G0–M2 stars increased as a power law of negative Ro.

In addition to Hα and X-ray emission, radio emission has also served as an important tracer of magnetic activity in the corona (White, Kundu, and Jackson 1989; Drake, Simon, and Linsky 1989), which the tight correlation known as the between X-ray and radio luminosities for magnetically active stars affirmed (Güdel and Benz 1993; Güdel et al. 1993; Güdel 1994). The Güdel-Benz relation, as it was named, spanned 5–6 orders of magnitude in F through M stars and solar flares independent of age, spectral class, binarity, or rotation period (Figure 1.5a). This observational link between coronal heating and magnetic particle acceleration processes further supported the previously described paradigm of stellar activity (Forbrich et al. 2011, and references therein). It was therefore expected that as the atmospheres of the lowest-mass dwarfs became increasingly cooler and more neutral, the lower Hα and X-ray luminosities (Mohanty and Basri 2003; West et al. 2004; Stelzer et al. 2006) would be accompanied by a corresponding decrease in radio luminosities and thus point to weaker magnetic fields in such ultracool dwarfs.

Hints of a divergence in magnetic activity first arose when Basri and Marcy (1995) took a closer look at the saturated regime for M7 and later objects. Quite unexpectedly, they found than an extremely rapidly rotating ($v \sin i \sim 40$ km s^{-1}) M9.5+ dwarf BRI 0021-0214 exhibited no Hα emission or lithium absorption, indicating that despite its fast rotation, it was not a young object. This object did not adhere to previously observed activity-rotation saturation or age-rotation spindown, which

[7] Ro $\sim P/\tau_c$, where P is the stellar rotation period and τ_c is the convective turnover time.

led them to suggest that the underlying relationship between rotation and activity changes and leads to a quenching of magnetic activity beginning in the the late-M spectral range. Mohanty and Basri (2003) confirmed a precipitous drop in both Hα surface flux and the normalized luminosity $L_{\mathrm{H}\alpha}/L_{\mathrm{bol}}$ in $\gtrsim$M9 dwarfs. Later, Reiners and Basri 2008, Reiners and Basri (2010), Berger et al. (2010), and McLean, Berger, and Reiners (2012) all observed evidence for a "supersaturation" effect in the activity-rotation relation, where $\log L_{\mathrm{X,H}\alpha}/L_{\mathrm{bol}}$ appear to decrease rather than remain constant with increasing $v \sin i$ or decreasing Ro (Figure 1.5b). It is important to note here that the supersaturation effect in X-ray emission is well-established, whereas evidence for Hα supersaturation is tentative and the downward trend may be an effect of the intrinsic scatter of $v \sin i$ as compared to Ro or rotation period. Even in the absence of a well-established downward trend, the data available do corroborate the findings by Mohanty and Basri (2003) and show a systematically lower level of Hα emission for M7 and later objects.

One possible interpretation of supersaturation is that the coolest dwarfs host weaker fields that are less efficient at dissipating magnetic energy to support active chromospheres or coronae. Supporting this picture was additional evidence of less effective magnetic braking in the latest-type objects, confirming initial findings by Basri and Marcy (1995). In particular, Browning et al. (2010) found that the fraction of fast rotators is greater for objects later than M3.5 than for M0–M2, and Reiners and Basri (2008) found that L and T dwarfs regardless of age appeared to be fast rotators. This behavior pointed to much slower spindown times and hinted that the large-scale magnetic fields and/or hot coronae that drive magnetic braking may wane in strength and/or temperature and perhaps become absent in the latest-type rapid rotators.

Concurrently, evidence of a dramatic decoupling between coronal heating and particle acceleration processes emerged. In a surprising discovery, Berger et al. (2001) detected the first brown dwarf in radio, LP 944-20 (M9). They observed both flaring and quiescent emission in its timeseries, which they attributed to gyrosynchrotron emission. Importantly, the radio emission was several orders of magnitude higher than what had been predicted by the Güdel-Benz relation. Their detection was in fact not anomalous, and an additional 15 low mass stars and brown dwarfs, ranging in spectral type from M7–L3.5, have been found to be radio sources in the last decade (Berger 2002; Burgasser and Putman 2005; Berger 2006; Phan-Bao et al. 2007; Antonova et al. 2007; McLean, Berger, and Reiners 2012; Route and Wolszczan

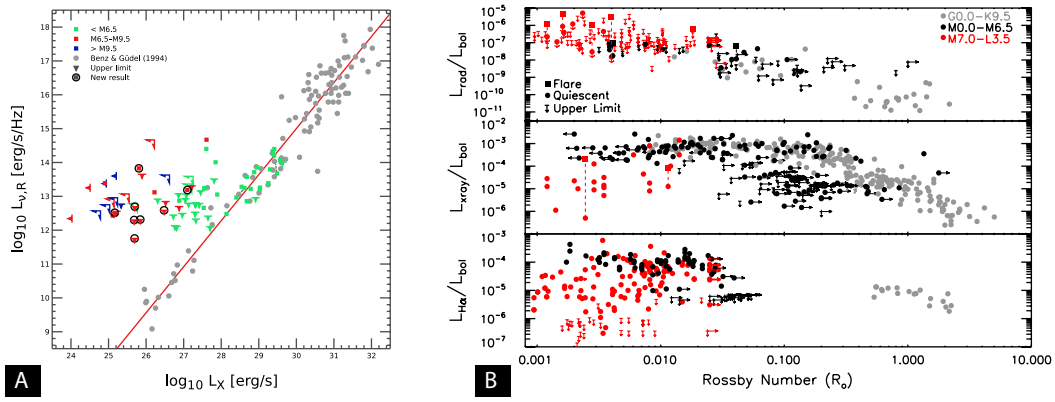

Figure 1.5: **(a)** The Güdel-Benz relation breaks down for objects with spectral type ∼M7 or later. Adapted from Williams, Cook, and Berger (2014) and reproduced by permission of the American Astronomical Society. **(b)** Some magnetic activity markers appear to drop off at low Rossby numbers but radio emission does not. Adapted from McLean, Berger, and Reiners (2012) and reproduced by permission of the American Astronomical Society.

2012; Burgasser et al. 2013; Williams, Cook, and Berger 2014; Burgasser, Melis, Todd, et al. 2015). Those with X-ray observations depart from the Güdel-Benz relation, pointing to a breakdown of the Güdel-Benz relation for objects later than M7 that activity-rotation saturation could not explain (Berger et al. 2010; Williams, Cook, and Berger 2014). In fact, McLean, Berger, and Reiners (2012) showed that in a departure from the activity-rotation saturation (<M7) or possible supersaturation (≥M7) observed in $L_{\mathrm{X,H}\alpha}/L_{\mathrm{bol}}$, $L_{\mathrm{radio}}/L_{\mathrm{bol}}$ does not appear to experience any saturation effects and instead continues to monotonically increase with decreasing Rossby numbers for their sample of 167 M0–L3.5 dwarfs. In the same study, they find that the radio luminosity shows no obvious correlation with Ro, indicating that the observed rise in $L_{\mathrm{radio}}/L_{\mathrm{bol}}$ is due to the decreasing bolometric luminosities of later-type dwarfs. This corroborated Berger et al. (2010) and Williams, Cook, and Berger (2014), who found that the breakdown in the Güdel-Benz relation appeared to be due to a suppression in X-ray luminosity rather than radio luminosity (Figure 1.5a).

It is important to note that in the Güdel-Benz breakdown regime, radio luminosity does not necessarily scale with magnetic field strength, as the radio luminosity is dependent largely on the population of the accelerated electrons. Nevertheless, the presence of radio emission required magnetic fields even at very low masses. This was supported by Zeeman broadening studies showing that late-M dwarfs have average field strengths from ∼1–4 kG (Reiners and Basri 2007, 2010). Additionally,

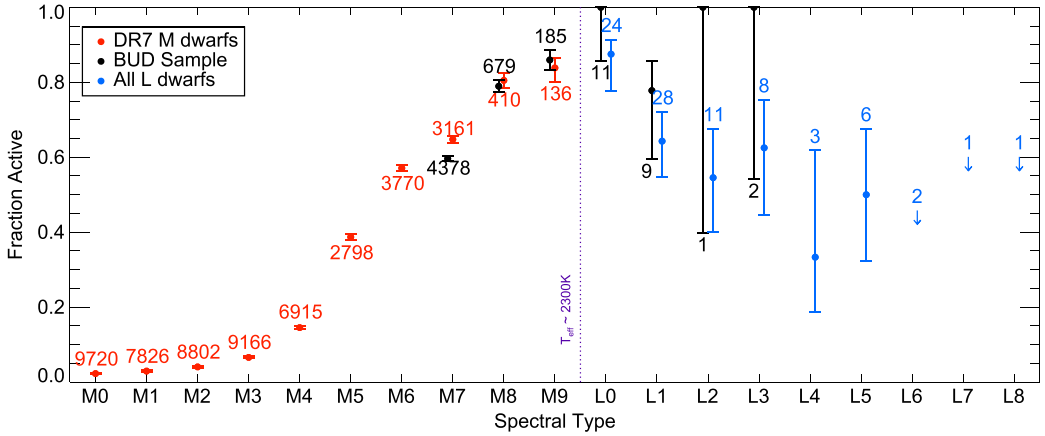

Figure 1.6: Hα emission persists through mid-L dwarfs despite their cool temperatures. Reproduced from Schmidt et al. (2015) by permission of the American Astronomical Society.

Zeeman Doppler imaging studies reconstructing magnetic field topologies of low-mass dwarfs have found evidence of ~kilogauss large-scale fields in late-M dwarfs (Morin et al. 2010). The presence of strong fields through late-M dwarfs thus eliminated the lack of magnetic fields as an explanation for the observed breaks in activity-rotation and the Güdel-Benz relation, and the decreasing X-ray activity is now attributed to the decoupling of the magnetic field from the increasingly neutral atmosphere and thus subsequent quenching of currents (Mohanty et al. 2002).

Such strong large-scale fields could potentially explain an intriguing observed rise in the Hα activity occurrence for ultracool dwarfs. A study of ~8000 SDSS M0–L4 dwarfs by West et al. (2004) found that the fraction of M stars that exhibit strong and persistent Hα emission steadily increases with later spectral type, reaching 73% by M8 before declining. A more recent study by Schmidt et al. (2015) extended the previous work to the latest-type M through L dwarfs, combining SDSS data with BOSS spectroscopy for a sample set of 11820 M7–L8 dwarfs. They found that the activity fraction in fact rises through late-M dwarfs and peaks at ~90% for L0 dwarfs before declining to ~50% for L5 dwarfs. The peak in activity fraction in may in part be explained by an evident sharp rise in activity lifetimes in mid-M dwarfs (West et al. 2008). Their analysis demonstrated that nonthermal heating of the chromosphere of late-M dwarfs is commonplace and sustained. The objects that West et al. (2004, 2008) and Schmidt et al. (2015) studied excluded close binary systems, implying that possible heating mechanisms are limited to magnetic activity or auroral activity (Hallinan et al. 2015; Kao et al. 2016). Supersaturation of X-rays

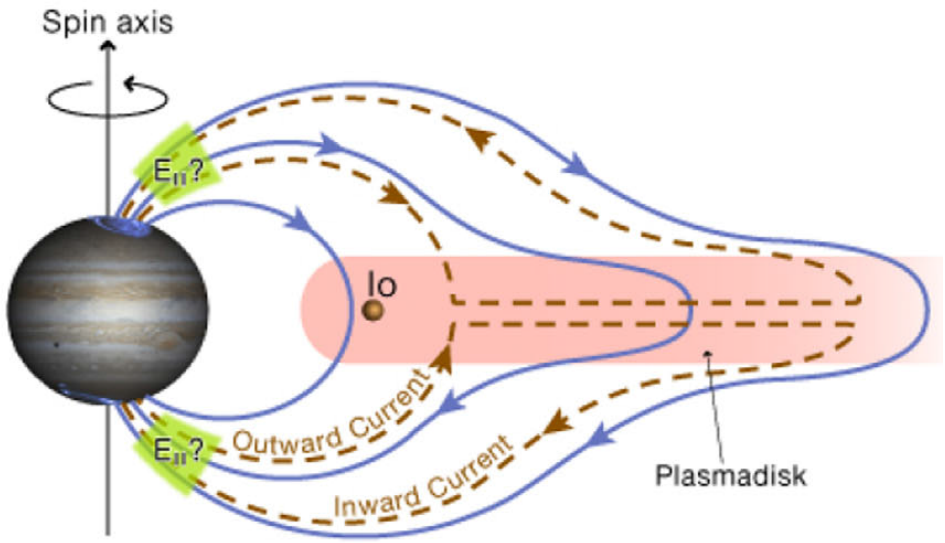

Figure 1.7: Jupiter aurorae can be generated via co-rotation breakdown of a plasma disk in its magnetosphere. Heuristically, its large-scale magnetic field is coupled to a surrounding hot ionized plasma disk generated by volcanic activity from its moon. This disk co-rotates with Jupiter but shears when the magnetic energy density no longer dominates the plasma energy density, thus driving field-parallel currents that are necessary for producing auroral emission. Reprinted from Bagenal et al. (2014) with permission of Springer, © Springer Science+Business Media Dordrecht 2014. Original figure caption: "The Iogenic magnetospheric plasma is coupled to the rotating planet via electrical currents (brown dashed lines) that flow along magnetic field lines (blue solid lines) to the auroral regions of Jupiter's atmosphere (adapted from Cowley and Bunce 2001)."

and the breakdown of the Güdel-Benz relation in late-type dwarfs indicate that the persistence in Hα emission in late-type dwarfs perhaps reflects the onset of a source of atmospheric heating that is different from magnetic reconnection, namely, auroral activity. In fact, observations of auroral activity in Solar System planets show that aurorae are associated with the funneling of electrons along large-scale fields into the upper atmospheres of the planets (Nichols et al. 2012; Hallinan et al. 2015; Kao et al. 2016).

The change in behavior of magnetic activity tracers in ≥M7 dwarfs, relative to rotation, spectral type, and to each other, tantalizingly hinted at the possibility that the dominant modes of magnetic activity may differ in the ultracool dwarf regime (≥M7) from those in hotter dwarfs.

1.3.3 Observations of Auroral Activity in Solar System Planets

If the stellar magnetic activity paradigm can be characterized by the dissipation of local sources of energy, then the magnetic activity processes observed occurring in Solar System Planets can in contrast be summarized as relying on an *external* power source, where large-scale current systems extending through the planetary magnetosphere act to transport energetic particles from the outer magnetosphere into the planet, generating auroral emission at X-ray, UV, optical, infrared, and radio wavelengths (Keiling et al. 2012; Bagenal et al. 2014; Badman et al. 2015, and references therein).

The three engines powering auroral emission as observed in our Solar System all rely on the large-scale (dipole) component of planetary fields and can be summarized thus:

Co-rotation breakdown of a rotating plasma disk in the magnetosphere of a planet can occur at large distances (~30–50 R_J for Jupiter) when rotational energy exceeds magnetic energy, driving strong field-aligned currents (Figure 1.7). Co-rotation breakdown powers the main auroral oval in Jupiter and dominates the Saturnian aurora (Cowley and Bunce 2001; Mauk and Bagenal 2012). This is a plausible mechanism for isolated brown dwarfs, but requires a means of populating and heating to mildly relativistic energies the requisite plasma disk.

Satellite interactions can also generate field-aligned currents when an orbiting satellite deep in a planetary magnetosphere with either its own magnetosphere or an ionosphere from volcanic activity appears to be moving relative to the magnetosphere of its host planet. The apparent current arising from this relative motion is transient and propagated by Alfvén waves, generating small footprints of intensely bright emission that dominate ultraviolet auroral emission (Hess and Delamere 2012, and references therein). Satellite-driven aurorae occur from the Jupiter-Io and Saturn-Enceladus interactions and are also plausible for isolated brown dwarfs. This possibility has understandably generated some excitement as a potential means of detecting brown dwarf moons.

Solar wind interactions with a planetary magnetosphere can drive currents powered by magnetic reconnection events between the planetary and interplanetary fields (Mauk and Bagenal 2012). The strength of auroral emission generated

by solar wind interactions scales with the incident stellar flux (Gallagher and Dangelo 1981), leading to predictions that magnetized hot Jupiters may emit radio emission several orders of magnitude brighter than Jupiter (Zarka et al. 2001). These predictions serve as the focus of several ongoing efforts to detect radio exoplanets. This mechanism dominates the auroral emission from Mercury, Earth, and Uranus but is unlikely to occur for isolated brown dwarfs.

As the electron beams from these field-aligned currents impact the planetary atmosphere, they generate auroral emission at various wavelength, with the Jovian auroral energy distributed as $\lesssim$0.1% X-ray, ~15% ultraviolet, ~1% optical, ~85% infrared, and $\lesssim$0.1% radio emissions (Ingersoll et al. 1998; Bhardwaj and Gladstone 2000; Perry et al. 1999; Badman et al. 2015). Of special relevance to this dissertation is that the optical component is expected to originate from Balmer line emission, and most of the infrared emission occurs between 2–4 μm and 7–14 μm from H_3^+ ro-vibrational transitions and thermal dissipation, respectively (Maillard and Miller 2011; Bhardwaj and Gladstone 2000).

The radio component of auroral emission occurs before the electron beam impacts the planet atmosphere and bears a more thorough discussion in §2 and §1.4 as it is the primary tool used and further developed in this dissertation.

1.4 Radio Activity in Brown Dwarfs

In the last decade since the initial detection of ~30% circularly polarized radio flares from the X-ray dim brown dwarf LP 944-20 by Berger et al. (2001), observations of the radio emission from low mass stars and brown dwarfs have opened a new window on magnetic activity in objects occupying the lowest end of the mass space. Initially, the broadband nature, measured lower-bound brightness temperatures ($\sim 10^9 (L/R_*)^{-2}$), and moderate fractional circular polarization (~30–40%) appeared consistent with a model of nonthermal gyrosynchrotron emission from an extended corona (Berger et al. 2005; Burgasser and Putman 2005).

Subsequent radio observations of brown dwarfs revealed ~100% circularly polarized short-duration (<10 min) flares with high brightness temperature ($\sim 10^{10} (L/R_*)^{-2}$) from the M8 V dwarf DENIS-P J104814.9-395604 — all hallmarks of coherent emission (Burgasser and Putman 2005). Shortly after, longer observations of similar emission from TVLM 513-46546 (M9), 2MASS J00361617+1821104 (L3.5), and LSR 1835+3259 (M8.5) showed that the flaring component was in fact periodic, and the short-duration periodicities (~1.96 hr, 2.84 ± 0.01 hr, and 3.08 ± 0.05 hr,

respectively) were consistent with $v \sin i$ measurements (Hallinan et al. 2006, 2007, 2008). This linked the pulsing emission to the rotation of the dwarfs rather than to periodic flaring or the orbital motion of a companion (e.g. Berger et al. 2005) and put strong constraints on the size of the emission region, further confirming the nonthermal and coherent nature of the emission (Hallinan et al. 2007).

However, the wide bandwidth of the observed flares appeared inconsistent with stellar coherent emission mechanisms, which are expected to have narrow bandwidth corresponding to the first or second harmonics of the plasma frequency $\nu_{p,\mathrm{GHz}} \approx 9n_e^{1/2}$, where n_e is the electron density in cm^{-3}, or cyclotron frequency $\nu_{c,\mathrm{GHz}} \approx 2.8B_{\mathrm{kG}}$. Plasma emission was especially unlikely, given that rising electron densities that track rising plasma emission frequencies become opaque to such emission at frequencies $\gtrsim$1 GHz (Dulk 1985), and ample evidence (discussed in §1.3.2) suggested increasingly neutral atmospheres in late M and L dwarfs that would not be compatible with high frequency plasma emission. In a breakthrough connecting brown dwarf observations to radio observations of Solar System planets, Hallinan et al. (2006) suggested that an electron cyclotron maser (ECM) mechanism could in fact remain consistent with wide bandwidths, if the masering mechanism occurred in a wide range of magnetic field strengths. Further supporting this interpretation was that ECM requires a tenuous electron density and/or a very strong local magnetic field such that the electron cyclotron frequency is much greater than the plasma frequency (Melrose 1973). The latter was plausible for cool brown dwarfs and the former was consistent with observed GHz emission frequencies.

Similar emission, largely attributed to an ECM mechanism, has in fact been observed to be produced along auroral magnetic field lines (Figure 1.8) from of all of the strongly magnetized Solar System planets: ~100% circularly or elliptically polarized, produced primarily along field-parallel precipitating electrons, rotationally modulated[8], beamed, at frequencies near the fundamental cyclotron frequency, high brightness temperature ($T_B \geq 10^{15}$), and originating from regions where plasma has been depleted such that $\nu_p/\nu_c \leq 0.1 - 0.2$ (Zarka 1998; Bagenal 1994; Galopeau, Zarka, and Le Queau 1989, and references therein). This emission includes both a component that can vary smoothly over timescales of several minutes and a bursty component with millisecond timescales and can extend from several tens of kilohertz up ~40 MHz for Jupiter or a few MHz for the other planets.

[8]The exception is for terrestrial auroral radio emission, which is dominated by the dynamics of the solar wind.

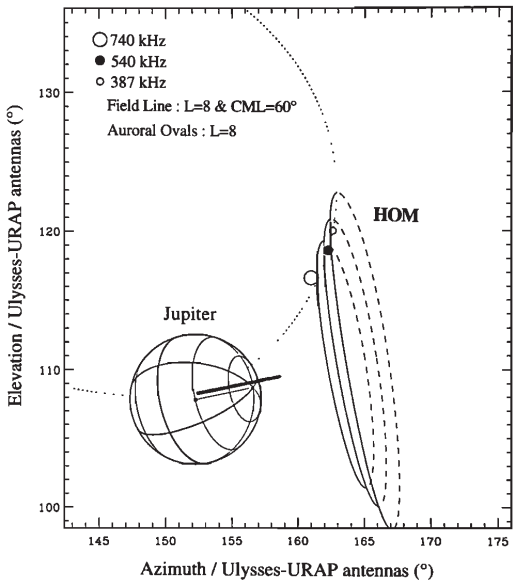

Figure 1.8: Average positions of Jovian radio emission at 387 kHz, 540 kHz, and 740 kHz (observed to be right-circularly polarized) measured by the Unified Radio and Plasma Wave Experiment on the Ulysses spacecraft. A model dipole magnetic field is offset from the rotation axis by 9.6°. Reprinted from Zarka (1998) with permission from Wiley, copyright 1998 by the American Geophysical Union. Originally adapted from Ladreiter, Zarka, and Lacacheux (1994) and reprinted with permission from Elsevier.

A component of the work presented in this dissertation explores a possible connection between auroral emission (i.e. the planetary magnetic activity paradigm) with radio emission. This is in part because such a connection may provide the key to overcoming what proved to be a persistent challenge preventing the application of ECM emission to studying magnetism in the coolest brown dwarfs: radio emission does not appear to be ubiquitous across brown dwarfs. Instead, detection fractions across M, L, and T dwarfs remain approximately constant at ∼10% (Route 2016). This number includes all radio detections of brown dwarfs, both pulsing and quiescent emission and comprises observations with the VLA (before and after upgrades to the JVLA) and with Arecibo, which is not sensitive to quiescent emission. Hence, even though ECM provides a one-to-one mapping between the emission frequency and magnetic field strengths in emitting regions when detected, the potential to extend magnetic field measurements to the substellar-planetary boundary — demonstrated by the timely detection of flaring radio emission from the T6.5 dwarf 2MASS J10475385+2124234 at ∼4 GHz (Route and Wolszczan 2012) — remained largely untapped without a more efficient means of discovering

ECM-emitting brown dwarfs (§3.3).

In addition to the pulsed component of brown dwarf radio emission is a 'quiescent' or non-pulsed component, with no or low fractional circular polarization ($\lesssim$30%) and can be mildly variable (e.g. Hallinan et al. 2008; Williams, Berger, and Zauderer 2013; Williams, Cook, and Berger 2014; Kao et al. 2016; Williams, Gizis, and Berger 2016). The mechanism responsible for this component of the emission remains unconfirmed, though spectral indices ranging from ~-1.5–2.1 and lower-bound brightness temperatures of order $10^8 - 10^9$ (e.g. Hallinan et al. 2006; Berger et al. 2009; Williams, Berger, and Zauderer 2013; Lynch, Mutel, and Güdel 2015) remain consistent with gyrosynchrotron emission. While the quiescent component of the emission has not been the focus of my thesis, evidence suggests that there may be a connection between the quiescent and pulsed radio components, which will become relevant for later chapters.

1.5 Overview of Dissertation Work

The work presented in this dissertation relies on a new interpretation of radio emission in brown dwarfs. Whereas radio emission has historically been attributed to stellar atmospheres heated by magnetic reconnection, my group has been working at the forefront of re-interpreting some radio emission as signatures of aurorae occurring on other worlds. This interpretation allowed me to efficiently find radio-emitting brown dwarfs and provide the first systematic test of magnetic dynamo models operating in planets through low-mass stars.

Departing from previous volume-limited brown dwarf radio searches, we implemented a selection strategy relying on the auroral activity paradigm in planets as applied to brown dwarfs. We selected six L7–T6.5 dwarfs with potential markers of auroral activity such as Hα emission and IR variability to observe at 4–8 GHz, leading to detections of five of targets (including four new radio brown dwarfs) with ~100–600 μJy peak pulse fluxes on minute timescales. My work quintupled the number of $\geq$L6 radio brown dwarfs and paved the way for testing dynamo theories in this mass regime.

To further develop ECM emission into a useable tool for testing dynamo models, I present a formalism for translating ECM magnetic field measurements into lower-bound surface-averaged field strengths independent of topologies and comparable to Zeeman broadening measurements, the dominant source of stellar measurements.

My work confirmed $\geq$2.5 kG local magnetic field strengths in dwarfs as late as

T6.5 and provided evidence that the dynamo operating in this mass regime may be inconsistent with a model unifying rapidly rotating, fully convective stars and planets that predicted magnetic energy is determined primarily by bolometric luminosity. This suggested that parameters beyond convected heat flux may influence brown dwarf magnetic field generation. Alternatively, scaling relationships between dynamo parameters may behave differently in cool brown dwarfs as compared to in planets.

In light of recent discoveries of Y dwarf infrared variability and to develop our understanding of magnetic fields at the substellar-planetary boundary, I observed two nearby exemplar IR variable Y dwarfs, WISE 0855-07 (~250 K) and WISE 1405+55 (~350 K) at 4–8 GHz. Although I did not detect any radio emission, this was the first such attempt and maps a path forward for measuring Y dwarf fields.

To provide the strongest constraints on magnetic fields in L/T dwarfs, I additionally extended initial observations of the detected L/T dwarfs from our initial pilot survey to 8–12 GHz and 12–18 GHz multiple rotation periods. I detected auroral pulses corresponding to localized ~3.7–6.2 kG fields. These measurements represent the strongest fields measured in the coolest brown dwarfs to date. I found that old brown dwarfs generate fields as strong as young brown dwarfs, further evidence that dynamos operating in the coolest brown dwarfs may not be solely luminosity-dominated. To study how rotation influences dynamo activity, I measured rotation periods between ~1.44–2.88 hr for my targets using the rotational modulation of auroral radio emission.

Finally, testing dynamo models requires magnetic field measurements for objects with a wide range of characteristics such as age, mass, and rotation rate. To widen the sample of radio-detected brown dwarfs, I have observed 33 L2.5–Y0 dwarfs with confirmed optical/IR variability. These are all of the known optical/IR variables that have not yet been observed at 4–8 GHz at the sensitivity that the recently-updated VLA can achieve. Analysis is ongoing, and I present preliminary results for two important objects: the third known IR-variable Y dwarf and a second canonical cloud variable T dwarf.

Chapter 2

METHODS: DEVELOPING AURORAL RADIO EMISSION INTO A TOOL FOR TESTING DYNAMO MODELS

[A portion of this discussion is excerpted from:]

Kao, M. M., G. Hallinan, J. S. Pineda, I. Escala, A. Burgasser, S. Bourke, and D. Stevenson. 2016. "Auroral Radio Emission from Late L and T Dwarfs: A New Constraint on Dynamo Theory in the Substellar Regime." *ApJ* 818, 24 (February): 24. doi:10.3847/0004-637X/818/1/24. arXiv: 1511.03661 [astro-ph.SR].

2.1 Testing Dynamo Models: Current Methods of Measuring Magnetic Fields

The dynamo models discussed in §1.2 demonstrate the numerous and varied attempts at establishing which physical characteristics govern fully convective dynamos, often with conflicting results. Though we have field measurements for objects as late as mid-L, the parameter range probed by late-L and T dwarfs is critical for constraining such models. However, data for such late-type objects is very sparse. As mentioned earlier, full convection sets in at ~0.35 $M_{\odot}$, and includes objects in the later half of M dwarfs (mostly fully convective stars), all L and T dwarfs (mostly brown dwarfs), as well as Y dwarfs/gas giant planets. These objects span a factor of ~300 mass range, and can have vastly different density profiles, rotation rates, luminosities, and atmospheric properties (e.g. conduction, chemistry, pressure support), to name a few properties. Thus, testing and constraining fully convective dynamos requires measuring magnetic field strengths for the orders-of-magnitude mass gap between stars and planets occupied by the coolest brown dwarfs (see Figure 1.3).

The confirmation of an electron cyclotron maser mechanism producing the pulsing component of brown dwarf radio emission provided a powerful means for probing magnetic field strengths and rotation periods of pulsing radio brown dwarfs, as the emission is produced at very near the fundamental cyclotron frequency rather than at a range of higher harmonics such as in gyrosynchrotron or synchrotron emission.

However, in order to compare magnetic field measurements from different studies (§2.2), it is important to first understand the different quantities and characteristics probed by available methods.

Zeeman Broadening

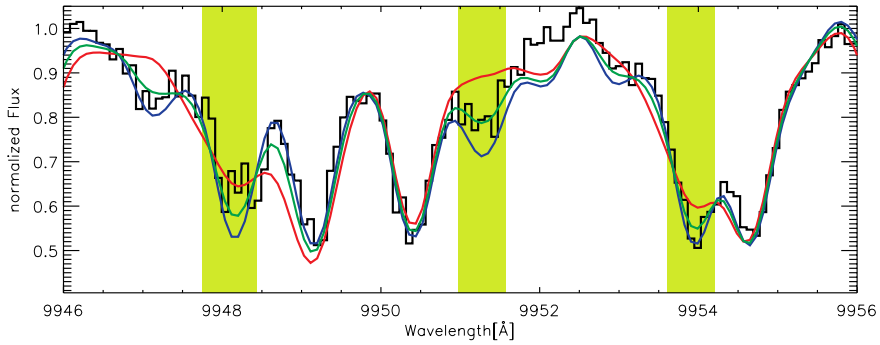

Figure 2.1: Without knowing Landé factors for FeH lines, it is possible to measure magnetic splitting by fitting template spectra of stars with known surface-averaged magnetic flux $B_Z f$. Here, the FeH band near 1 μm for LHS 2924 (M9) is shown, with template spectra for ~4 kG (red), ~0 kG (blue), and best fit 1.6 ± 0.2 kG (green). Light green regions indicate regions in the spectrum that are particularly sensitive to $B_Z f$. Figure adapted from Reiners and Basri (2007) and reproduced by permission of the American Astronomical Society.

Zeeman broadening measurements from spectral observations of magnetically sensitive lines provide mean surface field magnitudes B_s, averaged over the photospheric surface of stars, or in rare cases, averaged over the magnetically active regions of the star.

Magnetic fields can perturb the magnetic dipole moment of an electron in an atom or molecule, resulting in slight energy differences between different orbital angular momentum states for the same electron orbital. In the presence of strong magnetic fields, the electron angular momentum term in the Hamiltonian for a given orbital becomes important. This introduces a small but in some cases observable energy difference in transitions between the same set of electron orbitals but to different angular momentum orientations that is linearly proportional to the strength of the magnetic field. The result is that what is a single spectral line in the absence of a magnetic field splits into multiple lines in the presence of a strong magnetic field. The additional lines correspond to these energy differences, with a central core at the original spectral line wavelength (known as the π component) as well at lines at $\Delta\lambda_B$ blueward and redward of the core (known as σ components). The wavelength differences between the π and σ components are given as:

$$\Delta\lambda_B = \frac{\lambda_0^2 e g_{\rm eff} B}{4\pi m_e c^2} = 0.00467 g_{\rm eff} \left(\frac{\lambda_0^2}{1\ \mu{\rm m}}\right)\left(\frac{B}{1\ {\rm kG}}\right)\ {\rm nm}, \tag{2.1}$$

where B is the magnetic field strength, λ_0 is the transition wavelength when the magnetic field is absent, e is the electron charge, m_e is the electron mass, c is the speed of light, and $g_{\rm eff}$ is the dimensionless Landé factor for each component and is of order unity for magnetically sensitive lines.

While this splitting can be resolved on the Sun, the surface rotational velocity of most active stars is sufficient to smear out the individual lines, resulting in a Zeeman broadening effect rather than a full splitting effect. Additionally, the light from unresolved stars is integrated over the stellar disk, resulting in spectral line observations that probe the wide range of magnetic field strengths that can exist on the surface of a star. The resulting measurement $B_Z f$ thus returns a mean surface field strength with the topological information folded in as a filling factor f.

Because the splitting width scales quadratically with wavelength whereas intrinsic line width scales linearly, σ components can be resolved at near-IR wavelengths. When this occurs, the strengths of the σ and π components relative to the total line strength can determine the filling factor (Saar 1990; Valenti, Marcy, and Basri 1995; Johns-Krull and Valenti 1996, 2000). This requires atomic lines to be relatively isolated for comparison with continuum flux. M5 or later type objects suffer from spectra increasingly contaminated by molecular lines, and lines become dominated by pressure broadening. In cases where the Zeeman splitting cannot be resolved from the intrinsic line width, the filling factor remains entangled with the mean field and it is possible to measure only $B_{\rm s} = B_Z f$. Additionally, unresolved Zeeman splitting components require careful modeling and measurements of lines with very low Landé factors (magnetically insensitive) to distinguish Zeeman broadening from other sources such as thermal, collisional, and rotational broadening (Valenti, Marcy, and Basri 1995). Magnetic fields can also be diluted by the filling factor in Zeeman broadening, which typically is less than ~10% for active stars, making the σ components difficult to detect.

Reiners and Basri 2007 were able to measure mean field magnitudes by comparing the FeH features of 24 M2–M9 stars to reference spectra with known $B_Z f$ (Figure 2.1), with ~15%–30% uncertainties (Reiners 2012; Shulyak et al. 2010). The method described by Reiners and Basri 2006 is limited by the reference spectra; $B_Z f$ is measured in reference to a zero field spectrum and a 3.9 kG spectrum, so only fields less than 3.9 kG can be quantified, though it is unlikely that the object serving as the zero field reference is in fact magnetically inactive. Finally, Zeeman broadening techniques have yet to be successfully applied to objects beyond M9,

where rotational broadening blends known useful molecular lines and FeH and Ti lines saturate. Detailed theoretical treatments remain limited for determining the values of Landé factors and therefore the magnetic sensitivity of a given line (Berdyugina and Solanki 2002; Shulyak et al. 2010). Despite these limitations, Zeeman broadening provides a straightforward and convenient framework within which to interpret measurements when testing dynamo predictions.

Zeeman Doppler Imaging (ZDI)

Zeeman Doppler imaging provides approximate reconstructions of surface field topologies, by using the different polarization properties of the π versus σ components together with the Doppler effect to reconstruct magnetic field maps. Recovering some information about field topologies provides estimates of the magnetic energy in different field components (for example, the dipole).

First, we focus on the Zeeman broadening aspect of ZDI, which relies not only on the splitting phenomenon previously discussed but also on the polarization properties of the different line components. The π components are so-named because they emit linearly polarized radiation that is parallel to the magnetic field. This occurs because the π component arises from energy transitions between the same magnetic quantum numbers m (~electron orbital angular momentum vectors) of different orbitals. When $\Delta m = 0$, the angular dependence in the resulting wave function goes away. In contrast, the σ components arise from transitions where the electron orbital angular momentum vectors are different. This change in electron orbital angular momentum results in the small wavelength offsets from the π component as well as emission that is circularly polarized perpendicular to the magnetic field. Thus, when the magnetic field is parallel to an observer's line of sight, no emission from the π component is visible while emission from both of the σ components are visible in Stokes V (circularly polarized intensity). If the magnetic field is instead perpendicular to the line of sight, all of the π and σ components can all be observed in Stokes I (full intensity) and Stokes Q (linearly polarized intensity), but not in Stokes V. In theory, by observing the full polarization properties for the different Zeeman splitting components, it is possible to recover the mean magnetic field vector in the relevant region of the stellar disk.

Recovering spatial information requires the Doppler imaging aspect of ZDI and makes use of the full intensity emission measured by Stokes I. Strong magnetic fields emerging at the stellar surface act to essentially 'freeze' the convective motions of

fluids in that region, preventing the transport of heat and resulting in a dark spot with lower temperature than the surrounding material and less radiative flux. In an absorption line, this appears as a bump in the line. The position of this spot on the stellar disk can be determined by the wavelength range that this bump traverses as it rotates in and out of view from blueward to redward wavelengths.The nearer the spot resides to the rotational pole of the object, the smaller a range of wavelengths it will traverse.

As applied with existing instruments, ZDI measurements are only sensitive to larger-scale fields, especially in very dim and fast rotators, such as our objects. The sensitivity of ZDI is limited by current abilities to adequately resolve polarized flux. Inadequate resolution can lead to the apparent canceling out of observational signatures of opposite polarity fluxes and mask magnetic fields at smaller spatial scales. For this reason, ZDI is more sensitive to large-scale field structures that can be fully resolved by existing instruments (Reiners and Basri 2009; Yadav et al. 2015), and Morin et al. (2010) have found that the dipole energy can vary by ∼10–30%, with significant confusion between the dipole and quadrupole components. Additionally, instruments used to map the magnetic fields of cool stars were limited to two of the four Stokes parameters (I, V) until very recently (Rosén, Kochukhov, and Wade 2015), which further limits the sensitivity of ZDI in fully capturing magnetic field topologies. Finally, ZDI maps can vary widely depending on the particular entropy weighting prescription used when phase coverage is insufficient. Nonetheless, the sensitivity of ZDI to large-scale fields has provided vital insight into large-scale fields. Field topologies of stars appear to change from being dominated by a weak non-axisymmetric toroidal field to a strong axisymmetric poloidal field as they cross into the fully convective regime (Donati et al. 2008; Morin et al. 2008), and Morin et al. (2010) found evidence for bistable field topologies in late-M dwarfs, as discussed in §2.2.1.

While both Zeeman methods can probe the types of global magnetic field properties that are valuable for constraining dynamo models, they also suffer from several key shortcomings, as previously discussed. However, the most important shortcoming underscores the significance of the work presented in this dissertation: Using either of the Zeeman techniques to measure magnetic fields is currently impossible for objects beyond spectral type M9, yet the mass regime occupied by L and T dwarfs is critical for probing the efficacy of any fully convective dynamo model.

Electron Cyclotron Maser (ECM) Emission

Radio observations of electron cyclotron maser emission provide a new window for probing magnetic activity in a mass regime where Zeeman broadening techniques cannot currently reach. However, in contrast to Zeeman broadening methods, ECM emission by itself gives a single measurement with great accuracy of the *local* magnetic field strength in the region of the magnetosphere corresponding to the emission, rather than returning a globally averaged field or any topological information.

Electrons accelerated by magnetic field-aligned electric potential drops such as auroral current systems in planetary magnetospheres can reach nonthermal energy distributions (Calvert 1981; Chiu and Schulz 1978), leading to the amplification of the coherent emission at very near the fundamental cyclotron frequency by way of the electron cyclotron maser instability when magnetospheric conditions are such that the ratio between the plasma frequency $\omega_{\rm pe} = \sqrt{\frac{4\pi n_e e^2}{me}}$ and the electron-cyclotron frequency $\omega_{\rm ce} = \frac{eB}{m_e c}$ are very small:

$$\frac{\omega_{\rm pe}^2}{\omega_{\rm ce}^2} = \frac{4\pi n_e m_e c^2}{B^2} \ll 1\,, \tag{2.2}$$

where n_e is the local electron density, m_e is the electron mass, e is the electron charge, B is the local magnetic field strength, and c is the speed of light (Treumann 2006; Winglee 1985, and references therein).

The resulting radio emission can be identified by the following characteristics:

High degree of circular polarization Right circularly polarized (when propagating outward from a north magnetic pole) X-mode emission is expected to dominate, though the emission can be depolarized (Melrose 2006, e.g.), as has been observed in solar narrow-band and short decimeter and microwave spikes (Bastian, Benz, and Gary 1998).

Rotational Modulation ECM emission is highly beamed into a thin conical sheet with $\sim 1^\circ$ thickness and a wide opening angle that is expected to be nearly perpendicular to the direction of the magnetic field. The surface of this cone can pass through an observer's line of sight as the emitting object rotates, and the emission manifests as narrow pulse of comparatively bright and highly circularly polarized radio emission.

High brightness temperature Because ECM is a coherent process, its brightness temperature is much larger than the temperature of the electron kinetic energy and has been observed up to 10^{20} K.

Fine structure While ECM emission appears as wide-band pulses often spanning at least several GHz in frequency range, high resolution observations of auroral kilometric radiation (AKR) from Earth, Jupiter, and Saturn reveal narrow-band and short-lived pulse structures. In fact, rather than one continuous pulse through frequency, AKR actually consists of many small-scale micropulses that are highly time variable and narrowly-spaced in frequency, with widths of order ~10–1000 Hz. This fine structure is expected, as the emission arises from individually radiating sources corresponding to bunched groups of these local AKR sources traveling very rapidly through space, which may reflect small-scale structures in the electric field as has been observed in Earth's auroral regions (Gurnett, Kurth, and Scarf 1981; Pottelette et al. 1999; Treumann 2006, and references therein).

ECM emission at higher harmonics has been invoked to explain coherent radio bursts from the Sun and active stars (Bastian, Benz, and Gary 1998, and references therein), where the coronal density is such that second-harmonic cyclotron absorption may prevent escape of emission at the fundamental frequency. Indeed, it has been shown that emission at the second and higher harmonic can dominate when the ratio of the plasma frequency to the electron cyclotron frequency exceeds ~0.3 (Winglee 1985). However, in the case of our sample, this would require a local plasma density of $\sim 10^{11}$ cm^{-3}, more indicative of hot stellar coronae than the cool neutral atmospheres of late L and T dwarfs, motivating the assumption that we later make of emission at the fundamental electron cyclotron frequency.

Auroral ECM emission from the planets in our Solar System is produced very close to the fundamental electron cyclotron frequency local to the source region, providing an exquisite one-to-one mapping between emission frequency and magnetic field strength:

$$\nu_{\rm MHz} \sim 2.8 \times B_{\rm Gauss} \, . \tag{2.3}$$

Though intrinsically narrow-band ($\Delta\nu \ll \nu$), the emission can be detected over a wide range of frequencies, as the process operates efficiently over a range of heights above the planetary surface, which maps to a range of field strengths. Taking the Jovian case as an example, auroral radio emission is detected from 10 kHz to 40 MHz

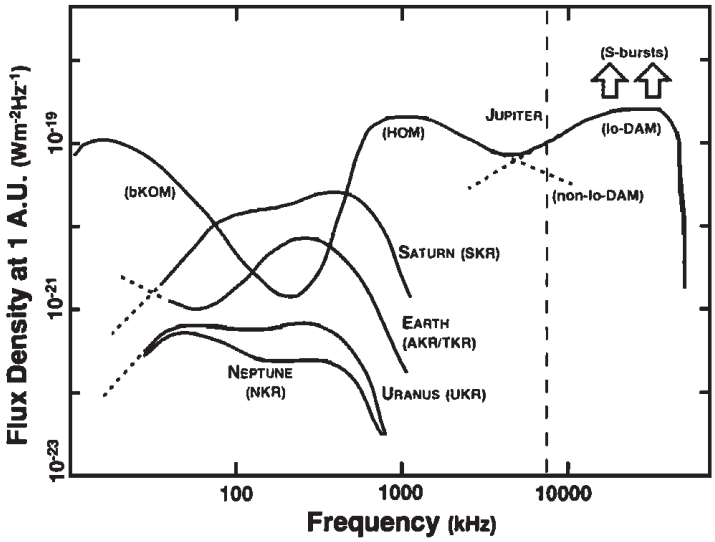

Figure 2.2: Average spectra of Solar System auroral emission, reprinted from Zarka (1998) with permission from Wiley, copyright 1998 by the American Geophysical Union. Originally adapted from Zarka (1992) with permission from Elsevier.

frequencies, with the lowest frequency emission originating in source regions out to >5 R_{Jup}, and the high frequency emission corresponding to the highest strength magnetic field regions (14 Gauss) just above the atmosphere in the auroral polar regions in the northern hemisphere (Zarka 1998).

This emission has additionally been observed in all of the other magnetized Solar System planets, and Figure 2.2 shows their radio spectra. Of special note is that auroral radio emission appears to cut off abruptly in all cases. This cutoff frequency corresponds to the strongest magnetic field strength the emitting electrons see before they impact the atmosphere and conditions for ECM no longer hold. Observed remotely, independent of knowledge of the source region or the electrodynamic engine powering the auroral currents, the high frequency cut-off of this emission provides a good means to determine the maximum magnetic field strength in the magnetospheres of the magnetized planets.

We utilize the highly circularly polarized component of the radio emission detected from our sample of cool brown dwarfs to similarly constrain the maximum magnetic field strengths in their magnetospheres, with a view to constraining the dynamo mechanism at work in their interiors. In the absence of a clear cutoff in emission, we note that any detection can be equated to a robust lower limit on a maximum surface magnetic field strength. While the detection of such ECM emission provides exquisite measurement of local magnetic field strengths at the source of the

radio emission, this must be translated to global parameters of particular use to dynamo modeling. Similarly, care must be taken in comparing these measurements with magnetic field measurements previously obtained for higher mass objects via Zeeman splitting/broadening and Zeeman Doppler imaging, as they are measuring distinct but complementary properties of the magnetic field. We address these issues in § 2.2.

Because the measured magnetic field magnitudes are dependent only on the frequency of the emission cutoff, measurements from radio observations are not subject to the same sources of uncertainty that affect the accuracy of Zeeman broadening measurements. However, ECM measurements also have limitations beyond only probing localized field strengths. In particular, they are likely primarily sensitive to large-scale fields and the data in isolation are not sufficient for reconstructing the field topology. Finally, without observing emission cutoffs, we are limited to interpreting our measurements as lower-bounds to global maximum surface field strengths.

2.2 A Simple Formalism for Comparing Magnetic Field Measurements

2.2.1 Magnetic Field Topology

Radio observations of highly circularly polarized pulsed emission yield precise measurements of local magnetic field strengths in the magnetospheres of our objects. However, translating them to a global field strength useful for evaluating dynamo models requires topological information that is difficult to determine from radio observations alone.

Lynch, Mutel, and Güdel (2015) attempted to constrain the field topologies for two pulsing radio dwarfs by modeling their radio dynamic spectra, inferring localized loops and loss-cone ECM from their modeling. In contrast, Kuznetsov et al. (2012) similarly model the radio pulses of one of the dwarfs examined by Lynch, Mutel, and Güdel (2015) and found that a highly inclined dipole model with active longitudes for shell-type electron distributions reproduces the pulses with greater fidelity than a loss-cone distribution. Others have inferred dipole-dominated (Yu et al. 2011), quadrupole-dominated (Berger et al. 2009), or small-scale-dominated (Cook, Williams, and Berger 2014; Williams, Cook, and Berger 2014) field geometries for pulsing radio dwarfs. Similar extrapolations have been made for Jovian radio emission using the Exoplanetary and Planetary Radio Emissions Simulator (Hess, Cecconi, and Zarka 2008; Hess et al. 2011). However, the latter use a plethora

of additional information to help constrain their calculation, including information on the radio source distribution, the beaming in the planetary environment, a planetary magnetic field model, and precise knowledge of the planetary inclination to the line of sight, none of which are currently available for the dynamic spectra of ultracool dwarfs. We do not attempt to recover the field topologies of our objects here.

Instead, we consider the case where a dipole drives the observed emission. Although direct confirmation of the electrodynamic engine(s) at work in our objects is required to infer whether our magnetic field measurements are indeed of the dipole component or are instead from higher order components, we note that detailed observations of the magnetized Solar System planets show that the dipole component is most likely to produce auroral emission. Specifically, interactions between the large-scale planetary magnetic field with the solar wind (Isbell, Dessler, and Waite 1984), the planetary field with orbiting moons such as the Jupiter-Io current system (Goldreich and Lynden-Bell 1969), and co-rotation breakdown of a plasma sheet in the planetary magnetosphere drive the electrodynamic engines of the Solar System planets (Hill 2001; Cowley and Bunce 2001; Bagenal et al. 2014; Badman et al. 2015, and references therein). In all cases, energy is coupled into the upper atmosphere from distances sufficient for the planetary dipole components to dominate.

For our objects, magnetosphere-ionosphere (M-I) coupling via co-rotation breakdown or satellite interaction have been proposed as likely drivers (Schrijver et al. 2011; Nichols et al. 2012; Hallinan et al. 2015). We first consider satellite interaction. For a brown dwarf with a rocky satellite, the Roche limit occurs at $\sim 3.7 R_*$ (Murray and Dermott 1999). Even at this minimum distance, dipole fields dominate over higher order fields that are a factor of 3 stronger at the surface. In comparison, corotation breakdown occurs at 30–50R_J for Jupiter (Cowley and Bunce 2001; Hill 2001; Vogt et al. 2011, and references therein), and at 3–4R_S for Saturn (Stallard et al. 2010). In these cases, dipole fields of surface field strengths ~2–50 times weaker than a quadrupole surface field would dominate at the corotation breakdown radius.

Zeeman Doppler imaging by Morin et al. (2010, hereafter JM10) suggests that objects significantly below the fully convective boundary with ~kilogauss large-scale fields are dipole-dominated, with the majority of their magnetic energy lying in the dipole component. Specifically, they find that magnetic topologies of 11 M5–M8 dwarfs fall into either a strong or weak large-scale field regime (strong LSF

and weak LSF, respectively). In the strong LSF regime, the large-scale field is of order kilogauss with 66–90% of the reconstructed magnetic energy in the dipole component and is temporally stable over at least ~3 years, the length of the study. In the weak LSF regime, multipolar field topologies with much weaker ~0.1 kG large-scale fields vary significantly on year timescales. If the results of Morin et al. (2010) apply to late L and T dwarfs, then objects in the strong LSF regime are unlikely to host quadrupolar fields a factor of three or more times stronger than the dipole component, and the dipole field would drive the M-I coupling currents.

In contrast, Williams, Cook, and Berger (2014) argue that weak LSF objects may be X-ray dim/radio bright (departing from the Güdel-Benz relation) instead of X-ray bright/radio dim (more aligned to the Güdel-Benz relation). They suggest that objects in the weak LSF regime likely experience less magnetic activity than objects in the strong LSF regime, hypothesizing that the decreased magnetic activity in weak LSF objects result in correspondingly underluminous X-ray emission, but that small-scale reconnection events can provide a source of radio-emitting electrons. However, we note that in the standard reconnection model of chromospheric heating, X-ray and radio luminosities are tightly correlated (Güdel and Benz 1993; Güdel 2002; Benz and Güdel 2010; Forbrich et al. 2011, and references therein), except for extremely small solar flares, which are in fact comparatively radio underluminous rather than X-ray dim/radio bright. Accordingly, the presence of small-scale reconnection events from a strong small-scale field (as in the weak LSF regime) would result in objects that adhere more closely to the Güdel-Benz relation.

Instead, the lowering of fractional ionization can explain the relative decrease in X-ray luminosities (Mohanty et al. 2002). This does not necessarily impact the radio emission, which is produced above the photosphere or chromosphere irrespective of the mechanism by which it is produced and does not necessarily have the same dependence on fractional ionization as coronal heating. It is also important to note that previous Zeeman broadening studies for 9 of the 11 stars studied in JM10 measured mean surface field magnitudes of order kilogauss (Reiners and Basri 2007; Reiners, Basri, and Browning 2009), regardless of which field regime the star occupied. This implied that the small-scale fields rather than the large-scale ones are quite strong in the weak-field regime. However, in such a scenario, we note that even though the current understanding of M-I coupling does not require the fields to be dipolar, they must be large-scale and strong (kilogauss or stronger to fit observations), precluding the possibility that even strong small-scale fields could

drive the M-I coupling.

In the case that JM10 does not extend to our objects, late L and T dwarfs may in fact be more analogous to gas giant planets than to M-dwarfs. Jupiter and Saturn are both dipole-dominated, with the quadrupole and octupole moments at ∼20% of the dipole moment in Jupiter (Acuna and Ness 1976), and the quadrupole moment in Saturn only ∼7% of its dipole moment (Russell 1993). Despite significant higher order moments present in the Jovian field, the auroral radio emission produced by Jupiter is thought to be dominated by the dipolar field component (Hill 2001).

While it is possible for higher order components to drive M-I coupling currents, it is clear that the dipole field can efficiently generate auroral currents. Therefore, we treat the dipole case and will revisit alternatives when additional information on the magnetic fields of ultracool dwarfs becomes apparent.

2.2.2 Relating Magnetic Fields Measured from Auroral Radio Emission to Zeeman Techniques

Under the assumption that auroral emission can be associated with the dipole component of the magnetic field, we now relate magnetic field measurements from radio aurorae to those obtained from Zeeman broadening and Zeeman Doppler imaging observations so that we may later compare our ECM measurements to model predictions, which use Zeeman-based measurements.

To estimate the lowest possible bound on the global rms surface field strength of an object from a single local radio-derived measurement, we consider an idealized dipole case, which we will adjust as additional topological information becomes available. Our interest in obtaining a conservative lower limit allows us to assume the following simplifications for all of our objects:

1. The magnetic field is perfectly dipolar (the presence of higher order fields will positively contribute to the rms surface field).

2. The lower bound field strength measured from our ECM observations, B_{ECM}, is the field strength at the magnetic pole at the photosphere. In reality, the emission likely samples the field at a location that does not correspond exactly with the magnetic pole. Moreover, until we observe a frequency cutoff, the emission corresponds to a location in the magnetosphere that is a nonzero altitude above the photosphere, so the actual surface polar field strength can only be equal or greater in all cases.

3. Brown dwarfs are perfect spheres.

We calculate the mean surface dipole field, beginning with the expression for a dipole field,

$$\vec{B}(\vec{r}) = \frac{\mu_0}{4\pi}\left[\frac{3\hat{n}(\hat{n}\cdot\vec{m})-\vec{m}}{|\vec{r}|^3}\right], \tag{2.4}$$

where $\hat{n} = \vec{r}/|\vec{r}|$ is the unit vector in the direction to the point on the sphere for which the field strength is calculated and $\vec{m}$ is the magnetic dipole moment. Averaging over the surface of the star shows that the mean squared surface field strength due to the dipole field is

$$\langle B^2_{\rm s,dip}\rangle = \frac{1}{2}B^2_{\rm ECM}\ . \tag{2.5}$$

In the case where our objects have purely dipolar fields, $\langle B_{\rm s,dip}\rangle^{1/2}$ would be equivalent to the mean surface field magnitude $B_{\rm s} = B_Z f$ as measured by Zeeman broadening, with a filling factor of 100%. Where our objects do not have purely dipolar fields, we consider two cases. If higher order fields are anti-aligned with the dipole field, such that they contribute negatively to the magnetic flux at the pole, then $\langle B_{\rm s,dip}\rangle^{1/2}$ as calculated above will underestimate the lower bound of the mean surface field magnitude. If higher order fields are aligned with the dipole such that they contribute positively to the flux at the magnetic pole, then the field strength measured from radio emission will overestimate the rms surface dipole field.

To understand the severity of such a possible overestimation, we return to the Morin et al. 2010 study. While Morin, Dormy, et al. 2011; Morin, Delfosse, et al. 2011 interpret the result as possible evidence for a dynamo bistability, Kitchatinov, Moss, and Sokoloff 2014 have also proposed that it is evidence of an M-dwarf magnetic cycle. No objects have been observed to be in a transition between the strong field and weak field regimes, suggesting that if such a transition occurs, as in a magnetic cycle, the transition is very fast and is unlikely to impact the interpretation of our field measurements. We know from the observed ECM emission and our discussion in §2.2.1 that our objects likely occupy the strong LSF regime of a possible bistable dynamo or magnetic cycle. This implies relatively weak higher order fields, limiting any overestimation of the mean surface field magnitude.

Chapter 3

AURORAL RADIO EMISSION FROM LATE L AND T DWARFS: A NEW CONSTRAINT ON DYNAMO THEORY IN THE SUBSTELLAR REGIME

[Adapted from:]

Kao, M. M., G. Hallinan, J. S. Pineda, I. Escala, A. Burgasser, S. Bourke, and D. Stevenson. 2016. "Auroral Radio Emission from Late L and T Dwarfs: A New Constraint on Dynamo Theory in the Substellar Regime." *ApJ* 818, 24 (February): 24. doi:10.3847/0004-637X/818/1/24. arXiv: 1511.03661 [astro-ph.SR].

3.1 Abstract

We have observed 6 late-L and T dwarfs with the Karl G. Jansky Very Large Array (VLA) to investigate the presence of highly circularly polarized radio emission, associated with large-scale auroral currents. Previous surveys encompassing ~60 L6 or later targets in this spectral range have yielded only one detection. Our sample includes the previously detected T6.5 dwarf 2MASS 10475385+2124234 as well as 5 new targets selected for the presence of Hα emission or optical/infrared photometric variability, which are possible manifestations of auroral activity. We detect 2MASS 10475385+2124234, as well as 4 of the 5 targets in our biased sample, including the strong IR variable SIMP J01365662+0933473 and bright Hα emitter 2MASS 12373919+6526148, reinforcing the possibility that activity at these disparate wavelengths is related. The radio emission frequency corresponds to a precise determination of the lower-bound magnetic field strength near the surface of each dwarf and this new sample provides robust constraints on dynamo theory in the low mass brown dwarf regime. Magnetic fields $\gtrsim$ 2.5 kG are confirmed for 5/6 targets. Our results provide tentative evidence that the dynamo operating in this mass regime may be inconsistent with predicted values from a recently proposed model. Further observations at higher radio frequencies are essential for verifying this assertion.

3.2 Introduction

An important outstanding problem in dynamo theory is understanding how magnetic fields are generated and sustained in fully convective stellar objects. Prevailing dynamo models for dwarf stars with an inner radiative zone and an outer convective envelope, like the Sun, are accepted to rely on the shearing at the interface between these two layers, where differential rotation is strongest (Parker 1975). Beyond spectral type ~M4, stars are fully convective and no longer possess the internal structures necessary to sustain such dynamos (Chabrier and Baraffe 1997). However, flaring M-dwarfs are characterized by kilogauss fields covering much of the stellar disk (Saar 1994; Johns-Krull and Valenti 1996), and the fraction of M, L, and T dwarfs that exhibit strong and persistent Hα emission, a magnetic activity tracer, rises through late-M dwarfs and peaks at ~90% for L0 dwarfs before declining to ~50% for L5 dwarfs (Gizis et al. 2000; West et al. 2004, 2008; Schmidt et al. 2015). Clearly, an alternative dynamo operates in low mass, fully convective stars. A number of models for possible dynamo mechanisms in this regime have been proposed (Chabrier and Küker 2006; Dobler, Stix, and Brandenburg 2006; Browning 2008; Christensen, Holzwarth, and Reiners 2009; Morin, Dormy, et al. 2011; Gastine et al. 2013), but constraining data on magnetic field strengths and topologies across a wide range of mass, age, rotation, and temperature are sorely lacking, particularly in the brown dwarf regime.

In a recent breakthrough, scaling laws derived from planetary dynamo calculations (Christensen and Aubert 2006) were demonstrated to be empirically consistent with the magnetic field strengths measured for fully convective stars (Christensen, Holzwarth, and Reiners 2009). This result argued for a single unifying principle that governs magnetic activity in rapidly rotating fully convective objects, spanning the mass range from stars to planets; specifically, that the energy flux available for generating the magnetic field sets the field strength. This principle states that the magnetic energy in these objects should scale approximately as $\propto \langle\rho\rangle^{1/3} q_0^{2/3}$, where $\langle\rho\rangle$ is the mean density in the dynamo region and q_0 is the bolometric flux. However, while this scaling law appears consistent with magnetic field measurements for Solar System planets and fully convective stars, data from the orders of magnitude mass gap occupied by rapidly rotating brown dwarfs and massive extrasolar planets are required to validate this principle.

Traditionally, the Zeeman effect has been one of the most powerful means to measure the strength, filling factor, and even large-scale field topology of stellar magnetic

fields, including those of fully convective stars. Zeeman broadening of atomic lines such as Fe I has been successfully used to recover the large-scale field topologies of active mid-M dwarfs, confirming that the high levels of coronal and chromospheric activity observed for these stars is indeed associated with strong magnetic fields (typically a few kiloGauss) covering a large fraction of the photosphere (with filling factors as high as ~50%) (Johns-Krull and Valenti 1996). Zeeman Doppler imaging, involving time-resolved high-resolution spectropolarimetry, has been successfully applied to mid- and late-M dwarf stars, both above and below the fully convective boundary (Donati et al. 2006). In some cases, strong large-scale poloidal fields are identified while in other cases weak large-scale fields with strong higher order components are found (Morin et al. 2010), suggesting that a bistable dynamo may operate in the very low-mass regime. Probing to even cooler temperatures, Reiners and Basri 2007 were able to use Zeeman broadening of magnetically sensitive molecular lines, such as FeH, to constrain the average surface magnetic fluxes of objects as late as M9. While these methods have been successful, a robust detection of Zeeman broadening has not been established for objects cooler than late M, as rapid rotational broadening causes blending of the desired molecular lines (Reiners and Basri 2006).

In the last decade, observations of the radio emission from low mass stars and brown dwarfs have opened a new window on magnetic activity in this regime. While the initial detection of quiescent emission from ~10% of targets (Berger 2006), possibly consistent with incoherent gyrosynchrotron emission, was itself anomalous (Berger et al. 2001), the later confirmation of a second component to the radio emission, manifested as periodic pulsar-like bursts of 100% circularly polarized emission, was even more unexpected (Hallinan et al. 2006, 2007). This emission is attributed to the electron cyclotron maser instability, and is of the same nature as the auroral emission produced by the magnetic planets in our Solar System via magnetosphere-ionosphere coupling. However, unlike the planets, where auroral radio emission is powered by interactions with the solar wind, orbiting satellites, and co-rotation breakdown, the nature of the electrodynamic engine powering auroral activity in ultracool dwarfs remains unclear (Hallinan et al. 2015).

What is clear is that electron cyclotron maser (ECM) emission is a very powerful tool for measuring magnetic fields. Produced at the electron cyclotron fundamental frequency $\nu_{\rm MHz} \sim 2.8 \times B_{\rm Gauss}$ (Treumann 2006, and references therein), it allows for very accurate measurements of local magnetic field strengths and rotation periods,

and it has provided some of the first confirmations of kilogauss fields for late M and L dwarfs (Burgasser and Putman 2005; Hallinan et al. 2006, 2007, 2008; Berger et al. 2009). Indeed, radio observations have been the only method thus far capable of direct magnetic field measurements for L dwarfs. Examining magnetic dynamo action in the mass gap between planets and stars requires radio data.

Over a dozen low mass stars and brown dwarfs, ranging in spectral type from M7–L5, have been found to be radio sources in the last decade (Berger et al. 2001; Berger 2002; Burgasser and Putman 2005; Berger 2006; Phan-Bao et al. 2007; Antonova et al. 2007; McLean, Berger, and Reiners 2012; Burgasser et al. 2013; Williams, Cook, and Berger 2014; Burgasser, Melis, Todd, et al. 2015). A subset of these objects have been the subject of lengthy follow-up campaigns that have revealed the presence of 100% circularly polarized, periodic pulses, with the pulse period typically 2–3 hours and consistent with rotation (Hallinan et al. 2006, 2007, 2008; Berger et al. 2009). More recently, magnetic field measurements have been extended much further, with the detection of the coolest radio brown dwarf yet detected, the T6.5 dwarf 2MASS J10475385+2124234 (hereafter 2M1047) by Route and Wolszczan 2012. They observed individual radio pulses from this object in multiple short duration observations at 4.75 GHz with the Arecibo observatory, resulting in a confirmed magnetic field strength of at least 1.7 kG near the surface of this extremely cool (∼900 K) object. The results of Route and Wolszczan (2012) highlight the unique capability of radio observations to measure magnetic fields in the critical L and T dwarf regime and demonstrates that the latest-type brown dwarfs can in fact host ∼kG field strengths.

However, this single detection came at substantial expense. In previous surveys totaling ∼60 L6 or later type objects, only one was detected (Antonova et al. 2013; Route and Wolszczan 2013), demonstrating that previous selection strategies (largely volume-limited) have been inefficient. Motivated by the radio detection of 2M1047, we present a pilot survey of 6 objects ranging in spectral type L7.5–T6.5, including the previously detected T6.5 dwarf 2M1047. We selected our targets using a new strategy, described in §3.3. We measure magnetic field strengths of the coolest brown dwarfs using auroral radio emission, and we study implications on fully convective magnetic dynamo theory.

3.3 Target Selection Strategy

In a departure from previous surveys, we have selected our objects for tracers of auroral emission at other wavelengths. This selection strategy is motivated by recent work by Hallinan et al. (2015) linking periodic auroral radio emission to Hα emission and optical broadband variability, as well as corroborating evidence that most radio-pulsing ultracool dwarfs exhibit weak Hα emission and/or optical/IR variability.

Hα and X-ray emission have been known for decades to scale as power laws of increasing surface rotation or decreasing Rossby number ($Ro \sim P/\tau_c$, where P is the stellar rotation period and τ_c is the convective turnover time) for main sequence F through mid-M stars, until around $Ro \sim 0.1$, when the activity-rotation scaling appears to saturate at a constant $\log L_{\mathrm{X,H}\alpha}/L_{\mathrm{bol}}$ (Pallavicini et al. 1981; Soderblom et al. 1993; Stauffer et al. 1994; Delfosse et al. 1998; Pizzolato et al. 2003; Reiners, Basri, and Browning 2009; McLean, Berger, and Reiners 2012). Additionally, flaring and quiescent radio emission observed in dwarf stars have been attributed to magnetic activity in the corona (White, Kundu, and Jackson 1989; Drake, Simon, and Linsky 1989), and in fact, X-ray and radio luminosities for magnetically active stars are tightly correlated on the Güdel-Benz relation, spanning 5–6 orders of magnitude and including F through M stars and solar flares (Güdel and Benz 1993). The Güdel-Benz relation holds for active stars independent of age, spectral class, binarity, or rotation period. It suggests that coronal heating and particle acceleration via magnetic fields are related processes (Forbrich et al. 2011, and references therein).

However, beyond $\gtrsim$M7, magnetic activity trends appear to diverge. L and T dwarfs regardless of age appear to be fast rotators (Reiners and Basri 2008), suggesting that they do not spin down with age like M dwarfs. $\gtrsim$M7 dwarfs also exhibit systematically weaker Hα emission despite being fast rotators, while $L_{\mathrm{X}}/L_{\mathrm{bol}}$ decreases with increasing $v \sin i$ or decreasing Ro (Mohanty and Basri 2003; Reiners and Basri 2008, 2010; Berger et al. 2010; McLean, Berger, and Reiners 2012). In a similar vein, the Güdel-Benz relation appears to break down for objects later than M7 due to a suppression of X-ray luminosities rather than radio luminosities, even when taking activity-rotation saturation into account (Berger et al. 2010; Williams, Cook, and Berger 2014), suggesting that magnetic activity in L and T dwarfs is no longer dominated by rotation (Cook, Williams, and Berger 2014; Williams, Cook, and Berger 2014). Although radio, Hα, and X-ray luminosities do not necessarily scale with magnetic field strength, their continued emission requires magnetic fields

even at very low masses. Zeeman broadening and Zeeman Doppler imaging studies referenced in §3.2 confirm that ~kG fields persist in dwarfs as late as M7. In light of such magnetics fields, a simple explanation for the observed activity breakdowns may be the decoupling of magnetic fields from increasingly neutral atmospheres (Mohanty et al. 2002).

However, clearly nonthermal heating of the upper atmospheres of ultracool dwarfs is commonplace and sustained. The breakdown of activity trends in late-type dwarfs indicates that the persistence of Hα, X-ray, and radio emission perhaps reflects a departure from the standard chromospheric heating picture where magnetic fields locally interact with hotter and less neutral atmospheres. Instead, activity may be externally powered via auroral current systems such as magnetosphere-ionosphere (M-I) coupling currents, giving rise to auroral activity (Schrijver et al. 2011; Nichols et al. 2012; Hallinan et al. 2015). M-I coupling has been confirmed as a source of power for Jovian, Saturnian, and terrestrial auroral emissions (Hill 1979; Nichols et al. 2012; Bagenal et al. 2014; Badman et al. 2015, and references therein).

Recently, Hallinan et al. (2015) have established that radio emission may only be one manifestation of auroral activity, as is observed for the planets in our Solar System. These authors have shown that the M8.5 dwarf LSR J1835+3259 is simultaneously variable with the same periodicity in broadband optical, Balmer line, and pulsed radio emission. The radio and Hα luminosities, together with the synchronized variability, are consistent with the emission in all bands being powered by the same auroral currents. Hallinan et al. (2015) also postulated that there may be a causal relationship between auroral currents and some examples of the infrared variability (weather) observed for L and T dwarfs, though they presented no empirical data to support this hypothesis.

Such synchronized multiwavelength emission has been previously observed in other radio brown dwarfs. TVLM 513-46546 (M8.5) exhibited anticorrelated Sloan-g' and Sloan-i' lightcurves, which Littlefair et al. (2008) attributed to cloud phenomena, and Hα emission from 2MASSW J0746425+200032 (L0+L1.5) was variable with the same periodicity as its pulsed radio emission but at a 1/4-phase lag (Berger et al. 2009). In fact, all but one of the known radio-pulsing ultracool dwarfs also exhibit Hα emission and several are also confirmed optical/IR variables (Tinney and Reid 1998; Delfosse et al. 2001; Basri 2001; Hall 2002; Reid et al. 2002; Mohanty and Basri 2003; Fuhrmeister and Schmitt 2004; Lane et al. 2007; Schmidt et al. 2007; Littlefair et al. 2008; Berger et al. 2009; 2010; Reiners and Basri 2010; Harding et al.

2013; Antonova et al. 2013; Burgasser, Gillon, Melis, et al. 2015, and references therein).

Motivated by the above discussion, we strongly bias our samples for auroral activity by targeting only those dwarfs in this spectral range known to exhibit Hα emission and/or optical/IR variability.

3.4 Targets

2MASS 10475385+2124234. Discovered by Burgasser et al. 1999, 2M1047 was later classified as a T6.5 brown dwarf by Burgasser et al. 2006. Burgasser et al. 2003 detected weak Hα emission at the 2.2σ level with a flux of $f_{\mathrm{H}\alpha} = 5.9 \pm 2.7 \times 10^{-18}$ ergs cm^{-2} s^{-1}. In 2012, 2M1047 became the first T-dwarf detected in the radio, when Route and Wolszczan 2012 detected highly circularly polarized ($\gtrsim$72%) and bright flares at 4.75 GHz with ~1.3–2.7 mJy peak flux densities using the Arecibo telescope. Until this study, it has remained the only radio-detected ≥L6 dwarf. A follow-up study by Williams, Berger, and Zauderer 2013 at 5.8 GHz using the VLA found quasi-quiescent radio emission from this source with a flux density of 16.5 ± 5.1 μJy. Williams and Berger 2015 confirmed quiescent emission for 2M1047, measuring a flux density of 9.3 ± 1.5 μJy and 1.1 ± 1.5 μJy at 6–10 GHz for Stokes I and V, respectively, with low circular polarization ($\lesssim$28%). They also detected highly left-circularly polarized pulses (~50–100%) with a periodicity of ~1.77 hours up through 10 GHz. We include 2M1047 in our survey as a known quiescently emitting source and to examine long-term variability.

SIMP J01365662+0933473. SIMP0136 was discovered and classified as a T2.5 dwarf by Artigau et al. 2006. In a follow-up study, Artigau et al. 2009 reported J- and K_s-band photometric variability, with a peak-to-peak amplitude $\Delta J \sim 50$ mmag, an amplitude ratio of $\Delta K_s/\Delta J = 0.48 \pm 0.06$, and a period $P = 2.3895 \pm 0.0005$ hr. This was the first clearly periodic and high-amplitude detection of IR variability in a T-dwarf. They attributed the variability to clouds that are ~100 K colder than a surrounding cloud-free atmosphere in the brown dwarf. Using HST spectral mapping, Apai et al. 2013 found that models of low-temperature and thick clouds mixed with warmer and thin clouds can reproduce time-variable changes in the near-IR colors and spectra of SIMP0136, and they confirmed it had a stable variation period.

2MASS 10430758+2225236. 2M1043 was discovered and classified as an unusually red L8 dwarf by Cruz et al. 2007, which they speculated could be attributed to an

Table 3.1: Survey Targets

Object Name	Abbrev. Name	SpT	Parallax (mas)	Distance (pc)	$\mu_\alpha \cos\delta$ (mas/yr)	μ_δ (mas/yr)	Notes	Ref.
2MASS 10475385+2124234	2M1047	T6.5	94.73±3.81	10.56±0.52	-1714±7	-489±4	Hα, detected prior	1-7
2MASS 01365662+0933473	SIMP0136	T2.5	···	6.0±0.4	1241±9	-4±10	IR variability	8-10
2MASS 10430758+2225236	2M1043	L8	···	16.4±3.2	-134.7±11.6	-5.7±17.0	Hα emission	11-13
2MASS 12373919+6526148	2M1237	T6.5	96.07±4.78	10.42±0.52	-1002±8	-525±6	Hα, IR var?[a]	1 3 4 14-16
SDSS J12545393-0122474	SDSS1254	T2	75.71±2.88	13.21±0.50	-479±3	130±2	Hα, IR var?[b], binary?[c]	17 3 4 18-26
SDSS 04234858-0414035	SDSS0423	L7	65.93±1.7	15.17±0.39	-331±49	76±11	Hα, IR var, binary[d]	19 27-33

[a] (14) found no evidence of J-band variability whereas (16) reported variability at a level below the detection limits of (14)

[b] (22), (23), (24) found no IR variability in SDSS1254 above the $\sim 5-20$ mmag level, whereas (20) and (21) reported 'significant' J-band and spectroscopic variability, respectively.

[c] See (25), (26) and §3.7 and §3.4 for further discussion about possible multiplicity in SDSS1254.

[d] SDSS0423 has a known binary companion of spectral type T2.5 and orbital separation 0.″16 (31, 32, 33).

References. — (1) Burgasser et al. 1999; (2) Burgasser et al. 2006; (3) Vrba et al. 2004; (4) Burgasser et al. 2003; (5) Route and Wolszczan 2012; (6) Williams, Berger, and Zauderer 2013; (7) Williams and Berger 2015; (8) Artigau et al. 2006; (9) Artigau et al. 2009; (10) Apai et al. 2013; (11) Cruz et al. 2007; (12) Schmidt et al. 2010; (13) Pineda et al. 2016; (14) Burgasser, Liebert, et al. 2002; (15) Burgasser, Kirkpatrick, Reid, et al. 2000; (16) Artigau, Nadeau, and Doyon 2003; (17) Leggett et al. 2000; (18) Burgasser, Kirkpatrick, Brown, Reid, Burrows, et al. 2002; (19) Geballe et al. 2002; (20) Artigau, Nadeau, and Doyon 2003; (21) Goldman et al. 2008 (22) Koen, Matsunaga, and Menzies 2004; (23) Girardin, Artigau, and Doyon 2013; (24) Radigan et al. 2014; (25) Burgasser 2007; (26) Cushing et al. 2008; (27) Cruz et al. 2003; (28) Kirkpatrick et al. 2008; (29) Enoch, Brown, and Burgasser 2003; (30) Clarke et al. 2008; (31) Carson et al. 2011; (32) Burgasser et al. 2005; (33) Burgasser, Burrows, and Kirkpatrick 2006

unresolved binary. A follow-up study by Reid et al. 2008 using the NICMOS N1C1 camera on the Hubble Space Telescope found that no binary companion to 2M1043 was resolved, for mass ratios $q > 0.2$ and angular separations $\theta > 0\farcs3$. In the discovery paper, the authors also tentatively report possible Hα emission.

2MASS 12373919+6526148. 2M1237 was discovered by Burgasser et al. 1999 using data from the Two Micron All-Sky Survey (Skrutskie et al. 2006) and classified as a T6.5 dwarf by Burgasser, Liebert, et al. 2002. Burgasser, Kirkpatrick, Reid, et al. 2000; Burgasser, Liebert, et al. 2002 reported abnormally bright and persistent yet variable Hα emission, which was confirmed again by Burgasser et al. 2003. With fluxes ranging from $f_{\mathrm{H}\alpha} \sim 1\text{–}10\times10^{-17}$ erg cm^{-2} s^{-1}, the Hα luminosity is an order of magnitude higher than for any other T dwarf. Burgasser, Liebert, et al. 2002 found no evidence of short-term J-band variability and ruled out flaring as a possible variability mechanism. In contrast, Artigau, Nadeau, and Doyon 2003 reported variability at $\Delta J \sim 30$ mmag. Liebert and Burgasser 2007 ruled out a massive companion or youthful chromospheric activity as additional possible Hα variability mechanisms.

SDSS J12545393-0122474. SDSS1254 was discovered by Leggett et al. 2000 and independently classified as a T2 dwarf by both Burgasser, Kirkpatrick, Brown, Reid, Burrows, et al. 2002 and Geballe et al. 2002 and is the T2 spectral standard (Burgasser et al. 2006). Burgasser et al. 2003 reported weak Hα emission with flux $f_{\mathrm{H}\alpha} = 7.5 \pm 2.5 \times 10^{-18}$ erg cm^{-2} s^{-1}. Artigau, Nadeau, and Doyon 2003 reported 45±2 mmag J-band and 23±4 mmag H-band variability, and similarly, Goldman et al. 2008 report variable spectral features at 0.997 – 1.13 μm, with upper limits in the peak-to-peak flux variability calculated at the ∼4–60% levels. In contrast, Koen, Matsunaga, and Menzies 2004 found no evidence of variability above the 7, 6, and 10 mmag levels for J, H, and $\mathrm{K_s}$ bands during a ∼4-hour observation, and Girardin, Artigau, and Doyon 2013 found no evidence of J-band variability above 5 mmag. We note here that SDSS1254 appears to be sufficiently overluminous for its spectral type that it may in fact be an as-yet unresolved tight binary system (Burgasser 2007; Cushing et al. 2008).

SDSS 04234858-0414035. SDSS0423 was identified by Geballe et al. 2002 using data from the Sloan Digital Sky Survey (York et al. 2000). The authors classified it as a T0 dwarf on the basis of its infrared spectrum. However, using its optical spectrum, Cruz et al. 2003 classified it as an L7.5. Burgasser et al. 2005 showed that it is in fact a binary system of two brown dwarfs with spectral types L6±1 and

T2±1, consistent with the previous classifications. Both Burgasser et al. (2005) and Carson et al. (2011) reported the angular separation of the binary to be 0.″16, which we cannot resolve with our observations. For the purposes of comparing our magnetic field measurements to previous models, we adopt a conservative L7.5 classification. Monitoring in K_s band by Enoch, Brown, and Burgasser 2003 yielded only a possible detection of variability, whereas Clarke et al. 2008 reported J-band photometric variability with a peak-to-peak amplitude of 8.0 ± 0.8 mmag with a period of 2 ± 0.4 hr. SDSS0423 is additionally one of only a handful of late L/T-dwarfs to exhibit Hα emission, for which Kirkpatrick et al. 2008 reported an equivalent width of 3 Å.

3.5 Observations

We observed 6 objects spanning spectral range L7.5-T6.5 with the full VLA array in C-band (4–8 GHz), using the WIDAR correlator in 3-bit observing mode for 4 GHz bandwidth observations, in time blocks of 2 or 4 hours for 28 total program hours. Observations were performed between March and August 2013, during DnC and C configurations. We summarize target properties and observations in Table 3.1 and Table 3.2, respectively.

3.5.1 Calibrations

We calibrated our measurement sets using standard VLA flux calibrators 3C286 and 3C147 and nearby phase calibrators. After initially processing raw measurement sets with the VLA Calibration Pipeline, we manually flagged remaining RFI. Typical full-bandwidth sensitivity at DnC configuration for 2 hours on source in C-band is 3 μJy. Typical 3-bit observations reach an absolute flux calibration accuracy of ~5%. We obtained absolute flux by bootstrapping flux densities with standard VLA flux calibrators. Flux calibration accuracy may be reduced and result in systematically offset flux densities when gain calibrations interpolated from the phase calibrator are not sufficient to correct for the variation of gain phases with time. To account for this, our observations alternated between a nearby phase calibrator and the target source with typical cycle times of 30 minutes, and we obtained gain solutions for the phase calibrators that varied slowly and smoothly over time, suggesting that this source of error is negligible.

Table 3.2: Summary of Observations

Object	Band (GHz)	Obs. Date (2013)	Obs. Block (h)	Time on Source (s)	VLA Configuration	Synthesized Beam Dimensions (arcsec × arcsec)	RMS (μJy)	Phase Calibrator	Flux Calibrator
2M1047	4.0–8.0	05/19	4.0	12745	DnC	9.21×3.02	3.1	J1051+2119	3C286
SIMP0136	4.0–8.0	05/18	4.0	12995	DnC	8.64×3.10	5.4	J0203+1134	3C147
2M1043	4.0–8.0	05/25	4.0	13042.5	DnC	10.0×5.5	2.0	J1051+2119	3C286
	4.0–8.0	05/27	2.0	5825	DnC	9.82×5.47	4.9	J1051+2119	3C286
2M1237	4.0–8.0	05/21	2.0	5712.5	DnC	8.22×3.70	2.8	J1313+6735	3C286
SDSS1254 [a]	4.0–8.0	05-19	2.0	5685	DnC	9.70×3.55	4.0	J1246-0730	3C286
	4.0–8.0	05/26	2.0		DnC	···	···	J1246-0730	3C286
SDSS0423	4.0–8.0	08/30	4.0	13102.5	C	4.91×3.37	3.2	J0423-0120	3C147
	4.0–8.0	05/26	2.0	5907.5	DnC	11.52×5.96	4.0	J0423-0120	3C147
	4.0–8.0	05/25	2.0	5925	DnC	12.92×9.11	3.5	J0423-0120	3C147

[a] Unable to successfully calibrate measurement set taken on 2013-05-26 due to excessive noise.

3.5.2 Source Motion

The expected positions of the sources were determined using 2MASS coordinates (Skrutskie et al. 2006) and corrected for proper motion, provided in Table 3.1. Sources had moved by as much as 0.″8 due to proper motion during our observing program, in comparison to synthesized beam resolutions of at least a few arcseconds. Orbital motion corrections were not necessary for SDSS0423, a known binary with an orbital separation 0.″16. We compared the expected coordinates of our objects to their measured position and found that all objects were well within a synthensized beam of their predicted locations.

3.6 Results

3.6.1 Image Detections

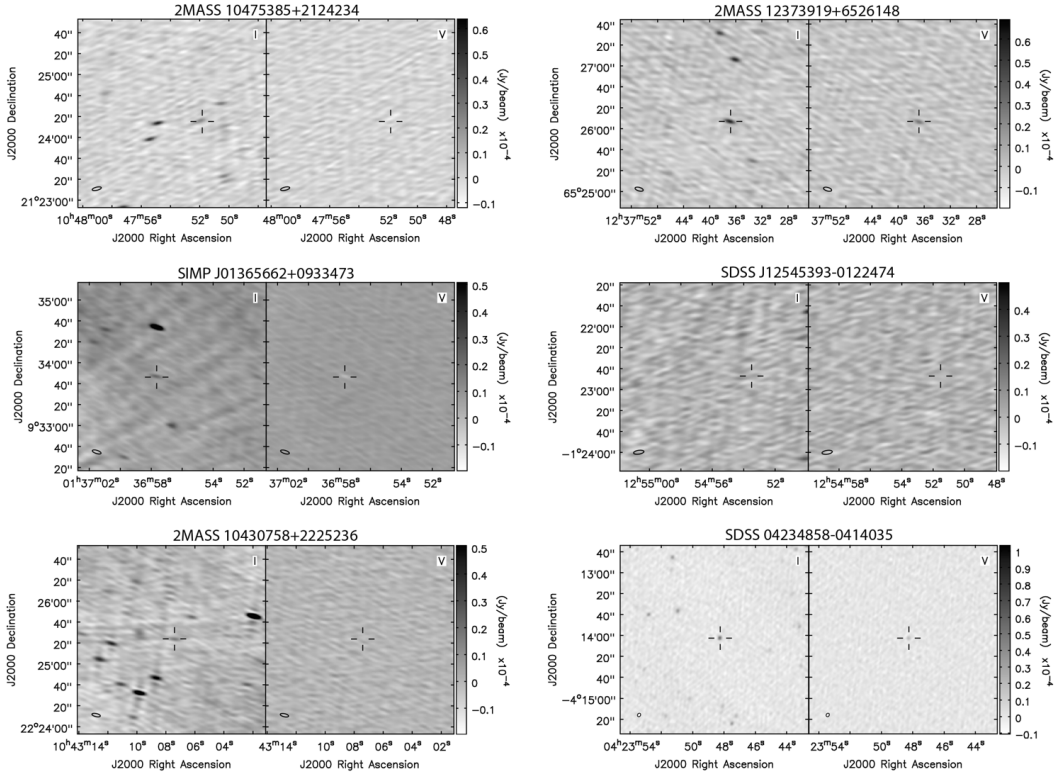

Figure 3.1: Stokes I (left) and V (right) images of all objects. Ellipse depicts synthesized beam. Measurement sets for objects with multiple observing blocks were concatenated prior to imaging. Sources were detected at the proper motion-corrected location for all objects except for SDSS1254.

We combined measurement sets for objects with multiple observing blocks using the CASA `concat` routine and then produced Stokes I and Stokes V images of each object (total and circularly polarized intensities, respectively) with the CASA

`clean` routine, modeling the sky emission frequency dependence with 2 terms and using Brigg's weighting with the robustness parameter set to 0.0, which we found resulted in a good trade-off between resolution and sensitivity for our observations. We searched for a point source at the proper motion-corrected coordinates of each target. Figure 3.1 shows the Stokes I and Stokes V images for all objects.

In contrast to previous surveys, all but one of our six targets were detected in Stokes I, with signal-to-noise ratios (SNR) ranging from 4.9 to 24.6 in the mean Stokes I flux density. Table 3.3 gives the measured mean flux density and rms noise of each detected (SNR ≥ 3) source. Flux densities and source positions were determined by fitting an elliptical Gaussian point source to the cleaned image of each object at its predicted coordinates, using the CASA task `imfit`. For the one undetected target, SDSS1254, we provide the measured mean Stokes I flux density and rms noise at the expected position of the source.

3.6.2 Timeseries Pulse Detections & Magnetic Field Strengths

We checked all targets for highly circularly polarized pulses in flux density to confirm the presence of ECM emission. Previous studies have searched for pulsed emission in Stokes I and V, but we have chosen to search for pulses in the rr and ll correlations (right- and left-circularly polarized, respectively) because signal to noise is a factor of $\sqrt{2}$ higher in cases where the pulsed emission is 100% circularly polarized.

Using the CASA plotting routine `plotms` to export the real UV visibilities averaged across all baselines, channels, and spectral windows of the rr and ll correlations, we created rr and ll timeseries for all measurement sets with time resolutions of 10s, 60s, and 600s at frequency ranges of 4–6 GHz, 6–8 GHz, and 4–8 GHz to check for frequency-dependent ECM emission cutoff. We do not check for pulses at frequency resolutions smaller than 2 GHz due to signal-to-noise concerns. Figure 3.2 shows the 4–8 GHz timeseries for each object.

Analysis of the timeseries shows significant evidence of at least one pulse for 2M1047, SIMP0136, SDSS0423, and 2M1043. Additionally, 2M1237 appears to exhibit very broad pulses or strongly variable emission. We confirm pulses by imaging right circularly polarized and/or left circularly polarized emission over the full width half maximum (FWHM) of each pulse and measuring integrated flux densities using the CASA routine `imfit` at the expected locations of our targets. We find that flux densities for imaged pulses are consistent with pulses observed in the timeseries within 3σ. For all objects except for 2M1237, we smooth our data

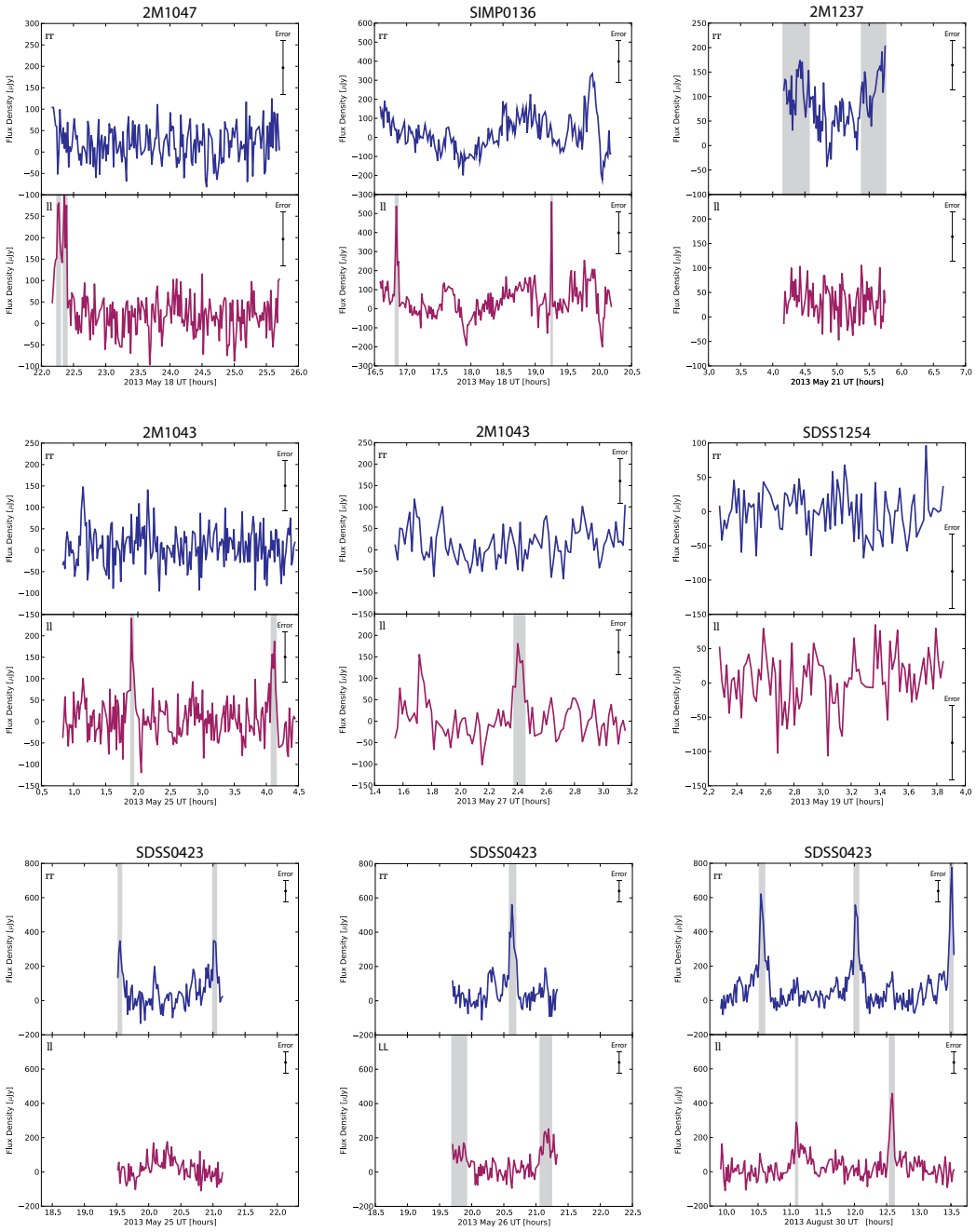

Figure 3.2: Timeseries of right-circularly polarized (rr) and left-circularly polarized (ll) flux densities for all calibrated measurement sets (blue and red, respectively). Data is averaged over 60s intervals; time interval for raw data was 5s seconds and all analysis was done with data averaged over 10s. Black error bars represent rms noise obtained in images and scaled to time bin lengths for a single correlation. Grey regions indicate FWHM of pulses with peak flux density $\geq$3.0, and all pulses have been verified with imaging. Total intensity is given by the Stokes I flux density, where I = (rr+ll)/2. Circularly polarized intensity is given by the Stokes V flux density, where V = (rr-ll)/2.

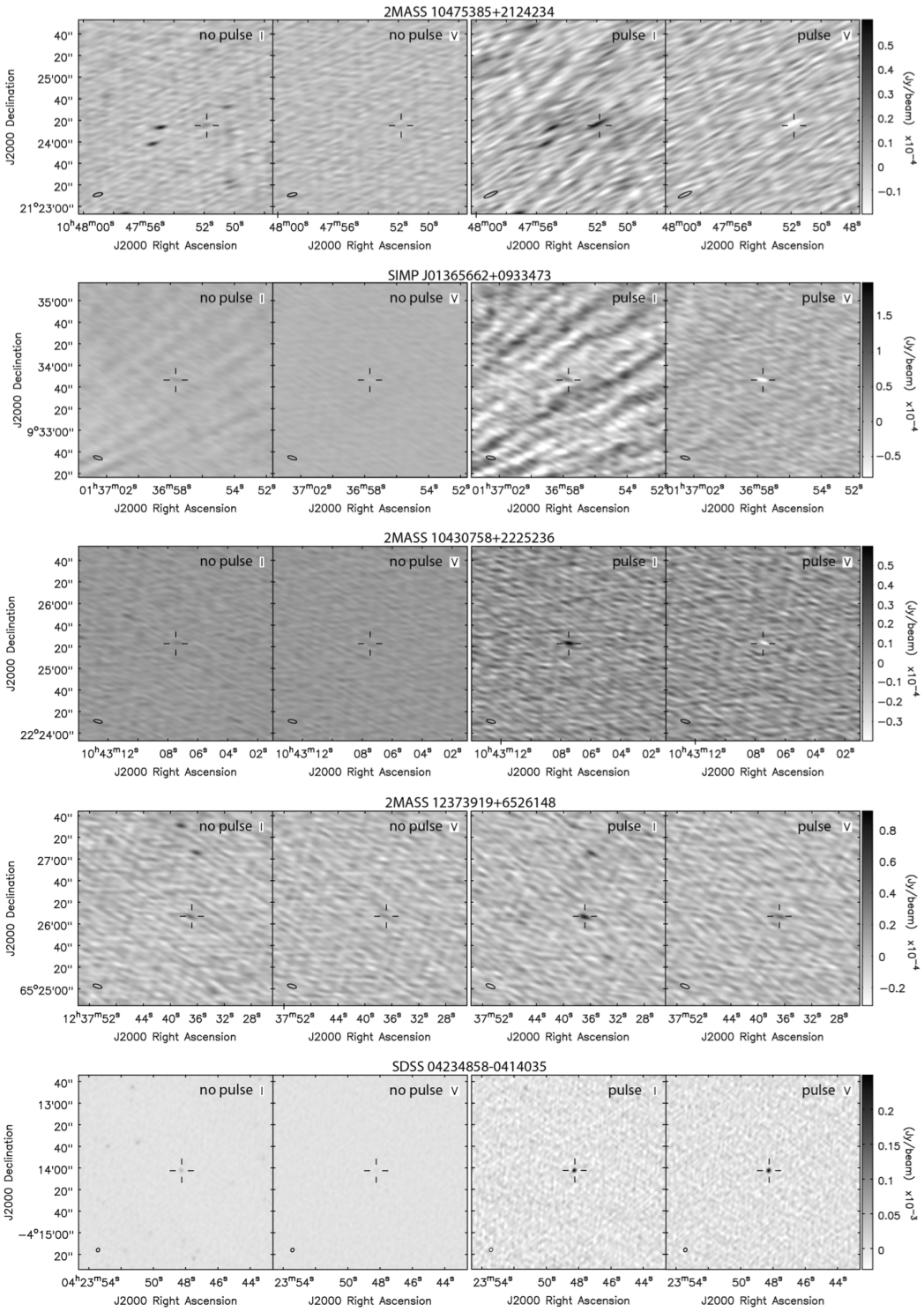

Figure 3.3: Stokes I and Stokes V flux densities for pulsed and quiescent emission. Pulsed emission for 2M1237 is averaged only over the later pulse, and SDSS0423 pulsed emission is averaged over the right-circularly polarized pulses only.

Table 3.3: Imaging and Timeseries Results

Object	Position Offset [a] (sigma)	Mean Stokes I (μJy)	Pulse #	Pulse Stokes I (μJy)	Pulse Stokes V (μJy)	SNR (I,V)	Pulse Circ. Poln (%) [b]	Quiescent Stokes I (μJy)	SNR	Quiescent Circ. Poln (%) [b]
2M1047	1.46	26.8±3.1	1	123.0±21.0	-95.0±15.0	5.9, 6.3	$-75.1^{+14.1}_{-14.9}$	17.5±3.6	4.9	$-40.6^{+23.4}_{-13.2}$
SIMP0136	0.36	34.4±5.4	2	>156.0±39.7 [c]	-233.0±24.9	3.9, 9.4	-63.6 [d]	33.3±5.9	5.6	-1.2 [d]
2M1043	0.79	11.7±2.4	3	87.0±11.8	-69.0±11.7	7.4, 5.9	$-77.9^{+15.1}_{-13.0}$	16.3±2.5	6.5	$-13.8^{+13.8}_{-15.9}$
2M1237 [e]	2.91	64.7±3.7	2? [f]	83.3±7.6	23.7±6.4	9.5, 3.7	$28.2^{+9.0}_{-7.5}$	43.3±7.3	5.9	$53.7^{+21.6}_{-14.6}$
	...	...	...	81.7±8.8	40.3±8.0	9.3, 5.0	$48.8^{+13.1}_{-9.7}$	...	...	...
SDSS1254	...	3.3±4.0	0	...	...	...	...	...	...	...
SDSS0423 [g]	0.42	54.1±2.2	10	225.4±12.4	220.0±12.2	18.2, 18.0	$97.3^{+0.8}_{-9.0}$	26.7±3.1	8.6	$14.4^{+11.5}_{-10.2}$
	...	...	...	135.0±9.8	-67.1±7.9	13.8, 8.5	$-49.4^{+6.1}_{-7.8}$	...	...	...

[a] The distance between the measured and expected coordinates, divided by the amplitude of the error ellipse in the offset direction, using concatenated images for objects with multiple observing blocks. 2MASS coordinate uncertainties and our own measurement uncertainties were included in error analysis.

[b] Reported polarization fractions are highest-likelihood values, given the measured Stokes I and Stokes V flux densities. Uncertainties reflect the upper and lower bounds of the 68.27% confidence intervals. Negative values indicate left circular polarization, and positive values indicate right circular polarization.

[c] Challenges with field source subtraction result in an underestimate of the true Stokes I flux density. Because circular polarization cannot exceed 100%, the Stokes V flux density gives a lower bound to the true Stokes I flux density (see c).

[d] We quote the lower bound of the 99.73% confidence interval for the percent circular polarization of SIMP0136 due to an underestimated Stokes I flux density.

[e] Due to the broadness of the two observed peaks in the rr timeseries of 2M1237, we report measurements separately for each peak. The top measurement is for the earlier peak and the bottom measurement is for the later peak.

[f] See §3.6.2 for discussion

[g] We observe two sets of pulses, six in the rr timeseries (top) and four in the ll timeseries (bottom).

over 60s, 90s, and 180s to measure the FWHM. We find that the FWHM is consistent within ~30s, except for the earlier ll pulse on 08/30/2013 for SDSS0423; when the smoothing is extended to 180s, the narrow peak smears out into the broader bump, and the returned FWHM is accordingly broader. For the purposes of measuring a mean pulsed flux, we use the narrower FWHM. Because of the broad nature of the peaks for 2M1237, we smooth over 180s, 270s, and 540s and find that the FWHM is consistent within ~450s.

We measure the mean pulsed Stokes I and V flux densities by imaging over all of the pulses with peak flux density ≥ 3.0 for each object and calculate the highest likelihood percent circular polarization of the mean pulsed flux, where negative and positive percentages correspond to left and right circular polarization, respectively. We report uncertainties that correspond to the upper and lower limits of the 68.27% confidence interval. We find that in all cases except for the first peak in 2M1237, the pulsed emission is highly circularly polarized (48.8–97.3%), consistent with ECM emission (Treumann 2006).

We additionally check for quiescent emission by removing the full width of each pulse from our data and imaging the remaining emission. We define the full width of the pulse as beginning and ending at the time bins nearest the pulse maximum that have flux densities less than or equal to the rms noise. We find that pulse widths for each object are consistent within ~60s (~500s for 2M1237) for all smoothing resolutions, and we select the widest returned width when removing each pulse. All objects with pulsed emission also exhibit quiescent emission with relatively low polarization fractions, except for 2M1237. In contrast, SDSS1254, for which no pulse is observed, does not exhibit any detectable quiescent emission above the rms noise. We report the characteristics of the pulsed and quiescent emission in Table 3.3.

Searching for the FWHM of 2M1047 reveals an apparent double peak, similar to what Williams and Berger (2015) observe. Based on the periodicity observed by Williams and Berger (2015), we classify this object as having a single pulse. However, in measuring the mean pulsed flux densities, we treat it as a double pulse and average over the FWHM of each pulse.

Two extremely bright sources near SIMP0136 resulted in poor Stokes I field source subtraction, and our reported Stokes I flux density is certainly an underestimate of the true flux density. We attempted to self-calibrate this field, but were only able to achieve ~10% improvement. Beam squint causes the nearby bright sources to also

appear in Stokes V but with much lower flux densities, and we therefore consider the Stokes V flux density of SIMP0136 to be more accurate. Because the degree of circular polarization cannot be greater than 100%, the Stokes V flux density in fact gives a lower bound on the actual Stokes I flux density. Due to its extremely bright Stokes V flux density, we conclude that pulses from SIMP0136 are highly circularly polarized.

We note that our observations only tentatively suggest that we observe ECM emission from 2M1237. Despite the broad nature of the peaks in 2M1237, it is possible that the timeseries in fact exhibits two pulses rather than simply being variable, with the broadness arising from a geometric effect. We report the flux densities and circular polarization fractions for each of the peaks in the 2M1237 rr timeseries, and we find that in fact the circular polarization fraction appears to vary from peak to peak, from ~30% to ~50% on a 2-hour time scale. Some of the variability may arise from the incomplete phase coverage, such that the earlier peak is averaged down more than the later peak. Whereas the other radio-detected objects all exhibit marked differences in polarization fractions between pulsed and quiescent emission, the 'quiescent' emission from 2M1237 exhibits ~50% circular polarization, which is similar to what we observe in at least one of the peaks. This could be consistent with a geometry in which the ECM-emitting region of the magnetosphere is always visible, which would also explain the broadness of the peaks. Additional monitoring of 2M1237 for full phase coverage is necessary to determine the nature of these peaks.

Three possibilities may account for why we do not observe a pulse from SDSS1254: (1) SDSS1254 does not produce ECM emission, (2) SDSS1254 produces ECM emission with a cutoff frequency lower than 4.0 GHz, or (3) we did not observe it during a pulse and the auroral activity is variable. Table 3.3 summarizes timeseries data for all objects. All detected pulses extend into the 6.0–8.0 GHz band, indicating that observations at higher frequencies are required to detect and measure an emission cutoff. We conservatively use the center of the top band, 7.0 GHz, to calculate corresponding lower bound maximum surface field strengths of 2.5 kG.

3.7 Estimating Physical Parameters of Brown Dwarfs

To best inform our comparison of our results to dynamo models, we estimate the relevant physical parameters for our brown dwarfs

Effective temperatures (T_{eff}) and surface gravities (log g) were estimated for our

Table 3.4: Brown Dwarf Physical Parameters

Object	Spectral Type	T_{eff} [a] (K)	log g [a] (cm s^{-2})	Age [b] (Gyr)	Mass [b] ($M_\odot$)	Adopted T_{eff} [c] (K)	Adopted log g [c] (cm s^{-2})	Adopted Age [c] (Gyr)	Adopted Mass [c] ($M_\odot$)
2M1047	T6.5	888^{+33}_{-33}	$5.34^{+0.11}_{-0.46}$	>2.5	>0.026	869^{+35}_{-29}	$5.29^{+0.10}_{-0.28}$	>2.5	>0.026
		850^{+62}_{-47}	$5.23^{+0.18}_{-0.25}$	>2.5	>0.026				
SIMP0136	T2.5	1104^{+51}_{-63}	$4.78^{+0.35}_{-0.40}$	$0.6^{+1.1}_{-0.3}$	$0.022^{+0.015}_{-0.012}$	1089^{+62}_{-54}	$4.79^{+0.26}_{-0.33}$	$0.6^{+1.1}_{-0.3}$	$0.022^{+0.015}_{-0.012}$
		1073^{+112}_{-87}	$4.79^{+0.39}_{-0.52}$	$0.7^{+1.1}_{-0.3}$	$0.022^{+0.015}_{-0.012}$				
2M1043 [d]	L8	1012^{+64}_{-90}	$3.94^{+0.13}_{-0.09}$	$0.6^{+3.4}_{-0.3}$	$0.011^{+0.011}_{-0.005}$	1390±180	···	$0.6^{+4.6}_{-0.3}$	$0.011^{+0.011}_{-0.005}$
		1229^{+212}_{-260}	$4.28^{+0.49}_{-0.34}$	$0.6^{+4.6}_{-0.3}$	$0.011^{+0.011}_{-0.005}$				
2M1237	T6.5	851^{+36}_{-32}	$5.39^{+0.08}_{-0.26}$	>3.4	>0.028	831^{+31}_{-27}	$5.34^{+0.08}_{-0.17}$	>3.4	>0.028
		810^{+51}_{-43}	$5.28^{+0.15}_{-0.21}$	>3.4	>0.028				
SDSS1254	T2	1079^{+56}_{-63}	$4.52^{+0.41}_{-0.35}$	$0.49^{+0.51}_{-0.21}$	$0.017^{+0.015}_{-0.008}$	1070^{+69}_{-52}	$4.57^{+0.30}_{-0.27}$	$0.49^{+0.51}_{-0.21}$	$0.017^{+0.015}_{-0.008}$
		1061^{+127}_{-83}	$4.62^{+0.43}_{-0.40}$	$0.49^{+0.48}_{-0.21}$	$0.017^{+0.015}_{-0.008}$				
SDSS0423 [e]	L7+T2.5	1084^{+71}_{-41}	$4.25^{+0.34}_{-0.18}$	$0.42^{+0.62}_{-0.17}$	$0.015^{+0.021}_{-0.006}$	1678^{+174}_{-137}	···	$0.43^{+0.62}_{-0.17}$	$0.015^{+0.021}_{-0.006}$
		1150^{+198}_{-114}	$4.50^{+0.57}_{-0.35}$	$0.43^{+0.61}_{-0.17}$	$0.014^{+0.020}_{-0.006}$				
Gl 570D	T7.5	817^{+32}_{-36}	$5.02^{+0.19}_{-0.48}$	$2.4^{+1.6}_{-1.7}$	$0.024^{+0.011}_{-0.010}$	799^{+40}_{-32}	$4.96^{+0.18}_{-0.32}$	$2.4^{+1.6}_{-1.7}$	$0.024^{+0.011}_{-0.010}$
		781^{+73}_{-53}	$4.90^{+0.32}_{-0.37}$	$2.4^{+1.6}_{-1.7}$	$0.024^{+0.011}_{-0.010}$				
HN Peg B	T2.5	1054^{+51}_{-66}	$4.60^{+0.37}_{-0.44}$	$0.6^{+0.6}_{-0.3}$	$0.018^{+0.016}_{-0.009}$	1043^{+59}_{-51}	$4.64^{+0.28}_{-0.32}$	$0.6^{+0.6}_{-0.3}$	$0.018^{+0.017}_{-0.009}$
		1032^{+107}_{-77}	$4.67^{+0.40}_{-0.45}$	$0.6^{+0.6}_{-0.2}$	$0.017^{+0.015}_{-0.009}$				

[a] (Top) cf. Gl 570D, (Bottom) cf. HN Peg B. Calibrators Gliese 570D and HN Peg B included for reference. Minus and plus errors define the 68.27% confidence interval.

[b] Mass and age estimates from evolutionary models of Baraffe et al. (2003), using input parameters determined from (top) cf. Gl 570D and (bottom) cf. HN Peg B. Minus and plus errors define the 68.27% confidence interval, determined from 10,000 samples. In cases where >20% of input parameter samples fall outside of the Baraffe et al. (2003) models, lower limits are within 84.13% confidence.

[c] Adopted values are averages from cf. Gl 570D and cf. HN Peg B, except for 2M1043 and SDSS0423.

[d] Assuming no detection of Li in the optical spectrum in Cruz et al. (2007). Due to poor fit calibration for this object, we adopt instead T_{eff} calculated by applying the Liu, Dupuy, and Leggett 2010 bolometric correction to 2MASS H-band magnitude, typical brown dwarf radius $0.90 \pm 0.15 R_J$, and conservative mass estimate 70 ± 10 M_J. We do not adopt a value for log g and instead use the adopted mass and radius to calculate $< \rho >$ in Figure 3.4.

[e] Parameter fits are based on the unresolved spectrum of the binary system and are thus highly suspect. We adopt instead T_{eff} calculated from bolometric magnitude in Vrba et al. 2004, typical brown dwarf radius $0.90 \pm 0.15 R_J$, and conservative mass estimate 70 ± 10 M_J. We do not adopt a value for log g and instead use the adopted mass and radius to calculate $< \rho >$ in Figure 3.4.

sample following an updated version of the method described in (Burgasser, Burrows, and Kirkpatrick 2006). We used low-resolution near-infrared spectra from (a) the SpeX Prism Library (Burgasser 2014); (b) data from Cruz et al. 2004; Burgasser et al. 2004; Liebert and Burgasser 2007; Siegler et al. 2007; Burgasser et al. 2008) and (c) the indices H_2O-J and K/H defined in (Burgasser et al. 2006; Burgasser, Burrows, and Kirkpatrick 2006), which are orthogonally sensitive to temperature and surface gravity variations in T dwarf near-infrared spectra. The indices were measured on solar metallicity BTSettl08 spectral models (Allard, Homeier, and Freytag 2011) spanning T_{eff} = 600–1300 K and log g = 3.5–5.5 dex (cgs units). To calibrate these indices, we used the spectra of two brown dwarf companions with broad-band model-fit parameters: Gliese 570D (T7.5; Burgasser, Kirkpatrick, Cutri, et al. 2000) for which Geballe et al. (2001) determine T_{eff} = 804±20 K and log g = 5.14±0.14 dex; and HN Peg B (T2.5; Luhman et al. 2007) for which Leggett et al. (2008) determine T_{eff} = 1115 K and log g = 4.81 dex. Scaling the corresponding model indices to be in agreement with these sources, we then identified the locus of model parameters for which these indices agree with the measured values for our six sources to within 3σ.

Results are shown in Table 3.4, which compares values from each of the calibrators separately. For 2M1047, SIMP0136, 2M1237, and SDSS1254 we adopt the mean parameters from both Gliese 570D and HN Peg B calibrations. Note that values for 2M1237 are in agreement with those reported in Liebert and Burgasser (2007), while we find a slightly cooler T_{eff} for SDSS1254 and a log g on the low end of values reported by Cushing et al. (2008). The uncertainties for 2M1043 are fairly large and are most likely due to substantial differences between source and calibrator spectral types (a suitable late L dwarf calibrator was not available). Finally, while we report results for SDSS0423, these are highly suspect given the binary nature of this source (Burgasser et al. 2005). Reported parameter uncertainties reflect uncertainties in the parameters selected to represent the calibrators Gliese 570D and HN Peg B and define the lower and upper bounds of the range relative to the central value that account for 68.27% of the set.

The high surface gravities inferred for 2M1047 and 2M1237 indicate old ages and relatively high (substellar) masses. These were estimated from evolutionary models of Baraffe et al. (2003) by drawing ten thousand T_{eff}–log g pairs from each distribution to determine the mean and standard deviations. In both cases, >50% of input parameter samples fall outside of the Baraffe et al. (2003) models and

may result in significantly skewed mean values, so we give lower limits within 84.13% confidence. For these sources we infer ages of >2.5 and >3.4 Gyr and masses of >0.026 and >0.028 $M_\odot$ within 84.13% confidence, respectively. In contrast, SDSS1254 is matched to a very young age (~500 Myr) and low mass ~0.017 $M_\odot$). Note that Cushing et al. (2008) report disagreement in log g values based on evolutionary models (log g = 4.7–4.9) and spectral model fits (log g = 5.0–5.5), which these authors speculate may be due to unresolved multiplicity. Our difficulties in inferring the properties of 2M1043 may be related to this source's unusual cloud properties, as it is one of the reddest L8 dwarfs known ($J - K_s$ = 1.97±0.08). Its reported optical spectrum shows no indication of Li I absorption (Cruz et al. 2007) implying a mass ~0.011 $M_\odot$ and age ~600 Myr, although this feature may have been masked by poor continuum detection.

For objects whose parameters are not well constrained by the above method, we follow Vrba et al. 2004 and adopt a typical radius of 0.90±0.15 R_J from the Burgasser 2001 study of radius distribution in Burrows et al. 1997 L and T dwarf evolutionary models. We adopt a typical late-L mass range of 70 ± 10 M_J. For 2M1043, we apply a bolometric correction calculated for spectral type L8 using the polynomial fit from Liu, Dupuy, and Leggett 2010 to the 2MASS H-band magnitude. Using $M_{\odot,\mathrm{bol}}$ = 4.7554 ± 0.0004 mag and $L_{\odot,\mathrm{bol}}$ [1] = 3.827(±0.0014) × 10^{33} erg s^{-1}, we convert the bolometric magnitude to an effective temperature T_{eff} = 1390 ± 180 K. For SDSS0423, we adopt $T_{\mathrm{eff}} = 1678^{+174}_{-137}$ K as derived by Vrba et al. 2004. We include these parameters in Table 3.4.

3.8 Discussion

3.8.1 Comparison to a Power-Based Dynamo Scaling Relation

The ECM emission from our sample is detected across the entire band of our observations, which spans 4–8 GHz. Thus, in the absence of a clear cut-off in the emission, we can place a lower limit to the maximum surface magnetic field strength of 2.5 kG for all of our detected sample. This assumes the emission is produced at the fundamental electron cyclotron frequency, rather than a higher harmonic, as is the case for Solar System planets.

We now attempt to test the scaling law presented by Christensen, Holzwarth, and Reiners 2009 (hereafter C09). C09 showed that for planets and fully convective and rapidly rotating (P<4 days) stars, the convected energy flux available may generate

[1] Adopted from Eric Mamajek's Star Notes:
https://sites.google.com/site/mamajeksstarnotes/basic-astronomical-data-for-the-sun

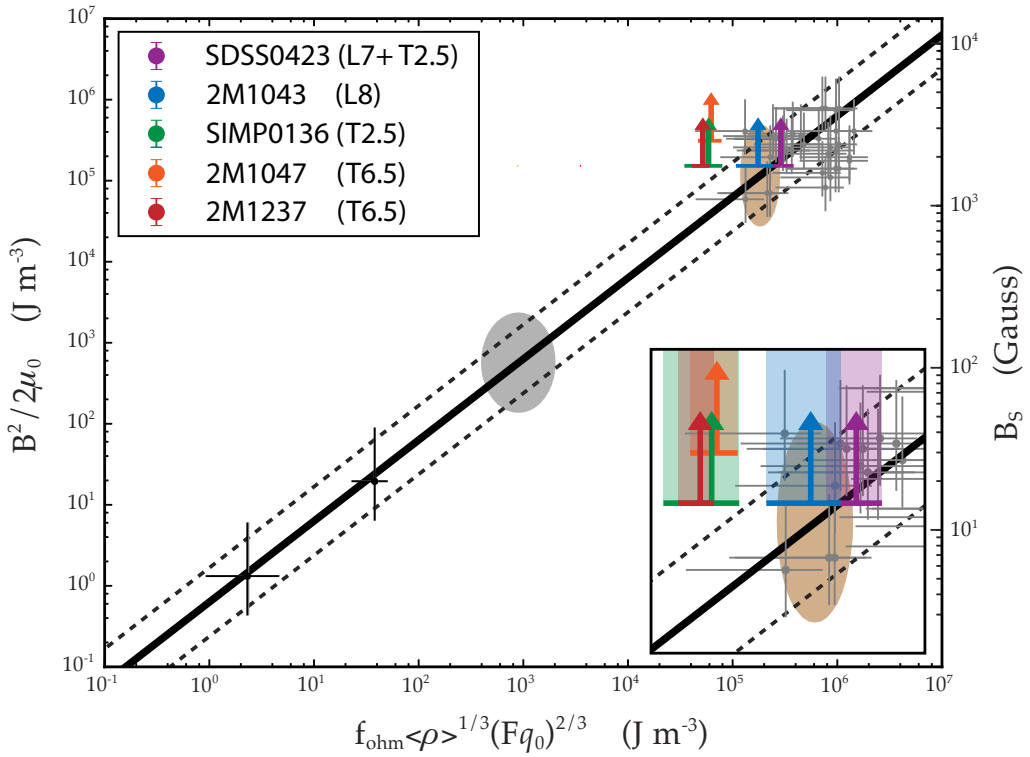

Figure 3.4: Reproduction of Figure 2 from Christensen, Holzwarth, and Reiners 2009, showing their proposed dynamo scaling relation with 3σ uncertainties for fully convective, rapidly rotating objects (black solid line and dashed lines, respectively). Grey points represent T Tauri stars and old M dwarfs. Black points represent Earth and Jupiter. The brown ellipse indicates the predicted position for a 1500 K brown dwarf and the grey ellipse indicates the predicted position for a 7 M_J exoplanet. Our detected targets are overplotted, with upward arrows to indicate that our measurements are lower bounds and horizontal bars to indicate estimated uncertainties. The inset shows more clearly our estimated uncertainties. We adopt a minimum surface field strength of 2.5 kG for our newly detected objects. For 2M1047, we adopt 3.6 kG as measured by Williams and Berger 2015.

the magnetic field strength. In a departure from prevailing dynamo scaling laws, the central tenet to their model was an energy balance between kinetic and magnetic energies and ohmic dissipation and convective heat transport, rather than a force balance between the Coriolis, Lorentz, buoyancy, and pressure forces (Christensen and Aubert 2006). Surprisingly, they found that the magnetic field strength is independent of both magnetic diffusivity and rotation rate and instead depends strongly only on the buoyancy flux and dynamo size. In particular, they show that for Jupiter, Earth, and a sample of stars including T Tauri stars, old M-dwarfs, and

main sequence stars with P<4 days, the following relation is empirically consistent:

$$\langle B^2 \rangle / (2\mu_0) = c f_{\rm ohm} \langle \rho \rangle^{1/3} (F q_0)^{2/3} \ . \tag{3.1}$$

Here, $\langle B^2 \rangle$ is the squared magnetic field averaged over the whole volume of the dynamo region rather than the surface of the star. $f_{\rm ohm}$ is the ratio of ohmic dissipation to total dissipation and is nominally assumed to be $f_{\rm ohm} \approx 1$. F is a volume average of the temperature scale height divided by the length scale of the largest convective structures, and for their purposes, C09 assume $F = 1$ and 1.19 for stars and Jupiter, respectively. For the purposes of our analysis, we adopt $F = 1$. q_0 is the bolometric flux at the outer boundary of the dynamo regions, which C09 obtain from the effective surface temperatures of the stars. Finally, μ_0 is permeability, $\langle \rho \rangle$ is the mean density of the dynamo region, and c is a proportionality constant. Figure 3.4 reproduces this scaling law. Significantly, the wide mass range that the above empirical relation describes tantalizingly hints that the scaling law may be generalizable for all convection-driven dynamos.

The C09 model calls for the mean internal field strength $\langle B \rangle$ of dynamo regions, and an ideal test of their model would utilize direct measurements of the magnetic field inside of the dynamo itself. However, measuring these data is impossible. Instead, they estimate $\langle B \rangle$ in several ways. The most direct observational tests available to C09 are Zeeman broadening measurements from spectral observations of Ti I lines in T Tauri stars by Johns-Krull 2007 and K and M stars by Saar 1996 and FeH lines in M-dwarfs by Reiners and Basri 2007. C09 additionally adapt ZDI data of mid M-dwarfs by Morin et al. 2008.

The lower bound mean surface field magnitude $B_{\rm s,dip}$ that we calculated for our objects allows us to very straightforwardly compare our field measurements with those predicted by C09. We treat $B_{\rm s,dip}$ for each object as a lower bound Zeeman broadening measurement $B_{\rm s}$ and convert it to $\langle B \rangle$ by following C09 and multiplying by a factor of $\langle B \rangle / B_{\rm s} \approx 3.5$, which they report is the typical ratio found in their geodynamo simulations. In a recent study of 2M1047, Williams and Berger 2015 detected a pulse at ~10 GHz, corresponding to a lower bound surface field strength of 3.6 kG for this object. We adopt this value in our comparison to field strengths predicted by C09.

We overlay our most conservative field constraints from auroral radio emission on our reproduction of the C09 scaling law in Figure 3.4. All of our T dwarfs depart mildly from the C09 scaling relation, suggesting four possibilities: (1) parameters beyond

convective flux and dynamo size may influence magnetic fields in brown dwarfs, (2) brown dwarfs have a systematically larger value for the parameter converting external field to internal field, (3) their fields are systematically stronger at the poles than what a dipole predicts, or (4) their field topologies are not dominated by dipoles. These possibilities would not necessarily undermine the basic premises of the proposed scaling law but simply add more uncertainty to the precision with which it can applied.

It is important to remember that dynamo scaling laws are powerful tools for elucidating which general physical characteristics and behaviors matter, but they describe an inherently chaotic process and the laws are not deterministic. It is possible that C09 may in fact be largely conceptually correct in the scaling law that they propose, but the parameters on which their law depends may differ from group to group. For instance, the dynamo region extends over ~6–10 orders of magnitude in density in low mass stars (Saumon, Chabrier, and van Horn 1995). The outermost part of the dynamo action is in a region that is much less dense than the mean density of the dynamo region, yet that could well be the region that determines the observed field because it is closest to the outer boundary. Another possibility is that the appropriate density to use may be defined differently between brown dwarfs and low mass stars. Additionally, parameters such $\langle B \rangle / B_s$ depend on boundary conditions, rotation rate, density structure, specific properties of the outer insulating shell (present in Jupiter and brown dwarfs, but not in low mass stars), etc. Finally, the C09 model is specific to dipole-dominated fields (>35% of field strength in the dipole component), so a departure from the relation may indicate field topologies dominated by higher-order fields.

Nevertheless, it is notable that some of our objects have lower bound field strengths that are systematically higher than what C09 predict when using parameter definitions that they adopted. The dynamo surface in Jupiter is at ~$0.85 R_J$ (Guillot et al. 2004), whereas it is near the surface of M-dwarfs. For our objects, the dynamo surface may be more interior than in M-dwarfs, causing the adopted values of q_0, $\langle \rho \rangle$, and B_s to increase. However, B^2 rises faster than $\langle \rho \rangle^{1/3} (q_0)^{2/3}$ as a function of internal radius, independent of field topologies, so our T dwarfs may in fact depart more dramatically. Pushing subsequent studies to higher frequencies to observe emission cutoffs will be necessary to obtain the best possible constraints for field measurements derived from auroral radio emission.

3.8.2 Implications of Auroral Radio Emission Correlated with Brown Dwarf Weather and Hα Emission

Prior to our work, radio surveys of ~60 ≥L6 objects yielded only one detection (Antonova et al. 2013; Route and Wolszczan 2013), resulting in a detection rate of just ~1.4%. In contrast, we have achieved a notably higher detection rate of 4/5 objects, not including the previously-detected 2M1047, by departing from previous target selection strategies and biasing our targets for previously confirmed Hα emission, or in the case of SIMP0136, optical/IR variability. Several of our objects also exhibited tentative IR variability. Selection effects from inclination angles or increased instrument sensitivity may contribute to our dramatically higher success rate, but it is also clear that biasing our sample for optical auroral emission provides a good means to finding radio-emitting brown dwarfs.

While the relationship between IR variability and auroral radio emission remains uncertain, our results are intriguing when viewed in the context of brown dwarf weather. J-band variability appears to be common in L and T dwarfs (Enoch, Brown, and Burgasser 2003; Clarke et al. 2008; Radigan et al. 2014; J. Radigan 2014; Buenzli et al. 2014; Metchev et al. 2015). Included in our target sample is the canonical dust-variable T-dwarf SIMP0136, which exhibits large-amplitude (>5%) IR variability. Also included were tentatively low-amplitude variable objects SDSS0423, 2M1237, and SDSS1254. Clouds in brown dwarf atmospheres have been proposed to interpret observed photometric and spectroscopic variability, and where objects have been observed at multiple wavelengths, some proposed models rely on patchy clouds of variable thicknesses and temperatures (Marley, Saumon, and Goldblatt 2010; Burgasser et al. 2014; Apai et al. 2013) to explain wavelength-dependent variability. Our results point to the possibility that an additional variability mechanism may be at play, as postulated by Hallinan et al. 2015.

The success of our selection strategy is especially compelling in light of simultaneous radio and optical spectroscopic observations of the M8.5 dwarf LSR J1835+3259 (hereafter LSR J1835) by Hallinan et al. 2015, whose results in fact motivated our selection strategy. Their study shows features in the radio dynamic spectrum and in the optical spectrum that vary either in phase or anti-phase with each other, with a 2.84-hr period that corresponds to the known rotation period of LSR J1835. Hallinan et al. 2015 assert that auroral current systems can explain the Balmer line emission and observed multi-wavelength periodicity. Specifically, they argue that the downward spiraling population of electrons that gives rise to the observed

ECM emission also causes collisional excitation of the neutral hydrogen in the atmosphere upon impact, with subsequent de-excitation via line emission powering the observed Balmer emission. Additionally, the electron current supplies the brown dwarf atmosphere with excess free electrons, possibly contributing to increased H^- opacity in the auroral feature. The increased H^- opacity would cause the upper atmosphere of the auroral feature to become optically thick, appearing lower in temperature than the photosphere. Such an auroral H^- 'cloud' could explain the phased and anti-phased lightcurves at various wavelengths observed in both LSR J1835 and TVLM 513-46546 (Littlefair et al. 2008), another M8.5 brown dwarf known to emit both quiescent and periodically pulsing radio emission as well as Hα, with a lasting ~0.4-period offset between the optical emission and the radio pulses (Hallinan et al. 2007; Berger et al. 2008; Wolszczan and Route 2014; Lynch, Mutel, and Güdel 2015).

Our results corroborate the unified auroral model proposed by Hallinan et al. 2015 for even the coolest dwarfs. In late-L and T dwarfs such as our targets, molecular hydrogen dominates the atomic hydrogen in the atmosphere, and observed photometric variability may in part be explained by localized heating of the atmosphere within the auroral feature by the precipitating electron beam. Morley, Marley, Fortney, and Lupu 2014 showed that heating of the atmosphere at different depths perturbs the pressure vs. temperature profile and can indeed cause spectral variability. Regardless of where in the atmosphere heating occurs, the highest amplitude variability occurs in absorption features redward of ~2.2 μm, which could lead to variability in the K and L bands. Encouragingly, K_s-band variability has been observed in SIMP0136, as well as tentatively for SDSS0423, and Metchev et al. 2015 report that 36^{+26}_{-17}% of T dwarfs vary by ≥0.4% at 3–5 μm. However, the incidence rate for dust variability is much higher than for auroral emission (Buenzli et al. 2014; Radigan et al. 2014; J. Radigan 2014; Metchev et al. 2015; Heinze, Metchev, and Kellogg 2015; Kirkpatrick et al. 2000; Burgasser et al. 2003; Cruz et al. 2007; Kirkpatrick et al. 2008; Pineda 2016), suggesting that auroral emission may only play a role in some cases, such as the highly variable SIMP0136. Finally, we note that even in the absence of atomic hydrogen, Hα emission can still occur. The incoming populations of free electrons and protons can recombine to excited states or the molecular hydrogen may dissociate to excited atomic hydrogen, subsequently de-exciting via Balmer emission.

In addition to the possible correlation with IR variability, all previous detections of

pulsed radio emission from ultracool dwarfs have been accompanied by detectable levels of quiescent radio emission, with no reported detections of pulsed emission in isolation. Although the properties of the quiescent emission are consistent with incoherent synchrotron or gyrosynchrotron emission, the physical processes governing the pulsed and quiescent emission are likely causally related, with the possibility of a shared electrodynamic engine powering the emission.

To better understand the relationship between Hα, radio, and IR variability, additional simultaneous multi-wavelength observations and detailed models investigating atmospheric heating from the auroral currents are needed.

3.9 Conclusions

We detected 5 of 6 late-L/T dwarfs in the 4–8 GHz band, including first detections for 4 objects, quintupling the number of radio-detected objects later than spectral type L6. For 4 of our objects, including previously-detected 2M1047, we observe highly circularly polarized pulsed emission. We also tentatively observe circularly polarized pulsed emission from a fifth object, 2M1237. All of our objects with pulsed emission also exhibit quiescent emission, as is the case for all previously detected radio brown dwarfs. This suggests that pulsed and quiescent phenomena are almost certainly related, though the mechanism for quiescent emission is still unclear.

Biasing our sample for Hα emission or optical/IR variability provides a good means to finding these objects, implying that the Hα emission may be the optical counterpart of auroral activity observed in the radio. We additionally note that several of our objects are either confirmed or tentative IR-variable sources, including the well-known dust variable SIMP0136. Viewed in light of recent studies by Hallinan et al. 2015 and Morley, Marley, Fortney, and Lupu 2014, our radio detections hint that auroral activity may also be related to brown dwarf weather in some cases.

Our data confirm kilogauss magnetic fields down to spectral type T6.5, demonstrating the efficacy of ECM as a tool for probing the magnetic fields of the coolest dwarfs in a mass gap that is critical for informing fully convective dynamo models.

We develop a framework for comparing magnetic field measurements derived from electron cyclotron maser emission to measurements derived from Zeeman broadening and Zeeman Doppler imaging techniques. Using our framework, we provide strong constraints for rms surface field strengths in late-L/T dwarfs and demonstrate that our T dwarfs have magnetic fields that may be inconsistent with the Chris-

tensen, Holzwarth, and Reiners 2009 model. This suggests that parameters beyond convective flux may influence magnetic field generation in brown dwarfs.

3.10 Acknowledgements

MMK thanks Jackie Villadsen, E. Sterl Phinney, Ulrich Christensen, and Shri Kulkarni for illuminating and helpful conversations.

This publication makes use of data products from the Two Micron All Sky Survey, which is a joint project of the University of Massachusetts and the Infrared Processing and Analysis Center/California Institute of Technology, funded by the National Aeronautics and Space Administration and the National Science Foundation.

The National Radio Astronomy Observatory is a facility of the National Science Foundation operated under cooperative agreement by Associated Universities, Inc.

JSP was supported by a grant from the National Science Foundation Graduate Research Fellowship under grant no. DGE-1144469.

Facilities: JVLA

Chapter 4

CONSTRAINTS ON AURORAL RADIO EMISSION FROM Y DWARFS

4.1 Abstract

As an initial pilot study of magnetism in Y dwarfs, we have observed two of the three known IR variable Y dwarfs WISE J085510.83-071442.5 and WISE J140518.40+553421.4 with the Karl G. Jansky Very Large Array (VLA) from 4–8 GHz to investigate the presence of quiescent radio emission as a proxy for highly circularly polarized radio emission associated with large-scale auroral currents. Measurements of magnetic fields on Y-dwarfs, currently only possible by observing auroral radio emission, are essential for constraining fully convective magnetic dynamo models. We do not detect any pulsed or quiescent radio emission, down to rms noise levels of 23 and 4.0 μJy for WISE J085510.83-071442.5 and WISE J140518.40+553421.4 respectively. The fractional detection rate of radio emission from T dwarfs is $\sim$10% and suggests that a much larger sample of deep observations of Y dwarfs is needed to rule out radio emission in the Y dwarf population. The significance of a single detection provides strong motivation for such a search.

4.2 Introduction

An important outstanding problem in dynamo theory is understanding how magnetic fields are generated and sustained in fully convective objects, spanning both stars and planets. Whereas prevailing dynamo models for dwarf stars with an inner radiative zone and an outer convective envelope rely on the strong differential rotation at the interface between the two layers to power $\alpha\Omega$ dynamos (Parker 1975), fully convective dwarfs do not support such a dynamo, but exhibit tracers of activity down to T6.5 (Gizis et al. 2000; West et al. 2008; Schmidt et al. 2015; Berger et al. 2001; Berger 2002; Burgasser and Putman 2005; Berger 2006; Phan-Bao et al. 2007; Antonova et al. 2007; McLean, Berger, and Reiners 2012; Burgasser et al. 2013; Williams, Cook, and Berger 2014; Burgasser, Melis, Todd, et al. 2015; Kao et al. 2016; Route and Wolszczan 2016; Pineda et al. 2016). In fact, Zeeman broadening and Zeeman Doppler imaging studies confirm average surface magnetic field magnitudes of order kilogauss on dwarfs as late as M9 (Saar 1994; Johns-Krull and Valenti 1996; Donati et al. 2006; Reiners and Basri 2007; Morin et al. 2010),

and pulsed radio emission associated with ~kG fields has been observed on objects as late as T6.5 (Route and Wolszczan 2012; Kao et al. 2016; Williams, Gizis, and Berger 2016; Route and Wolszczan 2016). Instead of the $\alpha\Omega$ dynamo, these fully convective objects must rely on alternate dynamo mechanisms to support such fields.

A number of models for possible dynamo mechanisms in this regime have been proposed (e.g. Browning 2008; Simitev and Busse 2009; Christensen, Holzwarth, and Reiners 2009; Morin, Dormy, et al. 2011; Gastine et al. 2013) but constraining data on magnetic field strengths and topologies across a wide range of mass, age, rotation rate, and temperature are sorely lacking, particularly in the brown dwarf regime. L, T, and Y dwarfs probe the lowest end of the substellar mass and temperature space—a regime that is necessary for validating and constraining any fully convective dynamo model. In particular, even a single Y dwarf magnetic field measurement would be very significant. For example, a recent breakthrough dynamo scaling relation predicts that convected energy flux sets magnetic energy in fully convective stars through planets (Christensen, Holzwarth, and Reiners 2009). Any ~kilogauss Y dwarf measurement unequivocally challenges this model.

Traditional techniques that rely on Zeeman broadening have successfully measured the strength, filling factor, and large-scale field topologies of objects as late as M9 (Johns-Krull and Valenti 1996; Donati et al. 2006; Reiners and Basri 2007; Morin et al. 2010). However, rotational broadening of magnetically sensitive lines and limited sensitivity prevent these techniques from accessing L and later dwarfs (Reiners and Basri 2006).

Detections of highly circularly polarized pulsed radio emission currently provide our only window into magnetic field measurements for L, T, and Y dwarfs. This emission is attributed to the electron cyclotron maser (ECM) instability (Hallinan et al. 2007), which is also responsible for producing the auroral radio emission from all of the magnetized planets in our Solar System (Zarka 2007). This magnetic activity is distinct from the standard chromospheric heating picture, where magnetic fields locally interact with hotter and less neutral atmospheres to drive transient, small-scale currents such as magnetic reconnection events and coronal loops (). Instead, brown dwarf magnetic activity appear to be more analogous to what has been observed in Jupiter, in which tracers of magnetic activity such as Hα and radio emission are powered by an external source, the outer magnetosphere, via auroral current systems such as magnetosphere-ionosphere coupling currents that give rise to auroral activity (Nichols et al. 2012; Bagenal et al. 2014).

ECM emission is a very powerful tool for measuring magnetic fields, and it has provided some of the first confirmations of kilogauss fields for late M and L dwarfs (Burgasser and Putman 2005; Hallinan et al. 2006, 2007, 2008; Berger et al. 2009). While emission at the second and higher harmonics can dominate when the ratio of the plasma frequency to the electron cyclotron frequency exceeds ~0.3 (Winglee 1985), local plasma densities in the neutral atmospheres of late L, T, and Y dwarfs indicate emission dominated by the fundamental frequency for the frequencies typically observed (a few GHz). Indeed, observations of the Solar System planets show emission at almost exactly the fundamental electron cyclotron frequency $\nu_{\rm MHz} \sim 2.8 \times B_{\rm Gauss}$ (Treumann 2006, and references therein). ECM emission frequencies in the coolest brown dwarfs therefore uniquely and accurately identify the local magnetic field strengths in the regions of the magnetosphere from where the emission originates. Near the surface of the atmosphere, where the magnetic field is the strongest and produces the highest frequency emission, electrons begin interacting with the atmosphere and can no longer freely gyrate about the field lines, causing a sharp drop-off in the emission (Zarka 1998). This high frequency ECM emission cut-off corresponds to the lower bound of the maximum large-scale magnetic field strengths in the coolest substellar objects.

Historically, radio detections of brown dwarfs are very rare; previous radio surveys encompassing objects later than M7 have yielded a ~10% detection rate (Berger 2006), and until 2016, only one detection out of ~60 L6 or later targets (Antonova et al. 2013; Route and Wolszczan 2013). In a previous study, we developed a selection strategy for biasing survey targets based on possible optical and infrared tracers of auroral activity (Kao et al. 2016). Our selection process was motivated by **(a)** low-amplitude I-band variability detected in known auroral radio emitters (Harding et al. 2013); **(b)** simultaneous radio and optical spectroscopic observations of an M8.5 dwarf showing Balmer line and optical broadband continuum variability tracking auroral radio pulses (Hallinan et al. 2015); and **(c)** predictions of increased emission at K-band or longer wavelengths from localized atmospheric heating (e.g. an impacting auroral current) (Morley, Marley, Fortney, and Lupu 2014).

Using our selection strategy, we detected highly circularly polarized radio emission for four of five pilot targets at 4–8 GHz, confirming >2.5 kG magnetic fields. By carefully comparing the magnetic field measurements derived from radio emission to measurements derived from Zeeman broadening and Zeeman Doppler imaging, we provided tentative evidence that the dynamo operating in this mass regime may be

inconsistent with predicted values from Christensen, Holzwarth, and Reiners 2009. This suggested that parameters beyond convective flux may influence magnetic field generation in brown dwarfs.

To access the strongest constraints on fully convective dynamo models, pushing magnetic field measurements to Y dwarfs and eventually exoplanets such as hot Jupiters is critical. While previous searches for radio emission from exoplanets have been attempted, this paper is the first such attempt for Y-dwarfs and is motivated by the success of our above described selection strategy and recent discoveries of variability at near- and/or mid-infrared bands for three Y-dwarfs, WISE J140518.39+553421.3, WISE J085510.83-071442.5, and WISEP J173835.52+273258.9 (Cushing et al. 2016; Esplin et al. 2016; Leggett et al. 2016). While these detections of variability have been quite reasonably attributed to variations in atmospheric temperature/opacity (weather), it has been argued that similar phenomena can be driven by auroral currents for the ~10% of objects that exhibit radio pulsing (Hallinan et al. 2015; Kao et al. 2016). If so, aurora may play a role in some cloud variability cases but not all, as the radio fractional detection rates are low (Route 2016) compared cloud phenomena, where up to ~80% of L/T transition brown dwarfs may be strong variables and ~60% of L and T dwarfs outside of spectral types L9–T3.5 may be more moderate variables (Radigan et al. 2014).

In exoplanets, the primary driver of auroral emission is expected to be the interaction of the planetary magnetosphere with the stellar wind, and emission intensities therefore depend strongly on incident stellar wind flux (Gallagher and Dangelo 1981; Gurnett et al. 2002). Attempts to detect hot Jupiter radio emission have thus far been unsuccessful (e.g. Hallinan et al. 2013; Murphy et al. 2015; Bower et al. 2016).

In isolated brown dwarfs, the likely drivers for auroral emission include the corotation breakdown of a plasma sheet in the brown dwarf magnetosphere (Hill 2001; Cowley and Bunce 2001) or the current generated by the relative motion of a planetary satellite with respect to the brown dwarf magnetosphere (Zarka 2007). As such, radio power from isolated brown dwarfs is not limited by incident stellar wind flux but instead depends on plasma availability and the voltage drop generated across auroral current systems driven by large-scale magnetic fields (Nichols et al. 2012). If Y dwarfs have atmospheres similar to gas giant planets, predicted atmospheric ionization fractions would be sufficient for auroral current systems to form (Helling et al. 2013; Rodriguez-Barrera et al. 2015). If the generation of strong large-scale

magnetic fields is indeed dependent on convected energy (i.e. temperature), early Y dwarf radio detection fractions may be unlikely to depart precipitously from the ∼10% detection fraction observed to be constant for L0–T6.5 (Pineda 2016; Route and Wolszczan 2016, and references therein), as brown dwarfs spend their lifetimes gravitationally contracting and cooling along the L-T-Y spectral sequence.

We present here an initial pilot study of two nearby exemplar Y dwarfs with evidence of IR variability.

4.3 Targets

For our study, we selected two of the three known IR-variable Y dwarfs. Our selection strategy is motivated by the success of our previous survey, in which we detected both pulsed and quiescent radio emission in 5/6 late L and T dwarfs by selecting for tracers of auroral emission at other wavelengths (Kao et al. 2016), specifically Hα and infrared variability. Although neither of the targeted Y dwarfs have confirmed Hα emission, their IR variability is similar in nature to that of SIMP J01365662+0933473 (hereafter SIMP0136), a clearly periodic and high-amplitude IR variable T-dwarf lacking Hα emission (Pineda et al. 2016) that exhibited ∼200 μJy ECM pulses in our previous survey. Clouds in brown dwarf atmospheres have been proposed to interpret observed photometric and spectroscopic variability (Marley, Saumon, and Goldblatt 2010; Burgasser et al. 2014; Apai et al. 2013), but the Kao et al. (2016) results point to the possibility that an additional variability mechanism may be at play in some cases, e.g. extreme variables like SIMP0136, as postulated by Hallinan et al. 2015. We stress that brown dwarf weather is much more prevalent than radio emission, so at least some fraction of that variability is likely causally unrelated. Target properties are listed in Table 4.1.

WISE J085510.83-071442.5. WISE 0855-07 was identified as a high proper motion object in the Wide-field Infrared Survey Explorer (WISE) catalog (Wright et al. 2010) by Luhman (2014), with a parallax corresponding to ∼2.2 pc. The authors estimated that 225 K < $T_{\rm eff}$ < 260 K, and noting that it was the reddest known T or Y dwarf, tentatively identified it as a Y dwarf. In a followup study, Faherty et al. (2014) confirmed 225 K < $T_{\rm eff}$ < 250 K, and a tentative $J3$ detection provided evidence that WISE 0855-07 may host sulfide and water ice clouds. The presence of atmospheric water vapor and clouds was confirmed by a 4.5–5.2 μm spectrum obtained by Skemer et al. (2016). In contrast, Luhman and Esplin (2016) were unable to conclusively constrain the presence of clouds or non-equilibrium chemistry in

Table 4.1: Survey Targets

Object Name	Abbrev. Name	SpT	Parallax (mas)	Distance (pc)	$\mu_\alpha \cos\delta$ (mas/yr)	μ_δ (mas/yr)	Ref.
WISE J085510.83-071442.5	WISE 0855-07	Y	449±8	2.23±0.04	-8118±8	680±7	1–2
WISE J140518.40+553421.4	WISE 1405+55	Y0.5p? [a]	129±19	$7.8^{+1.3}_{-1.0}$	-2263±47	288±41	3–6

[a] Cushing et al. (2016) identified that the p? had been mistakenly dropped by Schneider et al. (2015).

References. — (1) Luhman 2014; (2) Luhman and Esplin 2016; (3) Cushing et al. 2016; (4) Dupuy and Kraus 2013; (5) Cushing et al. 2011; (6) Kirkpatrick et al. 2011

Table 4.2: Summary of Observations

Object	Band (GHz)	Obs. Date (2015)	Obs. Block (h)	Time on Source (s)	VLA Configuration	Synthesized Beam Dimensions (arcsec × arcsec)	I, V RMS (μJy)	Phase Calibrator	Flux Calibrator
WISE 0855-07	4.0–8.0	05/22	4.0	11862	BnA	9.21 × 3.02	23, 6.0	J0902-1415	3C286
WISE 1405+55	4.0–8.0	05/16	4.0	12360	BnA	1.38 × 1.21	4.0, 36	J1419+5423	3C295 [a]

[a] 3C295 was fully resolved and unsuitable for flux calibrations. Instead, we transferred flux calibrations using 3C286 of an archival measurement set containing observations of our phase calibrator.

its atmosphere when comparing of photometry in six optical and near-IR bands to model predictions. Finally, Esplin et al. (2016) reported variability at 3.6 and 4.5 μm with peak-to-peak amplitudes between 3–5% and also found insufficient evidence for water ice clouds in the atmosphere. Periodicity in the observed variability was inconclusive, with periods ranging between 6.8–9.0 hr at 3.6 μm and 5.3–9.3 hr at 4.5 μm for two different epochs.

WISE J140518.40+553421.4. WISE 1405+55 was discovered and initially classified as a Y0p? dwarf by Cushing et al. (2011), who noted that its H-band peak was ~60 Å redder than the Y0 spectral standard. They estimated $T_{\rm eff}$ ~350 K, log g ~5.00, and M ~30 $M_{\rm J}$. *Hubble Space Telescope (HST)* spectroscopy by Schneider et al. (2015) reclassified it as Y0.5, and confirmed that 350 K < $T_{\rm eff}$ < 400 K, and 5.0 < log g < 5.5. Cushing et al. (2011) estimated the spectroscopic distance at 3.8 pc, while the estimated photometric distance is 8.6 pc (Kirkpatrick et al. 2011). Parallax measurements confirm a distance of $7.8^{+1.3}_{-1.0}$ pc (Dupuy and Kraus 2013). WISE 1405+55 is the first Y dwarf from which photometric variability was detected, at 3.6 and 4.5 μm with semi-amplitudes of 3.5% and a period of ~8.5 hr (Cushing et al. 2016). The authors reported that current cloud and hot-spot models cannot reproduce the observed variability.

4.4 Observations

We observed both Y dwarfs with the full VLA array in C-band (4–8 GHz), using the WIDAR correlator in 3-bit observing mode for 4 GHz bandwidth observations, in time blocks of 4 hours each. Observations were taken on 22 May and 16 May 2015 for WISE 0855-07 and WISE 1405+55, respectively, during BnA configuration. We summarize target observations in Table 4.2.

Searching for rotationally modulated auroral pulses can be time intensive, requiring more than one full rotation period to observe at least two pulses. Due to the longer rotational periods for our targets, we elected to search for quiescent radio emission as a proxy for pulsed emission, with the aim to follow up any quiescent detections for pulsed emission at a later date. This choice was motivated by the fact that detections of quiescent radio emission accompany all previous auroral pulse detections (Hallinan et al. 2007, 2008; Burgasser and Putman 2005; Berger et al. 2009; Kao et al. 2016) and vice versa, as in the cases of pulsing dwarfs detected by Arecibo (insensitive to quiescent emission) when followed up with the VLA (Route and Wolszczan 2012; Williams, Berger, and Zauderer 2013; Route 2016;

Williams, Gizis, and Berger 2016). This suggests that physical processes governing the quiescent and pulsed radio components may be related, possibly sharing an electrodynamic engine. Indeed, Pineda (2016) shows that Hα luminosities correlate with quiescent radio luminosities for known M7–T8 auroral pulse emitters.

Targeting quiescent emission brings additional advantages. First, while Jovian auroral emission cuts off at ~40 MHz (14 Gauss), its quiescent emission is broadband up to a few GHz (Zarka 2007). Likewise, auroral brown dwarfs emit pulses at $\gtrsim$4–10 GHz and quiescent emission up to ~100 GHz (e.g. Williams et al. 2015). Y dwarf quiescent emission likely falls in this range, regardless of magnetic field strengths. Second, observations spanning 10 years confirm that the quiescent emission is temporally stable (e.g. Hallinan et al. 2006; Gawroński, Goździewski, and Katarzyński 2016), though we note two exceptions where late-type objects (M9.5 and L2.5) show long term variability in the quiescent emission (Antonova et al. 2007; Berger et al. 2010).

4.5 Calibrations

Table 4.3: Archival measurements sets for J1419+5423

Project #	Obs. Date (M/D/Y)	Block ID	Flux Calibrator	Flux (Jy)
15A-102	02/08/2015	30105159	3C286	1.17593 ± 0.000058
14A-483	08/10/2014	29584695	3C286	1.3839 ± 0.0013
14A-483	09/03/2014	29606143	3C286	1.3968 ± 0.0013

We calibrated our measurement sets using the standard VLA flux calibrator 3C286, and nearby phase calibrators. Typical full-bandwidth sensitivity at BnA configuration for 3.5 hours on source in C-band is 1.8 μJy, with typical 3-bit observations reaching an absolute flux calibration accuracy of ~5%. Flux calibration accuracy may be reduced and result in systematically offset flux densities when gain calibrations interpolated from the phase calibrator are not sufficient to correct for the variation of gain phases with time. To account for this, our observations alternated between a nearby phase calibrator and the target source with typical cycle times of 20 minutes, and we obtained gain solutions for the phase calibrators that varied slowly and smoothly over time, suggesting that this source of error is negligible.

We initially processed both measurement sets with the VLA Calibration Pipeline and obtained absolute flux by bootstrapping flux densities with the observed flux calibrators. For WISE 0855-07, a nearby bright quasar with flux density ~0.3 Jy

limited initial sensitivity for the full measurement set to 153 μJy. After self calibrating, sensitivity increased to 23 μJy, for a dynamic range exceeding $\sim 10^4$. For WISE 1405+55 we kept initial flags from the calibration pipeline before proceeding with a manual calibration.

Flux calibrator 3C295 was observed for WISE 1405+55, but it was fully resolved and could not be used to satisfactorily flux calibrate. Instead, we located the measurement set nearest in time to our observations in the VLA archive containing observations of the same phase calibrator that we used, quasar J1419+5423. These observations were taken on 08 February 2015 in B configuration at C band using 3C286 as a flux calibrator. After flux calibrating J1419+5423 with 3C286 in this archived measurement set, we transferred the flux calibrations to the phase calibrator field in our own measurement set, from which we then determined bandpass solutions. We also calibrated two other archival measurement sets from 10 August 2014 and 03 September 2014 containing observations of J1419+5423 at C band in D configuration to check for time variability in its flux density. Measurements of the J1419+5423 flux densities in all epochs are listed in Table 4.3. Based on the above ~month timescales, we expect the measured flux of J1419+5423 and therefore WISE 1405+55 to be accurate within ~20%.

4.6 Results

Table 4.4: Imaging and Timeseries Results

Object	Mean Stokes I (μJy)	3σ Upper Limit Stokes I (μJy)	Mean Stokes V (μJy)	3σ Upper Limit Stokes V (μJy)	Pulse (#)
WISE 0855-07	···	<69 [a]	0.0 ± 6.0	<18.0	0
WISE 1405+55	−3.4 ± 4.0	<12.0	−4.5 ± 3.6	<10.8	0

[a] Stokes I image was contaminated by a ~0.3 Jy nearby source.

We produced Stokes I and Stokes V images of each object (total and circularly polarized intensities, respectively) with the CASA `clean` routine, modeling the sky emission frequency dependence with two terms and using natural weighting. We searched for a point source at the proper motion-corrected coordinates of each target. Fits did not converge for the Stokes I image of WISE 0855-07, and an examination by eye confirms the lack of a point source. Figure 4.1 shows the Stokes I and Stokes V images for both objects. We fitted an elliptical Gaussian point source to the cleaned image of each object at its predicted coordinates using using the CASA task `imfit`, and Table 4.4 gives the measured mean flux density, rms noise, and 3σ

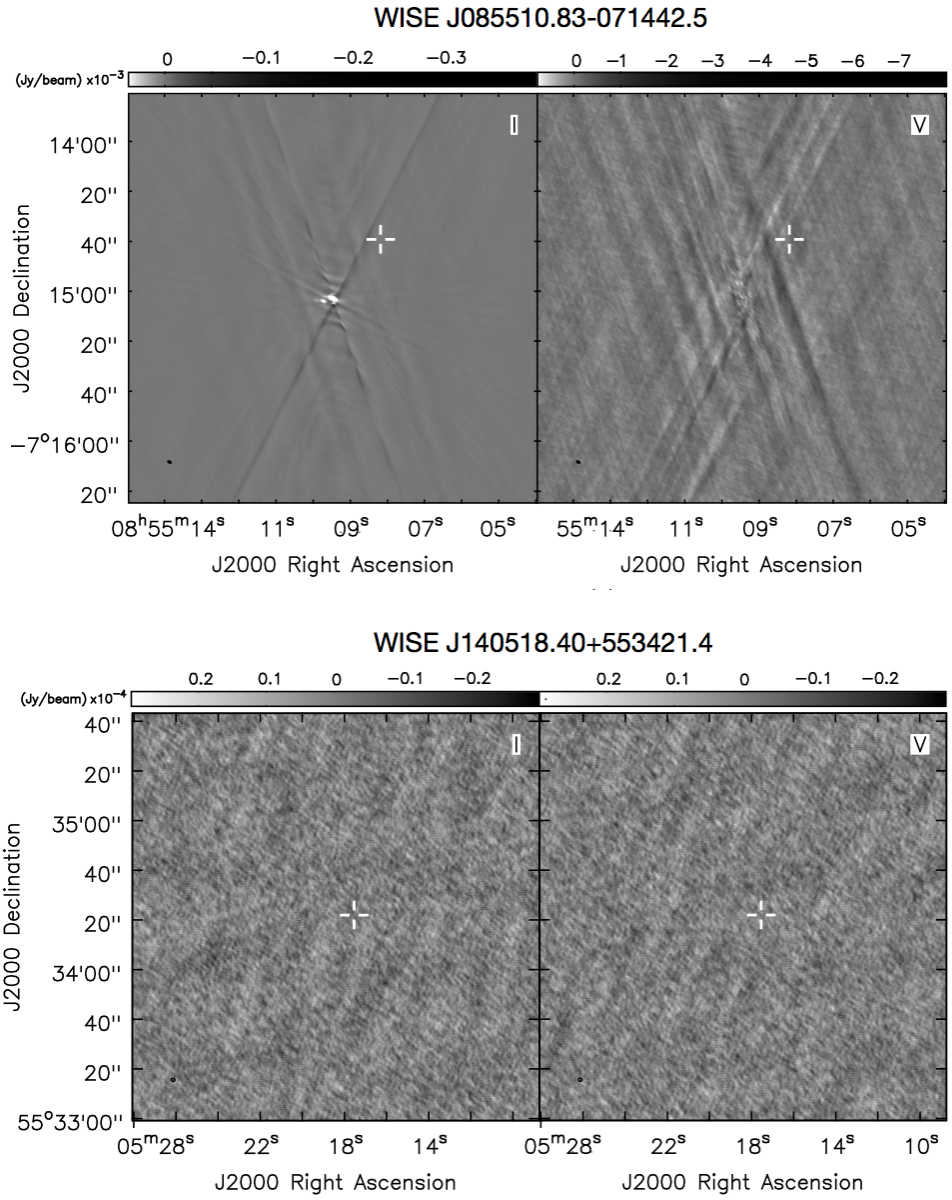

Figure 4.1: Stokes I (left) and V (right) images of both objects. Ellipse in bottom left-hand corner depicts synthesized beam. Crosshairs indicate proper motion corrected coordinates. No point sources were detected.

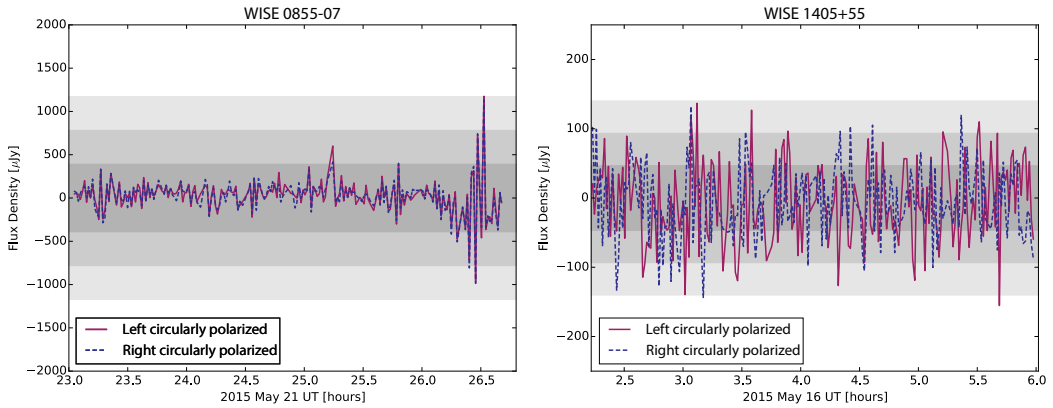

Figure 4.2: Timeseries of rr- and ll-correlated (blue and red, respectively) flux densities averaged over 60 s intervals. Grey regions indicate 1- , 2-, and 3σ rms noise. No pulses are detected.

upper limits for each source.

We did not detect any radio emission from either Y-dwarf, down to rms noise levels of 4.0 μJy for WISE 1405+55 and 23 μJy for for WISE 0855-07. To check for any pulsed emission that may have been averaged down to undetectable levels in a 4-hour image, we created 4–8 GHz, 4–6 GHz, and 6–8 GHz timeseries of the right- and left-circularly polarized emission at the expected locations for both targets, following the procedure outlined in §5.2 of Kao et al. (2016). Figure 4.2 shows the 4–8 GHz timeseries for each object. We do not detect any circularly polarized radio pulses or quiescent emission for either Y-dwarf.

4.7 Discussion

Despite the decreased sensitivity in the Stokes I imaging for WISE 0855-07, the nearness of our targets allows us to place stringent constraints on their radio luminosities. We compare the 3σ upper limits to quiescent emission flux densities observed for other radio brown dwarfs in Figure 4.3. These upper limits are consistent with the trend that cooler objects tend to be less radio bright than warmer ultracool dwarfs, but the data do not provide sufficient evidence for or against a break in this trend.

By itself, a lack of any detectable quiescent emission from WISE 1405+55 cannot unequivocally rule out any pulsed radio emission at 4–8 GHz. However, future studies demonstrating a systematic absence of detectable radio emission at these frequencies may be evidence for the onset of a dynamo distinct from those operating in late M, L, and T dwarfs. For WISE 0855-07, the rms noise that we achieved in our

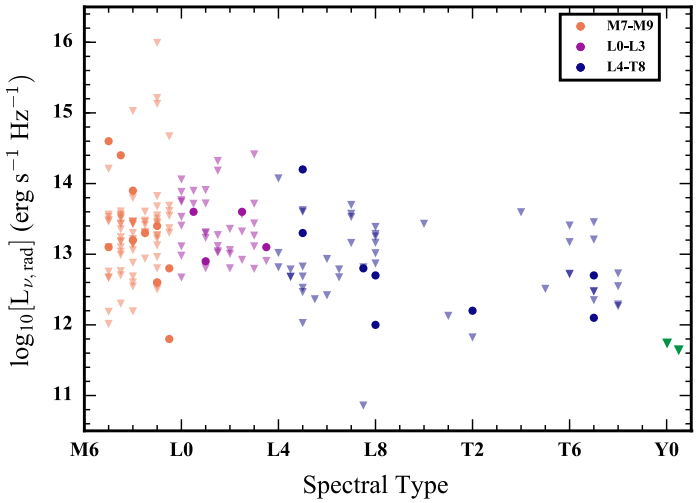

Figure 4.3: Quiescent emission radio luminosities as a function of spectral type. Upper limits are triangles and detections are circles. WISE 0855-07 and WISE 1405+55 are the green triangles in the bottom right. Figure adapted from Pineda (2016).

images is not enough to rule out the possible presence of quiescent emission at the tens of μJy level. Stokes V does not suffer from the same dynamic range limitations experienced by Stokes I from the contaminating nearby bright quasar, but quiescent emission from brown dwarfs has been observed to be much less strongly circularly polarized (e.g. Kao et al. 2016). Observing WISE 0855-07 for its full rotational period to search for circularly polarized pulsed emission is the only conclusive means to rule out ECM emission from 4–8 GHz.

A detection of pulsed, circularly polarized radio emission from either WISE 0855-07 or WISE 1405+55 would have indicated the presence of large-scale magnetic fields of at least 2.5 kG. In the absence of any detectable radio emission from our targets, we cannot conclusively provide any strong constraints on magnetic field strengths in either object. If quiescent radio emission is indeed linked to pulsed radio emission, the following possibilities may account for why we do not observe quiescent or pulsed radio emission from our targets: (1) WISE 0855-07 and WISE1405+55 do not produce detectable auroral radio emission and (2) currents powering auroral activity in these Y-dwarfs are variable in nature. Thus far, only two late-type objects have demonstrated long-term extreme radio variability, the L2.5 dwarf 2MASS J05233822-1403022 and the M9.5 dwarf BRI 0021 (Antonova et al. 2007; Berger et al. 2010).

In case (1), ECM emission will not occur if the engine for driving such emission

is not present, despite the presence of sufficiently strong fields. In fact, Zeeman broadening measurements confirm mean surface field strengths in M7–M9 dwarfs that are strong enough to drive ECM emission at several GHz, yet most of these strongly magnetized brown dwarfs have not been detected in radio (e.g. Reiners and Basri 2010; Antonova et al. 2013, and references therein). As an illustration, if the primary driver for ECM emission in isolated brown dwarfs is corotation breakdown of a plasma sheet in the magnetosphere (Cowley and Bunce 2001; Hill 2001; Bagenal et al. 2014; Badman et al. 2015, and references therein), slower rotation may prevent such corotation breakdown from occurring (Nichols et al. 2012). Indeed, Esplin et al. (2016) and Cushing et al. (2016) have reported rotational periods derived from infrared variability at 8.5 hours and 5.3–9.3 hours for WISE 0855-07 and WISE 1405+55 respectively. In comparison, all pulsing radio brown dwarfs have reported rotational periods between 1.77 and 3.89 hours (Pineda 2016, and references therein).

In case (2), necessary conditions for the occurrence of large-scale auroral current systems include (a) the presence of mildly relativistic populations of free electrons within the large-scale magnetospheres of our objects (b) the presence of strong, large-scale magnetic fields, and (c) the presence of a satellite magnetosphere or ionosphere for aurora generated by satellite-interactions. With regards to the first condition, sufficiently intermittent periods of volcanic activity from a satellite may cause time varying auroral activity. In the Jupiter system, vigorous volcanic activity from Io replenishes the plasma torus on a timescale of ~19 days, and its density, temperature, and composition can vary up to a factor of two (Delamere and Bagenal 2003). Long-term monitoring show that the brightness of Jovian auroral satellite footprints (Io, Ganymede) can vary by a factor of ~2–10, and the brightest emission coincides with when the satellites approach the center of the plasma torus, where denser plasma is expected to generate a stronger interaction. (GéRard et al. 2006; Serio and Clarke 2008; Grodent et al. 2009; Wannawichian, Clarke, and Nichols 2010). For the second condition, a magnetic cycle in which large-scale fields evolve into small-scale fields may cause time variation in auroral activity (e.g. Kitchatinov, Moss, and Sokoloff 2014; Yadav et al. 2016; Route 2016). As an illustration of the third condition, Enceladus also can (rarely) generate a detectable auroral footprint with high amplitude variability (factor of ~3) over a timescale of a few hours, which is attributed to its time-variable cryo-volcanism (Pryor et al. 2011).

While the data preclude concrete conclusions about magnetic field strengths and

auroral generation mechanisms in Y dwarfs, longer-term monitoring is necessary to resolve the possibilities discussed in case (2). For case (1), a broader sample of cool dwarfs spanning a range of masses and rotation rates will provide insight into whether there are any associated dependencies for either. Given that all known radio pulsing brown dwarfs are fast rotators, an initial focus on Y dwarfs with short rotation periods would be especially compelling.

4.8 Conclusions

We have observed two Y dwarfs known to display evidence of IR variability for radio emission due to auroral magnetospheric currents. In the interest of conserving limited telescope time resources, we elected to initially search for quiescent radio emission as a proxy for pulsed emission, aiming to follow up any quiescent detections with comprehensive search for pulsed emission. We did not detect any radio emission. Targets such as WISE 0855-07 that have nearby bright contaminating radio sources will require a more methodical search for pulsed radio emission in Stokes V to rule out auroral radio emission. Follow-up observations of initially quiet targets such as WISE 1405+55 will be key for ruling out time variability in auroral current systems.

The limiting factor for Y dwarf radio detections is not sensitivity but rather the number of sources observed. Detection fractions for L0–L9 and T0–T6.5 spectral ranges remain constant at ~9.8% (6/61) and ~10.3% (4/39). True fractions are likely higher, since these include surveys before the upgraded VLA and with Arecibo, which is insensitive to quiescent emission (Pineda 2016; Route and Wolszczan 2016, and references therein). Assuming a similarly conservative detection fraction for early Y dwarfs, an observing program with at least ten additional targets will have a ~60% chance of detecting at least one Y dwarf. While quiescent radio luminosities depend weakly on spectral type (Pineda 2016), selection effects bias the known Y dwarf population to be very nearby and exposure times can be adjusted to further mitigate sensitivity concerns. Future surveys will require a combination of more objects and deeper observations to provide meaningful constraints on Y dwarfs magnetic fields.

4.9 Acknowledgements

The National Radio Astronomy Observatory (NRAO) is a facility of the National Science Foundation operated under cooperative agreement by Associated Universities, Inc.

MMK was supported by the NRAO Grote Reber Doctoral Fellowship. JSP was supported by a grant from the National Science Foundation Graduate Research Fellowship under grant no. DGE-1144469.

Facilities: JVLA

Chapter 5

THE STRONGEST MAGNETIC FIELDS ON THE COOLEST BROWN DWARFS

5.1 Abstract

We have used the Jansky VLA to observe a sample of 5 known aurorally emitting late-L and T dwarfs ranging in age from ∼0.2–3.4 Gyr. We observed each target for seven hours, extending to higher frequencies than previously attempted for this sample. We establish proportionally higher limits on maximum surface magnetic field strengths while simultaneously placing constraints on rotation periods through detections of repeating pulses. Observations at 8–12 GHz yield measurements of 3.7–4.1 kG localized field strengths (corresponding to minimum mean surface fields between 2.7–2.9 kG) on four of our targets, including the archetypal cloud variable T2.5 dwarf SIMP J01365663+0933473 recently proposed to be a member of the Carina-Near moving group and thus a possible planetary-mass object. We detect a highly circularly polarized radio pulse at 16.5–18 GHz for the T6.5 dwarf 2MASS 10475385+2124234, corresponding to a localized 6.2 kG field strength and minimum mean surface field of 4.4 kG. We measure rotation periods between ∼1.44–2.88 hr for all targets, supporting either i) the emerging consensus in convective dynamo models that rapid rotation may be important for producing strong dipole fields or ii) rapid rotation is a key ingredient for driving the current systems powering auroral radio emission. We do not detect a clear cutoff in the pulsed emission for any targets, which would correspond to a maximum local surface magnetic field strength. However, we do observe evidence of variable structure in the frequency-dependent timeseries of our targets on timescales shorter than a rotation period, suggesting a higher degree of variability in the current systems near the surfaces of brown dwarfs, where emission at the highest frequencies are expected to probe. Finally, we find that old brown dwarfs may generate fields as strong as young brown dwarfs.

5.2 Introduction

Characterizing magnetic fields in the coolest dwarfs and eventually exoplanets can provide valuable insight into the formation, emission, and evolution of planets through stars. For instance, they are key players in disk accretion onto pre-main-

sequence T Tauri stars (Hartmann, Herczeg, and Calvet 2016), affecting planet formation mechanisms. Plasma flow across magnetic field lines drive large-scale currents in brown dwarf and planetary systems, producing auroral emission that likely contributes to the optical and infrared variability traditionally attributed to atmospheric clouds (e.g. Artigau et al. 2009; Radigan et al. 2014; Hallinan et al. 2015; Badman et al. 2015; Kao et al. 2016). Magnetic fields have been invoked to explain fundamental properties such as inflated radii in planets and stars (Batygin and Stevenson 2010; Kervella et al. 2016). Finally, they can mitigate the erosion of planetary atmospheres from strong stellar winds and coronal mass ejections, a special concern for planets in the habitable zones of M dwarfs and young stars (Vidotto et al. 2013; Brain et al. 2015; Leblanc et al. 2015).

To characterize such magnetic fields, it is important to understand the physical principles driving field generation in fully convective objects, which remains an open question in dynamo theory. Applications of convective dynamos span a wide breadth of cases, including rocky planet inner cores, gas giant planets, brown dwarfs, and low-mass stars. Fully convective objects cannot rely on strong differential rotation occurring between radiative and convective zones to help drive their dynamos. However they still exhibit magnetic activity like Hα, X-ray, and radio emission (e.g. Berger et al. 2001, 2005; McLean, Berger, and Reiners 2012; Schmidt et al. 2015; Pineda et al. 2016), and kilogauss fields have been confirmed for M, L, and T dwarfs (e.g. Reiners and Basri 2007, 2009; Morin et al. 2010; Hallinan et al. 2006, 2007, 2008; Route and Wolszczan 2012; Kao et al. 2016). Turbulence dissipates fossil fields within ~10–100 years (Chabrier and Küker 2006), implying that a dynamo must continuously regenerate these strong fields.

Efforts to elucidate magnetic behaviors of fully convective objects have included many fruitful investigations into the role of rotation. For instance, Hα and X-ray emission are both tracers of hot chromospheres and coronae in F through mid-M stars heated in part by magnetic processes (Vernazza, Avrett, and Loeser 1981; Schmitt and Rosso 1988; Ulmschneider 2003). Rotation appears to affect such magnetic processes, as Hα and X-ray emission scale with increasing surface rotation or decreasing Rossby[1] number, which measures the effect of the Coriolis force in the inertial part of the fluid flow (the convective time derivative of velocity). At Ro ~ 0.1, the activity-rotation scaling appears to saturate at a constant $\log L_{\mathrm{X,H}\alpha}/L_{\mathrm{bol}}$ (McLean, Berger, and Reiners 2012), indicating a possible saturation of the influence

[1] Quantified as Ro $\sim P/\tau_c$, where P is the stellar rotation period and τ_c is the convective turnover time.

of rotation on dynamo activity in mid-M and earlier type dwarfs. However, the neutral atmospheres of dwarfs $\gtrsim$M7 may preclude magnetic heating processes of similar nature from occurring in the coolest brown dwarfs (Mohanty et al. 2002), underscoring the need for an alternative way to evaluate magnetism on the coolest brown dwarfs.

Indeed, $\gtrsim$M7 dwarfs exhibit systematically weaker Hα emission while $L_{\rm X}/L_{\rm bol}$ decreases with increasing $v \sin i$ or decreasing Ro (Mohanty and Basri 2003; Reiners and Basri 2008, 2010; Berger et al. 2010; McLean, Berger, and Reiners 2012), and the Güdel-Benz relation appears to break down for objects later than M7 due to a suppression of X-ray luminosities, even when taking activity-rotation saturation into account (Berger et al. 2010; Williams, Cook, and Berger 2014). Rather than relying on proxies for magnetic activity to test the role of rotation in fully convective magnetism, direct measurements would be more ideal.

Models explore how different parameters quantifying competing forces such as Lorentz, buoyancy, and Coriolis affect energy exchange mechanisms at play in the magnetohydrodyamics occurring in dynamo regions. These models observe various dependencies between global magnetic field behaviors such as field topologies, magnetic energy, and time variation to observable object parameters such as luminosity, rotation, and age (e.g., Browning 2008; Christensen, Holzwarth, and Reiners 2009; Yadav et al. 2016), and testing them requires a means to probe magnetism in the coolest objects. For instance, in a recent breakthrough, scaling laws derived from planetary dynamo calculations appear to be dominated by convected energy flux, quantified by bolometric luminosity, rather than rotation (Christensen and Aubert 2006). Excitingly, these laws appeared to be empirically consistent with the magnetic field strengths measured for fully convective stars (Christensen, Holzwarth, and Reiners 2009). However, this scaling relation could not be verified for an important class of fully convective objects, cool brown dwarfs, because the only existing means of measuring magnetic fields relied on the Zeeman broadening of atomic and molecular lines (e.g., Johns-Krull and Valenti 1996; Donati et al. 2006; Reiners and Basri 2007; Morin et al. 2010), which existing limitations in instrumentation and knowledge of Landé factors preclude from extending to L and later dwarfs (Reiners and Basri 2006).

The unexpected detection of quiescent and flaring radio emission from the M9 brown dwarf LP 944-20 at 4.9 and 8.5 GHz with the Very Large Array at the beginning of this millennium violated the tightly correlated Güdel-Benz relation linking coronal

heating and magnetic particle acceleration (Güdel and Benz 1993) and heralded an unexpected new window into brown dwarf magnetism (Berger et al. 2001). This discovery paved the way to the subsequent detection of rotationally modulated and highly circularly polarized radio pulses attributed to the electron cyclotron maser (ECM) instabilty (Hallinan et al. 2006, 2007), which is the same process driving auroral radio emissions in the magnetized Solar System planets (Zarka 1998).

The identification of auroral ECM emission from brown dwarfs was a crucial step to probing magnetic field strengths on the coolest brown dwarfs. For cool brown dwarfs with largely neutral atmospheres where collisions are negligible (the ratio of the plasma frequency to the electron cyclotron frequency is very small), emission occurs very near the electron cyclotron fundamental frequency $\nu_{\rm MHz} \sim 2.8 \times B_{\rm Gauss}$ (Treumann 2006, and references therein). While it cannot provide detailed insight into global magnetic field properties and the absence of such emission does not necessarily imply the absence of strong magnetic fields, detections of auroral radio emission provide powerfully direct measurements of field strengths at emitting locations within the magnetosphere.

In contrast, magnetic field measurements from the Zeeman broadening of magnetically sensitive spectral lines can return filling factor and surface-averaged field strengths with ∼15%–30% uncertainties (Valenti, Marcy, and Basri 1995; Johns-Krull and Valenti 1996, 2000; Reiners and Basri 2007; Reiners 2012; Shulyak et al. 2010). Zeeman Doppler imaging adds the ability to spatially distinguish different regions of different field strengths and reconstruct surface field topologies by fitting spectropolarimetric observations to those synthetically generated from test magnetic maps. Structure of opposite polarity on scales smaller than a spatial resolution element can cancel out, so ZDI is preferentially sensitive to the largest scales (Reiners and Basri 2009; Yadav et al. 2015), with significant confusion between the dipole and quadrupole components, and ∼10–30% uncertainties in dipole energies (Morin et al. 2010). Observations only probing some and not all of the Stokes parameters are further constrained in their abilities to fully capture complex field topologies (Rosén, Kochukhov, and Wade 2015).

While auroral radio emission is likely only sensitive to large-scale fields, a careful interpretation of the measurements allows for comparison to Zeeman broadening measurements and paves the way to extending observational tests of fully convective dynamos to the coolest brown dwarfs (Kao et al. 2016).

However, efficient detection of brown dwarf auroral radio emission eluded as-

tronomers for over a decade, with an overall detection rate of just ∼10% in previous volume-limited surveys (Antonova et al. 2013; Route 2016). Moreover, only one detection out of ∼60 L6 or later targets had been achieved before 2016 (Route and Wolszczan 2012), seriously hindering the application of ECM emission to testing dynamos mechanisms in the mass and temperature gap between planets and stars. Yet, the unprecedented discovery of a T6.5 dwarf emitting at ∼4 GHz demonstrated that such emission could indeed extend to objects probing the substellar-planetary boundary (Route and Wolszczan 2012).

Unexpectedly strong ∼kilogauss magnetic fields measured on brown dwarfs with ECM emission belied initial interpretations of weak X-ray emission in radio-bright brown dwarfs as evidence of very weak fields, and in fact Mohanty et al. (2002) showed that the decoupling of magnetic fields from the neutral atmospheres of these cool brown dwarfs could explain the weak X-ray emission. Instead of coronal heating processes, recent studies link ECM emission to other tracers of Solar System auroral activity such as Hα emission and optical broadband variability (Harding et al. 2013; Hallinan et al. 2015; Pineda et al. 2016), suggesting a new model for magnetic activity in the coolest brown dwarfs: auroral emission.

We previously developed and tested a selection strategy for identifying likely ECM-emitting brown dwarf candidates making use of the emerging connection between auroral emissions and ECM and selecting targets with known Hα emission and/or optical/infrared variability (Kao et al. 2016). This selection strategy led to the detection of ECM emission in four out of five new L7–T6.5 brown dwarf pilot targets at 4–8 GHz, confirming >2.5 kG magnetic fields. A subsequent study confirmed detectable levels of Hα emission for all but one of these targets (Pineda et al. 2016).

The addition of this collection of radio brown dwarf magnetic field measurements to the single previous measurement from the T6.5 dwarf 2MASS 10475385+2124234 (Route and Wolszczan 2012; Williams and Berger 2015) represented the tightest observational constraints on fully convective dynamo theory to date. Comparisons of ECM-derived magnetic field measurements to Zeeman-based measurements tentatively suggested that dynamos operating in the coolest brown dwarfs may in fact produce fields that differ from values predicted by the luminosity-driven Christensen, Holzwarth, and Reiners (2009) model.

Higher frequency measurements of these objects can provide yet tighter constraints, motivating this work. Observations of ECM auroral emissions in the Solar System

planets demonstrate that the emission drops off at a cut-off frequency corresponding to the strength of the field near the surface of the object, when interactions with the atmosphere begin to interrupt ECM emission processes. The persistence of highly circularly polarized and pulsing emission in our targets throughout the previously observed 4–8 GHz bandwidth suggested that the emitting electrons were still traversing the magnetospheres of our targets toward increasing magnetic flux. A detection of a cutoff in the ECM emission would provide the tightest radio-derived constraints on brown dwarf magnetic fields, and in fact none has yet been detected in any brown dwarfs to date.

Finally, the rotational modulation of auroral ECM emission provides a means of measuring rotational periods and eventually testing dynamo models examining the role of rotation by observing our known auroral radio emitters for longer time blocks to achieve full rotational phase coverage. Previous studies verify that pulse periods are consistent with rotational broadening from spectral lines (Berger et al. 2005; Hallinan et al. 2006, 2008; Berger et al. 2009).

In this work, we present new 8–12 GHz and 12–18 GHz observations of targets detected in our previous 4–8 GHz pilot survey (§5.4, §5.5.1). We carefully trace the evolution of auroral ECM pulses through 1- or 1.5- GHz sub-bands (§5.5.2, §5.6.2) and measure rotation periods (§5.5.3). Finally, we comment on implications for dynamo theory (§5.6).

5.3 Targets

Our sample of targets are discussed in Kao et al. (2016) but is again summarized here with updated literature for completeness. All targets are known to emit ECM emission at 4–8 GHz (Kao et al. 2016).

2MASS 10475385+2124234. 2M1047 is a T6.5 dwarf with known weak $[L_{\mathrm{H}_\alpha}/L_{\mathrm{bol}}]\sim$ 5.5 (Pineda et al. 2016) and was the first T-dwarf detected at radio frequencies (Route and Wolszczan 2012). The detected emission was highly circularly polarized ($\gtrsim$72%) at 4.75 GHz. Follow-up observations detected detected both quiescent and ECM emission up to 10 GHz (Williams, Berger, and Zauderer 2013; Williams and Berger 2015), the latter of which was used to measure a ~1.77 hr rotation period up through 10 GHz. We included 2M1047 in our pilot survey to examine long-term variability and detected both pulsed and quiescent emission through 8 GHz. Using H_2O and K/H indices, Kao et al. 2016 derived $T_{\mathrm{eff}} = 869^{+35}_{-29}$ K, >0.026 $M_\odot$ estimated mass, and >2.5 Gyr age.

Table 5.1: Survey Targets

Object Name	Abbrev. Name	SpT	Parallax (mas)	Distance (pc)	$\mu_\alpha \cos\delta$ (mas/yr)	μ_δ (mas/yr)	Notes	Ref.
2MASS 10475385+2124234	2M1047	T6.5	94.73±3.81	10.56±0.52	-1714±7	-489±4	Hα, detected prior	1-7
2MASS 01365662+0933473	SIMP0136	T2.5	···	6.0±0.4	1241±9	-4±10	IR variability	8-10
2MASS 10430758+2225236	2M1043	L8	···	16.4±3.2	-134.7±11.6	-5.7±17.0	Hα emission	11-13
2MASS 12373919+6526148	2M1237	T6.5	96.07±4.78	10.42±0.52	-1002±8	-525±6	Hα, IR var?[a]	1 3 4 14-16
SDSS 04234858-0414035	SDSS0423	L7[c]	65.93±1.7	15.17±0.39	-331±49	76±11	Hα, IR var, binary[c]	19 27-33

[a] (14) found no evidence of J-band variability whereas (16) reported variability at a level below the detection limits of (14)

[b] (22), (23), (24) found no IR variability in SDSS1254 above the $\sim 5-20$ mmag level, whereas (20) and (21) reported 'significant' J-band and spectroscopic variability, respectively.

[c] SDSS0423 has a known binary companion of spectral type T2.5 and orbital separation 0.″16 (31, 32, 33).

References. — (1) Burgasser et al. 1999; (2) Burgasser et al. 2006; (3) Vrba et al. 2004; (4) Burgasser et al. 2003; (5) Route and Wolszczan 2012; (6) Williams, Berger, and Zauderer 2013; (7) Williams and Berger 2015; (8) Artigau et al. 2006; (9) Artigau et al. 2009; (10) Apai et al. 2013; (11) Cruz et al. 2007; (12) Schmidt et al. 2010; (13) Pineda et al. 2016; (14) Burgasser, Liebert, et al. 2002; (15) Burgasser, Kirkpatrick, Reid, et al. 2000; (16) Artigau, Nadeau, and Doyon 2003; (17) Leggett et al. 2000; (18) Burgasser, Kirkpatrick, Brown, Reid, Burrows, et al. 2002; (19) Geballe et al. 2002; (20) Artigau, Nadeau, and Doyon 2003; (21) Goldman et al. 2008 (22) Koen, Matsunaga, and Menzies 2004; (23) Girardin, Artigau, and Doyon 2013; (24) Radigan et al. 2014; (25) Burgasser 2007; (26) Cushing et al. 2008; (27) Cruz et al. 2003; (28) Kirkpatrick et al. 2008; (29) Enoch, Brown, and Burgasser 2003; (30) Clarke et al. 2008; (31) Carson et al. 2011; (32) Burgasser et al. 2005; (33) Burgasser, Burrows, and Kirkpatrick 2006

SIMP J01365662+0933473. SIMP0136 is a T2.5 dwarf well known for periodic (P = 2.3895 ± 0.0005 hr) and high-amplitude (>5%) J- and K_s-band photometric variability (Artigau et al. 2009; Croll et al. 2016). High-amplitude infrared variability appears to occur at a higher rate in L/T transition dwarfs (Radigan et al. 2014; J. Radigan 2014) and has been attributed to the onset of patchy clouds (Marley, Saumon, and Goldblatt 2010; Apai et al. 2013; Burgasser et al. 2014; Radigan et al. 2014) to explain wavelength-dependent variability. No Hα emission has been detected down to $[L_{H_\alpha}/L_{bol}] < -6.6$ but it has anomalously strong Li I at EW = 6.6 ± 1.0 and 7.8 ± 1.0 Å for two different nights and is the latest-type object with a clear lithium detection (Pineda et al. 2016). Kao et al. (2016) derived $T_{eff} = 1089^{+62}_{-54}$, $0.022^{+0.015}_{-0.012}$ $M_\odot$ estimated mass, and $0.6^{+1.1}_{-0.3}$ Gyr age. Recently, Gagné et al. (2017) reported that SIMP0136 may be a member of the ~200 Myr-old Carina-Near moving group. Using an empirical measurement of its bolometric luminosity and the the Saumon and Marley 2008 models, they inferred R = 1.22 ± 0.01 R_J, which together predicted T_{eff} = 1098 ± 6K and M = 12.7 ± 1.0 M_J. New $v \sin i$ measurements and its photometric periodicity further constrained $R > 1.01 \pm 0.02$ R_J and $M < 42.6^{+2.5}_{-2.4}$ M_J.

2MASS 10430758+2225236. 2M1043 is an unusually red L8 dwarf with previously reported tentative Hα emission (Cruz et al. 2007). Pineda et al. (2016) confirm $[L_{H_\alpha}/L_{bol}] = -5.8 \pm 0.2$ as well as a tentative Li I absorption line with EW = 10 ± 3 Å. Kao et al. (2016) derived T_{eff} = 1390 ± 180 K, $0.011^{+0.011}_{-0.005}$ $M_\odot$ estimated mass, and $0.6^{+4.6}_{-0.3}$ Gyr age.

2MASS 12373919+6526148. 2M1237 is a T6.5 dwarf with anomalously hyperactive Hα emission at $[L_{H_\alpha}/L_{bol}] \sim -4.2$ (Burgasser, Kirkpatrick, Reid, et al. 2000; Burgasser, Liebert, et al. 2002; Burgasser et al. 2003; Liebert and Burgasser 2007) with conflicting evidence of J-band variability (Burgasser, Liebert, et al. 2002; Artigau, Nadeau, and Doyon 2003). Kao et al. (2016) derived $T_{eff} = 831^{+31}_{-27}$ K, >0.028 $M_\odot$ estimated mass, and >3.4 Gyr age.

SDSS 04234858-0414035. SDSS0423 is an L6/T2 binary with 0.″16 separation (Burgasser et al. 2005; Carson et al. 2011) and strong Hα emission (EW = 3 Å) and Li I absorption (EW = 11 Å) (Kirkpatrick et al. 2008). Pineda et al. (2016) confirm Hα EW = 2.95 ± 0.3 Å and Li I EW = 11.1 ± 0.4 Å. It additionally exhibits J- and K-band but no I_c photometric variability (Enoch, Brown, and Burgasser 2003; Clarke et al. 2008; Wilson, Rajan, and Patience 2014). Kao et al. (2016) derived $T_{eff} = 1678^{+174}_{-137}$ K, $0.015^{+0.021}_{-0.006}$ $M_\odot$ estimated mass, and $0.49^{+0.62}_{-0.17}$ Gyr age.

Table 5.2: Summary of Observations

Object	Band (GHz)	Obs. Date (2013)	Obs. Block (h)	Time on Source (s)	VLA Config.	Synthesized Beam Dimensions (arcsec × arcsec)	I, V RMS (μJy)	Phase Calibrator	Flux Calibrator	Ref. Set Frequency (GHz)
2M1047	12.0–18.0	05/18	7.0	20870	BnA	$0\farcs62 \times 0\farcs50$	1.7 , 1.8	J1051+2119	3C295	14.064
SIMP0136	8.0–12.0	05/17	7.0	20870	BnA	$0\farcs66 \times 0\farcs37$	1.3 , 1.1	J0149+0555	3C48	···
2M1043	8.0–12.0	05/20	7.0	20612	BnA	$0\farcs60 \times 0\farcs33$	1.0 , 1.0	J1051+2119	3C295	11.064
2M1237	8.0–12.0	05/18	7.0	21484	BnA	$0\farcs69 \times 0\farcs43$	1.0 , 1.1	J1339+6328	3C295	8.464
SDSS0423	8.0–12.0	05/30	7.0	17234	BnA	$0\farcs68 \times 0\farcs37$	1.2 , 1.4	J0423-0120	3C147	···

Table 5.3: Comparison of Phase Calibrator Flux Densities

Object	Ref. Freq 8.464 GHz (mJy)	Ref. Freq 11.064 GHz (mJy)	Ref. Freq 14.064 GHz (mJy)	Ref. Freq 16.564 GHz (mJy)
2M1047	···	···	603.7 ± 0.4	561.1 ± 0.2
2M1043	466.4 ± 1.2	469.0 ± 1.3	···	···
2M1237	173.3 ± 1.0	185.0 ± 1.0	···	···

5.4 Observations

We observed 4 objects with previous C-band (4–8 GHz) detections spanning spectral range L7.5–T6.5 at X-band (8–12 GHz) as well as one T6.5 object with a previous X-band detection at Ku-band (12–18 GHz) with the full VLA. We used the WIDAR correlator in 3-bit observing mode for 4 GHz or 6 GHz bandwidth observations with 2s integrations in 7-hour time blocks for 35 total program hours. Observations took place during May 2015 in BnA configuration. Table 5.1 and Table 5.2 summarize target properties and observations, respectively.

5.4.1 Calibrations

For SIMP0136 and SDSS0423, we calibrated our measurement sets using standard VLA flux calibrators 3C48 and 3C147, respectively, and nearby phase calibrators. Flux calibrators were observed at the beginning and end of each observing block and interpolated. After initially processing raw measurement sets with the VLA Calibration Pipeline, we manually flagged remaining RFI. Strong time-dependent RFI resulted in ∼71 minutes of data loss near the end of the observing block for SDSS0423. Typical full-bandwidth sensitivity at BnA configuration for 7-hour observing blocks (∼5.5 hours and ∼4 hours on source) is 1.2 μJy and 2.1 μJy for X and Ku bands, respectively. Typical 3-bit observations reach an absolute flux calibration accuracy of ∼5% by bootstrapping flux densities with standard VLA flux calibrators. To correct for flux errors resulting from gain phase variation over our observing window, we alternated between target and phase calibrator integrations, with 15- and 6-minute cycle times for X and Ku bands, respectively. Our gain solutions varied slowly and smoothly over time and without any ambiguous phase wraps, suggesting that this source of error is negligible.

For 2M1047, 2M1043, and 2M1237, we observed the flux calibrator 3C295, which is typically recommended only for low-frequency observations in compact configurations. This calibrator was fully resolved at both X and Ku bands for our observations. For targets observed at X bands (2M1043 and 2M1237), we modified the VLA scripted pipeline to use A configuration 8.464 GHz and 11.064 GHz model images observed on 02/16/2016 by VLA staff to set flux levels and determine bandpass solutions. The emission from 3C295 is stable within 1% over 24–28 years for X and Ku bands (Perley and Butler 2013). Because the lobed structure of 3C295 is resolved at our observing frequencies and the VLA sky sensitivity fringes are wavelength-dependent, we expect there to be a discrepancy in flux densities bootstrapped using these different images of 3C295. To estimate the additional

uncertainty in flux densities introduced by calibrating with 3C295, we compared the flux densities of each target's phase calibrator as bootstrapped by the different model images of 3C295. We list these flux densities in Table 5.3. These comparisons suggest that the flux densities of 2M1043 and 2M1237 have an additional ∼1–7% uncertainty. We repeated the same process for our Ku band target (2M1047) but instead used model images of 3C295 at 14.064 GHz and 16.564 GHz, which we expect to introduce an additional ∼8% uncertainty.

We flagged all data from 12–12.8 GHz during the first ∼34 minutes of our target observing scans for 2M1047 due to strong RFI. After manually flagging remaining RFI, we average all of the measurements sets down in time from 2s integrations to 10s for faster processing.

5.4.2 Source Motion

We corrected the 2MASS coordinates (Skrutskie et al. 2006) of our targets using the proper motion measurements listed in Table 5.1 to obtain expected source positions. For the known binary SDSS0423, we did not correct for orbital motion because its 0.″16 orbital separation is well within the synthesized beam resolution.

5.5 Results

5.5.1 Image Detections

Table 5.4: Summary of initial imaging detections

Object	Right Ascension (hh mm ss.ss)	Declination (dd mm ss.ss)	Stokes I (μJy)	Stokes V (μJy)	Stokes I SNR (σ)
2M1047	10 47 51.78	+21 24 14.90	21.9±1.3	3.9±1.5	16.8
SIMP0136	01 36 57.86	+09 33 47.00	85.7±1.3	-23.8± 1.1	65.9
2M1043	10 43 07.44	+22 25 23.31	9.5±1.0	-4.7±1.0	9.5
2M1237	12 37 36.58	+65 26 05.70	35.0±1.0	16.9±1.2	35.0
SDSS0423	04 23 48.23	-04 14 02.15	15.4±1.2	-0.5±1.4	12.9

We produced Stokes I and Stokes V images of each object (total and circularly polarized intensities, respectively) with the CASA `clean` routine, modeling the sky emission frequency dependence with one term and using natural weighting. We searched for a point source at the proper motion-corrected coordinates of each target. For our targets calibrated with 3C295, we selected a single calibrated measurement set as a reference set, noted in Table 5.4. We performed all subsequent reduction and analysis on this reference set.

We detected each of our five targets in Stokes I, with signal-to-noise ratios (SNR)

Table 5.5: 2M1047: Pulsed and Quiescent Emission

		Pulse 1	Pulse 2	Pulse 3	Pulse 4	Pulse 5	Pulse 6	Quiescent
12–18GHz								
Stokes I[a]	(μJy)	42±14.7	58±16.8	61±9.2	53±11.4	71±11.6	41±6.9	10.4±2.2
Stokes V[a]	(μJy)	-40±14.4	23.0±10.8	-48±14.9	-21±13.6	-56±10.6	-23±6.4	0.8±1.8
SNR	(I, V)	2.9, 2.8	3.5, 2.1	6.6, 3.2	4.6, 1.5	6.1, 5.3	5.9, 3.6	4.7, 0.4
Circ. Poln[b]	(%)	$-85.3^{+40.6}_{-5.5}$	$-36.6^{+15.6}_{-30.7}$	$-77.0^{+27.4}_{-12.9}$	$-37.9^{+24.3}_{-30.1}$	$-76.8^{+16.8}_{-13.8}$	$-54.6^{+14.7}_{-21.6}$	$7.4^{+19.9}_{-17.6}$
12–13.5GHz								
Stokes I[a]	(μJy)	113±29.3	142±18.6	<28.2	<26.3	<27.0	73±12.8	25.7±3.5
Stokes V[a]	(μJy)	-131±24.0	-77±19.3	<27.1	<25.9	<26.2	-5.2±16.1	5.1±4.2
SNR	(I, V)	3.9, 5.5	7.6, 4.0	···	···	···	5.7, 0.3	7.3, 1.2
Circ. Poln[b]	(%)	(-71.1, -48.5)	$-53.3^{+13.0}_{-18.2}$	···	···	···	$-6.9^{+22.5}_{-23.9}$	$19.5^{+18.2}_{-15.9}$
13.5–15GHz								
Stokes I[a]	(μJy)	<35.0	<23.9	<26.8	<24.0	<24.1	<13.9	0.6±4.5
Stokes V[a]	(μJy)	<36.8	<22.8	<27.2	<25.3	<23.7	<13.6	3.0±4.2
SNR	(I, V)	···	···	···	···	···	···	0.1, 0.7
Circ. Poln[b]	(%)	···	···	···	···	···	···	$51.6^{+22.1}_{-101.6}$
15–16.5GHz								
Stokes I[a]	(μJy)	<25.8	<22.1	119±25.6	99±19.6	86±24.2	<12.9	21.5±3.5
Stokes V[a]	(μJy)	<25.9	<22.6	-85±23.9	-29±23.3	-63±20.9	<13.7	6.7±3.4
SNR	(I, V)	···	···	4.6, 3.6	5.1, 1.2	3.6, 3.0	···	6.1, 2.0
Circ. Poln[b]	(%)	···	···	$-68.3^{+20.6}_{-19.0}$	$-28.2^{+22.4}_{-28.3}$	$-68.0^{+24.8}_{-19.5}$	···	$30.4^{+20.0}_{-14.8}$
16.5–18GHz								
Stokes I[a]	(μJy)	<33.1	<30.1	<34.3	<30.4	112±28.5	<18.0	13±4.7
Stokes V[a]	(μJy)	<36.2	<29.6	<31.7	<33.3	-113±24.7	<17.6	3.7±5.2
SNR	(I, V)	···	···	···	···	3.9, 4.6	···	2.8, 0.7
Circ. Poln[b]	(%)	···	···	···	···	(-63.5, -27.2)	···	$25.2^{+40.2}_{-41.9}$

[a] Reported flux densities are integrated over the FWHM of the full-bandwidth 60 s resolution data. Initial point source Gaussian fits with floating peak location and semi-major and semi-minor axes are performed on all pulses. For consistency, we select the highest signal-to-noise pulse as a benchmark and perform a second iteration of fits while holding the benchmark peak location and semi-major and semi-minor axes constant. Fixing fit parameters can result in overestimated uncertainties on the integrated and peak flux densities, so we report the rms image noise as the uncertainty.

[b] Reported polarization fractions are highest-likelihood values, given the measured Stokes I and Stokes V flux densities. Uncertainties reflect the upper and lower bounds of the 68.27% confidence intervals. Negative values indicate left circular polarization, and positive values indicate right circular polarization. Lower-bound 68.27% and 99.73% confidence intervals are given for objects with 100% circular polarization.

ranging from 9.5–65.9 in the mean Stokes I flux density. Table 5.4 gives the measured mean flux density and rms noise of each source. Flux densities and source positions were determined by fitting an elliptical Gaussian point source to the cleaned image of each object at its predicted coordinates using the CASA task `imfit`.

5.5.2 Timeseries Pulse Detections & Magnetic Field Strengths

We used the `clean` routine to model all sources within a primary beam of our targets and subtract these sources from the UV visibility data using the CASA `uvsub` routine to prevent sidelobe contamination in our targets' timeseries. We then added phase delays to our visibility data using the CASA `fixvis` routine to place our targets at the phase center.

We checked all targets for highly circularly polarized flux density pulses to confirm the presence of ECM emission. Rather than searching for pulsed emission in Stokes

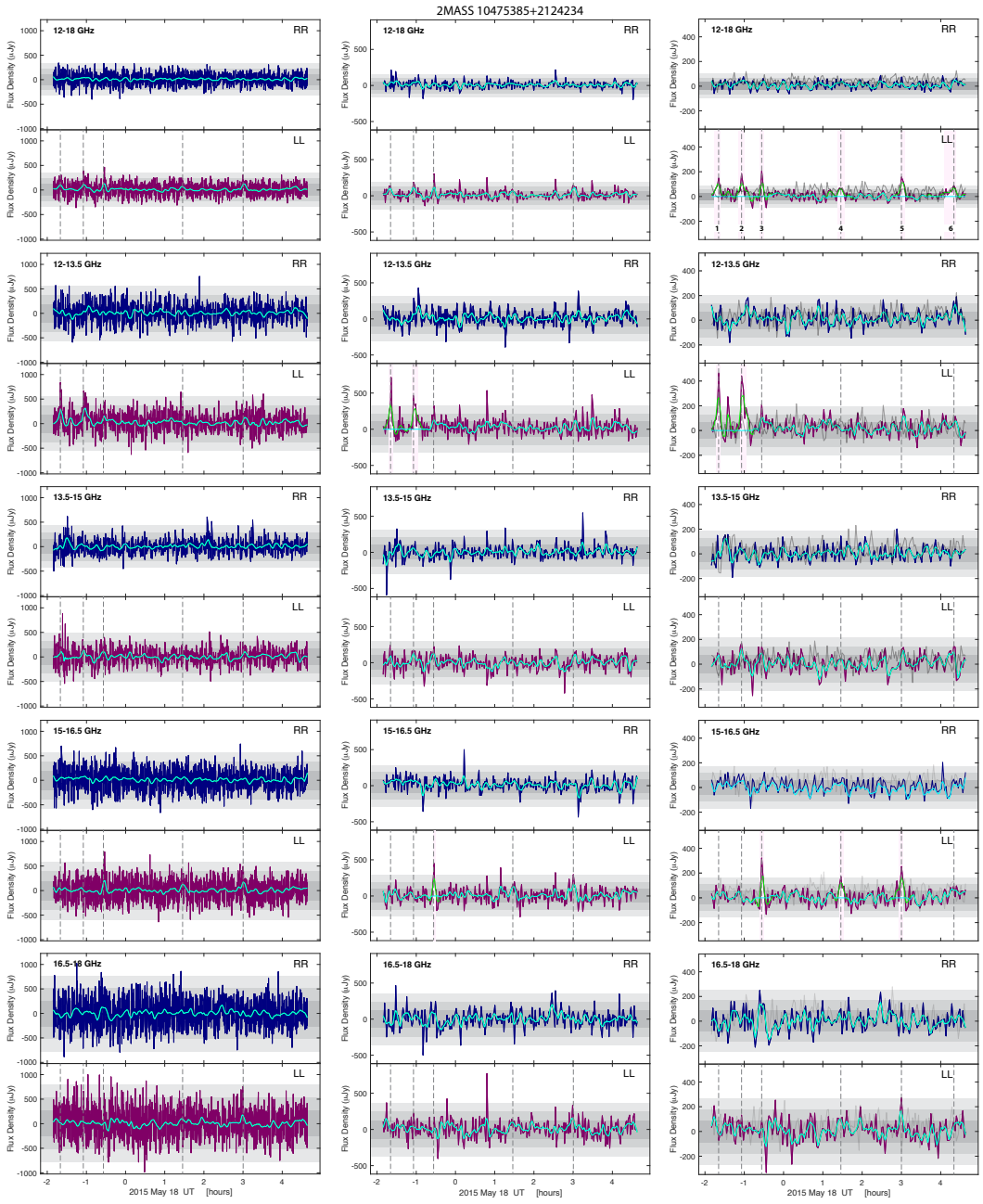

Figure 5.1: 10s, 60s, and 120s timeseries of rr- and ll-correlated (blue and maroon, respectively) flux densities for 2M1047 showing the emergence of apparent pulses at 12–13.5 GHz and 15–16.5 GHz. Green lines are smoothed timeseries used for identifying pulse candidates and overlaid cyan lines show removed pulse candidates for calculating rms noise and imaging quiescent emission. Light blue and pink bars highlight pulses verified with imaging, and grey dashed lines are aligned to 12–13.5 GHz and 15–16.5 GHz pulse peaks. Grey regions indicates 1σ, 2σ, and 3σ rms noise. Comparison timeseries of a nearby object are plotted in dark grey in the 120s column.

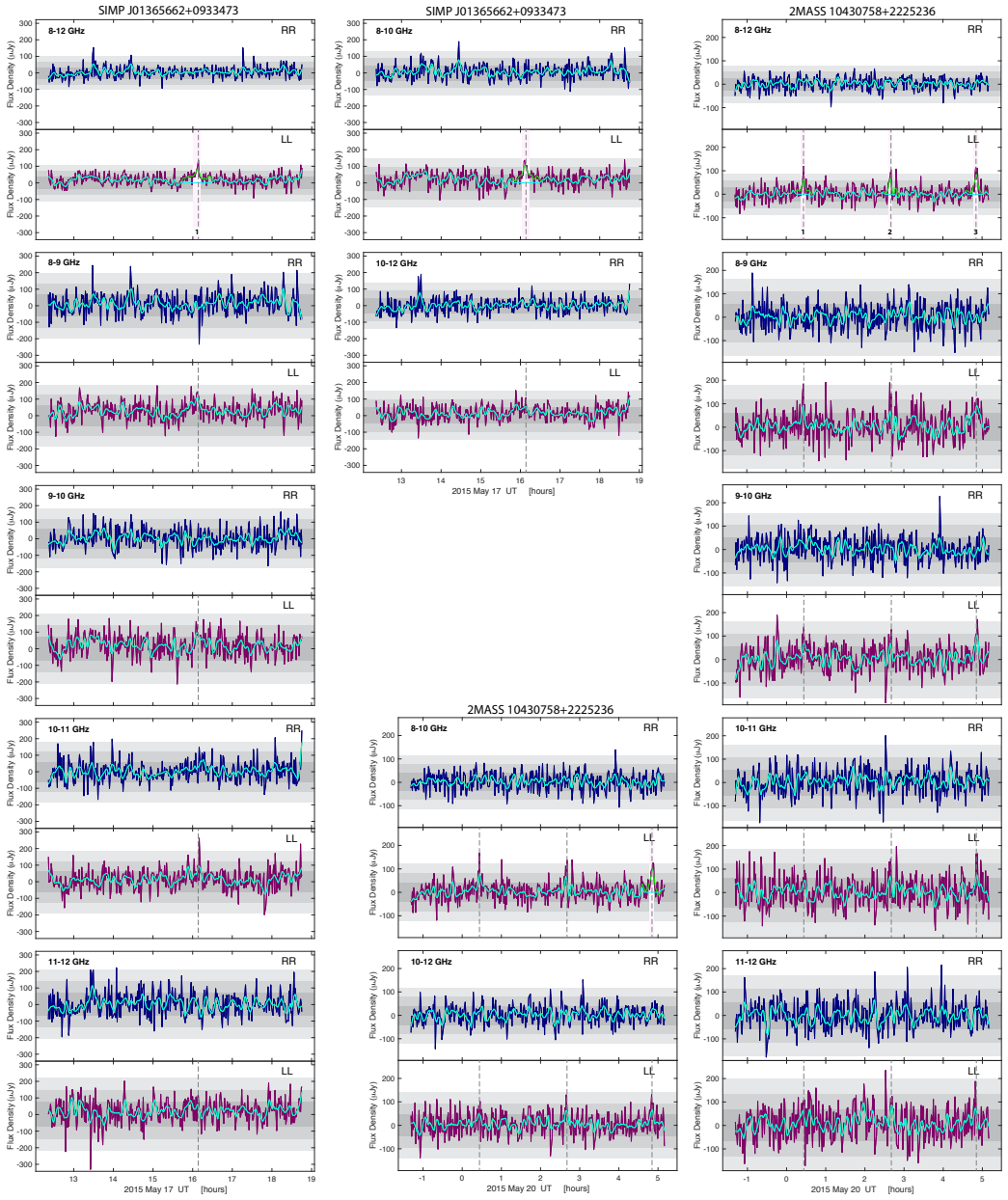

Figure 5.2: 60s timeseries of rr- and ll-correlated (blue and maroon, respectively) flux densities for SIMP0136 and 2M1043. Green lines are smoothed timeseries used for identifying pulse candidates and overlaid cyan lines show removed pulse candidates for calculating rms noise and imaging quiescent emission. Light blue and pink bars highlight pulses verified with imaging, and grey dashed lines are aligned to pulse peaks. Grey regions indicates 1σ, 2σ, and 3σ rms noise.

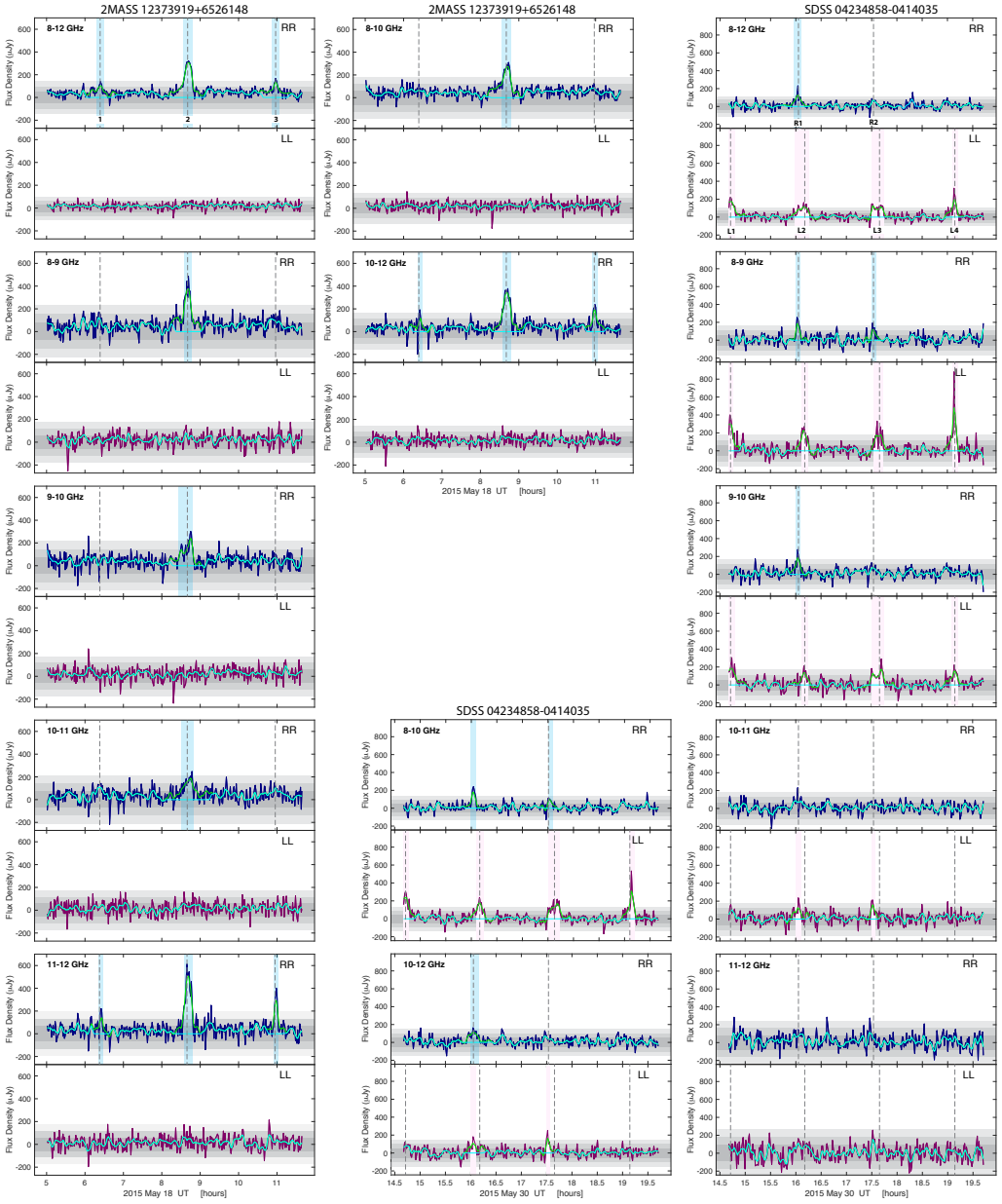

Figure 5.3: 60s timeseries of rr- and ll-correlated (blue and maroon, respectively) flux densities for 2M1237 and SDSS0423. Green lines are smoothed timeseries used for identifying pulse candidates and overlaid cyan lines show removed pulse candidates for calculating rms noise and imaging quiescent emission. Light blue and pink bars highlight pulses verified with imaging, and grey dashed lines are aligned to pulse peaks. Grey regions indicates 1σ, 2σ, and 3σ rms noise.

Table 5.6: SIMP0136 & 2M1043: Pulsed and Quiescent Emission

		SIMP0136		2M1043			
		Pulse 1	Quiescent	Pulse 1	Pulse 2	Pulse 3	Quiescent
8–12 GHz							
Stokes I[a]	(μJy)	51.1±5.7	12.4±1.22	65±5.3	79±6.9	58±5.8	5.2±1.2
Stokes V[a]	(μJy)	-39±6.5	-8.9±1.2	-59±6.5	-21.7±5.3	-37±6.4	-0.3±1.0
SNR	(I, V)	9.0, 6.0	10.2, 7.4	12.3, 9.1	11.4, 4.1	10.0, 5.8	4.3, 0.3
Circ. Poln[b]	(%)	$-75.4^{+13.7}_{-13.6}$	$-71.1^{+10.3}_{-13.3}$	$-90.2^{+12.8}_{-5.4}$	$-27.3^{+6.6}_{-7.9}$	$-63.2^{+11.1}_{-14.5}$	$-5.5^{+20.1}_{-22.2}$
8–10 GHz							
Stokes I[a]	(μJy)	64.1±4.9	20.9±1.8	76±8.9	66±8.0	57.6±8.8	5.2±1.5
Stokes V[a]	(μJy)	-43.0±6.4	-8.1±1.8	-59±7.8	-37±10.1	-50.9±9.2	2.8±1.3
SNR	(I, V)	13.1, 6.7	11.6, 4.5	8.5, -7.6	8.2, 3.7	6.5, 5.5	3.5, 2.2
Circ. Poln[b]	(%)	$-66.7^{+10.2}_{-12.4}$	$-38.5^{+8.5}_{-10.2}$	$-76.6^{+11.6}_{-13.0}$	$-55.2^{+14.8}_{-18.8}$	$-86.4^{+20.2}_{-7.4}$	$49.8^{+29.2}_{-22.9}$
10–12 GHz							
Stokes I[a]	(μJy)	38.3±8.5	7.2±2.1	33±7.2	82±11.7	55±8.8	2.8±1.8
Stokes V[a]	(μJy)	-24.8±9.0	-8.3±1.5	<10.8	-14±10.7	-29±8.6	-2.6±1.3
SNR	(I, V)	4.5, 2.8	3.4, 5.5	4.6, ···	7.0, 1.3	6.2, 3.4	1.6, 2.0
Circ. Poln[b]	(%)	$-61.8^{+23.2}_{-22.6}$	(-69.9, -38.0)	···	$-16.7^{+12.6}_{-14.9}$	$-51.4^{+14.6}_{-21.3}$	$-68.7^{+46.1}_{-17.3}$
8–9 GHz							
Stokes I[a]	(μJy)	71±14.6	18.7±2.2	60±14.6	53±13.5	57±12.7	7.5±2.4
Stokes V[a]	(μJy)	-62±10.7	-6.9±2.0	-80±16.0	-33±15.3	-47.3±10.2	2.6±1.9
SNR	(I, V)	4.9, 5.8	8.5, 3.4	4.1, 5.0	3.9, 2.2	4.5, 4.6	3.1, 1.4
Circ. Poln[b]	(%)	$-83.8^{+19.6}_{-9.3}$	$-36.4^{+10.2}_{-13.4}$	(-73.0, -35.6)	$-58.5^{+28.6}_{-24.6}$	$-79.2^{+21.1}_{-12.4}$	$31.5^{+34.6}_{-23.1}$
9–10 GHz							
Stokes I[a]	(μJy)	36.3±12.3	14.0±2.4	87±12.1	74±13.2	61±11.7	3.9±1.9
Stokes V[a]	(μJy)	-29.8±12.2	-9.8±2.1	-52±14.3	-52±16.4	-53±15.0	2.2±2.2
SNR	(I, V)	3.0, 2.4	5.8, 4.7	7.2, 3.6	5.6, 3.2	5.2, 3.5	2.1, 1.0
Circ. Poln[b]	(%)	$-73.9^{+36.4}_{-14.4}$	$-68.0^{+15.4}_{-18.3}$	$-58.6^{+15.9}_{-20.0}$	$-68.1^{+22.9}_{-18.7}$	$-83.8^{+29.5}_{-8.0}$	$46.0^{+30.8}_{-61.4}$
10–11 GHz							
Stokes I[a]	(μJy)	38.3±12.0	4.2±2.6	37±16.2	66±15.7	<13.8	2.2±2.2
Stokes V[a]	(μJy)	-28.1±12.0	-6.6±1.8	-34±15.2	-18±18.4	<14.3	0.6±1.9
SNR	(I, V)	3.2, 2.3	1.6, 3.7	2.3, 2.2	4.2, 1.0	···	1.0, 0.3
Circ. Poln[b]	(%)	$-67.0^{+32.4}_{-19.6}$	(-58.3, -0.5)	$-78.0^{+45.3}_{-10.4}$	$-25.8^{+27.1}_{-32.8}$	···	$15.3^{+49.7}_{-65.8}$
11–12 GHz							
Stokes I[a]	(μJy)	<14.6	11.2±3.1	42±15.6	91±17.6	<15.4	7.0±2.6
Stokes V[a]	(μJy)	<14.7	-11.3±2.9	-33±17.2	-8±15.8	<14.6	-7.7±2.2
SNR	(I, V)	···	3.6, 3.9	2.7, 1.9	5.2, 0.5	···	2.7, 3.5
Circ. Poln[b]	(%)	···	(-59.0, -16.4)	$-69.4^{+44.5}_{-16.7}$	$-8.5^{+17.5}_{-19.7}$	···	(-55.3, -5.0)

[a] Reported flux densities are integrated over the FWHM of the full-bandwidth 60 s resolution data. Initial point source Gaussian fits with floating peak location and semi-major and semi-minor axes are performed on all pulses. For consistency, we select the highest signal-to-noise pulse as a benchmark and perform a second iteration of fits while holding the benchmark peak location and semi-major and semi-minor axes constant. Fixing fit parameters can result in overestimated uncertainties on the integrated and peak flux densities, so we report the rms image noise as the uncertainty.

[b] Reported polarization fractions are highest-likelihood values, given the measured Stokes I and Stokes V flux densities. Uncertainties reflect the upper and lower bounds of the 68.27% confidence intervals. Negative values indicate left circular polarization, and positive values indicate right circular polarization. Lower-bound 68.27% and 99.73% confidence intervals are given for objects with 100% circular polarization.

Table 5.7: 2M1237: Pulsed and Quiescent Emission

		Pulse 1	Pulse 2	Pulse	Quiescent
8–12GHz					
Stokes I[a]	(μJy)	39.1±4.6	161±6.2	65.0±4.5	27.2±1.4
Stokes V[a]	(μJy)	34±5.9	124.2±5.3	47±4.4	11.0±1.4
SNR	(I, V)	8.5,5.8	26.0, 23.4	14.4, 10.7	19.4, 7.9
Circ. Poln[b]	(%)	$85.8^{+7.9}_{-18.3}$	$77.0^{+4.8}_{-4.1}$	$72.0^{+9.5}_{-7.5}$	$40.3^{+5.9}_{-5.3}$
8–10GHz					
Stokes I[a]	(μJy)	36±8.6	166±9.0	39.1±8.3	36.5±1.8
Stokes V[a]	(μJy)	28±8.7	133.9±7.8	10.4±8.0	10.8±1.7
SNR	(I, V)	4.2, 3.2	18.4, 17.2	4.7, 1.3	20.3, 6.4
Circ. Poln[b]	(%)	$73.6^{+15.5}_{-26.2}$	$80.4^{+7.0}_{-5.8}$	$25.4^{+26.2}_{-19.2}$	$29.5^{+5.1}_{-4.7}$
10–12GHz					
Stokes I[a]	(μJy)	56±8.4	213±9.3	76.5±9.5	28.9±1.8
Stokes V[a]	(μJy)	34±7.6	176±9.5	62.5±7.9	14.0±1.8
SNR	(I, V)	6.7, 4.5	22.9, 18.5	8.1, 7.9	16.1, 7.8
Circ. Poln[b]	(%)	$59.4^{+19.2}_{-13.2}$	$82.5^{+6.2}_{-5.3}$	$80.5^{+11.4}_{-12.5}$	$48.2^{+7.5}_{-6.4}$
8–9GHz					
Stokes I[a]	(μJy)	37.2±12.3	206±11.2	47.6±11.2	35.3±2.6
Stokes V[a]	(μJy)	50.2±13.2	149±8.8	11.9±9.8	12.8±2.3
SNR	(I, V)	3.0, 3.8	18.4, 17.0	4.2, 1.2	13.6, 5.6
Circ. Poln[b]	(%)	(62.6, 11.1)	$72.1^{+6.5}_{-5.2}$	$23.7^{+27.3}_{-19.2}$	$36.1^{+7.7}_{-6.6}$
9–10GHz					
Stokes I[a]	(μJy)	43±12.0	99±12.1	<12.0	28.0±2.5
Stokes V[a]	(μJy)	13±12.4	98±9.4	<11.6	6.0±2.2
SNR	(I, V)	3.6, 1.0	8.2, 10.4	···	11.2, 2.7
Circ. Poln[b]	(%)	$28.0^{+34.7}_{-27.9}$	(80.6, 61.0)	···	$21.2^{+8.7}_{-7.7}$
10–11GHz					
Stokes I[a]	(μJy)	68±12.7	94±11.1	47±11.7	22.0±2.5
Stokes V[a]	(μJy)	35±9.7	75±9.9	39±10.5	15.5±1.9
SNR	(I, V)	5.4, 3.6	8.5, 7.6	4.0, 3.7	8.8, 8.2
Circ. Poln[b]	(%)	$49.8^{+22.2}_{-13.1}$	$78.7^{+12.2}_{-12.2}$	$78.2^{+12.5}_{-25.4}$	$69.6^{+13.8}_{-9.6}$
11-12GHz					
Stokes I[a]	(μJy)	38±11.1	284±11.7	166±11.8	22.3±2.7
Stokes V[a]	(μJy)	48±11.2	223±9.9	142±13.2	26.0±2.3
SNR	(I, V)	3.4, 4.3	24.3, 22.5	14.1, 10.8	8.3 , 11.3
Circ. Poln[b]	(%)	(66.3, 23.5)	$78.4^{+5.2}_{-4.4}$	$85.1^{+8.2}_{-9.4}$	(87.6, 69.8)

[a] Reported flux densities are integrated over the FWHM of the full-bandwidth 60 s resolution data. Initial point source Gaussian fits with floating peak location and semi-major and semi-minor axes are performed on all pulses. For consistency, we select the highest signal-to-noise pulse as a benchmark and perform a second iteration of fits while holding the benchmark peak location and semi-major and semi-minor axes constant. Fixing fit parameters can result in overestimated uncertainties on the integrated and peak flux densities, so we report the rms image noise as the uncertainty.

[b] Reported polarization fractions are highest-likelihood values, given the measured Stokes I and Stokes V flux densities. Uncertainties reflect the upper and lower bounds of the 68.27% confidence intervals. Negative values indicate left circular polarization, and positive values indicate right circular polarization. Lower-bound 68.27% and 99.73% confidence intervals are given for objects with 100% circular polarization.

Table 5.8: SDSS0423: Pulsed and Quiescent Emission

		Pulse R1	Pulse R2	Pulse L1	Pulse L2	Pulse L3	Pulse L4	Quiescent
8–12GHz								
Stokes I[a]	(μJy)	84.0±9.4	94.0±9.7	100±7.9	58.7±5.8	64.4±5.2	100±8.9	<1.7
Stokes V[a]	(μJy)	25±8.2	-3.8±8.3	-103±6.0	-50.0±6.6	-30.9±4.7	-118±8.9	<1.9
SNR	(I, V)	8.9, 3.0	9.7, 0.5	12.7, 17.2	10.1, 7.6	12.4, 6.6	11.2, 13.3	···
Circ. Poln[b]	(%)	$29.4^{+11.7}_{-9.4}$	$-4.0^{+8.8}_{-9.1}$	(-89.0, -75.5)	$-84.4^{+13.4}_{-9.0}$	$-47.7^{+7.4}_{-9.3}$	(-91.2, -76.6)	···
8–10GHz								
Stokes I[a]	(μJy)	91±11.6	104±9.1	113±10.2	70±9.4	80.5±5.2	151±12.3	<2.2
Stokes V[a]	(μJy)	46±10.1	28±10.9	-121.6±10.6	-65.4±10.0	-45.4±5.7	-150±15.0	<2.2
SNR	(I, V)	7.8, 4.6	11.4, 2.6	11.1, 11.5	7.5, 6.5	15.5, 8.0	12.3, 10.0	···
Circ. Poln[b]	(%)	$49.8^{+15.7}_{-10.8}$	$26.7^{+11.5}_{-10.3}$	(-87.0, -69.8)	$-91.8^{+19.8}_{-3.4}$	$-56.2^{+7.3}_{-8.8}$	$-98.7^{+15.7}_{1.2}$	···
10–12GHz								
Stokes I[a]	(μJy)	82±13.9	57±15.9	76.8±14.4	48±10.0	64±11.6	<13.9	<2.4
Stokes V[a]	(μJy)	-7±13.5	-26±12.6	-37±11.9	4.3±8.5	-33±8.2	<15.3	<2.5
SNR	(I, V)	5.9, 0.5	3.6, 2.1	5.3, 3.1	4.8, 0.5	5.5, 4.0	···	···
Circ. Poln[b]	(%)	$-8.3^{+16.5}_{-18.2}$	$-42.4^{+19.4}_{-30.7}$	$-46.6^{+14.1}_{-23.0}$	$8.6^{+20.4}_{-18.0}$	$-49.9^{+11.8}_{-21.1}$	···	···
8–9GHz								
Stokes I[a]	(μJy)	64±16	127.0±10.2	114.6±17.1	70±12.6	92±7.6	221±18.6	<2.8
Stokes V[a]	(μJy)	69±15.4	25.0±13.7	-140.0±16.1	-80±12.5	-49±9.8	-192±20.3	<2.8
SNR	(I, V)	4.0, 4.5	12.5, 1.8	7.5, 12.7	5.6, 6.4	12.1, 5.0	11.9, 9.5	···
Circ. Poln[b]	(%)	(65.1, 26.7)	$19.6^{+11.4}_{-10.6}$	(-91.7, -77.0)	(76.8, -48.2)	$-52.9^{+10.6}_{-12.8}$	$-86.3^{+11.2}_{-7.9}$	···
9–10GHz								
Stokes I[a]	(μJy)	150±18.7	101±14.8	91±14.6	65±11.8	67±8.2	88±19.7	<2.9
Stokes V[a]	(μJy)	39±15.5	33±14.8	-107±14.0	-57±12.0	-42±8.7	-101±20.4	<2.9
SNR	(I, V)	8.0, 2.5	6.8, 2.2	6.2, 7.6	5.5, 4.7	8.2, 4.8	4.5, 5.0	···
Circ. Poln[b]	(%)	$25.6^{+12.4}_{-9.9}$	$32.0^{+18.2}_{-13.8}$	(-81.4, -56.7)	$-84.9^{+22.8}_{-8.1}$	$-61.8^{+12.8}_{-17.2}$	(-70.0, -34.0)	···
10–11GHz								
Stokes I[a]	(μJy)	79±17.5	53±19.9	80±16.0	83±17.9	61±10.3	< 21.9	<2.8
Stokes V[a]	(μJy)	11±20.6	-20±16.5	-24±16.1	13±16.5	-47±10.0	< 20.1	<2.8
SNR	(I, V)	4.5, 0.5	2.7, 1.2	5.0, 1.5	4.6, 0.8	5.9, 4.7	···	···
Circ. Poln[b]	(%)	$13.3^{+84.0}_{-95.6}$	$-33.2^{+123.4}_{-66.5}$	$-28.8^{+64.8}_{-69.2}$	$15.0^{+79.5}_{-73.3}$	$-74.9^{+49.2}_{-25.0}$	···	···
11-12GHz								
Stokes I[a]	(μJy)	<23.8	<22.0	<29.4	<17.1	<13.3	<25.1	<4.3
Stokes V[a]	(μJy)	<24.2	<21.9	<32.4	<17.1	<12.7	<25.5	<5.4
SNR	(I, V)	···	···	···	···	···	···	···
Circ. Poln[b]	(%)	···	···	···	···	···	···	···

[a] Reported flux densities are integrated over the FWHM of the full-bandwidth 60 s resolution data. Initial point source Gaussian fits with floating peak location and semi-major and semi-minor axes are performed on all pulses. For consistency, we select the highest signal-to-noise pulse as a benchmark and perform a second iteration of fits while holding the benchmark peak location and semi-major and semi-minor axes constant. Fixing fit parameters can result in overestimated uncertainties on the integrated and peak flux densities, so we report the rms image noise as the uncertainty.

[b] Reported polarization fractions are highest-likelihood values, given the measured Stokes I and Stokes V flux densities. Uncertainties reflect the upper and lower bounds of the 68.27% confidence intervals. Negative values indicate left circular polarization, and positive values indicate right circular polarization. Lower-bound 68.27% and 99.73% confidence intervals are given for objects with 100% circular polarization.

I and V, we elected to search for pulses in the rr and ll correlations (right- and left-circularly polarized, respectively), where signal to noise is a factor of $\sqrt{2}$ higher in cases where the pulsed emission is 100% circularly polarized, as is expected in an ideal case of ECM emission.

Using the CASA plotting routine `plotms` to export the real UV visibilities averaged across all baselines, channels, and spectral windows of the rr and ll correlations at 10s, 60s, and 120s time resolutions, we created rr and ll timeseries for all X-band targets at 8–9 GHz, 9–10 GHz, 10–11 GHz, 11-12 GHz, 8–10 GHz, 10–12 GHz, and 8–12 GHz bandwidths to check for frequency-dependent ECM emission cutoff. We repeat the same procedure for 2M1047 but divide the total bandwidth into 12–13.5 GHz, 13.5–15 GHz, 15–16.5 GHz, 16.5–18 GHz, 12–15 GHz, 15–18 GHz, and 12–18 GHz. Figures 5.1, 5.2, and 5.3 show the timeseries for each object.

We identify pulses using the following method: we smooth each timeseries with a locally weighted first degree polynomial regression (LOESS) and a smoothing window of 2.5% of the on-target time to prevent anomalous noise spikes, typically very narrow with ~single time resolution element widths, from erroneously being identified as a pulse while also preventing the smearing out of slightly wider legitimate pulses. We then identify 2σ outlier peaks in the smoothed timeseries and measure the full width half maximum (FWHM) of the smoothed pulse, where we use the rms of the timeseries as a proxy for any quiescent emission. In reality, these peaks lie above twice the quiescent emission, since the rms includes the peaks. Approximating each pulse as Gaussian, we define the full width of each pulse as three times the FWHM and remove each pulse from the raw timeseries. These initial steps remove the strongest pulses present in the timeseries that may cause weaker pulses from being automatically identified. Finally, we repeat the process once more to identify any other pulse candidates. Because sensitivity can be a concern at narrow time resolutions and bandwidths in the timeseries, we elected to conservatively set the detection threshold for this second iteration at 2σ and separately verify the pulses by imaging each candidate pulse in Stokes I and V and comparing flux densities with that of the non-pulsed (quiescent) emission.

Highly circularly polarized pulses are clearly evident in the 10s, 60s, and 120s sub-band timeseries for 2M1047, 2M1237, and SDSS0423. For 2M1043, pulses do not become clearly evident until the data are averaged across the full 8–12 GHz bandwidth. In contrast, SIMP0136 appears to have broadly variable radio emission with a single broad peak that is persistent across 60s and 120s sub-band timeseries.

Infrared cloud variability studies of SIMP0136 suggest that its rotation period is ~2.4 hr. This *a priori* knowledge of the expected pulse periodicity allows us to search for pulses at expected occurrence times in our observing block. A pulse occurring before the above-noted timeseries peak would have directly coincided with a phase calibrator observation and thus possibly preventing its detection. A pulse occurring after would have taken place near the middle of the target integration block, when phase errors would be greatest and may possibly smear out flux from a pulse. To check for the effects of phase errors on flux densities, we imaged a bright nearby object at 01h36m47.63s +09d34m4.25s and well within the ~4.5 arcmin primary beam during 'edge' observing scans directly adjacent to a phase calibration scan and 'middle' scans that are sandwiched by the edge scans and therefore likely to suffer from the worst phase calibration errors. We measured only a $3.2 \pm 1.8\%$ decrease in flux, suggesting that phase calibration errors cannot account for a possible missing pulse.

One of the 12–13.5 GHz pulses for 2M1047 occurs during the time range when strong RFI caused all 12–12.8 GHz data to be flagged, which affects noise properties. As a check, we additionally create timeseries for a nearby object at 10h47m54.95s +21d24m13.40s and search for correlated variability, which we include in the 120s 2M1047 timeseries figures. This comparison object does not exhibit any evidence of highly circularly polarized pulses at any of the frequencies or timestamps associated with the pulses detected for 2M1047.

We confirm pulses with Stokes I and V by imaging over the 60s FWHM of each pulse and measuring integrated Stokes I and Stokes V flux densities using the CASA routine `imfit` at the expected locations of our targets and list measurements for only the pulses with unambiguous imaging along with rms noise limits for the rest. We calculate the highest likelihood percent circular polarization, where negative and positive percentages correspond to left and right circular polarization, respectively. We report uncertainties that correspond to the upper and lower limits of the 68.27% confidence interval and record the evolution of pulse flux densities across sub-bands in Table 5.5 (2M1047), Table 5.6 (SIMP0136 & 2M1043), Table 5.7 (2M1237), and Table 5.8 (SDSS0423). Some pulses appear to have Stokes V fluxes that are higher than the Stokes I fluxes, which is not physically possible. However, these anomalous excess flux densities are all within the rms noise. For objects with 100% circular polarization, we give the lower-bounds of the 68.27% and 99.73% confidence intervals on the circular polarization.

Table 5.9: Periodogram Results

Object	Lomb-Scargle (hr)	Plavchan (hr)	BLS (hr)	Adopted [a] (hr)
2M1047	$0.59^{+0.02}_{-0.02}$	$1.78^{+0.07}_{-0.06}$	$1.77^{+0.05}_{-0.05}$	$1.78^{+0.07}_{-0.06}$
SIMP0136	$2.33^{+0.43}_{-0.32}$	$2.88^{+0.34}_{-0.27}$	$2.74^{+0.80}_{-0.50}$	$2.88^{+0.34}_{-0.27}$
2M1043	$2.36^{+0.42}_{-0.31}$	$2.19^{+0.15}_{-0.12}$	$2.21^{+0.14}_{-0.13}$	$2.21^{+0.14}_{-0.13}$
2M1237	$2.21^{+0.59}_{-0.39}$	$2.28^{+0.10}_{-0.09}$	$2.28^{+0.13}_{-0.12}$	$2.28^{+0.10}_{-0.09}$
SDSS0423	$1.44^{+0.19}_{-0.15}$	$1.49^{+0.11}_{-0.10}$	$1.47^{+0.13}_{-0.11}$	$1.47^{+0.13}_{-0.11}$

[a] Adopted periods correspond to the periodogram-returned period for each object that resulted in the phase-folded timeseries with the most visual agreement in pulse overlaps.

We additionally measure quiescent emission by removing the full width of each pulse across the entire 4- or 6-GHz bandwidth from our data and imaging the remaining emission, shown in Figure 5.4 and Figure 5.5. Curiously, SDSS0423 does not appear to have any detectable quiescent emission above 1.7 μJy for the full 8–12 GHz bandwidth, while the quiescent emission from SIMP0136 is unexpectedly highly circularly polarized at ~70% We report the characteristics of the pulsed and quiescent emission in Tables 5.5, 5.6, 5.7, and 5.8.

5.5.3 Rotation Period Measurements

Magnetic dynamos act essentially by converting available energy into magnetic energy. While the Christensen, Holzwarth, and Reiners (2009), hereafter C09, model explored a link between convected and magnetic energies, another potential source of energy is the kinetic energy provided by rotation. To that end, efforts have long been made to understand the effects of rotation on dynamo activity, including comparing magnetic activity tracers such as Hα and X-ray emission to rotation rates or Rossby numbers (Pallavicini et al. 1981; Soderblom et al. 1993; Stauffer et al. 1994; Delfosse et al. 1998; Pizzolato et al. 2003; Reiners, Basri, and Browning 2009; McLean, Berger, and Reiners 2012). However, the absence of hot coronae in the coolest brown dwarfs and the possible divergence of Hα drivers between hotter M dwarfs and the coolest L and T dwarfs make comparing direct magnetic field measurements to rotation rates particularly valuable in the ultracool dwarf regime. A combination of field-strength dependent emission frequencies and rotational modulation allow aurorally pulsing radio brown dwarfs to probe rotationally dependent magnetism.

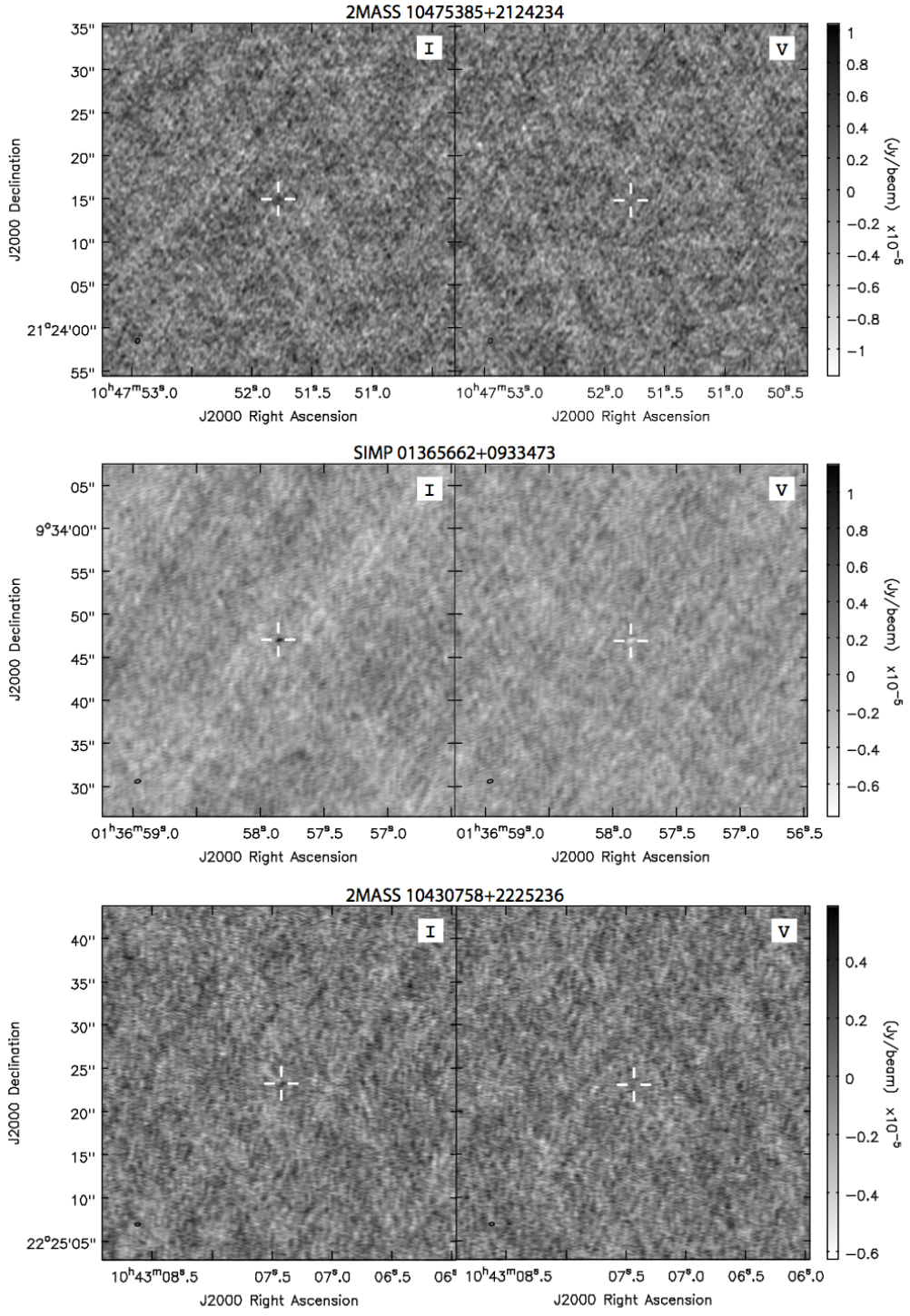

Figure 5.4: 12–18 GHz Stokes I and Stokes V images of quiescent emission for 2M1047 and 8–12 GHz Stokes I and Stokes V images of quiescent emission for SIMP0136 and 2M1043.

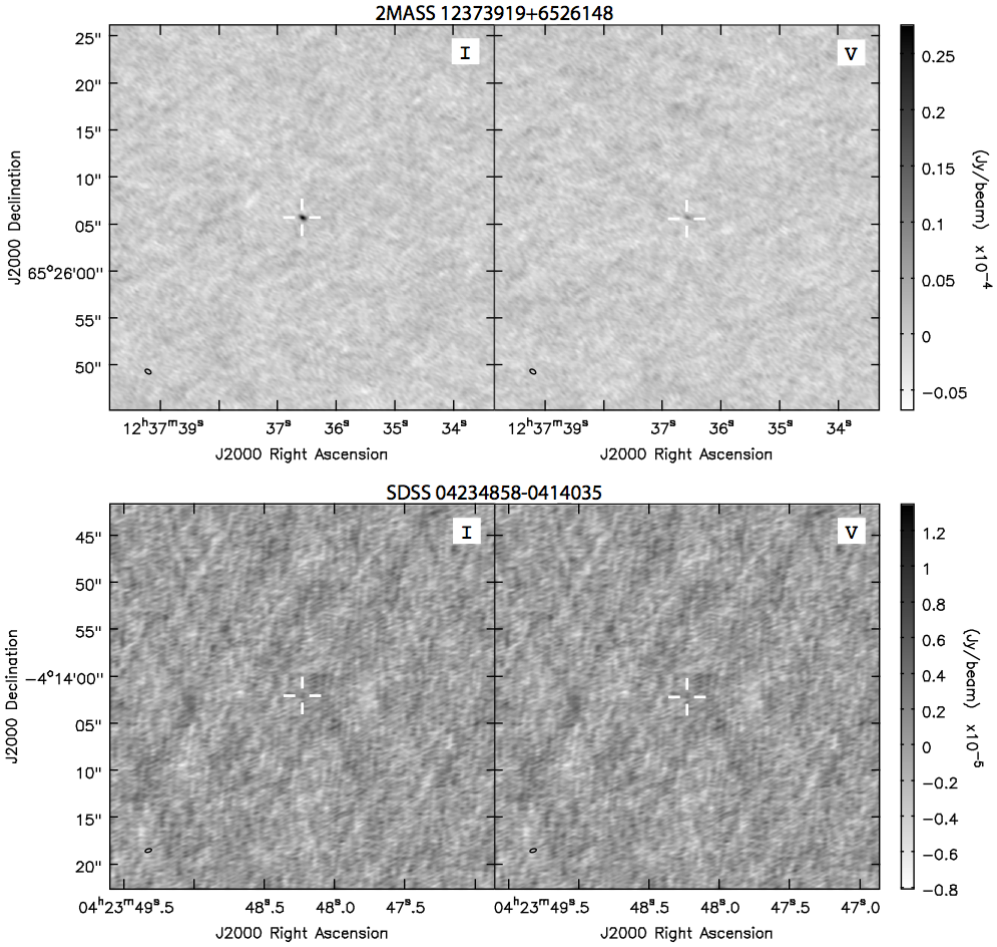

Figure 5.5: 8–12 GHz Stokes I and Stokes V images of quiescent emission for 2M1237 and SDSS0423. No quiescent emission is detectable from SDSS0423.

To date, all pulsing radio brown dwarfs with rotation period measurements have reported rotational periods between 1.77 and 3.89 hours (Pineda 2016, and references therein). If this trend continues to hold true for our targets, the long durations of our observing blocks present us with the opportunity to measure rotation periods using auroral pulse timing. Indeed, a visual inspection of timeseries suggest coverage of multiple rotation periods for at least SDSS0423, 2M1237, and 2M1043.

Recent efforts by Williams and Berger (2015) and Route and Wolszczan (2016) attempted to measure rotation periods for the pulsing brown dwarfs 2M1047, WISEPC J112254.73+255021.5 (T6), and TVLM 513-46546 (M9). These authors use a variety of methods to evaluate pulse periodicities, including the phase dispersion minimization technique (PDM, Stellingwerf 1978), a Levenberg-Marquardt algorithm minimizing a measure of the dimensionless separation between a time t and

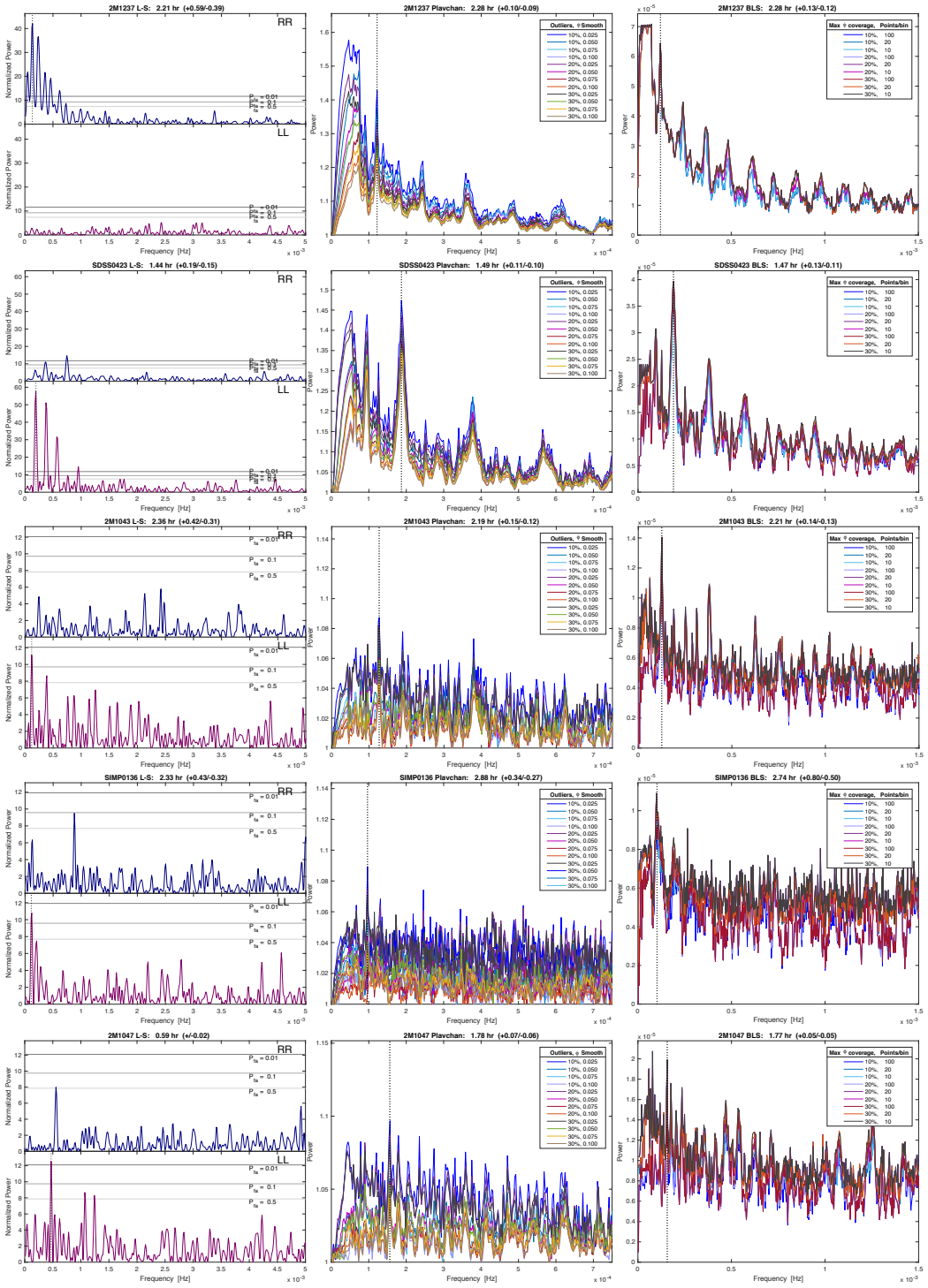

Figure 5.6: From left to right: Lomb-Scargle (L-S), Plavchan, and Box-fitting Least Squares (BLS) periodograms. Relative powers of peaks between RR and LL timeseries are shown for L-S periodogram, and grey horizontal lines denote power thresholds for 0.5, 0.1, and 0.01 false alarm probabilities. Plavchan and BLS periodograms are for timeseries corresponding to correlations with strongest L-S peaks. Vertical dotted lines correspond to adopted period for that algorithm.

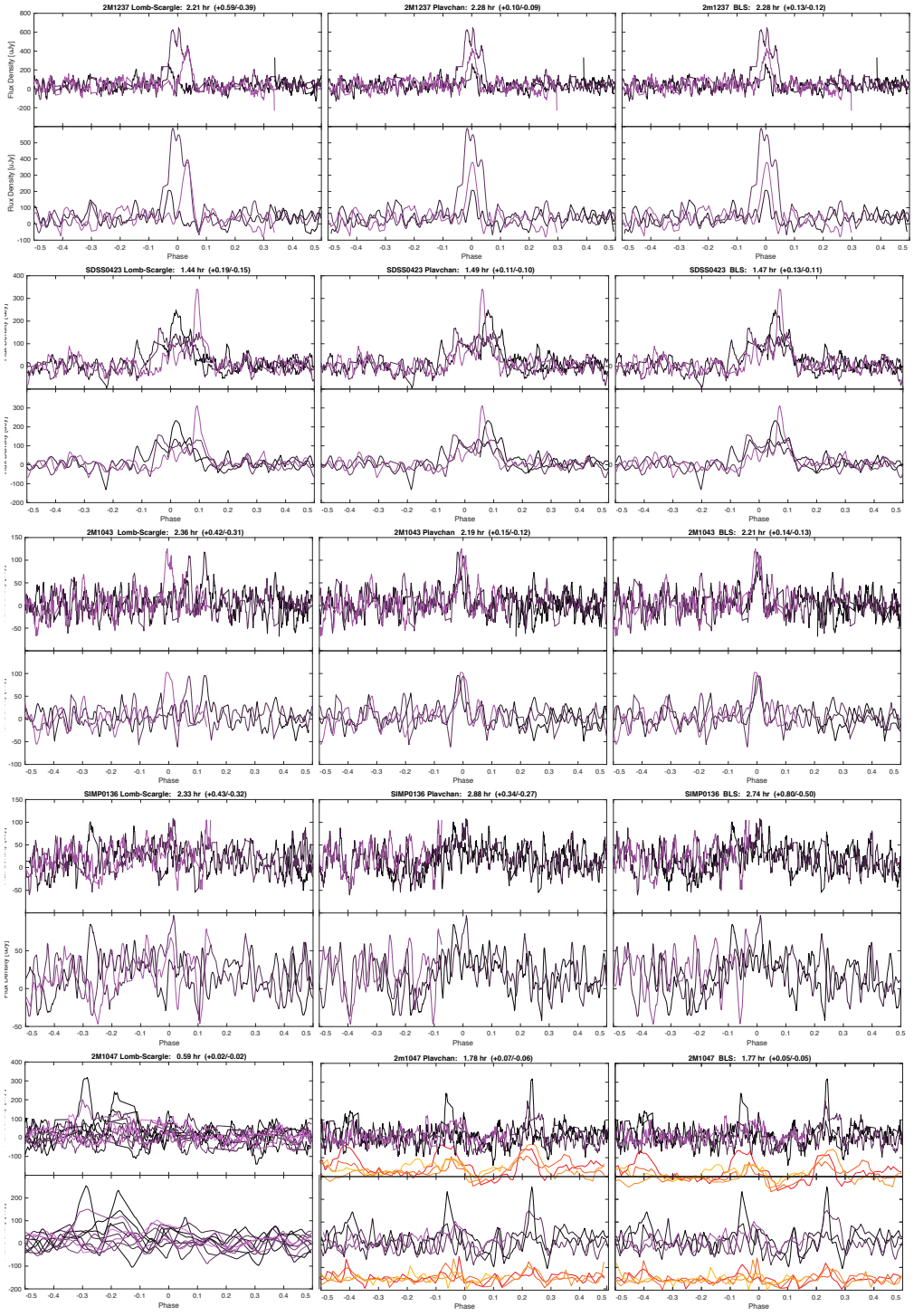

Figure 5.7: From left to right: Phase-folded 10s timeseries using periods from Lomb-Scargle (L-S), Plavchan, and Box-fitting Least Squares (BLS) periodograms. Top panels are raw data, bottom panels are smoothed data. 60s timeseries are overplotted in orange.

the nearest pulse, and a Monte Carlo approach fitting pulse time-of-arrivals (TOAs) with the pulsar timing code TEMPO[2]. PDM can detect small-amplitude periodically variable (including non-sinusoidal) signals in noisy data with a large number of irregularly sampled observations, as is the case for our timeseries. However, it relies on phase binning the data, which can introduce period aliasing. In their implementation of the Levenberg-Marquardt approach, Williams and Berger (2015) initialized the algorithm with a period near the mean of the timing spacing between subsequent pulses observed in their timeseries to avoid convergence to arbitrarily small values arising from their defined metric. While the timeseries certainly appear visually periodic, it is not clear if multiple pulses are appearing per rotation, as is possible depending on the inclination angle (Pineda 2016). This initialization may bias toward the first harmonic. Additionally, this method relies on identifying the locations of pulses a priori, which is difficult to achieve with confidence and accuracy for our data. Finally, Route and Wolszczan (2016) noted that TOAs are difficult to precisely determine owing to varying pulse profiles, and they benefitted from fitting the timeseries of relatively bright ~mJy pulses, an order of magnitude brighter than the pulses in our targets.

Our data are well-sampled with respect to pulse widths but very noisy and may contain low-amplitude or wide duty cycle pulses. Some pulses do not become apparent until the data have been averaged to 60s or 120s resolutions and other pulses have multiple peaks, further introducing uncertainty when attempting to accurately identify pulses and their arrival times. For these reasons, we elected not to pursue a Levenberg-Marquardt or Monte Carlo TOA fitting and instead employ three independent algorithms widely used in exoplanet transit and radial velocity searches. Using these algorithms has the added benefit of independently verifying the pulses that we identified in §5.5.2. The first is the classic Lomb-Scargle periodogram, which relies on decomposing timeseries into Fourier components and is optimized to identify sinusoidally-shaped periodic signals in time-series data, making this algorithm most appropriate for testing periodicity in broader pulses such as those observed in the SDSS0423 and SIMP0136 timeseries or even our targets' quiescent emission. The second method is the Plavchan periodogram, a brute force method that derives periodicities in a method similar to that employed by PDM, but circumvents period aliasing because it is binless (Plavchan et al. 2008; Parks et al. 2014). The Plavchan algorithm is not dependent on pulse shape and thus is sensitive to both sinusoid-dominated variability and other pulse profiles.

[2]http://tempo.sourceforge.net/

Finally, the shapes of some of the pulses bear resemblance to inverse light curves of planet transits, for which the Box-fitting Least Squares (BLS) algorithm is optimized (Kovács, Zucker, and Mazeh 2002).

We generate periodograms for all of our objects using the 10s time-averaged time-series for the full bandwidth data and at all sub-bands using the MATLAB Lomb-Scargle function `plomb` and the NASA Exoplanet Archive Periodogram Service[3] for Plavchan and BLS periodograms. The Plavchan algorithm depends on two input parameters: number of outliers and fractional phase smoothing width, which we vary between 10%–30% of total data points and 0.025 - 0.1, respectively. BLS depends on three input parameters: number of points/bin, minimum fractional period coverage by pulse, and maximum fraction period coverage. For BLS, we hold the minimum fractional period coverage constant at 0.01, and we vary the number of points/bin and maximum fractional period coverage between 10–100 and 0.1–0.3, respectively. In most cases, the recovered periodicities do not depend much on these parameters and we discuss exceptions below.

We compare peaks with false alarm probability less than 10% returned by the the Lomb-Scargle algorithm to the most significant periods returned by the other algorithms in Figure 5.6 and visually inspect periods by phase-folding the timeseries in Figure 5.7 with the most significant period returned by each algorithm. In all cases except for 2M1047, periods returned by each algorithm are consistent within uncertainties, defined as the FWHM of the power peaks. We list periods returned by each algorithm in Table 5.9 and adopt the periods that result in the folded timeseries with the most visual agreement in pulse overlaps.

The data for 2M1237 do not appear to provide enough phase coverage to adequately sample periods longer than ~3.77 hours, with Plavchan peak power locations at and longer than this period changing dramatically depending on input variables and especially on the fractional amount of outliers. Specifically, the periodograms with a lower fraction of allowed outliers are biased in favor of a period that is approximately twice that favored by periodograms with higher allowed outlier fractions because the large-amplitude pulse in the timeseries deviates strongly from the mean amplitude of the smaller pulses before and after it. Therefore, when the algorithm is not allowed to ignore points from this strong pulse, it will favor a rotation period that generates a timeseries akin to one with a main transit and a secondary eclipse. Additional phase

[3]https://exoplanetarchive.ipac.caltech.edu/cgi-bin/Pgram/nph-pgram

coverage to characterize the variability behavior of the pulse profile is necessary to resolve the ambiguity between period harmonics.

A similar ambiguity exists for 2M1047. The Lomb-Scargle periodogram returns a ∼0.59 hr period, while Plavchan returns 1.77 hr, and BLS returns either ∼3.54 hr or ∼1.77 hr depending on the maximum allowed rotation pulse phase coverage and phase binning. Happily, these periods are all harmonics, indicating a non-spurious origin. Similar to 2M1237, the longest period is favored by the BLS algorithm for the cases with the least number of data points per bin, emphasizing the significance of the strongest peaks. The Plavchan periodogram also reflects this behavior, although its most significant period is consistently ∼1.77 hr irrespective of input parameters. For ground-based transit surveys, a typical number of points per bin is of order a few tens to a hundred, which would correspond to a ∼1.77 hr period. This period is consistent with that measured by Williams and Berger (2015) using 10-hr C-band (4–6 GHz) observations. We therefore adopt this period.

At ∼2.88 hr, the recovered periodicity for SIMP0136 is slightly longer than its ∼2.4 hr photometric periodicity and it appears to be based on the variability in the quasi-quiescent emission. However, we caution that our data has only a limited 7 hr baseline as compared to photometric studies, which span many hours over several nights, including a recent 18-night study (Croll et al. 2016). We analyzed the 4–8 GHz data and find that the C-band period appears consistent with ∼2.88 hr, but the data is even less conclusive since the total C-band observing block was only 4 hours long. The radio rotation period of Saturn has been observed to drift, but only by ∼1% (Galopeau and Lecacheux 2000). The nature of the quiescent component of brown dwarf radio emission remains unconfirmed (see §5.6.1), but the high degree of circular polarization observed in this component for SIMP0136 could indicate a coherent mechanism. If this is the case, we speculate that the difference in periods may be evidence of a moon interaction similar to the Io-Jupiter interaction, which produces an auroral 'footprint' that tracks the orbit of Io relative to Jupiter (Ray and Ergun 2012). Because the mechanism generating the non-pulsed but varying quiescent emission and its location within the brown dwarf system remain unknown while the infrared variability is expected to occur within the brown dwarf atmosphere, we adopt the rotation period constrained by photometric studies for our discussion in §5.6.

5.6 Discussion

5.6.1 The Curious Case of Highly Circularly Polarized and/or Disappearing Quiescent Emission

Kao et al. (2016) noted that all previously detected radio brown dwarfs exhibited detectable levels of quiescent emission and Pineda 2016 showed that the quiescent radio luminosities correlated with Hα luminosities for confirmed auroral emitters (i.e. with clear rotational modulation in the highly circularly polarized emission component). This hinted of a connection between pulsed and quiescent radio processes. However, we do not observe detectable levels of quiescent emission from SDSS0423 for 8–12 GHz or individual 1- or 2-GHz sub-bands, down to rms noise levels of ~1.7–4.3 μJy. Kao et al. (2016) measured a 4–8 GHz mean quiescent flux density of 26.7±3.1 μJy, which corresponds to a lower limit spectral index of $\alpha \leq -3.2 \pm 0.2$ and a mildly relativistic power-law electron distribution with index $\delta \approx 5.0$ if there is no variability in the quiescent emission and we assume an upper 3σ detection limit of 5.1 μJy. In the stellar case, typical spectral indices for quiescent radio emission from active M dwarfs are much flatter at ~-0.3 (e.g. Güdel et al. 1993; Güdel 1994, and references therein), though there may be fundamental differences for the brown dwarf case. While abundant evidence exists that much of the quiescent emission from ultracool dwarfs exhibits behavior consistent with incoherent synchrotron or gyrosynchrotron emisssion (e.g. Ravi et al. 2012; Williams et al. 2015), there have been some objects that depart from this model.

It is possible that at least some component of the 'quiescent' (non-pulsed) emission may be coherent, as the steep spectral index implied by the drop-off in quiescent emission is atypical (but not impossible) for nonthermal gyrosynchrotron or synchrotron emission (Dulk 1985; Melrose 2006) and may be more indicative of an emission cutoff. Such a model has been proposed for solar quiescent emission with electron power-law indices $\delta \approx 2 - 4$ and weak ~100 G fields (Pallavicini, Willson, and Lang 1985; White, Kundu, and Jackson 1989; White and Franciosini 1995; Umana, Trigilio, and Catalano 1998), including both plasma and gyrosynchrotron emission. Evidence for a coherent mechanism at play in the quiescent component precedes the data presented here. For instance, the L3.5 dwarf 2MASS J00361617+1821104 exhibits broadly varying emission with duty cycles ~30% of the rotational period (Berger 2002; Hallinan et al. 2008). This emission could be decomposed to a periodic and highly circularly polarized component, which Hallinan et al. (2008) attributed to ECM, and also a component that was largely unpolarized for two out

of three of the observed rotation periods. In the third rotation period, this component emitted two narrower peaks up to ∼75% right and left circular polarization, respectively. This same feature was observed in data separated by 18 months, which demonstrated the longevity of this high degree of circular polarization and ruled out incoherent gyrosynchrotron as a mechanism. To explain the observed short-term variability in the degree of polarization, Hallinan et al. (2008) argued that local conditions in the emitting region could plausibly depolarize the emission, a phenomenon that commonly occurs in the strongly circularly polarized millisecond spikes of solar radio emission, such that polarization fractions can range from 0–10% (Benz 1986).

Similarly, Williams, Gizis, and Berger (2016) reported emission varying over 20–40 min timescales in the T6 dwarf WISEP J112254.73+255021.5, including clear ∼10 min bursts in right circular polarization as well as a more broadly varying component and less clear variability in the left circularly polarized flux density, with spectral index $\alpha = -1.5 \pm 0.3$. Particularly noteworthy is the consistently high degree of circular polarization (>50%) present for nearly the entire duration of their 162 min observation. This is similar to what we observe(d) in SIMP0136 and 2M1237, which have a much flatter spectrum than SDSS0423 if no variability is assumed, with spectral indices $\alpha = -1.9 \pm 0.4$ and $\alpha = -0.9 \pm 0.3$, respectively. In contrast, Williams and Berger 2015 reported 'quasi-quiescent' emission from 2M1047 at 4–8 GHz that was not circularly polarized yet still showed evidence of possible variability with ∼60 μJy amplitude over a ∼20 min timescale and a flat spectral index of $\alpha = 0.9 \pm 1.0$.

In the case that the non-pulsed emission is coherent, plasma emission is unlikely because the plasma density in a cool brown dwarf such as SDSS0423 is expected to be tenuous in comparison to the Solar corona, and the plasma frequency scales with the electron density as $\nu_p \propto n_e^{1/2}$. For a gas to exhibit plasma-like behaviors, electron-electron interactions should dominate over electron-neutral interactions. In models of thermal ionization for temperatures characteristic of M–T dwarfs, Rodriguez-Barrera et al. (2015) find that whereas M dwarfs can expect $\sim 10^{-1}$ fraction of ionization in their atmospheres, this rapidly drops to $\sim 10^{-4} - 10^{-3}$ for 1000 K objects. Additionally, the presence of plasma would correlate with X-ray emission, but L and later brown dwarfs remain underluminous in X-ray compared to their warmer counterparts (Williams, Cook, and Berger 2014). Finally, the free-free

opacity $\tau_{\rm ff}$ for plasma emission is

$$\tau_{\rm ff} = 46 s^{-4} \nu_{p,\rm GHz}^2 T_6^{-3/2} \left(\frac{H}{30 \text{ Mm}} \right), \tag{5.1}$$

where s is the emission harmonic (typically emitted at the fundamental or second harmonics), ν_p is the plasma emission frequency for that harmonic, T is the temperature given in 10^6 K, and H is the density scale height along the emission path. In the Sun, which has coronal temperature $\sim 10^6$ K, plasma emission is rarely observed observed above $\sim$1 GHz owing to strong reabsorption (Dulk 1985; Güdel 2002, and references therein). The other plausible mechanism would be ECM emission in the form of superposed flares, as observed for 2MASS J00361617+1821104 (Hallinan et al. 2008). However, if the mechanism generating this quiescent emission is indeed related to the pulsed emission, the presence of the pulses observed in the same frequency bands would preclude the observed cutoff, unless the emitting regions traced different magnetic field strengths. This scenario could account for the strong circular polarization of the non-flaring emission from SIMP0136, 2M1237, and WISEP J112254.73+255021.5.

Another likely explanation is that the quiescent emission may exhibit long-term variability. Such variability has been previously reported in other brown dwarfs. For instance, Antonova et al. (2007) did not detect any radio emission from a 9 hr observation (with 3σ upper limit $\sim$45 μJy) of 2MASS J05233822-1403022 (L2.5) on 2006 September 23, which Berger et al. (2010) also reported for observations on 30 December 2008. Archival data analyzed by Antonova et al. (2007) revealed that this same object was also not detected on 03 May 2004 with 3σ upper limit of 42 μJy, yet it was detected sans flare on 17 May 2004 with flux density 95 ± 19 μJy and also on 18 June 2004 with flux density 230 ± 17 μJy, the latter of which was previously reported by Berger (2006). Similarly, Berger et al. (2010) reported no detectable emission from BRI 0021 (M9.5) with 3σ upper limits of 54 μJy and 48 μJy for 4.9 GHz and 8.5 GHz, despite a previous marginal detection of its quiescent emission at 40 ± 13 μJy as well as a flare with a peak flux density of 360 ± 70 μJy. In the case that the quiescent emission is variable over longer timescales, long-term monitoring of radio brown dwarfs would be necessary to quantify how much the current detection rate underestimates the true detection rate and may warrant revisiting previously undetected objects with Hα or infrared variability such as SDSS J12545393-0122474 (Kao et al. 2016).

The possible quiescent emission drop-off observed in SDSS0423 and the high degree

of circular polarization in the non-pulsed emission from SIMP0136 and 2M1237 together highlight the question: Where is the line between pulsed and quiescent emission? Is it possible for ECM emission to also manifest as quiescent (not pulsed) emission?

5.6.2 Intermittent Pulses: Implications for ECM Emission Frequency Cutoff

At these high frequencies, pulses appear to be more intermittent compared to previous 4–8 GHz observations (Route and Wolszczan 2012; Williams and Berger 2015; Kao et al. 2016), with short-duration variability in both time and frequency. For instance, while the central pulse in 2M1237 is present at all bandwidths, the rightmost peak is clearly apparent only at 11–12 GHz. In SDSS0423, there are two faint right-circularly polarized pulses in 8–9 GHz, but the right pulse appears to drop out at higher frequencies. In 2M1047, there appears to be a multi-peaked or long-lived left-circularly polarized pulse at 12.8–13.5 GHz early in the observing block that drops out at higher frequencies, only to be replaced by three fainter left-circularly polarized pulses distributed throughout the entire observing block. This is in contrast to these objects' C-band (4–8 GHz) pulses, which Kao et al. (2016) reported to be present at all sub-bands.

This suggests that the conditions for current systems driving these auroral emissions may be much less stable or more variable close to the surface of the star, where fields are expected to be stronger. For instance, although large-scale fields appear necessary to drive Solar System auroral currents and the same may occur in isolated brown dwarfs such as our targets, as radiating electrons traverse these large-scale field lines inward, they will radiate at the frequencies corresponding to the magnetic fluxes that they see. Near the object surface, evolving and complex small-scale fields may also begin to emerge, and some fully convective dynamo models capable of generating kilogauss fields suggest that these small scale fields may be driven by convection near the surface, where convective turnover times are shorter and small-scale intermittent features begin to appear in convective flows. In contrast, more stable large-scale fields appear to be driven by slowly overturning convection in the deep interiors (Browning 2008).

Other examples of intermittent auroral pulse structures exist in the literature. As an example, the dynamic spectrum of LSR J1835+3259 shows one pulse per rotation extending through ∼4–8 GHz, one extending through ∼4–6 GHz, and one only extending through ∼4.5 GHz, with emission from each pulse appearing to fade

Table 5.10: Adopted Magnetic Fields

Object	Tentative $\nu_{\rm cutoff}$ [a] (GHz)	Local field $B_{\rm ECM}$ [b] (kG)	Min avg field $B_{\rm s,dip}$ [c] (kG)
2M1047	17.25	6.2	4.4
SIMP0136	10.5	3.7	2.7
2M1043	11.0	3.9	2.8
2M1237	11.5	4.1	2.9
SDSS0423	11.0	3.9	2.8

[a] Center of highest subband with imaging detection of ECM pulse.
[b] $B_{\rm ECM\ [kG]} = \nu_{\rm ECM\ [GHz]}$ / 2.8 (Treumann 2006)
[c] $\langle B^2_{\rm s,dip} \rangle = \frac{1}{2} B^2_{\rm ECM}$ (Kao et al. 2016)

away or renew again at different frequencies (Hallinan et al. 2015). Narrowband and intermittent pulses have also been observed in terrestrial, Jovian, and Saturnian auroral kilometric radiation (AKR). High-resolution dynamic spectra reveal that rather than one continuous pulse through frequency, AKR actually consists of many small-scale micropulses from individually radiating sources that are highly time variable and narrowly-spaced in frequency, with widths of order ∼10–1000 Hz corresponding to bunched groups of these local AKR sources traveling very rapidly through space. The origin of this fine structure remains unknown, but it is speculated that they may reflect a number of physical processes including propagation and absorption effects or small-scale field parallel current structures (Gurnett, Kurth, and Scarf 1981; Pottelette et al. 1999; Treumann 2006, and references therein).

While we do observe what appears to be the disappearance of highly circularly polarized pulsed auroral emission in SIMP0136, 2M1043, and SDSS0423 at 11–12 GHz, in light of the observed behavior in 2M1237 and 2M1047 and the above-discussed cases, we classify these dropoffs only as very tentative evidence of ECM emission cutoff. The known intermittent behavior of AKR suggests that observations through a much wider bandwidth of high frequencies are necessary to confirm a true emission cutoff.

5.6.3 Comparison to Luminosity-Driven Model

Previously, Kao et al. (2016) found tentative evidence of a T dwarf departure from a predominantly luminosity-driven dynamo for rapid rotators (P<4 days). This model extended planetary dynamo models to stellar-mass objects including T Tauri stars and old M-dwarfs, whose Zeeman broadening and Zeeman Doppler imaging measurements appeared to be empirically consistent with a scaling relationship

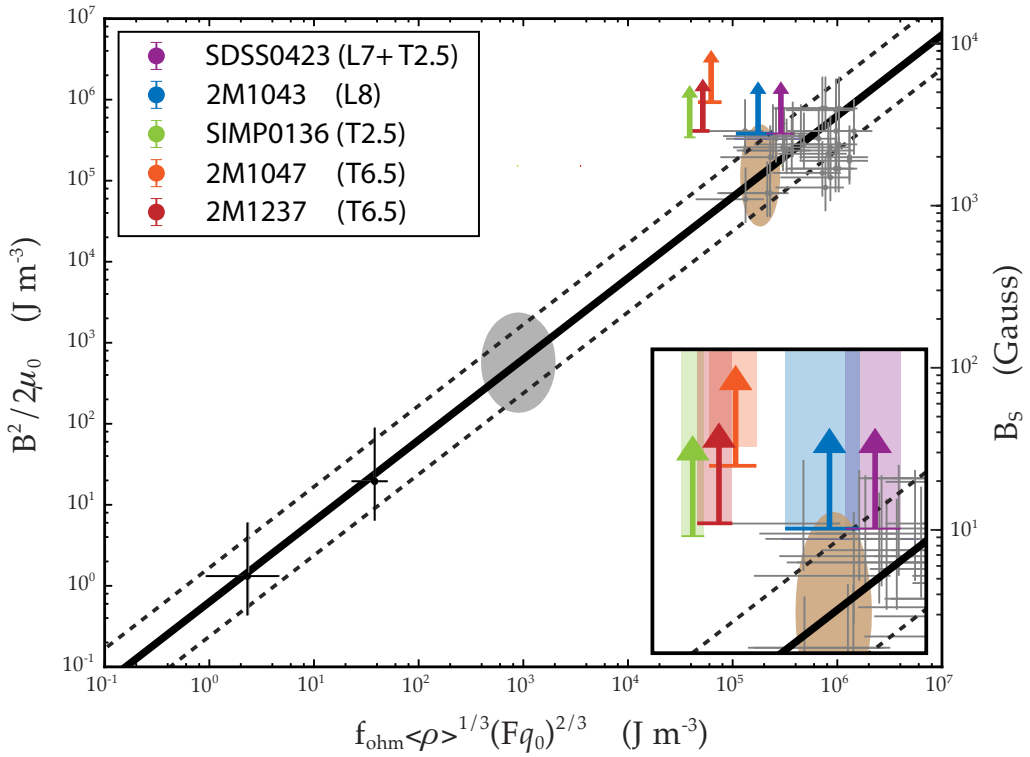

Figure 5.8: A comparison of estimated lower-bound magnetic field energies for our targets (overplotted arrows) to values predicted by the Christensen, Holzwarth, and Reiners (2009) scaling relation (black solid line) between convected energy density (x-axis, q_0) and magnetic energy density (left y-axis) of fully convective dipole-dominated rapid rotators. Black dashed lines are 3σ uncertainties on the model and horizontal bars on arrows are our estimated uncertainties. Previous constraints were T Tauri stars and old M dwarfs (gray crosses). Black points represent Earth and Jupiter. Brown and grey ellipses are predicted positions for a 1500 K brown dwarf and a 7 M_J exoplanet, respectively. Right y-axis values are predicted surface-averaged fields B_s.

linking magnetic field strength to convected energy flux and dynamo density and largely independent of both magnetic diffusivity and rotation rate (Christensen, Holzwarth, and Reiners 2009, hereafter C09). The broad span through planetary and stellar parameter spaces suggested that the scaling law may in fact present a unifying principle governing the magnetic field generation in all rapidly rotating, dipole-dominated fully convective objects – namely, that the bolometric flux q_0 sets the magnetic field strength averaged over the whole volume of the dynamo region $\langle B^2 \rangle$, with a weak dependence on the mean density of the dynamo region $\langle \rho \rangle$:

$$\langle B^2 \rangle \propto \langle \rho \rangle^{1/3} q_0^{2/3} \ . \tag{5.2}$$

However, a previous lack of magnetic field measurements in the orders-of-magnitude mass and luminosity gap between planets and stars prevented further testing of this exciting model.

Several possible scenarios could explain the observed tentative inconsistency between late L and T dwarf magnetic fields with the C09 model, and we refer the reader to the discussion in Kao et al. (2016) §6.4. Of particular note is that the C09 model is specific to dipole-dominated fields (>35% of field strength in the dipole component) in rapid rotators. It is therefore possible that higher order fields may dominate our objects. Without confirmed periods, an alternative was that several of our targets may be slower rotators.

Magnetic field topologies of our objects cannot be confirmed with only auroral radio emission, the frequency of which corresponds only to localized emitting regions in the magnetospheres of our targets. However, co-rotation breakdown models assuming Jovian-like ultracool dwarfs, with predominantly dipolar and axisymmetric magnetic fields and non-conducting atmospheres, show close agreement between modeled and observed auroral radio luminosities for TVLM 513-46546 (M9), LSR J1835+3259 (M8.5), and 2MASS J00361617+1821104 (L3.5) (Nichols et al. 2012). This model also predicted rotation periods between ~2.1–2.8 hr for 2M1047, which is not inconsistent with its measured rotation period. Additionally, while the exact nature of the electrodynamic engine — and therefore the magnetic field component powering the observed auroral emission— is not yet known, all of the known mechanisms for auroral emission in our Solar System rely on large-scale magnetic fields. Auroral emissions rely on coupling energy from locations where there is a large $v \times B$ into the magnetosphere (Nichols et al. 2012). This is best achieved by having strong magnetic fields far away from the planet. Dipoles drop off much slower than higher order fields and almost always dominate auroral power for this reason. This suggests that auroral radio emission likely probes the dipole components of our objects. Finally, ZDI studies indicate that fully convective M dwarfs appear to host ~kG mean fields regardless of if they are dominated by dipole or higher-order fields, and dwarfs with kilogauss dipoles have order-of-magnitude weaker multipole fields and vice versa (Morin et al. 2010), making it unlikely that our targets have multipole-dominated fields if this behavior extends to L and T dwarfs. Indeed, even if the emergent structure in auroral emission discussed in §5.6.2 indicates the presence of small-scale fields near the brown dwarf surface, the largest scale fields still appear to store the most magnetic energy (Browning 2008).

For a more detailed discussion of field topologies, we refer the reader to §6.3.1 in Kao et al. (2016).

Regarding the rapid rotation requirement for the C09 model, the periodicities that we recover in §5.5.3 unambiguously confirm that our targets are indeed rapid rotators, with rotation periods between ∼1.44–2.88 hours. While SIMP0136 does not have any clearly periodic pulse structure, infrared cloud variability studies suggest a rotation period of 2.3895 ± 0.0005 hr (Artigau et al. 2009; Croll et al. 2016). This rotation period is slightly inconsistent with the recovered periodicity in its quasi-quiescent emission, which we measure to be $2.88^{+0.34}_{-0.27}$ hr. Nevertheless, both periods fall well within the rapidly rotating regime such that Ro $\ll 0.1$.

Given the inconclusive evidence of ECM emission cutoff discussed in §5.6.2, we conservatively adopt ECM emission cutoff frequencies corresponding to the middle of the last sub-band with clear imaging detections of auroral pulses in Stokes I and V. Following the methodology outlined in Kao et al. (2016), we convert the local magnetic fields measured with ECM emission $B_{\rm ECM}$ to lower bound mean surface field magnitudes $B_{\rm s,dip}$ by assuming pure dipole fields for our objects, which we list in Table 5.10. As described in Kao et al. (2016), $B_{\rm s,dip}$ is equivalent to a lower bound Zeeman broadening measurement of a surface-averaged field strength B_s, and the presence of any higher-order fields would raise this estimate. We convert $B_{\rm s,dip}$ to a mean internal field strength $\langle B \rangle$ for comparison to the C09 relation by following the conversions outlined in C09 and summarized in Kao et al. (2016).

We present our resulting field constraints on a reproduction of the C09 scaling law in Figure 3.4, with x-axis values determined from the physical parameters of our targets summarized in §5.3. The T dwarfs 2M1047, 2M1237, and SIMP0136 clearly depart by an order of magnitude from C09 magnetic energy predictions. While the late L dwarfs lie near the outer bounds of the 3σ error on the scaling relationship, these are in fact conservative constraints. Values for our objects along the x-axis are dependent on the mean density of the dynamo region, and the bolometric flux at the outer boundary of the dynamo regions. For stellar objects, C09 assume that the dynamo boundary surface is approximately equal to the photospheric surface, such that they calculate the bolometric flux at the dynamo boundary using effective surface temperatures. Unlike hotter low-mass stars, cool brown dwarfs such as our targets are unlikely to have a conductive atmosphere, resulting in dynamo surfaces that are interior to the photospheric surfaces of our targets. Indeed, the dynamo surface in Jupiter may lie at ~ 0.85–$0.95 R_{\rm J}$ (Guillot et al. 2004; Duarte, Wicht, and

Gastine 2016). Since B^2 rises faster than $\langle\rho\rangle^{1/3}(q_0)^{2/3}$ as a function of radius (external to the dynamo region) for all field topologies, it is quite possible that our objects may further disagree with the C09 relation, tantalizingly hinting at a possible ultracool brown dwarf locus that may not age along the predicted luminosity-magnetic field sequence (Reiners and Christensen 2010) and calling for additional studies identifying aurorally pulsing radio brown dwarfs and characterizing their physical parameters.

5.6.4 Consideration of Age-Related Models

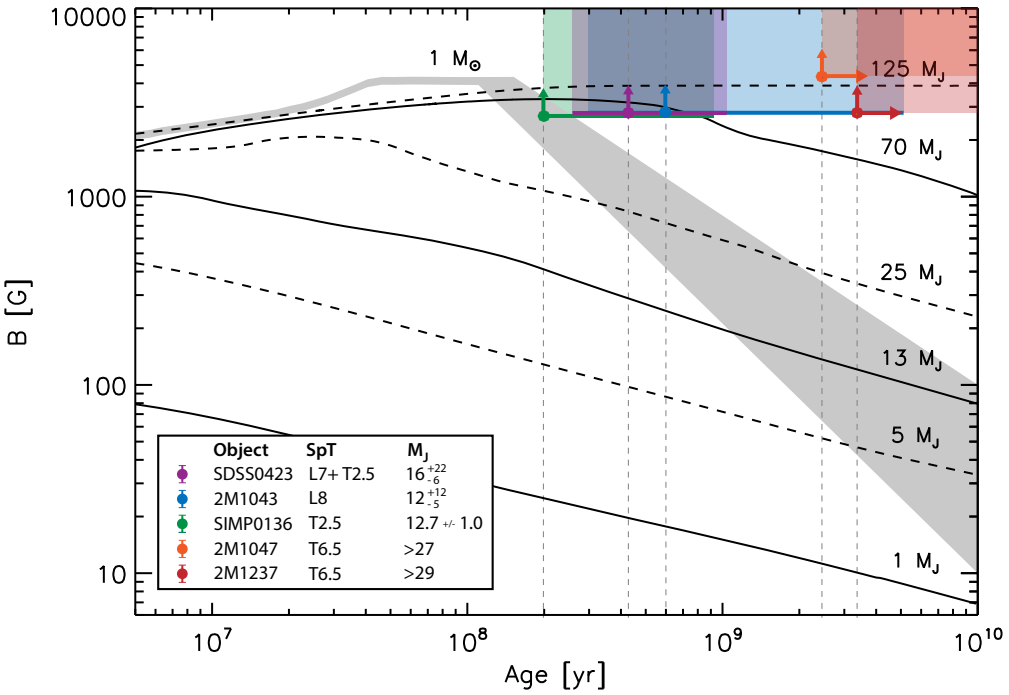

Figure 5.9: A comparison of estimated lower-bound magnetic field energies (colored circles with upward arrows) for our targets to age-related predictions that employ the dynamo scaling relationship from Christensen, Holzwarth, and Reiners (2009) and Burrows et al. (1993, 1997) brown dwarf evolutionary tracks. Overlapping age uncertainties are shown with colored regions for better clarity. The L dwarfs in our sample (2M1043 and 2M1047) did not appear to disagree strongly with the Christensen, Holzwarth, and Reiners (2009) relation. When considering age and mass dependencies in luminosity, the disagreement becomes more apparent. The presence of strong ~kilogauss fields across over an order of magnitude in ages is notable. Adapted from Reiners and Christensen (2010), with permission from Astronomy & Astrophysics, © ESO.

The possibility that magnetic energy may scale with luminosity in rapidly rotating

convective objects supports a picture in which brown dwarf magnetic fields are expected to decay with age as they cool through the L/T/Y spectral sequence and become increasingly less luminous. Indeed, Reiners and Christensen (2010) find that field strengths for gas giant planets and brown dwarfs wane by a factor of 10% when they apply brown dwarf evolutionary tracks to the C09 model to extrapolate how magnetic fields may evolve with age. While our T dwarf data already disagree somewhat with the C09 model, this disagreement does not necessarily render the C09 model incorrect and a disagreement was less clear for our L dwarfs. Instead, it is possible for the general principle to be true while the implementation requires fine-tuning, for instance in defining the various model control parameters for different classes of objects. Thus, considering global behaviors displayed by the various groups of objects spanning different parameter spaces can provide valuable insight.

To that end, the luminosity of a brown dwarf depends both on its age and its mass, so we have overplotted our objects on the age-mass-magnetic field predictions from (Reiners and Christensen 2010) in Figure 5.9. Given the disagreement between our objects and the C09 relation, it is no surprise that all of our objects also depart from these age-related predictions. However, accounting for the effects of age and mass on luminosity hints at a stronger departure from the Christensen, Holzwarth, and Reiners (2009) scaling law for our warmer but less massive and younger L dwarfs than was initially evident when mass and age were folded into luminosity. Regardless, a much larger sample is needed before any concrete conclusions can be drawn about how age affects convective dynamos, and the simplest prediction to test is whether objects similar masses have stronger fields when younger.

In the event that luminosity (T_{eff}) does not play a dominant role in brown dwarf dynamos, it is worth noting that magnetic field strengths do not appear to vary much by age across an order of magnitude between ~200–3.4 Gyr. Of course, no definitive ECM emission cutoff frequency has been observed for any brown dwarfs yet, including our targets, so the plotted mean surface field strengths are merely lower bounds and the future addition of constraints from higher frequencies and a broader range of ages, masses, and temperatures may yet reveal a correlation between age and field strength.

A potential caveat is that Reiners and Christensen (2010) use the Burrows et al. (1993, 1997) evolutionary tracks in their predictions, while Kao et al. (2016) used the BTSettl08 models (Allard, Homeier, and Freytag 2011), and Gagné et al. (2017) use the Saumon and Marley (2008) models in their analysis of SIMP0136. The use

of different evolutionary models across these three studies can call into question the validity of comparing ages, masses, and temperatures derived from different evolutionary models. However, the evolutionary tracks do not differ by the order of magnitude in luminosity or age that would be required to make our magnetic field observations consistent with the C09 relation.

Presenting our data within the context of age has an important implication for ongoing efforts to detect exoplanet radio emission. While such efforts have focused on hot Jupiters (which see high flux from host stars thus increasing the luminosity of solar-wind generated aurorae) and hot young exoplanets (Lazio and Farrell 2007; Lazio et al. 2010; Hallinan et al. 2013; Murphy et al. 2015; Lynch et al. 2017), old objects appear to also be capable of generating strong fields along with the associated radio emission. This calls into question the advantages of focusing on young systems, and broader searches may be warranted.

5.6.5 Consideration of Models Examining the Role of Rotation

Rotation has long been recognized as an important player in dynamo action, including in fully convective objects that do not have an obvious region of strong differential rotation that is thought to be necessary for the solar dynamo (Moffatt 1978; Steenbeck and Krause 1966; Charbonneau 2005). The role of rotation is most easily illustrated by a heuristic description of the two-part $\alpha\Omega$ dynamo. In the α effect, the rising and twisting of convective cells twists anchored magnetic field lines into loops thereby generating a current that drives a poloidal field. The Ω effect then relies on large-scale differential rotation to shear this poloidal field into a toroidal field, allowing the $\alpha\Omega$ cycle to continuously regenerate this time varying field. Such a dynamo may also occur in cooler, fully convective objects such as when strong zonal flows in the molecular layers of an object penetrate into more conductive regions to generate a secondary dynamo that tends to favor weaker multipolar fields (e.g. Gastine, Duarte, and Wicht 2012; Duarte, Gastine, and Wicht 2013; Gastine et al. 2014; Duarte, Wicht, and Gastine 2016).

Coriolis forces from rotation can also influence convective motions and therefore dependent dynamo mechanisms, for example by twisting rising and falling convection cells as in the α-effect (Durney 1981; Noyes et al. 1984). It is not surprising that some models have found that magnetic field strengths increase with rotation rate up to a saturation level for α^2 dynamos absent of differential rotation (Chabrier and Küker 2006). In other models, lower Rossby numbers Ro that indicate the

strong influence of rotation dynamics on convection tend to result in stronger dipole components (e.g. Christensen and Aubert 2006; Sreenivasan and Jones 2006; Olson and Christensen 2006; Yadav et al. 2016). Along similar lines, Browning (2008) found that differential rotation can in fact become established in a model of a fully convective 0.3 $M_\odot$ star with a resulting tradeoff between growing differential rotation driving up magnetic energy, until strong fields begin to suppress the differential rotation and consequently quench the magnetic energy. In contrast, the effect of solid-body rotation appears enough to maintain strong axisymmetric fields in simulations where Ro $\ll 1$, while slow rotators experience constant differential rotation and weaker average fields. In another variation of these observed rotation effects, some models of rapid rotators see the onset of dipole-dominated fields in addition to multipole-dominated fields in an apparent bistable dynamo (Gastine et al. 2013), which may generate field strengths with a predicted square root dependence on the rotation rate (Morin, Dormy, et al. 2011).

Indeed, recent reports of X-ray emission consistent with the X-ray activity-rotation relation in solar-type stars from four slowly rotating and fully convective M4–M5.5 dwarfs suggest that the $\alpha\Omega$ dynamo may operate in fully convective objects, supporting dynamo models that demonstrate emergent differential rotation in the fully convective regime (Wright and Drake 2016).

Our data confirm that thus far all of the known brown dwarf auroral emitters with measured rotation periods fall well within the limit of rapid rotation (Ro < 0.1), with measured rotation periods on the order of just a few hours compared to convective turnover times that are predicted to scale as $\tau_c \propto L_{\rm bol}^{-1/2}$ through M dwarfs (Noyes et al. 1984; Pizzolato et al. 2003). Of course, most brown dwarf radio detections have relied on short time baselines, biasing detections of radio brown dwarfs toward toward high rotation rates. This begs the question of whether rapid rotation rate is indeed important for generating strong large-scale kilogauss fields in the coolest brown dwarfs or is a requirement for driving auroral emissions or both.

Continuing to push magnetic field measurements to higher frequencies with the goal of measuring true ECM cutoff frequencies will provide insight into how and whether field strengths empirically depend on rotation.

5.6.6 First Radio Detection of Planetary-Mass Object?

Recently, Gagné et al. (2017) reported that the SIMP0136 may be a member of the ~200 Myr-old Carina-Near moving group based on its kinematics, with a field

interloper probability of only 0.0001%. Using an empirical measurement of its bolometric luminosity and the the Saumon and Marley 2008 models, they inferred $R = 1.22 \pm 0.01$ R_J, which together predicted $T_{eff} = 1098 \pm 6$ K and $M = 12.7 \pm 1.0$ M_J. New $v \sin i$ measurements and its photometric periodicity constrained its inclination angle at $i = 55.9^{+1.6^\circ}_{-1.5^\circ}$, giving a lower bound radius and corresponding upper bound on age and mass at $R > 1.01 \pm 0.02$ R_J and 910^{+26}_{-110} Myr with $M < 42.6^{+2.5}_{-2.4}$ M_J. Models of the photometric variability assuming a single spot are in agreement, constraining its inclination at $i < 60^\circ$, which would increase the lower bound radius to $R > 1.17 \pm 0.02$ R_J, further supporting the young age and low mass derived for SIMP0136 if it is indeed a member of the Carina-Near moving group.

With this new study, SIMP0136 may well be the first conclusively planetary-mass object with a radio detection, paving the way to testing planetary dynamos with hot young planetary-mass objects.

5.7 Conclusions

We detected auroral radio emission from four L7–T6.5 dwarfs up through 10–12 GHz, and one T6.5 object up through 16.5–18 GHz, corresponding to 3.7–6.2 kG local magnetic field strengths and 2.7–4.4 kG minimum surface averaged fields. Pulses appear to be more intermittent in frequency at higher frequencies compared to previous observations of lower frequency counterparts, which can be interpreted as evidence of a higher degree of variability in the conditions necessary to generate auroral radio emission near the surfaces of brown dwarfs. While we observe the fading out of auroral pulses at 11–12 GHz for some targets, observations at higher frequencies are necessary to affirm definitive cut-offs in the auroral radio emission. We additionally observe no detectable quiescent emission for SDSS0423 but do observe highly circularly polarized non-pulsed emission from SIMP0136 and in some sub-band also for 2M1237. The behavior of SDSS0423 may point to long term variability in the quiescent emission mechanism, while SIMP0136 and 2M1237 are more suggestive of coherent processes.

We have presented the strongest confirmed magnetic fields on the coolest brown dwarfs to date and represent the strongest direct constraints on dynamo theory at the substellar-planetary boundary. We have examined possible dynamo relationships depending on age, effective temperature, and rotation. We presented data suggesting that a scaling relation between convected energy flux and magnetic energy density (Christensen, Holzwarth, and Reiners 2009) may not fit. Using the rotational

modulation of auroral radio emission, we measured rotational periods between 1.47–2.88 hr. These short rotation periods are consistent with periods measured for earlier-type brown dwarfs using auroral radio emission and reiterates that rapid rotators can host strong large-scale fields. Finally, we find that our oldest targets (2M1047 and 2M1237, >2.5 Gyr) can generate fields that are as strong as those measured in our youngest targets (~200–600 Myr), suggesting that old exoplanets may also host fields with strengths comparable to their younger siblings and serving as preliminary and very tentative evidence that age dependence in dynamo mechanisms may be weak. The absence of an emission frequency cut-off means that we have not broken any degeneracies in our analyses and a larger, more characterized sample is required.

Included in our sample was the archetypal cloud variable SIMP0136, which was recently found to be a member of a nearby ~200 Myr moving group. This new constraint reduces its estimated mass to a mere 12.7 ± 1.0 M_J, possibly making SIMP0136 the first known planetary mass object detected in the radio. If SIMP0136 is indeed a field exoplanet, its detection demonstrates that auroral radio emission can open a new avenue to detecting exoplanets, including elusive rogue planets.

5.8 Acknowledgements

MMK thanks Jackie Villadsen for helping to troubleshoot calibrations, Rakesh Yadav for thoughtful and instructive discussions about dynamo modeling, and Cameron Voloshin for contributions to data presentation.

This publication makes use of data products from the Two Micron All Sky Survey, which is a joint project of the University of Massachusetts and the Infrared Processing and Analysis Center/California Institute of Technology, funded by the National Aeronautics and Space Administration and the National Science Foundation.

The National Radio Astronomy Observatory is a facility of the National Science Foundation operated under cooperative agreement by Associated Universities, Inc.

MMK was supported by the NRAO Grote Reber Doctoral Fellowship. JSP was supported by a grant from the National Science Foundation Graduate Research Fellowship under grant no. DGE-1144469.

Facilities: JVLA

Chapter 6

LOOKING AHEAD: INVESTIGATING THE RELATIONSHIP BETWEEN AURORAL RADIO EMISSION AND BROWN DWARF WEATHER

[The selection and observing strategies used for this work are the same as those used for Chapter 3. Accordingly, a portion of this chapter reuses text from previous chapters where appropriate to facilitate clarity.]

6.1 Abstract

Understanding changes in cloud composition and weather patterns provides critical insight into brown dwarf evolution and exoplanet weather. Recent results linking brown dwarf aurorae to optical/IR variability demonstrate that auroral emission may play an important yet unaccounted-for role in the cloudy atmospheres interpretation of brown dwarf photometric variability. We have observed 33 L, T, and Y 'cloud variable' brown dwarfs identified by optical and/or infrared cloud variability surveys with the Jansky Very Large Array at 4–8 GHz to study the relationship between brown dwarf aurorae and cloud phenomena, spanning L through T spectral types and a wide range of rotation periods.

6.2 Introduction

As transition objects between planets and low-mass stars, brown dwarfs share many characteristics with gas giant planets that make them ideal proxies for studying planetary atmospheric phenomena. Crucially, brown dwarfs can be much brighter than planets, making spectral observations and atmospheric modeling of brown dwarfs important tools for investigating the atmospheric physics and chemistry of their much dimmer planetary counterparts (Morley, Marley, Fortney, Lupu, et al. 2014). Additionally, because brown dwarfs spend most — if not all — of their lifetimes gravitationally contracting and cooling, the L-T-Y spectral sequence represents the evolutionary tracks of brown dwarfs. Our current picture of brown dwarf evolution relies on modeling and fitting spectra to constrain characteristics such as mass, age, temperature, and specific gravity. However, these models are highly dependent on our interpretation of cloud phenomena (Burgasser, Burrows, and Kirkpatrick 2006; Allard, Homeier, and Freytag 2011; Kao et al. 2016). Specifically, evolving spectra

may reflect changing opacities as different molecular species form and condense into clouds or rain out of the upper atmospheres, weather phenomena which are predicted to occur as brown dwarfs cool along the spectral sequence (Burrows, Sudarsky, and Hubeny 2006; Cushing et al. 2008; Morley et al. 2012; Morley, Marley, Fortney, and Lupu 2014).

Informing our current interpretation of brown dwarf atmospheres are photometric studies that demonstrate ubiquitous optical and infrared variability (Enoch, Brown, and Burgasser 2003; Clarke et al. 2008; Khandrika et al. 2013; Radigan et al. 2014; Heinze, Metchev, and Kellogg 2015; Metchev et al. 2015). In some cases, the variability is irregular in nature with more than one timescale (Bailer-Jones and Mundt 2001; Koen 2005; Metchev et al. 2015). In cases of periodic variability, cloud-derived rotation periods can be inconsistent with measured rotation velocities $v \sin i$ (J. M. Radigan 2013). Clouds in brown dwarf atmospheres have been proposed to interpret observed photometric and spectroscopic variability, and some models rely on patchy clouds at variable heights, thicknesses, and temperatures (Marley, Saumon, and Goldblatt 2010; Burgasser et al. 2014; Apai et al. 2013). Importantly, the increasingly neutral atmospheres of brown dwarfs have been invoked to provide a relatively straightforward interpretation of variability due to clouds rather than localized magnetic heating (Mohanty et al. 2002; J. M. Radigan 2013). Recent evidence shows that this assumption may not be true (Kao et al. 2016).

Fourteen low mass stars and brown dwarfs have been found to be radio sources in the last decade. A subset of these objects have been the subject of lengthy follow-up campaigns that have revealed the presence of 100% circularly polarized periodic pulses, with the pulse period consistent with rotation (Hallinan et al. 2007, 2008; Berger et al. 2009; Williams and Berger 2015; Kao et al. 2016). This emission is attributed to the electron cyclotron maser (ECM) instability, and is of the same nature as the auroral emission produced by the magnetized planets in our Solar System. In the last two years, three key studies have confirmed the auroral nature of such highly polarized pulsed emission. In a follow-up survey, 5/6 ECM-detected objects showed clearly periodic I-band variability associated with rotation periods, and the sixth object yielded a marginal detection (Harding et al. 2013). In simultaneous radio and optical spectroscopic observations of the M8.5 dwarf LSR J1835+3259, Hallinan et al. (2015) demonstrated that features in the radio dynamic spectrum and optical spectrum (including Balmer line and broadband continuum emission) in fact varied either in phase or anti-phase with each other, with a period that

corresponded to the known rotation period of LSR J1835+3259. Hallinan et al. (2015) argued that auroral current systems could explain the Balmer emission and observed multi-wavelength periodicity.

To explore a possible brown dwarf auroral paradigm, we recently proposed a small pilot survey of 6 objects including the only previously detected T-dwarf, 2MASS J10475385+2124234 (2MASS J1047+21) (Route and Wolszczan 2012), to search for further examples of auroral radio sources. Prior to our work, volume-limited radio surveys of ~60 ≥L4 objects yielded only one detection (Route and Wolszczan 2012; Antonova et al. 2013; Route and Wolszczan 2013), resulting in a detection rate of just ~1.4%. In contrast, we strongly biased our small sample to target only dwarfs known to exhibit Hα emission and/or optical/IR variability. We observed our sample of 6 objects with the VLA for 2–4 hours each at C band (4–8 GHz) during Semester 13A. We detected 5 out of our 6 objects, including 4 newly-detected radio emitting late L and T dwarfs, achieving a notably higher detection rate compared to previous efforts and reinforcing the possibility that optical/IR variability may be related to auroral radio emission (Kao et al. 2016).

While the relationship between optical/IR variability and auroral radio emission remains uncertain, our results are intriguing when viewed in the context of brown dwarf weather. Included in our pilot target sample was the canonical dust-variable T dwarf SIMP J01365662+0933473 (SIMP 0136), which exhibits large-amplitude (>5%) IR variability. Also included were 3 other tentatively low-amplitude variable objects. Although such variability is generally attributed to clouds, our results point to the possibility that an additional variability mechanism may be at play, as postulated by Hallinan et al. (2015).

In late L/T auroral emitters such as our targets, observed photometric variability may in part be explained by localized heating of the atmosphere within the auroral oval from the precipitating electron beam that drives auroral radio emission. Atmospheric heating at different depths perturbs the pressure vs. temperature profile and can indeed cause spectral variability (Morley, Marley, Fortney, and Lupu 2014). Regardless of where in the atmosphere heating occurs, the highest amplitude variability occurs in absorption features redward of ~2.2 μm, which could lead to variability in the K and L bands. Encouragingly, K_s-band variability has been observed in SIMP 0136 (Artigau et al. 2009), as well as tentatively for another of our targets J042348.57-041403.5AB (Enoch, Brown, and Burgasser 2003), and it is reported that 36^{+26}_{-17}% of T dwarfs may vary by ≥0.4% at 3–5 μm (Metchev et al. 2015).

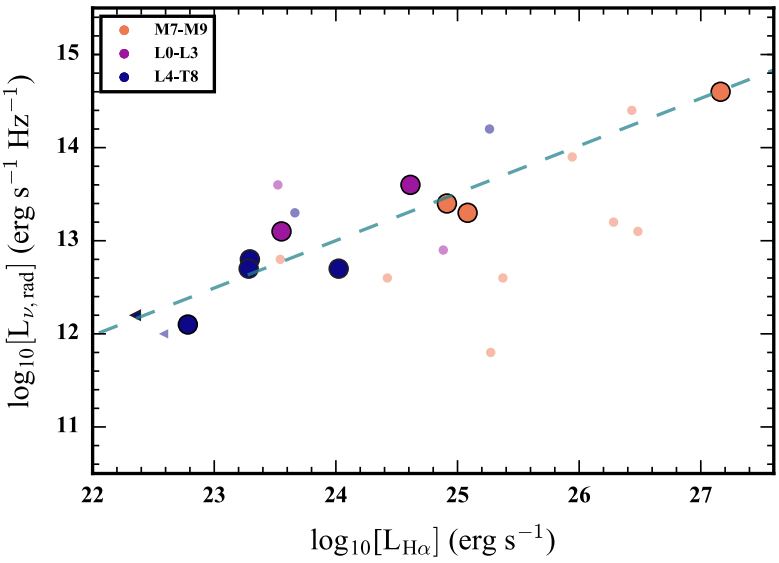

Figure 6.1: Quiescent radio and auroral tracer Hα luminosities correlate for radio-emitting brown dwarfs with confirmed periodic and highly circularly polarized pulses that are hallmarks of auroral emission (open circles), providing a means to efficiently search for brown dwarf radio aurora candidates. Figure is adapted with permission from Pineda (2016) and updated to include objects from Chapter 5.

6.2.1 Quiescent Radio Emission: A New Proxy for Auroral Radio Emission in Brown Dwarfs

Searching for rotationally modulated auroral pulses can be time intensive, requiring more than one full rotation period to observe at least two pulses. We are leveraging the relationship between quiescent and auroral radio emission to design a resource-efficient and effective survey.

Detections of quiescent radio emission accompany all previous auroral pulse detections (Hallinan et al. 2007, 2008; Berger et al. 2009; Kao et al. 2016). This suggests that physical processes governing the quiescent and pulsed radio components may be related, possibly sharing an electrodynamic engine. Indeed, Pineda (2016) showed that Hα luminosities correlate with quiescent radio luminosities for known M7–T8 auroral pulse emitters (Figure 6.1).

Targeting quiescent emission brings additional advantages. First, while Jovian auroral emission cuts off at ~40 MHz (14 Gauss), its quiescent emission is broadband up to a few GHz (Zarka 2007). Likewise, auroral brown dwarfs emit pulses at $\gtrsim$4–10 GHz and quiescent emission up to ~100 GHz (e.g. Williams et al. 2015). Y dwarf quiescent emission likely falls in this range, regardless of magnetic field strengths.

Second, observations spanning 10 years confirm that the quiescent emission is temporally stable (e.g. Hallinan et al. 2006; Gawroński, Goździewski, and Katarzyński 2016).

6.3 Targets

We have observed 33 targets spanning spectral range L2.5–Y0 and variability periods 1.4–13 hours. All but four of our objects are at 5–22 pc and will be detectable at $\geq 3\sigma$ significance if they have fluxes comparable to the dimmest object from Kao et al. (2016). The remaining four targets are at 27–30 pc, and we have included them because even at those distances, 3/5 of the original detected targets would have been detected.

We have selected all of our targets for confirmed variability at optical bands I and R (Heinze, Metchev, and Kellogg 2015) and/or infrared bands J, H and K (Clarke et al. 2008; Khandrika et al. 2013; Radigan et al. 2014; J. Radigan 2014; Buenzli et al. 2014; Metchev et al. 2015; Rajan et al. 2015). Our selection process is motivated by **(a)** recent results showing low-amplitude I-band variability at the ∼0.5–2.2% level for known auroral radio emitters (Harding et al. 2013), **(b)** optical line emission and broadband continnuum at wavelengths corresponding to I- and R-bands that vary with auroral radio emission and correspond to an auroral surface feature (Hallinan et al. 2015), **(c)** the coincidence of J-, H-, and K-band variability with newly confirmed auroral radio emitters (Kao et al. 2016), and **(d)** predictions of increased emission at wavelengths corresponding to K-band or longer due to localized atmospheric heating (Morley, Marley, Fortney, and Lupu 2014). Our target list represents all known optical/IR variables that have not yet been observed at C-band frequencies at the sensitivity that we will achieve with the recently-updated VLA.

Analysis is ongoing; however, two objects of interest with completed analyses are described below:

2MASS J21392676+0220226. 2M2139+02 is a canonical example of a high amplitude and period L/T transition cloud variable brown dwarf, with J-band amplitude as high as ∼26% and a 7.721±0.005 hr period (Radigan et al. 2012; Apai et al. 2013; Khandrika et al. 2013; Wilson, Rajan, and Patience 2014). It was classified as a T0 using its optical spectrum by Reid et al. (2008) and as T1.5 dwarf using its near infrared spectrum by Burgasser et al. (2006). It is more red than usual for a T1 or a T2 dwarf and Burgasser et al. (2010) report that it may be a binary, with inferred components corresponding to L8.5±0.7 and T3.5±1.0, though its binary

nature remain unconfirmed by HST NICMOS observations to orbital separations <1 AU (Radigan et al. 2012). It has an estimated ∼3 Gyr age and effective temperature $T_{\rm eff}$ = 1270 ± 100 K (Radigan et al. 2012) and a parallax of 101.5 ± 2.0 mas (Smart et al. 2013).

WISEP J173835.53+273258.9. WISE 1738+27 was discovered by Cushing et al. (2011) and classified as a Y0 dwarf with an effective temperature of 430^{+50}_{-40} K (Dupuy and Kraus 2013), and it serves as the Y0 spectral standard (Kirkpatrick et al. 2012) and a parallax of 111 ± 36 mas (Leggett et al. 2013). Rajan et al. (2015) previously reported that it exhibited no statistically significant J-band variability, though they were only able to place an upper limit of <20.3% on the amplitude. In contrast, Leggett et al. (2016) observed 4.5-μm variability characteristic of a double sinusoid with 6.0 ± 0.1 hr and 3.0 ± 0.1 hr periods and peak-to-peak amplitude 3%, whereas near infrared monitoring at 1 μm and Y and J bands are marginally consistent with a ∼3.0 hr period and amplitudes as high as ∼5–30%. The wavelength dependence and amplitude of the variability suggests atmospheric phenomena similar to what has been observed in the Solar System gas giant planets.

6.4 Observations

We observed each target for 2 hours for a total of 66 program hours at C-band using the full 4 GHz bandwidth available for ∼3 μJy sensitivity to quiescent emission in the 3-bit observing mode for the WIDAR correlator. We have elected to use quiescent emission as a proxy for auroral radio emission, bypassing more time-intensive full-period observations. Observations were taken between 02 April 2016 and 14 August 2016 during C, CnB, and B configurations.

6.4.1 Calibrations

We calibrated our measurement sets using the standard VLA flux calibrators 3C286, 3C48, and 3C147 as well as nearby phase calibrators. Typical full-bandwidth sensitivities at B, CnB, and C configurations for 2 hour observing blocks in C-band range from 2.6–3.3 μJy, and typical 3-bit observations reaching an absolute flux calibration accuracy of ∼5%. To account for phase errors in the flux calibration, we observed a nearby phase calibrator for two minutes per ∼20 minute cycle. Resulting gain solutions are satisfactory, varying smoothly without large jumps to introduce erroneous phase wraps.

We initially processed each measurement set using the VLA Calibration Pipeline, after which we flagged all remaining RFI and manually recalibrated as needed. As

a rule, all data between 4.0–4.4 GHz was discarded due to extremely bright and persistent RFI.

6.5 Preliminary Results

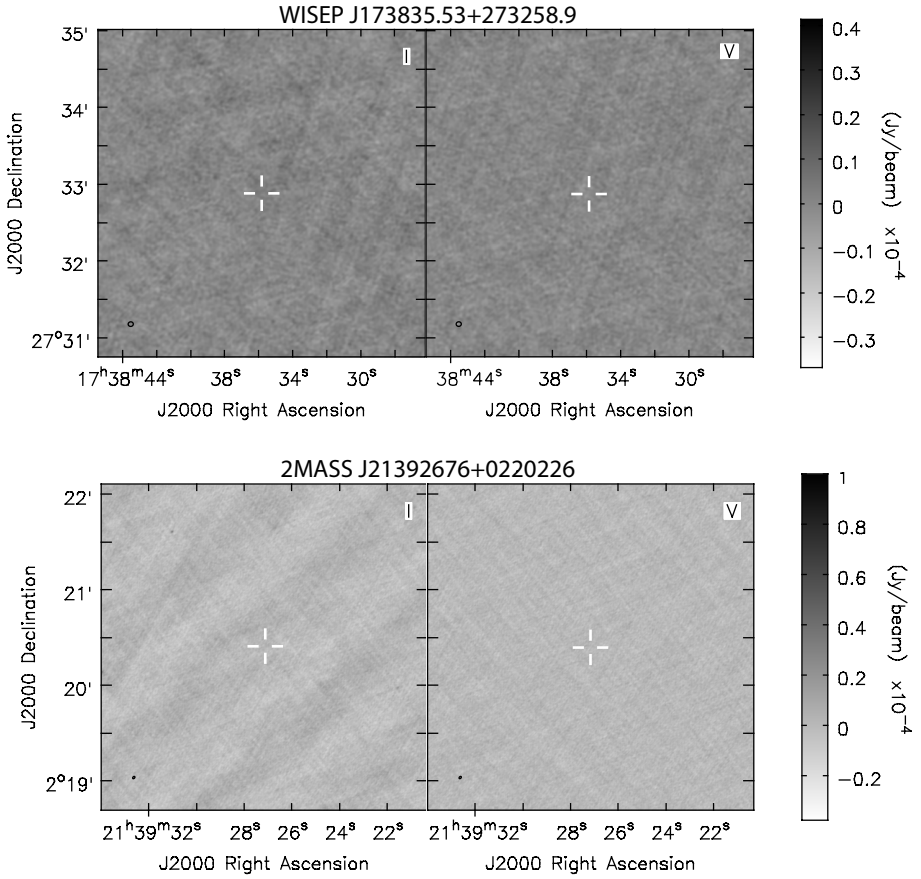

Figure 6.2: Stokes I (left) and V (right) images of both objects. Ellipse in bottom left-hand corner depicts synthesized beam. Crosshairs indicate proper motion corrected coordinates. No point sources were detected.

We produced Stokes I and Stokes V images of each object (total and circularly polarized intensities, respectively) with the CASA `clean` routine, modeling the sky emission frequency dependence with one term and using natural weighting. We searched for a point source at the proper motion-corrected coordinates of each target. Figure 6.2 shows the Stokes I and Stokes V images for both objects. We did not detect any radio emission from either 2M2139+02 or WISE 1738+27, down to rms noise levels of 3.3 μJy and 2.3 μJy, respectively.

To check for any pulsed emission that may have been averaged down to undetectable levels in a 4-hour image, we created 4–8 GHz, 4–6 GHz, and 6–8 GHz timeseries

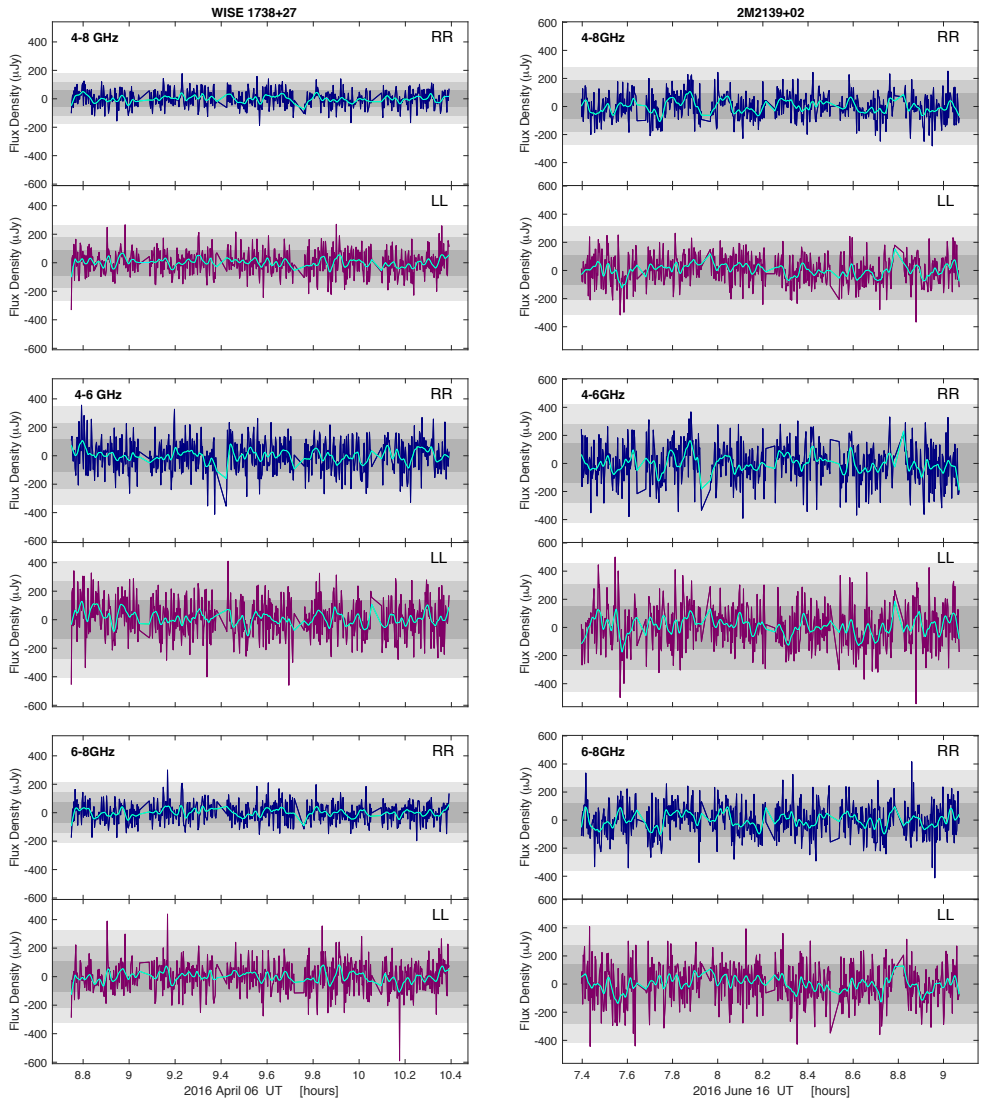

Figure 6.3: Timeseries of rr- and ll-correlated (blue and red, respectively) flux densities averaged over 10 s intervals. Green lines are smoothed timeseries used for identifying pulse candidates and overlaid cyan lines show removed pulse candidates for calculating rms noise and imaging quiescent emission. In all cases above, no pulses were detected, so cyan lines overlay green lines. Grey dashed lines are aligned to pulse peaks. Grey regions indicates 1σ, 2σ, and 3σ rms noise.

of the right- and left-circularly polarized emission at the expected locations for both targets, following the procedure outlined in §5.5.2. Figure 6.3 shows the 60s timeseries for each object. We do not detect any circularly polarized radio pulses or quiescent emission for either dwarf.

6.6 Science Impact

We summarize possible implications for this study which will be explored more completely once analysis is complete:

1. Guaranteed Implications for Brown Dwarf Weather

This survey will form the foundation of understanding the relationship between brown dwarf weather and auroral emission. Specifically, detections and non-detections alike will yield the first constraints on the occurrence rate of quiescent radio emission (a proxy for auroral activity) relative to cloud phenomena spanning the full L through T spectral sequence.

2. Implications for Brown Dwarf Aurorae

Our observations may coincide with auroral radio pulses from our objects. In these cases, the flux densities of our pulses combined with existing optical/IR variability data will inform multi-frequency studies constraining the power distribution of brown dwarf aurorae.

3. Implications for Magnetic Dynamo Models

In the event that we observe radio pulses, Kao et al. (2016) demonstrated that auroral radio emission is a uniquely powerful tool for measuring local magnetic field strengths. In fact, no other method can currently probe fields of ≥L0 objects (Reiners and Basri 2007). Auroral radio emission is produced and observed at the electron cyclotron frequency ($\nu_{\rm MHz} \sim 2.8 \times B_{\rm Gauss}$) (Treumann 2006) when the ratio of the plasma frequency is much less than the electron cyclotron frequency (Winglee 1985). Such conditions are met in the cool, neutral atmospheres of L and T dwarfs, and detections of auroral radio pulses yield very accurate measurements of magnetic field strengths and rotation periods. The original pilot study demonstrating the efficacy of our proposed survey led to the confirmation of ≥2.5 kG magnetic fields in large-scale configurations for dwarfs as cool as T6.5, with subsequent constraints on the magnetic dynamo mechanism at work in the interiors of fully convective objects spanning stars through planets (Kao et al. 2016). Any detections of auroral radio pulses in C-band will similarly yield magnetic field constraints of ≥2.5 kG for our target list.

4. Targets for a Future Survey

Even in cases where we observe only quiescent radio emission and no pulses, all instances of quiescent emission in ultracool (>M7) dwarfs have so far been linked to pulsed auroral radio emission and vice versa. Quiescent radio detections will therefore form the basis of a future, deeper study targeted toward observing auroral

radio pulses and rotation periods independent of the changing cloud compositions of our objects.

Chapter 7

CONCLUSIONS

At the outset of my dissertation, we knew little about the behaviors of magnetic fields in the coolest objects toeing the substellar-planetary boundary beyond the insights gleaned from our Solar System, observations of warmer brown dwarfs, and myriad predictions from stellar and planetary numerical models still striving to probe realistic parameters.

To push the boundaries of our knowledge and begin systematically probing the magnetic characteristics of the most enigmatic brown dwarfs, I have worked closely with my research group to bridge together expertise in the stellar and planetary communities and develop a new framework within which to interpret traditional markers of magnetic activity. Together, we have used the auroral paradigm as a launching pad for investigating whether aurorae occur on brown dwarfs, and if so, what the aurorae can reveal about the magnetospheric dynamics, atmospheres, interior dynamics, and magnetic field behaviors.

This thesis presents an exciting new avenue for interpreting dynamo theory by developing auroral radio emission as a more effective tool for studying magnetism on the coolest substellar objects. From the work presented here, it has become clear that strong and large-scale fields persist down to late T dwarfs, regardless of age, temperature (luminosity), and mass. It is also evident that fast rotation may play a role in generating such fields as well as the auroral emission we have observed.

However, one of the great joys of science is that even as we work to resolve questions, yet more questions arise, and much work remains to be done. I list here but a few of the possible avenues for exploration:

No magnetic field measurements of Y dwarfs currently exist, but for fully convective dynamo models to accurately predict exoplanet magnetic fields, pushing measurements to include Y dwarfs and eventually exoplanets is critical. Observing auroral emission is currently the only possible method for measuring field strengths on these coolest dwarfs. For the first time in six years since the discovery of Y dwarfs, the known Y dwarf population is large enough to conduct a statistically meaningful Y dwarf radio aurora study. Photometric studies demonstrate ubiquitous optical and infrared variability in L and T dwarfs (eg. Radigan et al. 2014; Heinze, Metchev,

and Kellogg 2015; Metchev et al. 2015), suggesting this may also be the case for Y dwarfs. To that end, I am leading a radio survey using quiescent radio emission to identify Y dwarf candidates likely to exhibit highly circularly polarized and pulsed radio aurorae and provide the first constraints on magnetic dynamos in these coolest, most planet-like brown dwarfs.

My dissertation provided the first test in the ultracool brown dwarf regime of a fully convective dynamo model focusing on rapidly rotating objects, which are one limiting case for dynamo models. However, models considering a range of rotation rates predict observable relationships between magnetic properties and rotation which the selection method that I presented in §3.3 may make possible to test. The observations presented in this dissertation lay the foundation for a comprehensive observational study of the role played by rotation in dynamo action, which will become more apparent as I push measurements to higher frequencies in search of the ECM cutoff frequency corresponding to fields nearest the surface of the atmosphere, where they are strongest. Additionally, characterizing the brown dwarfs in this comprehensive sample will lead to the possibility of teasing out information about the evolution of brown dwarf magnetic fields with age.

Beyond physical properties of brown dwarfs, another constraining characteristic of dynamos is the time variation of magnetic fields. A recent attempt pointed to circular polarization evolution in auroral radio pulses as indirect evidence of magnetic cycles in L/T dwarfs (Route 2016). They observed reversals in pulse polarizations, the appearance of both polarizations in double-peaked emission, and/or quiescent periods from five brown dwarfs over 3–5 years. However, the data are inconclusive; drifting magnetic poles and changing auroral cavity plasma conditions can reproduce the observed phenomena (Leto et al. 2016). Monitoring ECM cutoff frequencies in the coolest radio brown dwarfs over several years to search for fluctuations in their field strengths may provide more conclusive evidence of any magnetic cycles. The ECM emission cutoff frequency likely traces large-scale fields, and if either of the two scenarios are responsible, the cutoff frequencies should not evolve appreciably over time. However, waxing or waning field strengths accompanying polarization evolution would be more concrete evidence of changing magnetic topologies. Detections (or non-detections) of temporal variation in brown dwarf magnetic fields could provide smoking gun evidence to rule out dynamo models predicting time-independent (or time-dependent) behaviors.

BIBLIOGRAPHY

Acuna, M. H., J. E. P. Connerney, N. F. Ness, R. P. Lin, D. Mitchell, C. W. Carlson, J. McFadden, et al. 1999. "Global Distribution of Crustal Magnetization Discovered by the Mars Global Surveyor MAG/ER Experiment." *Science* 284 (April): 790. doi:10.1126/science.284.5415.790.

Acuna, M. H., and N. F. Ness. 1976. "The main magnetic field of Jupiter." *J. Geophys. Res.* 81 (June): 2917–2922. doi:10.1029/JA081i016p02917.

Allard, F., D. Homeier, and B. Freytag. 2011. "Model Atmospheres From Very Low Mass Stars to Brown Dwarfs." In *16th Cambridge Workshop on Cool Stars, Stellar Systems, and the Sun,* edited by C. Johns-Krull, M. K. Browning, and A. A. West, 448:91. Astronomical Society of the Pacific Conference Series. December. arXiv: 1011.5405 [astro-ph.SR].

Antonova, A., J. G. Doyle, G. Hallinan, A. Golden, and C. Koen. 2007. "Sporadic long-term variability in radio activity from a brown dwarf." *A&A* 472 (September): 257–260. doi:10.1051/0004-6361:20077231. arXiv: 0707.0634.

Antonova, A., G. Hallinan, J. G. Doyle, S. Yu, A. Kuznetsov, Y. Metodieva, A. Golden, and K. L. Cruz. 2013. "Volume-limited radio survey of ultracool dwarfs." *A&A* 549, A131 (January): A131. doi:10.1051/0004-6361/201118583. arXiv: 1212.3464 [astro-ph.SR].

Apai, D., J. Radigan, E. Buenzli, A. Burrows, I. N. Reid, and R. Jayawardhana. 2013. "HST Spectral Mapping of L/T Transition Brown Dwarfs Reveals Cloud Thickness Variations." *ApJ* 768, 121 (May): 121. doi:10.1088/0004-637X/768/2/121. arXiv: 1303.4151 [astro-ph.EP].

Artigau, É., S. Bouchard, R. Doyon, and D. Lafrenière. 2009. "Photometric Variability of the T2.5 Brown Dwarf SIMP J013656.5+093347: Evidence for Evolving Weather Patterns." *ApJ* 701 (August): 1534–1539. doi:10.1088/0004-637X/701/2/1534. arXiv: 0906.3514 [astro-ph.SR].

Artigau, É., R. Doyon, D. Lafrenière, D. Nadeau, J. Robert, and L. Albert. 2006. "Discovery of the Brightest T Dwarf in the Northern Hemisphere." *ApJ* 651 (November): L57–L60. doi:10.1086/509146. eprint: astro-ph/0609419.

Artigau, E., D. Nadeau, and R. Doyon. 2003. "T Dwarf Photometric Variability." In *Brown Dwarfs,* edited by E. Martin, 211:451. IAU Symposium. June.

Babcock, H. W. 1961. "The Topology of the Sun's Magnetic Field and the 22-YEAR Cycle." *ApJ* 133 (March): 572. doi:10.1086/147060.

Badman, S. V., G. Branduardi-Raymont, M. Galand, S. L. G. Hess, N. Krupp, L. Lamy, H. Melin, and C. Tao. 2015. "Auroral Processes at the Giant Planets: Energy Deposition, Emission Mechanisms, Morphology and Spectra." *Space Sci. Rev.* 187 (April): 99–179. doi:10.1007/s11214-014-0042-x.

Bagenal, F. 1994. "Empirical model of the Io plasma torus: Voyager measurements." *J. Geophys. Res.* 99 (June): 11043–11062. doi:10.1029/93JA02908.

Bagenal, F., A. Adriani, F. Allegrini, S. J. Bolton, B. Bonfond, E. J. Bunce, J. E. P. Connerney, et al. 2014. "Magnetospheric Science Objectives of the Juno Mission." *Space Sci. Rev.* (February): 1–69. doi:10.1007/s11214-014-0036-8.

Bailer-Jones, C. A. L., and R. Mundt. 2001. "Variability in ultra cool dwarfs: Evidence for the evolution of surface features." *A&A* 367 (February): 218–235. doi:10.1051/0004-6361:20000416. eprint: astro-ph/0012224.

Baraffe, I., G. Chabrier, T. S. Barman, F. Allard, and P. H. Hauschildt. 2003. "Evolutionary models for cool brown dwarfs and extrasolar giant planets. The case of HD 209458." *A&A* 402 (May): 701–712. doi:10.1051/0004-6361:20030252. eprint: astro-ph/0302293.

Basri, G. 2001. "Rotation and Hα Emission Above and Below the Substellar Boundary (CD-ROM Directory: contribs/basri)." In *11th Cambridge Workshop on Cool Stars, Stellar Systems and the Sun,* edited by R. J. Garcia Lopez, R. Rebolo, and M. R. Zapaterio Osorio, 223:261. Astronomical Society of the Pacific Conference Series.

Basri, G., and G. W. Marcy. 1995. "A surprise at the bottom of the main sequence: Rapid rotation and NO H-alpha emission." *AJ* 109 (February): 762–773. doi:10.1086/117319.

Bastian, T. S., A. O. Benz, and D. E. Gary. 1998. "Radio Emission from Solar Flares." *ARA&A* 36:131–188. doi:10.1146/annurev.astro.36.1.131.

Batygin, K., and D. J. Stevenson. 2010. "Inflating Hot Jupiters with Ohmic Dissipation." *ApJ* 714 (May): L238–L243. doi:10.1088/2041-8205/714/2/L238. arXiv: 1002.3650 [astro-ph.EP].

Benz, A. O. 1986. "Millisecond radio spikes." *Sol. Phys.* 104 (March): 99–110. doi:10.1007/BF00159950.

Benz, A. O., and M. Güdel. 2010. "Physical Processes in Magnetically Driven Flares on the Sun, Stars, and Young Stellar Objects." *ARA&A* 48 (September): 241–287. doi:10.1146/annurev-astro-082708-101757.

Berdyugina, S. V., and S. K. Solanki. 2002. "The molecular Zeeman effect and diagnostics of solar and stellar magnetic fields. I. Theoretical spectral patterns in the Zeeman regime." *A&A* 385 (April): 701–715. doi:10.1051/0004-6361:20020130.

Berger, E. 2002. "Flaring up All Over-Radio Activity in Rapidly Rotating Late M and L Dwarfs." *ApJ* 572 (June): 503–513. doi:10.1086/340301. eprint: astro-ph/0111317.

———. 2006. "Radio Observations of a Large Sample of Late M, L, and T Dwarfs: The Distribution of Magnetic Field Strengths." *ApJ* 648 (September): 629–636. doi:10.1086/505787. eprint: astro-ph/0603176.

Berger, E., S. Ball, K. M. Becker, M. Clarke, D. A. Frail, T. A. Fukuda, I. M. Hoffman, et al. 2001. "Discovery of radio emission from the brown dwarf LP944-20." *Nature* 410 (March): 338–340. eprint: astro-ph/0102301.

Berger, E., G. Basri, T. A. Fleming, M. S. Giampapa, J. E. Gizis, J. Liebert, E. Martin, N. Phan-Bao, and R. E. Rutledge. 2010. "Simultaneous Multi-Wavelength Observations of Magnetic Activity in Ultracool Dwarfs. III. X-ray, Radio, and Hα Activity Trends in M and L dwarfs." *ApJ* 709 (January): 332–341. doi:10.1088/0004-637X/709/1/332. arXiv: 0909.4783 [astro-ph.SR].

Berger, E., G. Basri, J. E. Gizis, M. S. Giampapa, R. E. Rutledge, J. Liebert, E. Martin, et al. 2008. "Simultaneous Multiwavelength Observations of Magnetic Activity in Ultracool Dwarfs. II. Mixed Trends in VB 10 and LSR 1835+32 and the Possible Role of Rotation." *ApJ* 676 (April): 1307–1318. doi:10.1086/529131. arXiv: 0710.3383.

Berger, E., R. E. Rutledge, N. Phan-Bao, G. Basri, M. S. Giampapa, J. E. Gizis, J. Liebert, E. Martin, and T. A. Fleming. 2009. "Periodic Radio and Hα Emission from the L Dwarf Binary 2MASSW J0746425+200032: Exploring the Magnetic Field Topology and Radius Of An L Dwarf." *ApJ* 695 (April): 310–316. doi:10.1088/0004-637X/695/1/310. arXiv: 0809.0001.

Berger, E., R. E. Rutledge, I. N. Reid, L. Bildsten, J. E. Gizis, J. Liebert, E. Martin, et al. 2005. "The Magnetic Properties of an L Dwarf Derived from Simultaneous Radio, X-Ray, and Hα Observations." *ApJ* 627 (July): 960–973. doi:10.1086/430343. eprint: astro-ph/0502384.

Bhardwaj, A., and G. R. Gladstone. 2000. "Auroral emissions of the giant planets." *Reviews of Geophysics* 38:295–354. doi:10.1029/1998RG000046.

Bower, G. C., L. Loinard, S. Dzib, P. A. B. Galli, G. N. Ortiz-León, C. Moutou, and J.-F. Donati. 2016. "Variable Radio Emission from the Young Stellar Host of a Hot Jupiter." *ArXiv e-prints* (August). arXiv: 1608.00962 [astro-ph.SR].

Brain, D. A., J. P. McFadden, J. S. Halekas, J. E. P. Connerney, S. W. Bougher, S. Curry, C. F. Dong, et al. 2015. "The spatial distribution of planetary ion fluxes near Mars observed by MAVEN." *Geophys. Res. Lett.* 42 (November): 9142–9148. doi:10.1002/2015GL065293.

Browning, M. K. 2008. "Simulations of Dynamo Action in Fully Convective Stars." *ApJ* 676 (April): 1262–1280. doi:10.1086/527432. arXiv: 0712.1603.

Browning, M. K., G. Basri, G. W. Marcy, A. A. West, and J. Zhang. 2010. "Rotation and Magnetic Activity in a Sample of M-Dwarfs." *AJ* 139 (February): 504–518. doi:10.1088/0004-6256/139/2/504.

Buenzli, E., D. Apai, J. Radigan, I. N. Reid, and D. Flateau. 2014. "Brown Dwarf Photospheres are Patchy: A Hubble Space Telescope Near-infrared Spectroscopic Survey Finds Frequent Low-level Variability." *ApJ* 782, 77 (February): 77. doi:10.1088/0004-637X/782/2/77. arXiv: 1312.5294 [astro-ph.SR].

Burgasser, A. J. 2001. "The Discovery and Characterization of Methane Bearing Brown Dwarfs and the Definition of the T Spectral Class." PhD diss., California Institute of Technology.

———. 2007. "Binaries and the L Dwarf/T Dwarf Transition." *ApJ* 659 (April): 655–674. doi:10.1086/511027. eprint: astro-ph/0611505.

———. 2014. "The SpeX Prism Library: 1000+ low-resolution, near-infrared spectra of ultracool M, L, T and Y dwarfs." In *Astronomical Society of India Conference Series,* 11:7–16. Astronomical Society of India Conference Series. arXiv: 1406.4887 [astro-ph.SR].

Burgasser, A. J., A. Burrows, and J. D. Kirkpatrick. 2006. "A Method for Determining the Physical Properties of the Coldest Known Brown Dwarfs." *ApJ* 639 (March): 1095–1113. doi:10.1086/499344. eprint: astro-ph/0510707.

Burgasser, A. J., K. L. Cruz, M. Cushing, C. R. Gelino, D. L. Looper, J. K. Faherty, J. D. Kirkpatrick, and I. N. Reid. 2010. "SpeX Spectroscopy of Unresolved Very Low Mass Binaries. I. Identification of 17 Candidate Binaries Straddling the L Dwarf/T Dwarf Transition." *ApJ* 710 (February): 1142–1169. doi:10.1088/0004-637X/710/2/1142. arXiv: 0912.3808 [astro-ph.SR].

Burgasser, A. J., T. R. Geballe, S. K. Leggett, J. D. Kirkpatrick, and D. A. Golimowski. 2006. "A Unified Near-Infrared Spectral Classification Scheme for T Dwarfs." *ApJ* 637 (February): 1067–1093. doi:10.1086/498563. eprint: astro-ph/0510090.

Burgasser, A. J., M. Gillon, J. K. Faherty, J. Radigan, A. H. M. J. Triaud, P. Plavchan, R. Street, E. Jehin, L. Delrez, and C. Opitom. 2014. "A Monitoring Campaign for Luhman 16AB. I. Detection of Resolved Near-infrared Spectroscopic Variability." *ApJ* 785, 48 (April): 48. doi:10.1088/0004-637X/785/1/48. arXiv: 1402.2342 [astro-ph.SR].

Burgasser, A. J., M. Gillon, C. Melis, B. P. Bowler, E. L. Michelsen, D. Bardalez Gagliuffi, C. R. Gelino, et al. 2015. "WISE J072003.20-084651.2: an Old and Active M9.5 + T5 Spectral Binary 6 pc from the Sun." *AJ* 149, 104 (March): 104. doi:10.1088/0004-6256/149/3/104. arXiv: 1410.4288 [astro-ph.SR].

Burgasser, A. J., J. D. Kirkpatrick, M. E. Brown, I. N. Reid, A. Burrows, J. Liebert, K. Matthews, et al. 2002. "The Spectra of T Dwarfs. I. Near-Infrared Data and Spectral Classification." *ApJ* 564 (January): 421–451. doi:10.1086/324033. eprint: astro-ph/0108452.

Burgasser, A. J., J. D. Kirkpatrick, M. E. Brown, I. N. Reid, J. E. Gizis, C. C. Dahn, D. G. Monet, et al. 1999. "Discovery of Four Field Methane (T-Type) Dwarfs with the Two Micron All-Sky Survey." *ApJ* 522 (September): L65–L68. doi:10.1086/312221.

Burgasser, A. J., J. D. Kirkpatrick, R. M. Cutri, H. McCallon, G. Kopan, J. E. Gizis, J. Liebert, et al. 2000. "Discovery of a Brown Dwarf Companion to Gliese 570ABC: A 2MASS T Dwarf Significantly Cooler than Gliese 229B." *ApJ* 531 (March): L57–L60. doi:10.1086/312522. eprint: astro-ph/0001194.

Burgasser, A. J., J. D. Kirkpatrick, J. Liebert, and A. Burrows. 2003. "The Spectra of T Dwarfs. II. Red Optical Data." *ApJ* 594 (September): 510–524. doi:10.1086/376756. eprint: astro-ph/0305139.

Burgasser, A. J., J. D. Kirkpatrick, I. N. Reid, J. Liebert, J. E. Gizis, and M. E. Brown. 2000. "Detection of Hα Emission in a Methane (T Type) Brown Dwarf." *AJ* 120 (July): 473–478. doi:10.1086/301423. eprint: astro-ph/0003291.

Burgasser, A. J., J. Liebert, J. D. Kirkpatrick, and J. E. Gizis. 2002. "A Search for Variability in the Active T Dwarf 2MASS 1237+6526." *AJ* 123 (May): 2744–2753. doi:10.1086/339836. eprint: astro-ph/0201382.

Burgasser, A. J., M. C. Liu, M. J. Ireland, K. L. Cruz, and T. J. Dupuy. 2008. "Subtle Signatures of Multiplicity in Late-type Dwarf Spectra: The Unresolved M8.5 + T5 Binary 2MASS J03202839-0446358." *ApJ* 681 (July): 579–593. doi:10.1086/588379. arXiv: 0803.0295.

Burgasser, A. J., M. W. McElwain, J. D. Kirkpatrick, K. L. Cruz, C. G. Tinney, and I. N. Reid. 2004. "The 2MASS Wide-Field T Dwarf Search. III. Seven New T Dwarfs and Other Cool Dwarf Discoveries." *AJ* 127 (May): 2856–2870. doi:10.1086/383549. eprint: astro-ph/0402325.

Burgasser, A. J., C. Melis, J. Todd, C. R. Gelino, G. Hallinan, and D. Bardalez Gagliuffi. 2015. "Radio Emission and Orbital Motion from the Close-encounter Star-Brown Dwarf Binary WISE J072003.20-084651.2." *AJ* 150, 180 (December): 180. doi:10.1088/0004-6256/150/6/180. arXiv: 1508.06332 [astro-ph.SR].

Burgasser, A. J., C. Melis, B. A. Zauderer, and E. Berger. 2013. "Detection of Radio Emission from the Hyperactive L Dwarf 2MASS J13153094-2649513AB." *ApJ* 762, L3 (January): L3. doi:10.1088/2041-8205/762/1/L3. arXiv: 1211.3479 [astro-ph.SR].

Burgasser, A. J., and M. E. Putman. 2005. "Quiescent Radio Emission from Southern Late-Type M Dwarfs and a Spectacular Radio Flare from the M8 Dwarf DENIS 1048-3956." *ApJ* 626 (June): 486–497. doi:10.1086/429788. eprint: astro-ph/0502365.

Burgasser, A. J., I. N. Reid, S. K. Leggett, J. D. Kirkpatrick, J. Liebert, and A. Burrows. 2005. "SDSS J042348.57-041403.5AB: A Brown Dwarf Binary Straddling the L/T Transition." *ApJ* 634 (December): L177–L180. doi:10.1086/498866. eprint: astro-ph/0510580.

Burrows, A., W. B. Hubbard, D. Saumon, and J. I. Lunine. 1993. "An expanded set of brown dwarf and very low mass star models." *ApJ* 406 (March): 158–171. doi:10.1086/172427.

Burrows, A., M. Marley, W. B. Hubbard, J. I. Lunine, T. Guillot, D. Saumon, R. Freedman, D. Sudarsky, and C. Sharp. 1997. "A Nongray Theory of Extrasolar Giant Planets and Brown Dwarfs." *ApJ* 491 (December): 856–875. eprint: astro-ph/9705201.

Burrows, A., D. Sudarsky, and I. Hubeny. 2006. "L and T Dwarf Models and the L to T Transition." *ApJ* 640 (April): 1063–1077. doi:10.1086/500293. eprint: astro-ph/0509066.

Burton, M. E., M. K. Dougherty, and C. T. Russell. 2009. "Model of Saturn's internal planetary magnetic field based on Cassini observations." *Planet. Space Sci.* 57 (December): 1706–1713. doi:10.1016/j.pss.2009.04.008.

Calvert, W. 1981. "The auroral plasma cavity." *Geophys. Res. Lett.* 8 (August): 919–921. doi:10.1029/GL008i008p00919.

Carson, J. C., M. Marengo, B. M. Patten, K. L. Luhman, S. M. Sonnett, J. L. Hora, M. T. Schuster, et al. 2011. "A Spitzer IRAC Imaging Survey for T Dwarf Companions around M, L, and T Dwarfs: Observations, Results, and Monte Carlo Population Analyses." *ApJ* 743, 141 (December): 141. doi:10.1088/0004-637X/743/2/141. arXiv: 1110.2191 [astro-ph.SR].

Chabrier, G., and I. Baraffe. 1997. "Structure and evolution of low-mass stars." *A&A* 327 (November): 1039–1053. eprint: astro-ph/9704118.

Chabrier, G., and M. Küker. 2006. "Large-scale α^2-dynamo in low-mass stars and brown dwarfs." *A&A* 446 (February): 1027–1037. doi:10.1051/0004-6361:20042475. eprint: astro-ph/0510075.

Charbonneau, P. 2005. "Dynamo Models of the Solar Cycle." *Living Reviews in Solar Physics* 2, 2 (June): 2. doi:10.12942/lrsp-2005-2.

Chiu, Y. T., and M. Schulz. 1978. "Self-consistent particle and parallel electrostatic field distributions in the magnetospheric-ionospheric auroral region." *J. Geophys. Res.* 83 (February): 629–642. doi:10.1029/JA083iA02p00629.

Christensen, U. R. 2010. "Dynamo Scaling Laws and Applications to the Planets." *Space Sci. Rev.* 152 (May): 565–590. doi:10.1007/s11214-009-9553-2.

Christensen, U. R., and J. Aubert. 2006. "Scaling properties of convection-driven dynamos in rotating spherical shells and application to planetary magnetic fields." *Geophysical Journal International* 166 (July): 97–114. doi:10.1111/j.1365-246X.2006.03009.x.

Christensen, U. R., V. Holzwarth, and A. Reiners. 2009. "Energy flux determines magnetic field strength of planets and stars." *Nature* 457 (January): 167–169. doi:10.1038/nature07626.

Clarke, F. J., S. T. Hodgkin, B. R. Oppenheimer, J. Robertson, and X. Haubois. 2008. "A search for J-band variability from late-L and T brown dwarfs." *MNRAS* 386 (June): 2009–2014. doi:10.1111/j.1365-2966.2008.13135.x.

Connerney, J. E. P., M. H. Acuna, P. J. Wasilewski, N. F. Ness, H. Reme, C. Mazelle, D. Vignes, R. P. Lin, D. L. Mitchell, and P. A. Cloutier. 1999. "Magnetic Lineations in the Ancient Crust of Mars." *Science* 284 (April): 794. doi:10.1126/science.284.5415.794.

Cook, B. A., P. K. G. Williams, and E. Berger. 2014. "Trends in Ultracool Dwarf Magnetism. II. The Inverse Correlation Between X-Ray Activity and Rotation as Evidence for a Bimodal Dynamo." *ApJ* 785, 10 (April): 10. doi:10.1088/0004-637X/785/1/10. arXiv: 1310.6758 [astro-ph.SR].

Cowley, S. W. H., and E. J. Bunce. 2001. "Origin of the main auroral oval in Jupiter's coupled magnetosphere-ionosphere system." *Planet. Space Sci.* 49 (August): 1067–1088. doi:10.1016/S0032-0633(00)00167-7.

Croll, B., P. S. Muirhead, J. Lichtman, E. Han, P. A. Dalba, and J. Radigan. 2016. "Long-term, Multiwavelength Light Curves of Ultra-Cool Dwarfs: II. The evolving Light Curves of the T2.5 SIMP 0136 & the Uncorrelated Light Curves of the M9 TVLM 513." *ArXiv e-prints* (September). arXiv: 1609.03587 [astro-ph.SR].

Cruz, K. L., A. J. Burgasser, I. N. Reid, and J. Liebert. 2004. "2MASS J05185995-2828372: Discovery of an Unresolved L/T Binary." *ApJ* 604 (March): L61–L64. doi:10.1086/383415. eprint: astro-ph/0402172.

Cruz, K. L., I. N. Reid, J. D. Kirkpatrick, A. J. Burgasser, J. Liebert, A. R. Solomon, S. J. Schmidt, P. R. Allen, S. L. Hawley, and K. R. Covey. 2007. "Meeting the Cool Neighbors. IX. The Luminosity Function of M7-L8 Ultracool Dwarfs in the Field." *AJ* 133 (February): 439–467. doi:10.1086/510132. eprint: astro-ph/0609648.

Cruz, K. L., I. N. Reid, J. Liebert, J. D. Kirkpatrick, and P. J. Lowrance. 2003. "Meeting the Cool Neighbors. V. A 2MASS-Selected Sample of Ultracool Dwarfs." *AJ* 126 (November): 2421–2448. doi:10.1086/378607. eprint: astro-ph/0307429.

Cushing, M. C., K. K. Hardegree-Ullman, J. L. Trucks, C. V. Morley, J. E. Gizis, M. S. Marley, J. J. Fortney, et al. 2016. "The First Detection of Photometric Variability in a Y Dwarf: WISE J140518.39+553421.3." *ApJ* 823, 152 (June): 152. doi:10.3847/0004-637X/823/2/152. arXiv: 1602.06321 [astro-ph.SR].

Cushing, M. C., J. D. Kirkpatrick, C. R. Gelino, R. L. Griffith, M. F. Skrutskie, A. Mainzer, K. A. Marsh, et al. 2011. "The Discovery of Y Dwarfs using Data from the Wide-field Infrared Survey Explorer (WISE)." *ApJ* 743, 50 (December): 50. doi:10.1088/0004-637X/743/1/50. arXiv: 1108.4678 [astro-ph.SR].

Cushing, M. C., M. S. Marley, D. Saumon, B. C. Kelly, W. D. Vacca, J. T. Rayner, R. S. Freedman, K. Lodders, and T. L. Roellig. 2008. "Atmospheric Parameters

of Field L and T Dwarfs." *ApJ* 678 (May): 1372–1395. doi:10.1086/526489. arXiv: 0711.0801.

de Pater, I., and J. J. Lissauer. 2001. *Planetary Sciences,* 544. December.

Delamere, P. A., and F. Bagenal. 2003. "Modeling variability of plasma conditions in the Io torus." *Journal of Geophysical Research (Space Physics)* 108, 1276 (July): 1276. doi:10.1029/2002JA009706.

Delfosse, X., T. Forveille, E. L. Martin, J. Guibert, J. Borsenberger, F. Crifo, C. Alard, et al. 2001. "New neighbours: II. An M9 dwarf at d ˜ 4 pc, DENIS-P J104814.7-395606.1." *A&A* 366 (February): L13–L17. doi:10.1051/0004-6361:20010001.

Delfosse, X., T. Forveille, C. Perrier, and M. Mayor. 1998. "Rotation and chromospheric activity in field M dwarfs." *A&A* 331 (March): 581–595.

Dobler, W., M. Stix, and A. Brandenburg. 2006. "Magnetic Field Generation in Fully Convective Rotating Spheres." *ApJ* 638 (February): 336–347. doi:10.1086/498634. eprint: astro-ph/0410645.

Donati, J.-F., T. Forveille, A. Collier Cameron, J. R. Barnes, X. Delfosse, M. M. Jardine, and J. A. Valenti. 2006. "The Large-Scale Axisymmetric Magnetic Topology of a Very-Low-Mass Fully Convective Star." *Science* 311 (February): 633–635. doi:10.1126/science.1121102. eprint: astro-ph/0602069.

Donati, J.-F., J. Morin, P. Petit, X. Delfosse, T. Forveille, M. Aurière, R. Cabanac, et al. 2008. "Large-scale magnetic topologies of early M dwarfs." *MNRAS* 390 (October): 545–560. doi:10.1111/j.1365-2966.2008.13799.x. arXiv: 0809.0269.

Drake, S. A., T. Simon, and J. L. Linsky. 1989. "A survey of the radio continuum emission of RS Canum Venaticorum and related active binary systems." *ApJS* 71 (December): 905–930. doi:10.1086/191402.

Dressing, C. D., and D. Charbonneau. 2013. "The Occurrence Rate of Small Planets around Small Stars." *ApJ* 767, 95 (April): 95. doi:10.1088/0004-637X/767/1/95. arXiv: 1302.1647 [astro-ph.EP].

Duarte, L. D. V., T. Gastine, and J. Wicht. 2013. "Anelastic dynamo models with variable electrical conductivity: An application to gas giants." *Physics of the Earth and Planetary Interiors* 222 (September): 22–34. doi:10.1016/j.pepi.2013.06.010.

Duarte, L. D. V., J. Wicht, and T. Gastine. 2016. "Physical conditions for Jupiter-like dynamo models." *ArXiv e-prints* (December). arXiv: 1612.02870 [astro-ph.EP].

Dulk, G. A. 1985. "Radio emission from the sun and stars." *ARA&A* 23:169–224. doi:10.1146/annurev.aa.23.090185.001125.

Dupuy, T. J., and A. L. Kraus. 2013. "Distances, Luminosities, and Temperatures of the Coldest Known Substellar Objects." *Science* 341 (September): 1492–1495. doi:10.1126/science.1241917. arXiv: 1309.1422 [astro-ph.SR].

Durney, B. R. 1981. "On a model of a slowly rotating solar convection zone." *ApJ* 244 (March): 678–694. doi:10.1086/158746.

Durney, B. R., D. S. De Young, and T. P. Passot. 1990. "On the generation of the solar magnetic field in a region of weak buoyancy." *ApJ* 362 (October): 709–721. doi:10.1086/169308.

Durney, B. R., D. S. De Young, and I. W. Roxburgh. 1993. "On the generation of the large-scale and turbulent magnetic fields in solar-type stars." *Sol. Phys.* 145 (June): 207–225. doi:10.1007/BF00690652.

Enoch, M. L., M. E. Brown, and A. J. Burgasser. 2003. "Photometric Variability at the L/T Dwarf Boundary." *AJ* 126 (August): 1006–1016. doi:10.1086/376598. eprint: astro-ph/0305048.

Esplin, T., K. Luhman, M. Cushing, K. Hardegree-Ullman, J. Trucks, A. Burgasser, and A. Schneider. 2016. "Photometric Monitoring of the Coldest Known Brown Dwarf with the Spitzer Space Telescope." *ArXiv e-prints* (September). arXiv: 1609.05850 [astro-ph.SR].

Faherty, J. K., C. G. Tinney, A. Skemer, and A. J. Monson. 2014. "Indications of Water Clouds in the Coldest Known Brown Dwarf." *ApJ* 793, L16 (September): L16. doi:10.1088/2041-8205/793/1/L16. arXiv: 1408.4671 [astro-ph.SR].

Forbrich, J., S. J. Wolk, M. Güdel, A. Benz, R. Osten, J. L. Linsky, M. McLean, L. Loinard, and E. Berger. 2011. "The Radio-X-ray Relation in Cool Stars: Are We Headed Toward a Divorce?" In *16th Cambridge Workshop on Cool Stars, Stellar Systems, and the Sun,* edited by C. Johns-Krull, M. K. Browning, and A. A. West, 448:455. Astronomical Society of the Pacific Conference Series. December. arXiv: 1012.1626 [astro-ph.SR].

France, K., C. S. Froning, J. L. Linsky, A. Roberge, J. T. Stocke, F. Tian, R. Bushinsky, et al. 2013. "The Ultraviolet Radiation Environment around M dwarf Exoplanet Host Stars." *ApJ* 763, 149 (February): 149. doi:10.1088/0004-637X/763/2/149. arXiv: 1212.4833 [astro-ph.EP].

France, K., R. O. Parke Loyd, A. Youngblood, A. Brown, P. C. Schneider, S. L. Hawley, C. S. Froning, et al. 2016. "The MUSCLES Treasury Survey. I. Motivation and Overview." *ApJ* 820, 89 (April): 89. doi:10.3847/0004-637X/820/2/89. arXiv: 1602.09142 [astro-ph.SR].

Fuhrmeister, B., and J. H. M. M. Schmitt. 2004. "Detection and high-resolution spectroscopy of a huge flare on the old M 9 dwarf DENIS 104814.7-395606.1." *A&A* 420 (June): 1079–1085. doi:10.1051/0004-6361:20035644. eprint: astro-ph/0403617.

Gagné, J., J. K. Faherty, A. J. Burgasser, É. Artigau, S. Bouchard, L. Albert, D. Lafrenière, R. Doyon, and D. C. Bardalez-Gagliuffi. 2017. "SIMP J013656.5+093347 is Likely a Planetary-Mass Object in the Carina-Near Moving Group." *ArXiv e-prints* (May). arXiv: 1705.01625 [astro-ph.SR].

Gallagher, D. L., and N. Dangelo. 1981. "Correlations between solar wind parameters and auroral kilometric radiation intensity." *Geophys. Res. Lett.* 8 (October): 1087–1089. doi:10.1029/GL008i010p01087.

Galopeau, P. H. M., and A. Lecacheux. 2000. "Variations of Saturn's radio rotation period measured at kilometer wavelengths." *J. Geophys. Res.* 105 (June): 13089–13102. doi:10.1029/1999JA005089.

Galopeau, P., P. Zarka, and D. Le Queau. 1989. "Theoretical model of Saturn's kilometric radiation spectrum." *J. Geophys. Res.* 94 (July): 8739–8755. doi:10.1029/JA094iA07p08739.

Gastine, T., L. Duarte, and J. Wicht. 2012. "Dipolar versus multipolar dynamos: the influence of the background density stratification." *A&A* 546, A19 (October): A19. doi:10.1051/0004-6361/201219799. arXiv: 1208.6093 [astro-ph.SR].

Gastine, T., J. Morin, L. Duarte, A. Reiners, U. R. Christensen, and J. Wicht. 2013. "What controls the magnetic geometry of M dwarfs?" *A&A* 549, L5 (January): L5. doi:10.1051/0004-6361/201220317. arXiv: 1212.0136 [astro-ph.SR].

Gastine, T., J. Wicht, L. D. V. Duarte, M. Heimpel, and A. Becker. 2014. "Explaining Jupiter's magnetic field and equatorial jet dynamics." *Geophys. Res. Lett.* 41 (August): 5410–5419. doi:10.1002/2014GL060814. arXiv: 1407.5940 [astro-ph.EP].

Gawroński, M. P., K. Goździewski, and K. Katarzyński. 2016. "Physical properties and astrometry of radio-emitting brown dwarf TVLM 513-46546 revisited." *MNRAS* (December). doi:10.1093/mnras/stw3329. arXiv: 1612.05656 [astro-ph.SR].

Geballe, T. R., G. R. Knapp, S. K. Leggett, X. Fan, D. A. Golimowski, S. Anderson, J. Brinkmann, et al. 2002. "Toward Spectral Classification of L and T Dwarfs: Infrared and Optical Spectroscopy and Analysis." *ApJ* 564 (January): 466–481. doi:10.1086/324078. eprint: astro-ph/0108443.

Geballe, T. R., D. Saumon, S. K. Leggett, G. R. Knapp, M. S. Marley, and K. Lodders. 2001. "Infrared Observations and Modeling of One of the Coolest T Dwarfs: Gliese 570D." *ApJ* 556 (July): 373–379. doi:10.1086/321575. eprint: astro-ph/0103187.

GéRard, J.-C., A. Saglam, D. Grodent, and J. T. Clarke. 2006. "Morphology of the ultraviolet Io footprint emission and its control by Io's location." *Journal of Geophysical Research (Space Physics)* 111, A04202 (April): A04202. doi:10.1029/2005JA011327.

Girardin, F., É. Artigau, and R. Doyon. 2013. "In Search of Dust Clouds: Photometric Monitoring of a Sample of Late L and T Dwarfs." *ApJ* 767, 61 (April): 61. doi:10.1088/0004-637X/767/1/61.

Gizis, J. E., D. G. Monet, I. N. Reid, J. D. Kirkpatrick, J. Liebert, and R. J. Williams. 2000. "New Neighbors from 2MASS: Activity and Kinematics at the Bottom of the Main Sequence." *AJ* 120 (August): 1085–1099. doi:10.1086/301456. eprint: astro-ph/0004361.

Goldman, B., M. C. Cushing, M. S. Marley, É. Artigau, K. S. Baliyan, V. J. S. Béjar, J. A. Caballero, et al. 2008. "CLOUDS search for variability in brown dwarf atmospheres. Infrared spectroscopic time series of L/T transition brown dwarfs." *A&A* 487 (August): 277–292. doi:10.1051/0004-6361:20065075. arXiv: 0801.2371.

Goldreich, P., and D. Lynden-Bell. 1969. "Io, a jovian unipolar inductor." *ApJ* 156 (April): 59–78. doi:10.1086/149947.

Grodent, D., B. Bonfond, A. Radioti, J.-C. Gérard, X. Jia, J. D. Nichols, and J. T. Clarke. 2009. "Auroral footprint of Ganymede." *Journal of Geophysical Research (Space Physics)* 114, A07212 (July): A07212. doi:10.1029/2009JA014289.

Güdel, M. 1994. "Quiescent microwave emission from late-type stars." *ApJS* 90 (February): 743–751. doi:10.1086/191899.

———. 2002. "Stellar Radio Astronomy: Probing Stellar Atmospheres from Protostars to Giants." *ARA&A* 40:217–261. doi:10.1146/annurev.astro.40.060401.093806. eprint: astro-ph/0206436.

Güdel, M., and A. O. Benz. 1993. "X-ray/microwave relation of different types of active stars." *ApJ* 405 (March): L63–L66. doi:10.1086/186766.

Güdel, M., J. H. M. M. Schmitt, J. A. Bookbinder, and T. A. Fleming. 1993. "A tight correlation between radio and X-ray luminosities of M dwarfs." *ApJ* 415 (September): 236–239. doi:10.1086/173158.

Guillot, T., D. J. Stevenson, W. B. Hubbard, and D. Saumon. 2004. "The interior of Jupiter." In *Jupiter. The Planet, Satellites and Magnetosphere,* edited by F. Bagenal, T. E. Dowling, and W. B. McKinnon, 35–57.

Gurnett, D. A., W. S. Kurth, G. B. Hospodarsky, A. M. Persoon, P. Zarka, A. Lecacheux, S. J. Bolton, et al. 2002. "Control of Jupiter's radio emission and aurorae by the solar wind." *Nature* 415 (February): 985–987.

Gurnett, D. A., W. S. Kurth, and F. L. Scarf. 1981. "Narrowband electromagnetic emissions from Saturn's magnetosphere." *Nature* 292 (August): 733–737. doi:10.1038/292733a0.

Hall, P. B. 2002. "2MASS 1315-2649: A High Proper-Motion L Dwarf with Strong Hα Emission." *ApJ* 580 (November): L77–L78. doi:10.1086/345549. eprint: astro-ph/0210351.

Hallinan, G., A. Antonova, J. G. Doyle, S. Bourke, W. F. Brisken, and A. Golden. 2006. "Rotational Modulation of the Radio Emission from the M9 Dwarf TVLM 513-46546: Broadband Coherent Emission at the Substellar Boundary?" *ApJ* 653 (December): 690–699. doi:10.1086/508678. eprint: astro-ph/0608556.

Hallinan, G., A. Antonova, J. G. Doyle, S. Bourke, C. Lane, and A. Golden. 2008. "Confirmation of the Electron Cyclotron Maser Instability as the Dominant Source of Radio Emission from Very Low Mass Stars and Brown Dwarfs." *ApJ* 684 (September): 644–653. doi:10.1086/590360. arXiv: 0805.4010.

Hallinan, G., S. Bourke, C. Lane, A. Antonova, R. T. Zavala, W. F. Brisken, R. P. Boyle, F. J. Vrba, J. G. Doyle, and A. Golden. 2007. "Periodic Bursts of Coherent Radio Emission from an Ultracool Dwarf." *ApJ* 663 (July): L25–L28. doi:10.1086/519790. arXiv: 0705.2054.

Hallinan, G., S. P. Littlefair, G. Cotter, S. Bourke, L. K. Harding, J. S. Pineda, R. P. Butler, et al. 2015. "Magnetospherically driven optical and radio aurorae at the end of the stellar main sequence." *Nature* 523 (July): 568–571. doi:10.1038/nature14619. arXiv: 1507.08739 [astro-ph.SR].

Hallinan, G., S. K. Sirothia, A. Antonova, C. H. Ishwara-Chandra, S. Bourke, J. G. Doyle, J. Hartman, and A. Golden. 2013. "Looking for a Pulse: A Search for Rotationally Modulated Radio Emission from the Hot Jupiter, τ Boötis b." *ApJ* 762, 34 (January): 34. doi:10.1088/0004-637X/762/1/34. arXiv: 1210.8259 [astro-ph.EP].

Harding, L. K., G. Hallinan, R. P. Boyle, A. Golden, N. Singh, B. Sheehan, R. T. Zavala, and R. F. Butler. 2013. "Periodic Optical Variability of Radio-detected Ultracool Dwarfs." *ApJ* 779, 101 (December): 101. doi:10.1088/0004-637X/779/2/101. arXiv: 1310.1367 [astro-ph.SR].

Hartmann, L., G. Herczeg, and N. Calvet. 2016. "Accretion onto Pre-Main-Sequence Stars." *ARA&A* 54 (September): 135–180. doi:10.1146/annurev-astro-081915-023347.

Heinze, A. N., S. Metchev, and K. Kellogg. 2015. "Weather on Other Worlds. III. A Survey for T Dwarfs with High-amplitude Optical Variability." *ApJ* 801, 104 (March): 104. doi:10.1088/0004-637X/801/2/104. arXiv: 1412.6733 [astro-ph.SR].

Helling, C., M. Jardine, C. Stark, and D. Diver. 2013. "Ionization in Atmospheres of Brown Dwarfs and Extrasolar Planets. III. Breakdown Conditions for Mineral Clouds." *ApJ* 767, 136 (April): 136. doi:10.1088/0004-637X/767/2/136. arXiv: 1301.7586 [astro-ph.EP].

Hess, S. L. G., B. Bonfond, P. Zarka, and D. Grodent. 2011. "Model of the Jovian magnetic field topology constrained by the Io auroral emissions." *Journal of Geophysical Research (Space Physics)* 116, A05217 (May): 5217. doi:10.1029/2010JA016262.

Hess, S. L. G., and P. A. Delamere. 2012. "Satellite-Induced Electron Acceleration and Related Auroras." *Washington DC American Geophysical Union Geophysical Monograph Series* 197. doi:10.1029/2011GM001175.

Hess, S., B. Cecconi, and P. Zarka. 2008. "Modeling of Io-Jupiter decameter arcs, emission beaming and energy source." *Geophys. Res. Lett.* 35, L13107 (July): 13107. doi:10.1029/2008GL033656.

Hill, T. W. 1979. "Inertial limit on corotation." *J. Geophys. Res.* 84 (November): 6554–6558. doi:10.1029/JA084iA11p06554.

———. 2001. "The Jovian auroral oval." *J. Geophys. Res.* 106 (May): 8101–8108. doi:10.1029/2000JA000302.

Holme, R., and J. Bloxham. 1996. "The magnetic fields of Uranus and Neptune: Methods and models." *J. Geophys. Res.* 101:2177–2200. doi:10.1029/95JE03437.

Huang, S.-S. 1959. "Occurrence of Life in the Universe." *American Scientist* 47 (September): 397–402.

———. 1960. "Life-Supporting Regions in the Vicinity of Binary Systems." *PASP* 72 (April): 106. doi:10.1086/127489.

Iess, L., N. J. Rappaport, R. A. Jacobson, P. Racioppa, D. J. Stevenson, P. Tortora, J. W. Armstrong, and S. W. Asmar. 2010. "Gravity Field, Shape, and Moment of Inertia of Titan." *Science* 327 (March): 1367. doi:10.1126/science.1182583.

Ingersoll, A. P., A. R. Vasavada, B. Little, C. D. Anger, S. J. Bolton, C. Alexander, K. P. Klaasen, W. K. Tobiska, and Galileo SSI Team. 1998. "Imaging Jupiter's Aurora at Visible Wavelengths." *Icarus* 135 (September): 251–264. doi:10.1006/icar.1998.5971.

Isbell, J., A. J. Dessler, and J. H. Waite Jr. 1984. "Magnetospheric energization by interaction between planetary spin and the solar wind." *J. Geophys. Res.* 89 (December): 10716–10722. doi:10.1029/JA089iA12p10716.

Johns-Krull, C. M. 2007. "The Magnetic Fields of Classical T Tauri Stars." *ApJ* 664 (August): 975–985. doi:10.1086/519017. arXiv: 0704.2923.

Johns-Krull, C. M., and J. A. Valenti. 1996. "Detection of Strong Magnetic Fields on M Dwarfs." *ApJ* 459 (March): L95. doi:10.1086/309954.

———. 2000. "Measurements of stellar magnetic fields." In *Stellar Clusters and Associations: Convection, Rotation, and Dynamos,* edited by R. Pallavicini, G. Micela, and S. Sciortino, 198:371. Astronomical Society of the Pacific Conference Series.

Kao, M. M., G. Hallinan, J. S. Pineda, I. Escala, A. Burgasser, S. Bourke, and D. Stevenson. 2016. "Auroral Radio Emission from Late L and T Dwarfs: A New Constraint on Dynamo Theory in the Substellar Regime." *ApJ* 818, 24 (February): 24. doi:10.3847/0004-637X/818/1/24. arXiv: 1511.03661 [astro-ph.SR].

Kay, C., M. Opher, and M. Kornbleuth. 2016. "Probability of CME Impact on Exoplanets Orbiting M Dwarfs and Solar-like Stars." *ApJ* 826, 195 (August): 195. doi:10.3847/0004-637X/826/2/195. arXiv: 1605.02683 [astro-ph.SR].

Keiling, A., E. Donovan, F. Bagenal, and T. Karlsson. 2012. "Auroral Phenomenology and Magnetospheric Processes: Earth and Other Planets." *Washington DC American Geophysical Union Geophysical Monograph Series* 197. doi:10.1029/GM197.

Kervella, P., A. Mérand, C. Ledoux, B.-O. Demory, and J.-B. Le Bouquin. 2016. "The red dwarf pair GJ65AB: inflated, spinning twins of Proxima." *ArXiv e-prints* (July). arXiv: 1607.04351 [astro-ph.SR].

Khandrika, H., A. J. Burgasser, C. Melis, C. Luk, E. Bowsher, and B. Swift. 2013. "A Search for Photometric Variability in L- and T-type Brown Dwarf Atmospheres." *AJ* 145, 71 (March): 71. doi:10.1088/0004-6256/145/3/71. arXiv: 1301.0545 [astro-ph.SR].

Khodachenko, M. L., I. Ribas, H. Lammer, J.-M. Grießmeier, M. Leitner, F. Selsis, C. Eiroa, et al. 2007. "Coronal Mass Ejection (CME) Activity of Low Mass M Stars as An Important Factor for The Habitability of Terrestrial Exoplanets. I. CME Impact on Expected Magnetospheres of Earth-Like Exoplanets in Close-In Habitable Zones." *Astrobiology* 7 (February): 167–184. doi:10.1089/ast.2006.0127.

Kirkpatrick, J. D., K. L. Cruz, T. S. Barman, A. J. Burgasser, D. L. Looper, C. G. Tinney, C. R. Gelino, et al. 2008. "A Sample of Very Young Field L Dwarfs and Implications for the Brown Dwarf "Lithium Test" at Early Ages." *ApJ* 689 (December): 1295–1326. doi:10.1086/592768. arXiv: 0808.3153.

Kirkpatrick, J. D., M. C. Cushing, C. R. Gelino, R. L. Griffith, M. F. Skrutskie, K. A. Marsh, E. L. Wright, et al. 2011. "The First Hundred Brown Dwarfs Discovered by the Wide-field Infrared Survey Explorer (WISE)." *ApJS* 197, 19 (December): 19. doi:10.1088/0067-0049/197/2/19. arXiv: 1108.4677 [astro-ph.SR].

Kirkpatrick, J. D., C. R. Gelino, M. C. Cushing, G. N. Mace, R. L. Griffith, M. F. Skrutskie, K. A. Marsh, et al. 2012. "Further Defining Spectral Type "Y" and Exploring the Low-mass End of the Field Brown Dwarf Mass Function." *ApJ* 753, 156 (July): 156. doi:10.1088/0004-637X/753/2/156. arXiv: 1205.2122 [astro-ph.SR].

Kirkpatrick, J. D., I. N. Reid, J. Liebert, J. E. Gizis, A. J. Burgasser, D. G. Monet, C. C. Dahn, B. Nelson, and R. J. Williams. 2000. "67 Additional L Dwarfs Discovered by the Two Micron All Sky Survey." *AJ* 120 (July): 447–472. doi:10.1086/301427. eprint: astro-ph/0003317.

Kitchatinov, L. L., D. Moss, and D. Sokoloff. 2014. "Magnetic fields in fully convective M-dwarfs: oscillatory dynamos versus bistability." *MNRAS* 442 (July): L1–L4. doi:10.1093/mnrasl/slu041. arXiv: 1401.1764 [astro-ph.SR].

Kivelson, M. G., K. K. Khurana, and M. Volwerk. 2002. "The Permanent and Inductive Magnetic Moments of Ganymede." *Icarus* 157 (June): 507–522. doi:10.1006/icar.2002.6834.

Koen, C. 2005. "I_C and R_C band time-series observations of some bright ultracool dwarfs." *MNRAS* 360 (July): 1132–1142. doi:10.1111/j.1365-2966.2005.09119.x.

Koen, C., N. Matsunaga, and J. Menzies. 2004. "A search for short time-scale JHK variability in ultracool dwarfs." *MNRAS* 354 (October): 466–476. doi:10.1111/j.1365-2966.2004.08208.x.

Kovács, G., S. Zucker, and T. Mazeh. 2002. "A box-fitting algorithm in the search for periodic transits." *A&A* 391 (August): 369–377. doi:10.1051/0004-6361:20020802. eprint: astro-ph/0206099.

Kuznetsov, A. A., J. G. Doyle, S. Yu, G. Hallinan, A. Antonova, and A. Golden. 2012. "Comparative Analysis of Two Formation Scenarios of Bursty Radio Emission from Ultracool Dwarfs." *ApJ* 746, 99 (February): 99. doi:10.1088/0004-637X/746/1/99. arXiv: 1111.7019 [astro-ph.SR].

Ladreiter, H. P., P. Zarka, and A. Lacacheux. 1994. "Direction finding study of Jovian hectometric and broadband kilometric radio emissions: Evidence for their auroral origin." *Planet. Space Sci.* 42 (November): 919–931. doi:10.1016/0032-0633(94)90052-3.

Lammer, H., H. I. M. Lichtenegger, Y. N. Kulikov, J.-M. Grießmeier, N. Terada, N. V. Erkaev, H. K. Biernat, et al. 2007. "Coronal Mass Ejection (CME) Activity of Low Mass M Stars as An Important Factor for The Habitability of Terrestrial Exoplanets. II. CME-Induced Ion Pick Up of Earth-like Exoplanets in Close-In Habitable Zones." *Astrobiology* 7 (February): 185–207. doi:10.1089/ast.2006.0128.

Lane, C., G. Hallinan, R. T. Zavala, R. F. Butler, R. P. Boyle, S. Bourke, A. Antonova, J. G. Doyle, F. J. Vrba, and A. Golden. 2007. "Rotational Modulation of M/L Dwarfs due to Magnetic Spots." *ApJ* 668 (October): L163–L166. doi:10.1086/523041. arXiv: 0709.1045.

Lazio, T. J., S. Carmichael, J. Clark, E. Elkins, P. Gudmundsen, Z. Mott, M. Szwajkowski, and L. A. Hennig. 2010. "A Blind Search for Magnetospheric Emissions from Planetary Companions to Nearby Solar-Type Stars." *AJ* 139 (Jan-

uary): 96–101. doi:10.1088/0004-6256/139/1/96. arXiv: 0910.3938 [astro-ph.EP].

Lazio, T. J., and W. M. Farrell. 2007. "Magnetospheric Emissions from the Planet Orbiting τ Bootis: A Multiepoch Search." *ApJ* 668 (October): 1182–1188. doi:10.1086/519730. arXiv: 0707.1827.

Leblanc, F., R. Modolo, S. Curry, J. Luhmann, R. Lillis, J. Y. Chaufray, T. Hara, et al. 2015. "Mars heavy ion precipitating flux as measured by Mars Atmosphere and Volatile EvolutioN." *Geophys. Res. Lett.* 42 (November): 9135–9141. doi:10.1002/2015GL066170.

Leggett, S. K., M. C. Cushing, K. K. Hardegree-Ullman, J. L. Trucks, M. S. Marley, C. V. Morley, D. Saumon, et al. 2016. "Observed Variability at 1um and 4um in the Y0 Brown Dwarf WISEP J173835.52+273258.9." *ArXiv e-prints* (July). arXiv: 1607.07888 [astro-ph.SR].

Leggett, S. K., T. R. Geballe, X. Fan, D. P. Schneider, J. E. Gunn, R. H. Lupton, G. R. Knapp, et al. 2000. "The Missing Link: Early Methane ("T") Dwarfs in the Sloan Digital Sky Survey." *ApJ* 536 (June): L35–L38. doi:10.1086/312728. eprint: astro-ph/0004408.

Leggett, S. K., C. V. Morley, M. S. Marley, D. Saumon, J. J. Fortney, and C. Visscher. 2013. "A Comparison of Near-infrared Photometry and Spectra for Y Dwarfs with a New Generation of Cool Cloudy Models." *ApJ* 763, 130 (February): 130. doi:10.1088/0004-637X/763/2/130. arXiv: 1212.1210 [astro-ph.SR].

Leggett, S. K., D. Saumon, L. Albert, M. C. Cushing, M. C. Liu, K. L. Luhman, M. S. Marley, J. D. Kirkpatrick, T. L. Roellig, and K. N. Allers. 2008. "HN Peg B: A Test of Models of the L to T Dwarf Transition." *ApJ* 682 (August): 1256–1263. doi:10.1086/589146. arXiv: 0804.1386.

Leighton, R. B. 1969. "A Magneto-Kinematic Model of the Solar Cycle." *ApJ* 156 (April): 1. doi:10.1086/149943.

Leto, P., C. Trigilio, C. S. Buemi, G. Umana, A. Ingallinera, and L. Cerrigone. 2016. "3D modelling of stellar auroral radio emission." *MNRAS* 459 (June): 1159–1169. doi:10.1093/mnras/stw639. arXiv: 1603.02423 [astro-ph.SR].

Liebert, J., and A. J. Burgasser. 2007. "On the Nature of the Unique Hα-emitting T Dwarf 2MASS J12373919+6526148." *ApJ* 655 (January): 522–527. doi:10.1086/509882. eprint: astro-ph/0609793.

Lillis, R. J., H. V. Frey, M. Manga, D. L. Mitchell, R. P. Lin, M. H. Acuña, and S. W. Bougher. 2008. "An improved crustal magnetic field map of Mars from electron reflectometry: Highland volcano magmatic history and the end of the martian dynamo." *Icarus* 194 (April): 575–596. doi:10.1016/j.icarus.2007.09.032.

Littlefair, S. P., V. S. Dhillon, T. R. Marsh, T. Shahbaz, E. L. Martin, and C. Copperwheat. 2008. "Optical variability of the ultracool dwarf TVLM 513-46546: evidence for inhomogeneous dust clouds." *MNRAS* 391 (November): L88–L92. doi:10.1111/j.1745-3933.2008.00562.x. arXiv: 0809.2193.

Liu, M. C., T. J. Dupuy, and S. K. Leggett. 2010. "Discovery of a Highly Unequal-mass Binary T Dwarf with Keck Laser Guide Star Adaptive Optics: A Coevality Test of Substellar Theoretical Models and Effective Temperatures." *ApJ* 722 (October): 311–328. doi:10.1088/0004-637X/722/1/311. arXiv: 1008.2200 [astro-ph.SR].

Lodders, K., and B. Fegley. 1998. *The planetary scientist's companion / Katharina Lodders, Bruce Fegley.*

Love, J. 1999. "Reversals and excursions of the geodynamo." *Astronomy and Geophysics* 40 (December): 14.

Luhman, K. L. 2014. "Discovery of a ~250 K Brown Dwarf at 2 pc from the Sun." *ApJ* 786, L18 (May): L18. doi:10.1088/2041-8205/786/2/L18. arXiv: 1404.6501.

Luhman, K. L., and T. L. Esplin. 2016. "The Spectral Energy Distribution of the Coldest Known Brown Dwarf." *AJ* 152, 78 (September): 78. doi:10.3847/0004-6256/152/3/78. arXiv: 1605.06655 [astro-ph.SR].

Luhman, K. L., B. M. Patten, M. Marengo, M. T. Schuster, J. L. Hora, R. G. Ellis, J. R. Stauffer, et al. 2007. "Discovery of Two T Dwarf Companions with the Spitzer Space Telescope." *ApJ* 654 (January): 570–579. doi:10.1086/509073. eprint: astro-ph/0609464.

Lynch, C. R., T. Murphy, D. L. Kaplan, M. Ireland, and M. E. Bell. 2017. "A search for circularly polarized emission from young exoplanets." *MNRAS* 467 (May): 3447–3453. doi:10.1093/mnras/stx354.

Lynch, C., R. L. Mutel, and M. Güdel. 2015. "Wideband Dynamic Radio Spectra of Two Ultra-cool Dwarfs." *ApJ* 802, 106 (April): 106. doi:10.1088/0004-637X/802/2/106. arXiv: 1405.3516 [astro-ph.SR].

Maillard, J., and S. Miller. 2011. "The Molecular Ion H_3^+ in Emission in Planetary Atmospheres." In *Molecules in the Atmospheres of Extrasolar Planets,* edited by J. P. Beaulieu, S. Dieters, and G. Tinetti, 450:19. Astronomical Society of the Pacific Conference Series. December.

Marley, M. S., D. Saumon, and C. Goldblatt. 2010. "A Patchy Cloud Model for the L to T Dwarf Transition." *ApJ* 723 (November): L117–L121. doi:10.1088/2041-8205/723/1/L117. arXiv: 1009.6217 [astro-ph.SR].

Mauk, B., and F. Bagenal. 2012. "Comparative Auroral Physics: Earth and Other Planets." *Washington DC American Geophysical Union Geophysical Monograph Series* 197. doi:10.1029/2011GM001192.

McLean, M., E. Berger, and A. Reiners. 2012. "The Radio Activity-Rotation Relation of Ultracool Dwarfs." *ApJ* 746, 23 (February): 23. doi:10.1088/0004-637X/746/1/23. arXiv: 1108.0415 [astro-ph.SR].

Melrose, D. B. 1973. "Coherent gyromagentic emission as a radiation mechanism." *Australian Journal of Physics* 26 (April): 229. doi:10.1071/PH730229.

———. 2006. "Depolarization of Radio Bursts Due to Reflection off Sharp Boundaries in the Solar Corona." *ApJ* 637 (February): 1113–1121. doi:10.1086/498499. eprint: astro-ph/0507531.

Metchev, S. A., A. Heinze, D. Apai, D. Flateau, J. Radigan, A. Burgasser, M. S. Marley, É. Artigau, P. Plavchan, and B. Goldman. 2015. "Weather on Other Worlds. II. Survey Results: Spots are Ubiquitous on L and T Dwarfs." *ApJ* 799, 154 (February): 154. doi:10.1088/0004-637X/799/2/154. arXiv: 1411.3051 [astro-ph.SR].

Moffatt, H. K. 1978. *Magnetic field generation in electrically conducting fluids.*

Mohanty, S., and G. Basri. 2003. "Rotation and Activity in Mid-M to L Field Dwarfs." *ApJ* 583 (January): 451–472. doi:10.1086/345097. eprint: astro-ph/0201455.

Mohanty, S., G. Basri, F. Shu, F. Allard, and G. Chabrier. 2002. "Activity in Very Cool Stars: Magnetic Dissipation in Late M and L Dwarf Atmospheres." *ApJ* 571 (May): 469–486. doi:10.1086/339911. eprint: astro-ph/0201518.

Morin, J., X. Delfosse, J.-F. Donati, E. Dormy, T. Forveille, M. M. Jardine, P. Petit, and M. Schrinner. 2011. "Evidence for dynamo bistability among very low mass stars." In *French Soc. of Astro and Astrophys. Proceedings,* edited by G. Alecian, K. Belkacem, R. Samadi, and D. Valls-Gabaud, 503–508. December. arXiv: 1208.3341 [astro-ph.SR].

Morin, J., J.-F. Donati, P. Petit, X. Delfosse, T. Forveille, L. Albert, M. Aurière, et al. 2008. "Large-scale magnetic topologies of mid M dwarfs." *MNRAS* 390 (October): 567–581. doi:10.1111/j.1365-2966.2008.13809.x. arXiv: 0808.1423.

Morin, J., J.-F. Donati, P. Petit, X. Delfosse, T. Forveille, and M. M. Jardine. 2010. "Large-scale magnetic topologies of late M dwarfs." *MNRAS* (October): 2269–2286. doi:10.1111/j.1365-2966.2010.17101.x. arXiv: 1005.5552 [astro-ph.SR].

Morin, J., E. Dormy, M. Schrinner, and J.-F. Donati. 2011. "Weak- and strong-field dynamos: from the Earth to the stars." *MNRAS* 418 (November): L133–L137. doi:10.1111/j.1745-3933.2011.01159.x. arXiv: 1106.4263 [astro-ph.SR].

Morley, C. V., J. J. Fortney, M. S. Marley, C. Visscher, D. Saumon, and S. K. Leggett. 2012. "Neglected Clouds in T and Y Dwarf Atmospheres." *ApJ* 756, 172 (September): 172. doi:10.1088/0004-637X/756/2/172. arXiv: 1206.4313 [astro-ph.SR].

Morley, C. V., M. S. Marley, J. J. Fortney, and R. Lupu. 2014. "Spectral Variability from the Patchy Atmospheres of T and Y Dwarfs." *ApJ* 789, L14 (July): L14. doi:10.1088/2041-8205/789/1/L14. arXiv: 1406.0863 [astro-ph.SR].

Morley, C. V., M. S. Marley, J. J. Fortney, R. Lupu, D. Saumon, T. Greene, and K. Lodders. 2014. "Water Clouds in Y Dwarfs and Exoplanets." *ApJ* 787, 78 (May): 78. doi:10.1088/0004-637X/787/1/78. arXiv: 1404.0005 [astro-ph.SR].

Murphy, T., M. E. Bell, D. L. Kaplan, B. M. Gaensler, A. R. Offringa, E. Lenc, N. Hurley-Walker, et al. 2015. "Limits on low-frequency radio emission from southern exoplanets with the Murchison Widefield Array." *MNRAS* 446 (January): 2560–2565. doi:10.1093/mnras/stu2253. arXiv: 1410.6819 [astro-ph.EP].

Murray, C. D., and S. F. Dermott. 1999. *Solar system dynamics.*

Nichols, J. D., M. R. Burleigh, S. L. Casewell, S. W. H. Cowley, G. A. Wynn, J. T. Clarke, and A. A. West. 2012. "Origin of Electron Cyclotron Maser Induced Radio Emissions at Ultracool Dwarfs: Magnetosphere-Ionosphere Coupling Currents." *ApJ* 760, 59 (November): 59. doi:10.1088/0004-637X/760/1/59. arXiv: 1210.1864 [astro-ph.SR].

Noyes, R. W., L. W. Hartmann, S. L. Baliunas, D. K. Duncan, and A. H. Vaughan. 1984. "Rotation, convection, and magnetic activity in lower main-sequence stars." *ApJ* 279 (April): 763–777. doi:10.1086/161945.

Olson, P., and U. R. Christensen. 2006. "Dipole moment scaling for convection-driven planetary dynamos." *Earth and Planetary Science Letters* 250 (October): 561–571. doi:10.1016/j.epsl.2006.08.008.

Pallavicini, R., L. Golub, R. Rosner, G. S. Vaiana, T. Ayres, and J. L. Linsky. 1981. "Relations among stellar X-ray emission observed from Einstein, stellar rotation and bolometric luminosity." *ApJ* 248 (August): 279–290. doi:10.1086/159152.

Pallavicini, R., R. F. Willson, and K. R. Lang. 1985. "Microwave observations of late-type stars with the Very Large Array." *A&A* 149 (August): 95–101.

Parker, E. N. 1955. "Hydromagnetic Dynamo Models." *ApJ* 122 (September): 293. doi:10.1086/146087.

———. 1975. "The generation of magnetic fields in astrophysical bodies. X - Magnetic buoyancy and the solar dynamo." *ApJ* 198 (May): 205–209. doi:10.1086/153593.

Parks, J. R., P. Plavchan, R. J. White, and A. H. Gee. 2014. "Periodic and Aperiodic Variability in the Molecular Cloud ρ Ophiuchus." *ApJS* 211, 3 (March): 3. doi:10.1088/0067-0049/211/1/3. arXiv: 1309.5300 [astro-ph.SR].

Perley, R. A., and B. J. Butler. 2013. "An Accurate Flux Density Scale from 1 to 50 GHz." *ApJS* 204, 19 (February): 19. doi:10.1088/0067-0049/204/2/19. arXiv: 1211.1300 [astro-ph.IM].

Perry, J. J., Y. H. Kim, J. L. Fox, and H. S. Porter. 1999. "Chemistry of the Jovian auroral ionosphere." *J. Geophys. Res.* 104 (July): 16541–16566. doi:10.1029/1999JE900022.

Phan-Bao, N., R. A. Osten, J. Lim, E. L. Martin, and P. T. P. Ho. 2007. "Discovery of Radio Emission from the Tight M8 Binary LP 349-25." *ApJ* 658 (March): 553–556. doi:10.1086/511061. eprint: astro-ph/0610046.

Pineda, J. S. 2016. "Multiwavelength Characterization of the Brown Dwarf Auroral Phenomenon – Establishing the Nature of the Electrodynamic Engine." PhD diss., California Institute of Technology. doi:10.7907/Z90C4SRW.

Pineda, J. S., G. Hallinan, J. D. Kirkpatrick, G. Cotter, M. M. Kao, and K. Mooley. 2016. "A Survey for Hα Emission from Late L Dwarfs and T Dwarfs." *ApJ* 826, 73 (July): 73. doi:10.3847/0004-637X/826/1/73. arXiv: 1604.03941 [astro-ph.SR].

Pizzolato, N., A. Maggio, G. Micela, S. Sciortino, and P. Ventura. 2003. "The stellar activity-rotation relationship revisited: Dependence of saturated and non-saturated X-ray emission regimes on stellar mass for late-type dwarfs." *A&A* 397 (January): 147–157. doi:10.1051/0004-6361:20021560.

Plavchan, P., M. Jura, J. D. Kirkpatrick, R. M. Cutri, and S. C. Gallagher. 2008. "Near-Infrared Variability in the 2MASS Calibration Fields: A Search for Planetary Transit Candidates." *ApJS* 175, 191-228 (March): 191–228. doi:10.1086/523644. arXiv: 0709.1182.

Pottelette, R., R. E. Ergun, R. A. Treumann, M. Berthomier, C. W. Carlson, J. P. McFadden, and I. Roth. 1999. "Modulated electron-acoustic waves in auroral density cavities: FAST observations." *Geophys. Res. Lett.* 26:2629–2632. doi:10.1029/1999GL900462.

Pryor, W. R., A. M. Rymer, D. G. Mitchell, T. W. Hill, D. T. Young, J. Saur, G. H. Jones, et al. 2011. "The auroral footprint of Enceladus on Saturn." *Nature* 472 (April): 331–333. doi:10.1038/nature09928.

Radigan, J. 2014. "An Independent Analysis of the Brown Dwarf Atmosphere Monitoring (BAM) Data: Large-amplitude Variability is Rare Outside the L/T Transition." *ApJ* 797, 120 (December): 120. doi:10.1088/0004-637X/797/2/120. arXiv: 1408.5919 [astro-ph.SR].

Radigan, J. M. 2013. "Weather on Substellar Worlds: A Study of Clouds, Variability and Binarity at the L/T Transition." PhD diss., Univ. of Toronto.

Radigan, J., R. Jayawardhana, D. Lafrenière, É. Artigau, M. Marley, and D. Saumon. 2012. "Large-amplitude Variations of an L/T Transition Brown Dwarf: Multi-wavelength Observations of Patchy, High-contrast Cloud Features." *ApJ* 750, 105 (May): 105. doi:10.1088/0004-637X/750/2/105. arXiv: 1201.3403 [astro-ph.SR].

Radigan, J., D. Lafrenière, R. Jayawardhana, and E. Artigau. 2014. "Strong Brightness Variations Signal Cloudy-to-clear Transition of Brown Dwarfs." *ApJ* 793, 75 (October): 75. doi:10.1088/0004-637X/793/2/75. arXiv: 1404.3247 [astro-ph.SR].

Rajan, A., J. Patience, P. A. Wilson, J. Bulger, R. J. De Rosa, K. Ward-Duong, C. Morley, F. Pont, and R. Windhorst. 2015. "The brown dwarf atmosphere monitoring (BAM) project - II. Multi-epoch monitoring of extremely cool brown dwarfs." *MNRAS* 448 (April): 3775–3783. doi:10.1093/mnras/stv181. arXiv: 1502.01346 [astro-ph.SR].

Ray, L. C., and R. E. Ergun. 2012. "Auroral Signatures of Ionosphere-Magnetosphere Coupling at Jupiter and Saturn." *Washington DC American Geophysical Union Geophysical Monograph Series* 197. doi:10.1029/2011GM001172.

Reid, I. N., K. L. Cruz, A. J. Burgasser, and M. C. Liu. 2008. "L-Dwarf Binaries in the 20-Parsec Sample." *AJ* 135 (February): 580–587. doi:10.1088/0004-6256/135/2/580.

Reid, I. N., J. D. Kirkpatrick, J. Liebert, J. E. Gizis, C. C. Dahn, and D. G. Monet. 2002. "High-Resolution Spectroscopy of Ultracool M Dwarfs." *AJ* 124 (July): 519–540. doi:10.1086/340805. eprint: astro-ph/0204285.

Reiners, A. 2012. "Observations of Cool-Star Magnetic Fields." *Living Reviews in Solar Physics* 9 (February): 1. doi:10.12942/lrsp-2012-1. arXiv: 1203.0241 [astro-ph.SR].

Reiners, A., and G. Basri. 2006. "Measuring Magnetic Fields in Ultracool Stars and Brown Dwarfs." *ApJ* 644 (June): 497–509. doi:10.1086/503324. eprint: astro-ph/0602221.

———. 2007. "The First Direct Measurements of Surface Magnetic Fields on Very Low Mass Stars." *ApJ* 656 (February): 1121–1135. doi:10.1086/510304. eprint: astro-ph/0610365.

———. 2008. "Chromospheric Activity, Rotation, and Rotational Braking in M and L Dwarfs." *ApJ* 684 (September): 1390–1403. doi:10.1086/590073. arXiv: 0805.1059.

———. 2009. "On the magnetic topology of partially and fully convective stars." *A&A* 496 (March): 787–790. doi:10.1051/0004-6361:200811450. arXiv: 0901.1659 [astro-ph.SR].

Reiners, A., and G. Basri. 2010. "A Volume-Limited Sample of 63 M7-M9.5 Dwarfs. II. Activity, Magnetism, and the Fade of the Rotation-Dominated Dynamo." *ApJ* 710 (February): 924–935. doi:10.1088/0004-637X/710/2/924. arXiv: 0912.4259 [astro-ph.SR].

Reiners, A., G. Basri, and M. Browning. 2009. "Evidence for Magnetic Flux Saturation in Rapidly Rotating M Stars." *ApJ* 692 (February): 538–545. doi:10.1088/0004-637X/692/1/538. arXiv: 0810.5139.

Reiners, A., and U. R. Christensen. 2010. "A magnetic field evolution scenario for brown dwarfs and giant planets." *A&A* 522, A13 (November): A13. doi:10.1051/0004-6361/201014251. arXiv: 1007.1514 [astro-ph.EP].

Rodriguez-Barrera, M. I., C. Helling, C. R. Stark, and A. M. Rice. 2015. "Reference study to characterize plasma and magnetic properties of ultracool atmospheres." *MNRAS* 454 (December): 3977–3995. doi:10.1093/mnras/stv2090. arXiv: 1509.02769 [astro-ph.EP].

Rosén, L., O. Kochukhov, and G. A. Wade. 2015. "First Zeeman Doppler imaging of a cool star using all four Stokes parameters." *ArXiv e-prints* (April). arXiv: 1504.00176 [astro-ph.SR].

Route, M. 2016. "The Discovery of Solar-like Activity Cycles Beyond the End of the Main Sequence?" *ArXiv e-prints* (September). arXiv: 1609.07761 [astro-ph.SR].

Route, M., and A. Wolszczan. 2012. "The Arecibo Detection of the Coolest Radio-flaring Brown Dwarf." *ApJ* 747, L22 (March): L22. doi:10.1088/2041-8205/747/2/L22. arXiv: 1202.1287 [astro-ph.SR].

———. 2013. "The 5 GHz Arecibo Search for Radio Flares from Ultracool Dwarfs." *ApJ* 773, 18 (August): 18. doi:10.1088/0004-637X/773/1/18. arXiv: 1306.1152 [astro-ph.SR].

———. 2016. "Radio Flaring from the T6 Dwarf WISEPC J112254.73+255021.5 with a Possible Ultra-short Periodicity." *ApJ* 821, L21 (April): L21. doi:10.3847/2041-8205/821/2/L21. arXiv: 1604.04543 [astro-ph.SR].

Russell, C. T. 1993. "Planetary magnetospheres." *Reports on Progress in Physics* 56 (June): 687–732. doi:10.1088/0034-4885/56/6/001.

Saar, S. H. 1990. "Magnetic Fields on Solar-like Stars: The First Decade." In *Solar Photosphere: Structure, Convection, and Magnetic Fields,* edited by J. O. Stenflo, 138:427–441. IAU Symposium.

———. 1994. "Infrared Measurements of Stellar Magnetic Fields." In *Infrared Solar Physics,* edited by D. M. Rabin, J. T. Jefferies, and C. Lindsey, 154:437. IAU Symposium.

———. 1996. *Recent Measurements of Stellar Magnetic Fields,* edited by Y. Uchida, T. Kosugi, and H. S. Hudson. Springer Netherlands.

Saar, S. H. 2001. "Recent Measurements of (and Inferences About) Magnetic Fields on K and M Stars (CD-ROM Directory: contribs/saar1)." In *11th Cambridge Workshop on Cool Stars, Stellar Systems and the Sun,* edited by R. J. Garcia Lopez, R. Rebolo, and M. R. Zapaterio Osorio, 223:292. Astronomical Society of the Pacific Conference Series.

Saar, S. H., and J. L. Linsky. 1985. "The photospheric magnetic field of the dM3.5e flare star AD Leonis." *ApJ* 299 (December): L47–L50. doi:10.1086/184578.

Saumon, D., G. Chabrier, and H. M. van Horn. 1995. "An Equation of State for Low-Mass Stars and Giant Planets." *ApJS* 99 (August): 713. doi:10.1086/192204.

Saumon, D., and M. S. Marley. 2008. "The Evolution of L and T Dwarfs in Color-Magnitude Diagrams." *ApJ* 689, 1327-1344 (December): 1327–1344. doi:10.1086/592734. arXiv: 0808.2611.

Schmidt, S. J., K. L. Cruz, B. J. Bongiorno, J. Liebert, and I. N. Reid. 2007. "Activity and Kinematics of Ultracool Dwarfs, Including an Amazing Flare Observation." *AJ* 133 (May): 2258–2273. doi:10.1086/512158. eprint: astro-ph/0701055.

Schmidt, S. J., S. L. Hawley, A. A. West, J. J. Bochanski, J. R. A. Davenport, J. Ge, and D. P. Schneider. 2015. "BOSS Ultracool Dwarfs. I. Colors and Magnetic Activity of M and L Dwarfs." *AJ* 149, 158 (May): 158. doi:10.1088/0004-6256/149/5/158. arXiv: 1410.0014 [astro-ph.SR].

Schmidt, S. J., A. A. West, S. L. Hawley, and J. S. Pineda. 2010. "Colors and Kinematics of L Dwarfs from the Sloan Digital Sky Survey." *AJ* 139 (May): 1808–1821. doi:10.1088/0004-6256/139/5/1808. arXiv: 1001.3402 [astro-ph.SR].

Schmitt, J. H. M. M., and C. Rosso. 1988. "EXOSAT observations of M dwarf stars in the solar neighborhood." *A&A* 191 (February): 99–108.

Schneider, A. C., M. C. Cushing, J. D. Kirkpatrick, C. R. Gelino, G. N. Mace, E. L. Wright, P. R. Eisenhardt, M. F. Skrutskie, R. L. Griffith, and K. A. Marsh. 2015. "Hubble Space Telescope Spectroscopy of Brown Dwarfs Discovered with the Wide-field Infrared Survey Explorer." *ApJ* 804, 92 (May): 92. doi:10.1088/0004-637X/804/2/92. arXiv: 1502.05365 [astro-ph.SR].

Schrijver, C. J., G. Aulanier, A. M. Title, E. Pariat, and C. Delannée. 2011. "The 2011 February 15 X2 Flare, Ribbons, Coronal Front, and Mass Ejection: Interpreting the Three-dimensional Views from the Solar Dynamics Observatory and STEREO Guided by Magnetohydrodynamic Flux-rope Modeling." *ApJ* 738, 167 (September): 167. doi:10.1088/0004-637X/738/2/167.

Schrijver, C. J., J. Cote, C. Zwaan, and S. H. Saar. 1989. "Relations between the photospheric magnetic field and the emission from the outer atmospheres of cool stars. I - The solar CA II K line core emission." *ApJ* 337 (February): 964–976. doi:10.1086/167168.

Schrijver, C. J., A. K. Dobson, and R. R. Radick. 1992. "Nearly simultaneous observations of chromospheric and coronal radiative losses of cool stars." *A&A* 258 (May): 432–448.

Schubert, G., J. D. Anderson, T. Spohn, and W. B. McKinnon. 2007. "Interior Composition, Structure and Dynamics of the Galilean Satellites." In *Jupiter,* edited by F. Bagenal, T. E. Dowling, and W. B. McKinnon, 281. March.

Schubert, G., and K. M. Soderlund. 2011. "Planetary magnetic fields: Observations and models." *Physics of the Earth and Planetary Interiors* 187 (August): 92–108. doi:10.1016/j.pepi.2011.05.013.

Serio, A. W., and J. T. Clarke. 2008. "The variation of Io's auroral footprint brightness with the location of Io in the plasma torus." *Icarus* 197 (September): 368–374. doi:10.1016/j.icarus.2008.03.026.

Shields, A. L., S. Ballard, and J. A. Johnson. 2016. "The Habitability of Planets Orbiting M-dwarf Stars." *ArXiv e-prints* (October). arXiv: 1610.05765 [astro-ph.EP].

Shulyak, D., A. Reiners, S. Wende, O. Kochukhov, N. Piskunov, and A. Seifahrt. 2010. "Modelling the molecular Zeeman-effect in M-dwarfs: methods and first results." *A&A* 523, A37 (November): A37. doi:10.1051/0004-6361/201015229. arXiv: 1008.2512 [astro-ph.SR].

Siegler, N., L. M. Close, A. J. Burgasser, K. L. Cruz, C. Marois, B. Macintosh, and T. Barman. 2007. "Discovery of a 66 mas Ultracool Binary with Laser Guide Star Adaptive Optics." *AJ* 133 (May): 2320–2326. doi:10.1086/513273. eprint: astro-ph/0702013.

Simitev, R. D., and F. H. Busse. 2009. "Bistability and hysteresis of dipolar dynamos generated by turbulent convection in rotating spherical shells." *Europhys. Lett.* 85 (January): 19001. doi:10.1209/0295-5075/85/19001. arXiv: 0904.0799 [physics.flu-dyn].

Skemer, A. J., C. V. Morley, K. N. Allers, T. R. Geballe, M. S. Marley, J. J. Fortney, J. K. Faherty, G. L. Bjoraker, and R. Lupu. 2016. "The First Spectrum of the Coldest Brown Dwarf." *ApJ* 826, L17 (August): L17. doi:10.3847/2041-8205/826/2/L17. arXiv: 1605.04902 [astro-ph.EP].

Skrutskie, M. F., R. M. Cutri, R. Stiening, M. D. Weinberg, S. Schneider, J. M. Carpenter, C. Beichman, et al. 2006. "The Two Micron All Sky Survey (2MASS)." *AJ* 131 (February): 1163–1183. doi:10.1086/498708.

Skumanich, A., C. Smythe, and E. N. Frazier. 1975. "On the statistical description of inhomogeneities in the quiet solar atmosphere. I - Linear regression analysis and absolute calibration of multichannel observations of the Ca/+/ emission network." *ApJ* 200 (September): 747–764. doi:10.1086/153846.

Smart, R. L., C. G. Tinney, B. Bucciarelli, F. Marocco, U. Abbas, A. Andrei, G. Bernardi, et al. 2013. "NPARSEC: NTT Parallaxes of Southern Extremely Cool objects. Goals, targets, procedures and first results." *MNRAS* 433 (August): 2054–2063. doi:10.1093/mnras/stt876. arXiv: 1306.4527 [astro-ph.SR].

Soderblom, D. R., J. R. Stauffer, J. D. Hudon, and B. F. Jones. 1993. "Rotation and chromospheric emission among F, G, and K dwarfs of the Pleiades." *ApJS* 85 (April): 315–346. doi:10.1086/191767.

Sreenivasan, B., and C. A. Jones. 2006. "The role of inertia in the evolution of spherical dynamos." *Geophysical Journal International* 164 (February): 467–476. doi:10.1111/j.1365-246X.2005.02845.x.

Stallard, T., H. Melin, S. W. H. Cowley, S. Miller, and M. B. Lystrup. 2010. "Location and Magnetospheric Mapping of Saturn's Mid-latitude Infrared Auroral Oval." *ApJ* 722 (October): L85–L89. doi:10.1088/2041-8205/722/1/L85.

Stauffer, J. R., J.-P. Caillault, M. Gagne, C. F. Prosser, and L. W. Hartmann. 1994. "A deep imaging survey of the Pleiades with ROSAT." *ApJS* 91 (April): 625–657. doi:10.1086/191951.

Stauffer, J. R., L. W. Hartmann, and D. W. Latham. 1987. "Rotational velocities of low-mass stars in the Hyades." *ApJ* 320 (September): L51–L55. doi:10.1086/184975.

Steenbeck, M., and F. Krause. 1966. "Erklärung stellarer und planetarer Magnetfelder durch einen turbulenzbedingten Dynamomechanismus." *Zeitschrift Naturforschung Teil A* 21 (August): 1285. doi:10.1515/zna-1966-0813.

Stellingwerf, R. F. 1978. "Period determination using phase dispersion minimization." *ApJ* 224 (September): 953–960. doi:10.1086/156444.

Stelzer, B., G. Micela, E. Flaccomio, R. Neuhäuser, and R. Jayawardhana. 2006. "X-ray emission of brown dwarfs: towards constraining the dependence on age, luminosity, and temperature." *A&A* 448 (March): 293–304. doi:10.1051/0004-6361:20053677. eprint: astro-ph/0511168.

Thompson, M. J., J. Toomre, E. R. Anderson, H. M. Antia, G. Berthomieu, D. Burtonclay, S. M. Chitre, et al. 1996. "Differential Rotation and Dynamics of the Solar Interior." *Science* 272 (May): 1300–1305. doi:10.1126/science.272.5266.1300.

Tinney, C. G., and I. N. Reid. 1998. "High-resolution spectra of very low-mass stars." *MNRAS* 301 (December): 1031–1048. doi:10.1046/j.1365-8711.1998.02079.x. eprint: astro-ph/9806004.

Treumann, R. A. 2006. "The electron-cyclotron maser for astrophysical application." *A&A Rev.* 13 (August): 229–315. doi:10.1007/s00159-006-0001-y.

Ulmschneider, P. 2003. "The Physics of Chromospheres and Coronae." In *Lectures on Solar Physics,* edited by H. M. Antia, A. Bhatnagar, and P. Ulmschneider, 619:232. Lecture Notes in Physics, Berlin Springer Verlag.

Umana, G., C. Trigilio, and S. Catalano. 1998. "Radio emission from Algol-type binaries. I. Results of 1992-1993 VLA survey." *A&A* 329 (January): 1010–1018.

Uno, H., C. L. Johnson, B. J. Anderson, H. Korth, and S. C. Solomon. 2009. "Modeling Mercury's internal magnetic field with smooth inversions." *Earth and Planetary Science Letters* 285 (August): 328–339. doi:10.1016/j.epsl.2009.02.032.

Valenti, J. A., G. W. Marcy, and G. Basri. 1995. "Infrared Zeeman analysis of epsilon Eridani." *ApJ* 439 (February): 939–956. doi:10.1086/175231.

Vernazza, J. E., E. H. Avrett, and R. Loeser. 1981. "Structure of the solar chromosphere. III - Models of the EUV brightness components of the quiet-sun." *ApJS* 45 (April): 635–725. doi:10.1086/190731.

Vidotto, A. A., M. Jardine, J. Morin, J.-F. Donati, P. Lang, and A. J. B. Russell. 2013. "Effects of M dwarf magnetic fields on potentially habitable planets." *A&A* 557, A67 (September): A67. doi:10.1051/0004-6361/201321504. arXiv: 1306.4789 [astro-ph.EP].

Vogt, M. F., M. G. Kivelson, K. K. Khurana, R. J. Walker, B. Bonfond, D. Grodent, and A. Radioti. 2011. "Improved mapping of Jupiter's auroral features to magnetospheric sources." *Journal of Geophysical Research (Space Physics)* 116, A03220 (March): 3220. doi:10.1029/2010JA016148.

Vrba, F. J., A. A. Henden, C. B. Luginbuhl, H. H. Guetter, J. A. Munn, B. Canzian, A. J. Burgasser, et al. 2004. "Preliminary Parallaxes of 40 L and T Dwarfs from the US Naval Observatory Infrared Astrometry Program." *AJ* 127 (May): 2948–2968. doi:10.1086/383554. eprint: astro-ph/0402272.

Wannawichian, S., J. T. Clarke, and J. D. Nichols. 2010. "Ten years of Hubble Space Telescope observations of the variation of the Jovian satellites' auroral footprint brightness." *Journal of Geophysical Research (Space Physics)* 115, A02206 (February): A02206. doi:10.1029/2009JA014456.

Wei, Y., M. Fraenz, E. Dubinin, J. Woch, H. Lühr, W. Wan, Q.-G. Zong, et al. 2012. "Enhanced atmospheric oxygen outflow on Earth and Mars driven by a corotating interaction region." *Journal of Geophysical Research (Space Physics)* 117, A03208 (March): A03208. doi:10.1029/2011JA017340.

West, A. A., S. L. Hawley, J. J. Bochanski, K. R. Covey, I. N. Reid, S. Dhital, E. J. Hilton, and M. Masuda. 2008. "Constraining the Age-Activity Relation for Cool Stars: The Sloan Digital Sky Survey Data Release 5 Low-Mass Star Spectroscopic Sample." *AJ* 135 (March): 785–795. doi:10.1088/0004-6256/135/3/785. arXiv: 0712.1590.

West, A. A., S. L. Hawley, L. M. Walkowicz, K. R. Covey, N. M. Silvestri, S. N. Raymond, H. C. Harris, et al. 2004. "Spectroscopic Properties of Cool Stars in the Sloan Digital Sky Survey: An Analysis of Magnetic Activity and a

Search for Subdwarfs." *AJ* 128 (July): 426–436. doi:10.1086/421364. eprint: astro-ph/0403486.

White, S. M., and E. Franciosini. 1995. "Circular polarization in the radio emission of RS canum venaticorum binaries." *ApJ* 444 (May): 342–349. doi:10.1086/175609.

White, S. M., M. R. Kundu, and P. D. Jackson. 1989. "Simple non-thermal models for the quiescent radio emission of dMe flare stars." *A&A* 225 (November): 112–124.

Williams, P. K. G., and E. Berger. 2015. "The Rotation Period and Magnetic Field of the T Dwarf 2MASSI J1047539+212423 Measured From Periodic Radio Bursts." *ArXiv e-prints* (February). arXiv: 1502.06610 [astro-ph.SR].

Williams, P. K. G., E. Berger, and B. A. Zauderer. 2013. "Quasi-quiescent Radio Emission from the First Radio-emitting T Dwarf." *ApJ* 767, L30 (April): L30. doi:10.1088/2041-8205/767/2/L30. arXiv: 1301.2321 [astro-ph.SR].

Williams, P. K. G., S. L. Casewell, C. R. Stark, S. P. Littlefair, C. Helling, and E. Berger. 2015. "The First Millimeter Detection of a Non-Accreting Ultracool Dwarf." *ApJ* 815, 64 (December): 64. doi:10.1088/0004-637X/815/1/64. arXiv: 1511.05559 [astro-ph.SR].

Williams, P. K. G., B. A. Cook, and E. Berger. 2014. "Trends in Ultracool Dwarf Magnetism. I. X-Ray Suppression and Radio Enhancement." *ApJ* 785, 9 (April): 9. doi:10.1088/0004-637X/785/1/9. arXiv: 1310.6757 [astro-ph.SR].

Williams, P. K. G., J. E. Gizis, and E. Berger. 2016. "Variable and polarized radio emission from the T6 brown dwarf WISEP J112254.73+255021.5." *ArXiv e-prints* (August). arXiv: 1608.04390 [astro-ph.SR].

Wilson, P. A., A. Rajan, and J. Patience. 2014. "The brown dwarf atmosphere monitoring (BAM) project. I. The largest near-IR monitoring survey of L and T dwarfs." *A&A* 566, A111 (June): A111. doi:10.1051/0004-6361/201322995. arXiv: 1404.4633 [astro-ph.SR].

Winglee, R. M. 1985. "Fundamental and harmonic electron cyclotron maser emission." *J. Geophys. Res.* 90 (October): 9663–9674. doi:10.1029/JA090iA10p09663.

Wolszczan, A., and M. Route. 2014. "Timing Analysis of the Periodic Radio and Optical Brightness Variations of the Ultracool Dwarf, TVLM 513-46546." *ApJ* 788, 23 (June): 23. doi:10.1088/0004-637X/788/1/23. arXiv: 1404.4682 [astro-ph.SR].

Wright, E. L., P. R. M. Eisenhardt, A. K. Mainzer, M. E. Ressler, R. M. Cutri, T. Jarrett, J. D. Kirkpatrick, et al. 2010. "The Wide-field Infrared Survey Explorer (WISE): Mission Description and Initial On-orbit Performance." *AJ* 140, 1868-1881 (December): 1868–1881. doi:10.1088/0004-6256/140/6/1868. arXiv: 1008.0031 [astro-ph.IM].

Wright, N. J., and J. J. Drake. 2016. "Solar-type dynamo behaviour in fully convective stars without a tachocline." *Nature* 535 (July): 526–528. doi:10.1038/nature18638. arXiv: 1607.07870 [astro-ph.SR].

Yadav, R. K., U. R. Christensen, J. Morin, T. Gastine, A. Reiners, K. Poppenhaeger, and S. J. Wolk. 2015. "Explaining the Coexistence of Large-scale and Small-scale Magnetic Fields in Fully Convective Stars." *ApJ* 813, L31 (November): L31. doi:10.1088/2041-8205/813/2/L31. arXiv: 1510.05541 [astro-ph.SR].

Yadav, R. K., U. R. Christensen, S. J. Wolk, and K. Poppenhaeger. 2016. "Magnetic Cycles in a Dynamo Simulation of Fully Convective M-star Proxima Centauri." *ApJ* 833, L28 (December): L28. doi:10.3847/2041-8213/833/2/L28. arXiv: 1610.02721 [astro-ph.SR].

York, D. G., J. Adelman, J. E. Anderson Jr., S. F. Anderson, J. Annis, N. A. Bahcall, J. A. Bakken, et al. 2000. "The Sloan Digital Sky Survey: Technical Summary." *AJ* 120 (September): 1579–1587. doi:10.1086/301513. eprint: astro-ph/0006396.

Yu, S., G. Hallinan, J. G. Doyle, A. L. MacKinnon, A. Antonova, A. Kuznetsov, A. Golden, and Z. H. Zhang. 2011. "Modelling the radio pulses of an ultracool dwarf." *A&A* 525, A39 (January): A39. doi:10.1051/0004-6361/201015580. arXiv: 1009.1548 [astro-ph.SR].

Yu, Z. J., H. K. Leinweber, and C. T. Russell. 2010. "Galileo constraints on the secular variation of the Jovian magnetic field." *Journal of Geophysical Research (Planets)* 115, E03002 (March): E03002. doi:10.1029/2009JE003492.

Zarka, P. 1992. "The auroral radio emissions from planetary magnetospheres - What do we know, what don't we know, what do we learn from them?" *Advances in Space Research* 12 (August): 99–115. doi:10.1016/0273-1177(92)90383-9.

———. 1998. "Auroral radio emissions at the outer planets: Observations and theories." *J. Geophys. Res.* 103 (September): 20159–20194. doi:10.1029/98JE01323.

———. 2007. "Plasma interactions of exoplanets with their parent star and associated radio emissions." *Planet. Space Sci.* 55 (April): 598–617. doi:10.1016/j.pss.2006.05.045.

Zarka, P., R. A. Treumann, B. P. Ryabov, and V. B. Ryabov. 2001. "Magnetically-Driven Planetary Radio Emissions and Application to Extrasolar Planets." *Ap&SS* 277 (June): 293–300. doi:10.1023/A:1012221527425.